Politecnico di Torino

Corso di Laurea Magistrale in Ingegneria Biomedica
A. A. 2021/2022
Sessione di Laurea Magistrale: Dicembre 2022

Development of nanotheranostic systems via Layer-by-Layer assembly for the treatment of osteosarcoma

Supervisors

Prof.ssa Chiara Tonda-Turo
Dr. Irene Carmagnola
Prof. Piergiorgio Gentile

Candidate

Simone Margini
Matricola: 288098

Declaration of work

I declare that this thesis is based on my own work and has not been submitted in any form for another degree at any University or any other tertiary education. Information derived from published and unpublished work of others have been acknowledged in the text and in the list of references given in the bibliography.

ABSTRACT

Osteosarcoma (OS) is a rare primary bone cancer with a worldwide incidence of 3.4 million people per year and it is most often diagnosed in children. Due to the limits of current cancer treatments, the development of nanotheranostic platforms, which combine the therapeutic potential of drug compounds with the diagnostic potential of imaging probes in the same vehicle, has attracted the attention of researchers in recent decades, enabling improvements in drug delivery to specific sites and real-time vehicle tracking.

Regarding the field of bioimaging, Quantum Dots (QD) are promising nanoparticles (NPs), but with poor biocompatibility. In this context, the use of carbon-based QD (CQDs) can improve cytocompatibility; thus, my project has been focused on the development of CQDs derived from different natural sources, such as chitin (CHCQDs) and ground coffee (GCCQDs).

Morphology, optical and physico-chemical properties of each CQDs were analysed by Fourier Transformed Infrared spectroscopy (FTIR-ATR), X-ray photoelectron spectroscopy (XPS), ζ-Potential, High-resolution transmission electron microscopy (HRTEM), and UV-Visible (UV-Vis), showing a round-shaped structure, negative surface charge, and excitation-dependent emission. Finally, their cytocompatibility was evaluated on neo-dermal fibroblasts by Live/Dead and PrestoBlue assays, showing high cell viability up to a concentration of 500 μg/mL of CQDs in culture medium.

Next, two different nanotheranostic systems by exploiting the immersive self-assembly layer-by-layer technique (LbL) have been developed. LbL represents an easy and versatile technology used in various fields to create multi-layered nanocoating. In this work, chitosan (CH) and Chondroitin Sulfate (CS) were used as polyelectrolytes for the deposition of seven layers for both systems produced. The first system involved the fabrication of a calcium phosphate (CaP) core containing Doxorubicin (DOXO) stabilized by the deposition of Poly(allylamine hydrochloride) (PAH) through a pumping system. Then, DOXO and GCCQDs were incorporated into the layers after dissolution in CH and CS, respectively. The second system was a drug codelivery (CQDs_7DD) consisting of a negative core of CHBOCQDs coated with CH and CS as polyelectrolytes containing DOXO and Docetaxel (DTX). As the outer layer, pure CH was deposited in both systems.

Using the saturation method, the final particles loaded with drugs and CQDs showed a size of about 100 nm with a spherical and mostly uniform morphology. The encapsulation efficiency (EE) of DOXO in the CaP system with seven layers (CaP_7DC) was 47.98 %, while CQDs_7DDs showed an EE of less than 30% for both drugs. The 7 layers in the systems ensure time-modulated drug release. In fact, both types of NPs are affected by the burst release effect in the first 24 hours (greater than 50 %), but the remaining amounts of drugs are released in the next 28 days.

Cell growth inhibition of U2OS and Saos-2 cells caused by NPs was evaluated using by Live/Dead, PrestoBlue and immunostaining assays. In the case of Saos-2, the synergistic effect of the two drugs in the CQDs_7DD

could be appreciated even for low particle concentrations. However, this did not occur for U2O2 cells. CaP_7DC showed an absence of Saos-2 cell viability for a NPs concentration of 500 µg/mL. A slightly different trend was observed for U2O2 cells. Finally, TEM analysis of the Saos-2 confirmed the therapeutic efficacy of these NPs by exploiting the enhanced permeability and retention (EPR) effect of cancer cells.

Acknowledgements

Questo percorso è giunto al capolinea. Sono stati due anni lunghi, tortuosi, ma ricchi di gioie ed emozioni. Dunque, è giunto il momento di rendere grazie alle persone che mi hanno aiutato in questo tragitto.

Vorrei ringraziare la Prof.ssa Chiara Tonda-Turo e la Dr.ssa Irene Carmagnola per avermi permesso di vivere l'avventura più bella della mia vita e per essere state sempre disponibili nei miei confronti.

Concedetemi qualche riga per ringraziare Piergiorgio.
Grazie, davvero.
Sei stato professore, psicologo e amico allo stesso tempo. Ho scoperto una umanità che non credevo le persone potessero avere. Ricordo ancora oggi come era iniziata (spoiler: non bene).
Nonostante questo, ti sei fidato ciecamente, dandomi l'opportunità di lavorare, di studiare, di capire e di dimostrare quello che valgo. E per questo ti sarò sempre grato.
Inoltre, grazie per essermi stato sempre vicino e per avermi trasmesso un pezzo della tua infinita passione per il tuo lavoro.

Un sincero ringraziamento va anche ad Annachiara e a Priscila per la loro disponibilità e per la loro fiducia smisurata nei miei confronti. Entrambe hanno creato un clima incredibile nei mesi passati a Newcastle, facendomi sentire a casa ogni singolo giorno passato insieme. Inoltre, siete tra le poche persone ad avermi capito e letto interiormente, aiutandomi ad affrontare le mie paure nei giorni meno virtuosi (e ce ne sono stati parecchi!).

Grazie a Roberta per essermi sempre stata vicina anche quando siamo stati lontani e per avermi aiutato e sostenuto negli ultimi mesi, tra le mie infinite difficoltà e paranoie. Nonostante tutto, il nostro legame è più forte che mai e sono veramente grato di averti accanto. Ti voglio tanto bene.

Infine, voglio ringraziare mamma Tamara e papà Massimiliano, insieme a mia sorella Aurora e a mio fratello Maurizio. Ah, dimenticavo Lillino, il nostro cagnolino.
Sono stati due anni di scelte importanti e voi mi avete supportato sempre e comunque, nonostante le mille difficoltà economiche e affettive. Noi abbiamo un legame speciale, indelebile e ci siamo sempre l'uno per l'altra, indistintamente dalle difficoltà o dalle gioie del momento.
Grazie per essermi stati vicino in questo lungo e intenso percorso.
Spero di avervi reso un po' più orgogliosi di me.

“To those who believe in their dreams”

Table of Contents

List of Figures

Chapter 1

Chapter 2

Chapter 3

List of Tables

Chapter 1

Chapter 2

Chapter 3

Chapter 1: Introduction to osteosarcoma and state of the art

1.1. Introduction to osteosarcoma

1.1.1. Bone

Bone is one of the fundamental units that make up the skeletal system of the human body that confers multiple functions: physical support and movement to the body, blood production due to the presence of bone marrow, electrolyte balance, acid-base balance ensured by the bone tissue that buffers the blood against excessive pH changes, and detoxification through absorption of heavy metals and other toxic elements in the blood (Kenneth S. Saladin, Anatomia Umana, Padova, Piccin-Nuova Libraria,2012, 3rd Edition).
Bone consists mainly of bone tissue, which is connective tissue in which the matrix is mineralized because of the deposition of calcium phosphate and other minerals. Specifically, the inorganic matter of the matrix consists of 85% hydroxyapatite, 10% calcium carbonate, and smaller amounts of magnesium, sodium, potassium, fluoride, sulphate, carbonate, and hydroxide ions (John D. Currey, Bones: structure and Mechanics, New Jersey, Princeton University Press, 2002). Inorganic matter is more present than organic matter, which consists of collagen and protein and carbohydrate complexes (Kenneth S. Saladin, Anatomia Umana, Padova, Piccin-Nuova Libraria,2012, 3rd Edition).
In general, bone exhibits a highly hierarchical structure in which there is an outer shell of dense white bone tissue (called cortical bone) enclosing some lesser organized tissue (spongy tissue), as shown in Fig. 1.
Cortical bone imparts rigidity, hardness and resistance to mechanical stress (Sultana and Wang, 2008). In general, cortical bone sections have concentric lamellaes organized into osteons, which are layers of matrix arranged concentrically around Havers' canal (which have nerves and vessels, both blood and lymphatic) (Frederich H. Martini, Michael J. Timmons, Robert B. Tallitsch, Anatomia Umana, Edises, 5th Edition, 2012). Other small channels are reserved for blood vessels, cells and their processes, which are necessary to keep it alive.
The spongy bone has an alveolar structure and consists of a network of variously oriented and intersecting bone fragments (spicules) and trabeculae, which delimit medullary cavities containing red (haematopoietic) and yellow (fatty) marrow (Frederich H. Martini, Michael J. Timmons, Robert B. Tallitsch, Anatomia Umana, Edises, 5th edition, 2012). The distribution of the trabeculae depends on the load lines; spongy bone is thus adapted to withstand stresses that are not too great but come from different directions (Sultana and Wang, 2008).
Moreover, the various parts of the bone communicate with each other (anastomoses) through transversely and obliquely arranged channels, called Volkmann's channels.

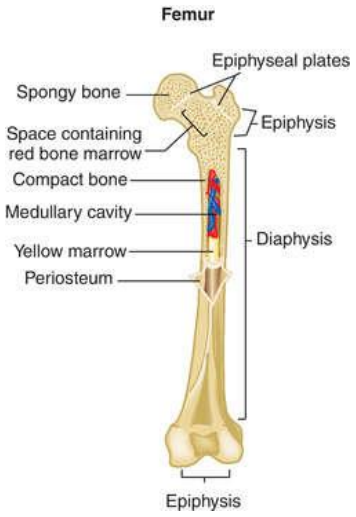

Fig. 2 Femur anatomy. Source: https://medical-dictionary.thefreedictionary.com/bone

The previously named tissues consist of cells and fibres. In detail:

- Osteogenic (osteoprogenitor) cells are stem cells originating from the embryonic mesenchyme and capable of differentiating into osteoblasts (Jane E. Aubin, 1999). They are most found in the endosteum, periosteum and central canals.
- Osteoblasts are cells that mineralize and synthesize the matrix of bone, in particular collagen, glycosaminoglycans, proteoglycans, and glycoproteins (Kenneth S. Saladin, Anatomia Umana, Padova, Piccin-Nuova Libraria,2012, 3rd Edition). These cells are highly hierarchically organized in rows in the endosteum and periosteum. In addition, osteoblasts do not undergo mitosis.
- Osteoblasts trapped within matrix lacunae are named osteocytes. The lacunae are connected to each other through canaliculi, allowing osteocytes physical communication through their own GAP junctions, thus promoting bone matrix remodelling, maintenance of homeostatic balance and bone density. In addition, osteocytes are also stress sensors through which it will be possible to regulate bone remodelling according to the stresses applied to the bone (Rinaldo Florencio-Silva et al., 2015).
- Osteoclasts are cells responsible for bone resorption. They are found mainly on the bone surface and develop from bone marrow stem cells. These cells have hydrogen pumps in their plasma membrane that secrete hydrogen ions into the extracellular fluid, which will attract chlorine ions present in said fluid (J. M. Hock et al., 2009). The space between osteoclast and bone is filled with hydrochloric acid (HCl) (with a pH of about 4), which is responsible for dissolving minerals in the bone (Fauci AS, Kasper DL, Braunwald E, Hauser SL, Longo DL, Kameson JL, Loscalzo J, Harrison's Principles of Internal Medicine, 17th edition). In addition, the resorption action is also mediated by osteoclast lysosomes, as they release enzymes that digest the organic component of bone.

1.1.2. Cancer

1.1.2.1. General features

According to oncologist Rupert Allan Willis, neoplasm or tumour is "*a mass of tissue that grows in excess and in an uncoordinated manner relative to normal tissues and persists in this state after the cessation of the stimuli that induced the process*". Tumours can be classified as benign or malignant.

Benign tumours tend to grow slowly and have well-defined boundaries, without spreading into local or distal structures of the body. Moreover, they are unlikely to recur once removed but some specific types of them can develop into malignant tumours (Aisha Patel, 2020). On the other hand, the term cancer identifies tumours with a malignant nature, highly known to be the second leading cause of death globally, with an estimated 9.6 million deaths in 2018 (https://www.who.int/health-topics/cancer#tab=tab_1).

Specifically, cancer refers to a broad group of diseases that can arise in almost any organ or tissue of the body where abnormal cells tend to proliferate in an uncontrolled manner, remaining undifferentiated (Meijers & De Boer, 2019), and then detach from the original tumour and enter the bloodstream or lymphatic system to spread to other areas of the body (Aisha Patel, 2020; Christine L. Chaffer and Robert A. Weinberg, 2011). The latter process is called *metastasization* and is a major cause of cancer death. Most metastatic cancers are manageable, but not curable, as currently available treatments can only alleviate symptoms, slowing tumour growth and improving quality of life (https://my.clevelandclinic.org/health/diseases/22213-metastasis-metastatic-cancer).

There are also other terms that describe tumours in a complementary way such as tumour stage and tumour grade. While the former indicates how large tumour is and how far it has spread in the body (low-grade tumours only recur in the same area, whereas high-grade tumours metastasize to other parts of the body and can recur anywhere in the body), the latter describes how abnormal characteristics of tumour cells are pronounced (https://www.airc.it).

Cancers are generally caused by alterations in genes that control cell behaviour; these genetic variations can also be inherited (Weinberg et al. 1996). However, there are other risk factors that can expose an individual more to possible future cancer, such as environment and lifestyle (such as tobacco, alcohol, poor diet, lack of physical activity, and being overweight) (Meijers & De Boer, 2019).

The implementation of screening analyses and increased access to available treatments in a timely manner are critical features to being able to counter cancer mortality rates.

However, the effects of this type of disease affect all areas of life, including the economy, making hospital care unaffordable for a not insignificant number of patients.

1.1.2.2. Cancer Hallmarks

According to Hanahan and Weinberg (2000), cancer possesses a group of common biological capabilities that enable its development, progression, and persistence. The hallmarks of cancer are: sustaining proliferative signalling, evading growth suppressors, resisting cell death, allowing replicative immortality, inducing angiogenesis, activating invasion and metastasis (Fig. 2A).

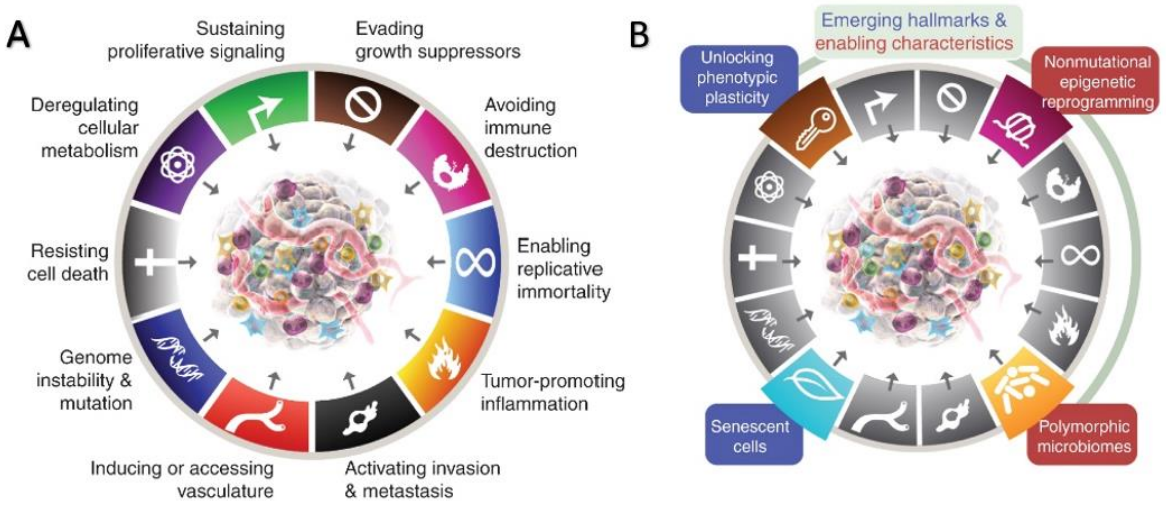

Fig. 2: The Hallmarks of Cancer, towards 2022.
A. The Hallmarks of Cancer currently include eight capabilities and two enabling features.
B. New version of the Hallmarks incorporating the emerging features proposed in 2022.
Source: Douglas Hanahan, 2022

The first Hallmark concerns the deregulation of cell homeostasis signals by producing growth factors by autocrine proliferative stimulation, by overexpressing cell surface receptors, by interchanging signals between tumour cells and normal cells infiltrated in the stroma, or by structurally modifying cell surface receptors to overcome ligand-mediated receptor activation (Cheng et al., 2008, Bhowmick et al., 2004).

Furthermore, mutations in the Ras oncoprotein can induce the disruption of intracellular negative feedback mechanisms for the attenuation of proliferative signalling, further enhancing uncontrolled proliferation (Wertz and Dixit, 2010, Cabrita and Christofori, 2008, Amit et al., 2007, Mosesson et al., 2008) that is one of the first intrinsic cellular defence mechanisms. Therefore, there is a trade-off between mitogenic stimulation and the avoidance of these anti-proliferative defences (Hanahan and Weinberg, 2000).

Cellular homeostasis is also obviated by the presence of the cell-cell contact inhibition mechanism in tumorigenesis. To evade growth suppressors, cancer cells exhibit various mechanisms that alter oncosopressors that govern the cells' decisions to proliferate or, alternatively, to activate senescence and apoptotic programmes (Hanahan and Weinberg, 2000).

There are several articles in the literature attesting that programmed cell death by apoptosis is one of the first natural barriers in response to physiological stresses or signalling imbalances resulting from oncogenes or DNA damage associated with hyperproliferation (Adams and Cory, 2007; Hanahan and Weinberg, 2011).

However, cancer cells develop several strategies to limit or circumvent apoptosis and the most common is the loss of function of tumour suppressor TP53 which normally induces apoptosis through upregulation of BH3 proteins Noxa and Puma in response to substantial levels of DNA breaks and other chromosomal abnormalities (Hanahan and Weinberg, 2000). Alternatively, tumours can achieve similar goals by increasing the expression of anti-apoptotic regulators (Bcl-2, Bcl-xL) and downregulating pro-apoptotic factors (Bax, Bim) or by short-circuiting the ligand-induced extrinsic death pathway (Hanahan and Weinberg, 2000; Adams and Cory, 2007).

Unlike healthy lineage cells, cancer cells can avoid the mechanisms of cellular senescence and apoptosis induced by the oncosuppressors pRB and TP53, thanks to the upregulated presence of telomerase, which adds telomeric repeat segments to the ends of telomeric DNA (Hanahan and Weinberg, 2000). Therefore, telomere elongation confers unlimited replicative potential to tumour cells (termed *'immortalised'*) leading towards the development of a neoplastic mass.

Like normal tissues, tumours need nourishment and to evacuate their waste products. Therefore, the tumour responds to the condition of cellular hypoxia by generating a neo-vasculature through the process of angiogenesis using aberrant signalling proteins (vascular endothelial growth factor-A (VEGF) and thrombospondin-1) that bind to vascular endothelial cell receptors (Ferrara, 2009, Mac Gabhann and Popel, 2008, Carmeliet, 2005; Hanahan and Weinberg, 2000).

This stage of tumorigenesis is closely related to the subsequent invasion and metastasising process of cancer cells (Talmadge and Fidler, 2010, Fidler, 2003). Thus, cancer cells invade locally into blood and lymphatic vessels close to the tumour, then transit through these systems and leak into the parenchyma of distant tissues, forming first nodules and then macroscopic lesions (Hanahan and Weinberg, 2000).

However, the regulators of invasion and metastasis are still largely unknown and their upregulated and downregulated functioning is very complex (Hanahan and Weinberg, 2011; Cavallaro and Christofori, 2004).

According to Hanahan and Weinberg (2011), the acquisition of these six acquired functional capacities of cancer cells is made possible by two enabling features. The first enabling characteristic is the loss of genomic stability in cancer cells resulting from defects in the 'gatekeepers' of the genome (defined by Kinzler and Vogelstein, 1997) and the partial loss of telomeric DNA (Artandi and DePinho, 2010) during tumour progression (Hanahan and Weinberg, 2011). Consequently, tumour cells acquire an enabling mutant genotype that allows their maintenance, growth and dominance in the tissue environment (Hanahan and Weinberg, 2011; Negrini et al., 2010; Salk et al., 2010).

The second enabling condition is the promotion of the inflammatory state by premalignant and malignant lesions caused by the cells of the immune system (Hanahan and Weinberg, 2011). In the literature, there are studies testifying to the chronic inflammatory condition resulting from the infiltration of immune system cells into tumours (Dvorak, 1986; Pagès et al., 2010). The main purpose of the inflammatory condition is to eradicate the tumour mass; however, it has been found that this condition facilitates tumour progression as

it provides several bioactive molecules to the tumour microenvironment that support the characteristic capabilities discussed above (DeNardo et al., 2010; Grivennikov et al., 2010; Qian and Pollard, 2010; Colotta et al., 2009; Karnoub and Weinberg, 2006-2007). Furthermore, inflammation can release reactive oxygen species, which are actively mutagenic for neighbouring tumour cells and accelerating their genetic evolution towards more malignant states (Hanahan and Weinberg, 2011).

In 2011, Weinberg and Hanahan also discussed two new emerging hallmarks. The first concerned the reprogramming of cellular energy metabolism in tumour cells to support continued cell growth and proliferation. Under normal conditions, glycolysis is favoured under anaerobic conditions, however, According to Hanahan and Weinberg (2011), tumour cells possess a programmed phenotype that enables them to reprogram their metabolism by restricting it exclusively to glycolysis under aerobic conditions through the placement of glycolytic intermediates in various biosynthetic pathways in the cytoplasm that are required for the assembly of new cells, the activation of oncogenes (RAS, MYC) and mutating tumour suppressors (TP53). In addition, glycolysis can be further enhanced under hypoxic conditions (Hanahan and Weinberg, 2011).

The second hallmarks discussed by Weinberg and Hanahan (2011) concerned the active evasion of tumour cells from attack and elimination by immune cells. Indeed, highly immunogenic tumour cells can deactivate key elements of the immunoediting mechanism, such as CD8+ cytotoxic T lymphocytes, CD4+ Th1 helper T lymphocytes or natural killer cells, by secreting TGF-β or other immunosuppressive factors (Hanahan and Weinberg, 2011). This phenomenon is particularly pronounced in immunodeficient organisms (Vajdic and van Leeuwen, 2009).

Recently, Hanahan (2022) discussed the inclusion of new parameters and enabling features in the conceptualisation of cancer (Fig. 2B). These new parameters are: unlocking phenotypic plasticity, non-mutational epigenetic reprogramming, the presence of polymorphic microbiomes, and the presence of senescent cells.

Briefly, it is argued that tumour cells can either dedifferentiate by reverting to progenitor-like cell states, or that they can circumvent the mechanism of cell transdifferentiation, whereby cells initially engaged in one differentiation pathway switch to a completely different developmental programme, thereby acquiring tissue-specific characteristics that were not preordained (Hanahan, 2022).

According to Hanahan (2022), addition to the previously discussed features of genome instability and mutation, there is another purely epigenetic reprogramming mode of tumour phenotypes termed 'non-mutational epigenetic reprogramming', which mediates embryonic development, differentiation and organogenesis of cells. Thus, it is hypothesised that certain epigenetic alterations may contribute to the acquisition of distinctive capabilities during tumour development and malignant progression.

Also interesting is the discussion of the ecosystem's barrier tissues created by bacteria and fungi (polyform microbiomes) as an enabling feature influencing cancer acquisition and development due to recent correlations between polyform microbiomes and host organism health (Thomas S et al., 2017).

According to Sager (1991), senescence has long been considered a protective mechanism against neoplasia; however, there are several works in the literature that testify how senescent cells stimulate tumour development and malignant progression through the activation of a senescence-associated secretory phenotype that release several bioactive proteins to the tumour microenvironment cells, preventing apoptosis and allowing induction of angiogenesis, invasion and metastasis and suppressing tumour immunity (Hanahan, 2022).

The hypothesis that certain cell phenotypes possess a transient and reversible senescence mechanism is also very interesting (De Blander H et al, 2021); however in-depth studies are needed to confirm this.

The development of all these different characteristics of cancer cells is contemporaneous with the formation and maintenance of an evolving "*tumour microenvironment*" formed not only by a heterogeneous set of cancer cells but also by a heterogeneous set of infiltrating and resident host cells (immune cells, stromal cells, blood vessels), secreted factors and proteins from the extracellular matrix (Fig. 3) (Nicole M et al., 2020).

Reciprocal cell-cell and cell/ECM interactions force stromal cells to lose their function and acquire new phenotypes that promote tumour cell development and invasion, leading towards increased multidrug resistance (Roghayyeh Baghban et al., 2020).

It is important to emphasise the role of fibroblasts in tumour genesis. These generally tend to suppress tumour formation, however, fibroblasts associated with the tumour microenvironment may promote tumour genesis due to their high proliferative capacity and cytokine release, but also due to their ability to produce extracellular matrix, causing tissue remodelling and inciting tumour angiogenesis (Hanahan and Weinberg, 2011). So, the inhibition of these characteristics is a key to the success of cancer treatments to block the growth, enhancement and spread of tumour tissue (Hanahan and Weinberg, 2011).

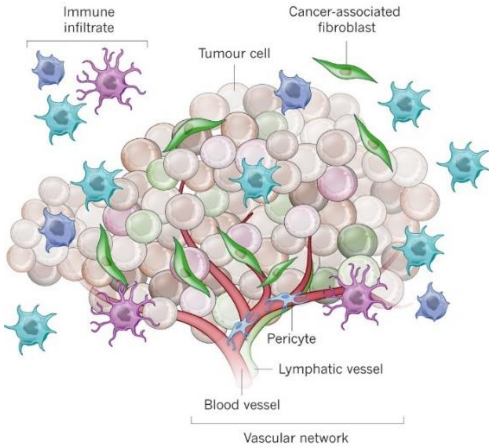

Fig. 3: Heterogeneity of tumour microenvironment. Source: Melissa R. Junttila & Frederic J. de Sauvage, 2013

1.1.3. Osteosarcoma

1.1.3.1. General features

Osteosarcoma is a rare primary malignant bone tumour that leads to the destruction of bone tissue and develops from defective differentiation of mesenchymal cells. (Raymond AK et al., 2009; https://www.cancer.net/cancer-types/osteosarcoma-childhood-and-adolescence/introduction).

1.1.3.2. Statistics

Seigel et al. (2022) estimate that in 2022 about 1,000 people in the United States of all ages will be affected by osteosarcoma and about half of these cases will occur in children and adolescents. Generally, osteosarcoma has a worldwide incidence of 3.4 per million people per year (Mirabello L. et al, 2009) and it makes up 2% of all cancers in children ages 0 to 14 and 3% of all cancers in teens ages 15 to 19; however, it can be diagnosed at any age (https://www.cancer.net/cancer-types/osteosarcoma-childhood-and-adolescence/statistics). In 2017 in Italy, the annual incidence of osteosarcoma is 0.17 cases per 100,000 inhabitants, i.e. 22% of primary malignant bone tumours (S. Busco et al. 2016).

Before the advent of chemotherapy (1970), the only available treatment was the amputation of the part circumscribed by the tumour (5-year survival rates for classic osteosarcoma were 20%) (A. Misaghi et al, 2018). In our days, thanks to the advent of chemotherapy and improved surgical practice, the 5-year overall survival rate estimated by Seigel R et al. (2022) for children aged 0-19 years with osteosarcoma is 68%, while the 5-year overall survival rate for people of all ages is 74%. However, if the cancer has metastasized, the 5-year survival rate is 27% (Simon MA et al., 1986; Seigel R et al., 2022).

1.1.3.3. Osteosarcoma Pathogenesis

A summary of the different factors contributing to the pathogenesis of osteosarcoma are shown in Tab.1.

Osteosarcoma shows a very wide range of incidence in terms of age; however, it tends to develop more in adolescence, therefore in the presence of high bone turnover where mesenchymal stem cells differentiate into osteoblastic cells (Mirabello L. et al, 2009).

According to Matthew L. Broadhead et al. 2010, defects in the osteogenic differentiation process are considered as a primary cause of the pathogenesis of osteosarcoma. In fact, under conditions of high bone turnover, these defects will be amplified by a deregulation of endogenous and exogenous factors due to an intrinsic under-expression of the transcriptional factor Runx2 (a factor that regulates the activity of bone morphogenetic proteins and is able to induce differentiation into an osteogenic lineage) or the defects may be amplified by non-native stimuli (e.g., pro-tumour inflammatory cytokines) (Sahitya K Denduluri et al., 2016).

Furthermore, abnormal expression of oncogenes and tumour suppressors are the molecular basis for the development of osteosarcoma. In the case of osteosarcoma, the c-Myc oncogene is generally over-expressed and correlates with increased cell invasiveness through activation of the MEK-ERK pathway, thus reducing apoptotic potential (Gamberi G. et al., 1998). Mutations in the tumour suppressor TP53 are commonly found in osteosarcoma cells and allow cells with damaged DNA repair mechanisms to evade apoptosis (Berman SD et al, 2008). A similar argument applies to Rb tumour suppressors that are regulators of the G1/S transition of the cell cycle and are found to be deficient in approximately 70% of all sporadic osteosarcoma cases (Sahitya K Denduluri et al, 2016).

Deregulation of cell signalling pathways, especially the insulin-like growth factor (IGF) signalling axis, is also an equally important piece in the development and progression of osteosarcoma (Richa Rathore and Brian A. Van Tine, 2021).

Moreover, inflammation and cytokine signalling have been strongly implicated in the tumorigenesis of osteosarcoma (Matthew L. Broadhead et al. 2010). Particularly interesting is the role of transforming growth factor β (TGF-β) as it is linked to the dedifferentiation of osteosarcoma cells into cancer stem cells which is a dynamic population associated with invasion, tumour migration (via MAPK activation), radio resistance and chemoresistance (Sahitya K Denduluri et al. 2016).

Interleukins also represent another important class of cytokines with a similar role in disease progression (Matthew L. Broadhead et al. 201). Interleukin 32, a pro-inflammatory cytokine, can promote invasion and migration of osteosarcoma cells through activation of the AKT pathway and upregulation of matrix metalloproteinases (Sahitya K Denduluri et al. 2016).

Another common feature in osteosarcoma is aneuploidy with chromosomal alterations (Judson Wlber Verissimo de Azevedo et al., 2019).

Generally, when tumour cells lose attachment to a basement membrane or matrix these should activate a mechanism of apoptosis called *anoikis* (Steven M Frisch et al., 2001). However, osteosarcoma cells exhibit resistance to apoptosis in this type of situation, promoting tumour angiogenesis which is essential for sustained osteosarcoma growth and metastatic development. Herein, VEGFs (which are pro-angiogenic factors) play an important role in upregulate matrix metalloproteinase, inducing antiapoptotic factors, and releasing other proangiogenic factors such as platelet-derived growth factor (PDGF) or angiopoietin 1 (Ziran Gao et al., 2019).

Moreover, bone invasion relies on interactions between osteoblasts and osteoclasts due to increased osteoclastic activity in bone-resorbing in some Osteosarcoma cases, facilitating further osteosarcoma cells invasion and the release of pro-resorptive cytokines. The main result is the formation of tumour–bone interface and it is made possible by the release of TGF-β from the degraded bone matrix (Isabel Fernandes et al., 2021).

In terms of immunogenicity, the osteosarcoma cells show intrinsic immunogenic properties due to their own genomic instability; in addition, immune responses can be influenced by the immune cells in the osteosarcoma microenvironment (Wu et al., 2020, cited in Isabel Fernandes et al., 2021).

FEATURES	STATUS	CORRELATION
6p21, 8q24 and 12q14 chromosome	Amplificated	Most common genomic alteration in Osteosarcoma
Heterozygosity of 10q21.1	Loss	Most common genomic alteration in Osteosarcoma
Li-Fraumeni or hereditary retinoblastoma	Positive	Extensive presence simultaneous with onset of osteosarcoma tumour
Activator protein 1 complex	Amplificated	Implicated in metastasis development
Myc	Amplificated	Resistance to chemotherapeutics
IGF (insulin-like growth factor)-I and IGF-II	Amplificated	Activate the PI3K and MAPK transduction pathways which cause increased proliferation and invasion, and reduced apoptosis of tumour cells
Parathyroid hormone-related peptide	Amplificated	Implicated in metastasis development
TGF-β	Overexpressed	Influences cell processes such as differentiation, proliferation, apoptosis and matrix production
VEGF	Action potentiated via phospholipase Cγ, protein kinase C and the c-Raf-MEK-MAPK cascades	promoting endothelial cell proliferation, migration and blood vessel maturation
Matrix metalloproteinases	Upregulated by VEGFs	Role in extracellular matrix degradation and in the invasion of surrounding tissues.
Wnt and Notch pathways	Activated	Pathways associated with tumorigenesis

Tab. 1: comparative table of factors expressed in osteosarcoma cells

The result of all these conditions is an imbalance between cell differentiation and proliferation that contributes to the creation of a malignant phenotype capable of unlimited proliferation, resistance to apoptosis, and evasion of senescence through DNA telomerases (Richa Rathore and Brian A. Van Tine, 2021).

As stated in the work of Sunetra Das et al. (2021), the study of genomic complexity has contributed to the discovery of mechanisms of immunosuppression associated with gene instability in osteosarcoma cells that could be exploited as future targets for new therapeutic approaches.

1.1.3.4. Classification

The histologic classification of bone tumours provided by the World Health Organization divides the different types of osteosarcomas according to their anatomical location (http://www.sarcomahelp.org/reviews/who-classification-sarcomas.html). Specifically, osteosarcoma can be central (also includes intramedullary tumours) and surface tumours. An extensive description of the different types of osteosarcomas can be found in the work of A. Misaghi et al. (2018) and will be briefly summarized in the following subsections.

1.1.3.4.1. Central Osteosarcomas

Conventional Osteosarcoma is the most common type of Osteosarcoma and can affect different types of individuals regardless of their age (http://www.sarcomahelp.org/reviews/who-classification-sarcomas.html). Generally, conventional osteosarcoma is a high-grade tumour and originates in the intramedullary cavity of the bone and then localizes mainly in the metaphysis of the long bones, as shown in Fig. 4 (Asif Saifuddin et al., 2019; Bielack SS et al., 2002, cited in Misaghi et al, 2018).
This type of tumour can be divided into osteoblastic, chondroblastic and fibroblastic depending on the predominant features of the cells (Misaghi et al, 2018).

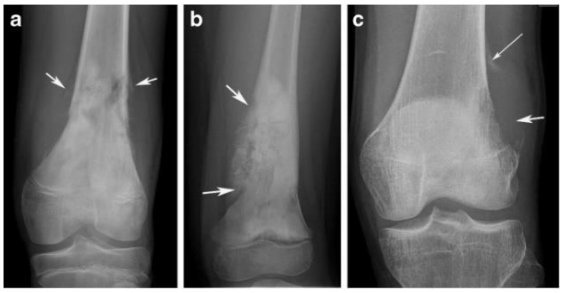

Fig. 4: Radiography of conventional osteosarcoma. White arrows indicate the tumour anatomical location. Source: Asif Saifuddin et al., 2019

Telangiectatic osteosarcoma accounts for 4% of osteosarcomas (Fletcher CD et al., 2002, cited in Misaghi et al, 2018). Histologically, telangiectatic osteosarcoma is characterized by dilated blood-filled cavities and high-grade sarcomatous cells on the septae and peripheral rim (Misaghi et al, 2018). Radiographically, telangiectatic osteosarcoma is in the metaphysis of the long bones and presents as an extensive eccentric lesion (Fig. 5) (https://tumoursurgery.org/tumour-education/bone-tumours/types-of-bone-tumours/telangiectatic-osteosarcoma.aspx).

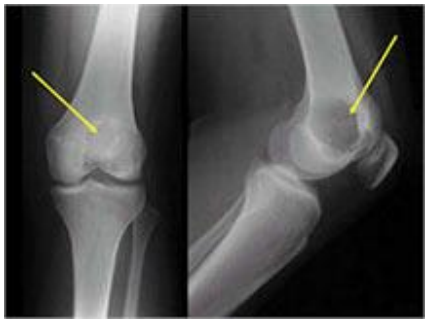

Fig. 5: Radiography of telangiectatic osteosarcoma. Yellow arrows indicate the tumour anatomical location. Source: (https://tumoursurgery.org/tumour-education/bone-tumours/types-of-bone-tumours/telangiectatic-osteosarcoma.aspx)

Small cell osteosarcoma constitutes 1-2% of cases and is characterized by the presence of small cells with hypopigmented round nuclei and poor nuclear polymorphism, as shown in Fig. 6 (Nakajima H et al.,1997, cited in Misaghi et al, 2018). Radiologically, a destructive process with eccentric and jagged areas can be visualized (Michael E. Mulligan et al. 1999).

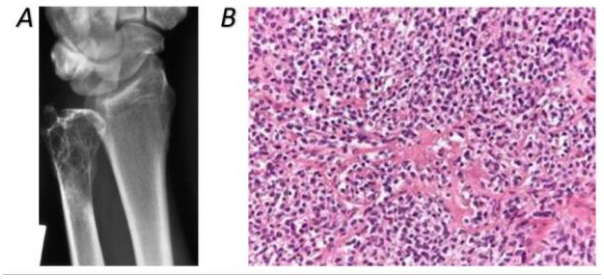

Fig. 6: A. Radiography of Small-Cell Osteosarcoma. Source: Michael E. Mulligan et al. 1999.
B. Histology of Small-Cell Osteosarcoma. Source: https://musculoskeletalkey.com/small-cell-osteosarcoma/

Low-grade osteosarcoma accounts for 1-2% of all osteosarcomas and predominantly affects adult individuals, localizing mainly in the long bones (Fletcher CD et al, 2002, cited in Misaghi et al, 2018).
This tumour is predominantly a fibroblastic osteosarcoma and can transform into a conventional osteosarcoma if not promptly recognized and treated (Fig. 7) (Misaghi et al, 2018; Makoto Endo MD et al, 2012; https://www.pathologyoutlines.com/topic/bonelgcentralosteo.html).

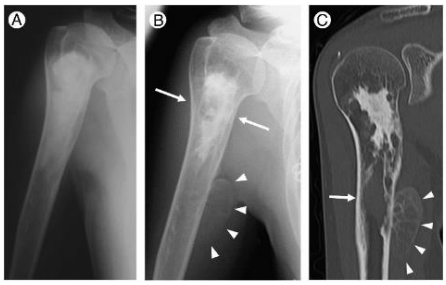

Fig. 7: Radiography of Low-Grade Osteosarcoma. Source: Makoto Endo MD et al. 2012

1.1.3.4.2. Superficial osteosarcomas

Parosteal osteosarcoma is a low-grade tumour that originates from the periosteum of long bones and shows a densely ossified and lobulated mass in radiological reports and parallel oriented streams of bone trabeculae in histological sections, as can be seen in Fig. 8 (Venkatesan Sampath Kumar et al., 2014; Klein MJet al., 2006, cited in Misaghi et al, 2018). The incidence rate of this tumour type settles at 4-6% of osteosarcomas (Misaghi et al, 2018).

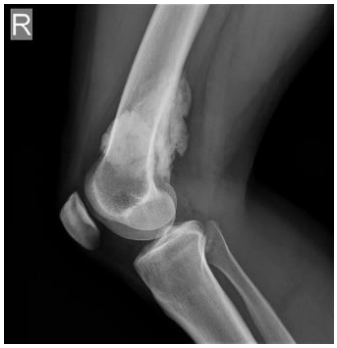

Fig. 8: Radiography of Parosteal Osteosarcoma. Source: https://radiopaedia.org/articles/parosteal-osteosarcoma-1?lang=us

Periosteal osteosarcoma is the rarest type of osteosarcoma tumours and develops between the cortex and the cambium layer of the periosteum producing a predominantly cartilaginous matrix with areas of calcification, as shown in Fig. 9 (Misaghi et al, 2018).

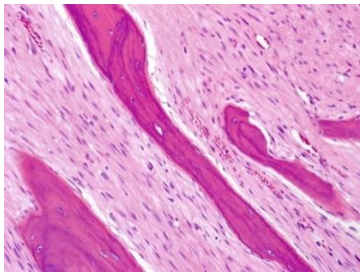

Fig. 9: Histology of Periosteal Osteosarcoma. Source: Carrie Y. Inwards & Doris E. Wenger, 2020

High-grade superficial osteosarcoma and is the rarest of osteosarcomas, showing radiologically as a superficial lesion with partial mineralization, with possible extension to surrounding soft tissues, as shown in Fig. 10 (Misaghi et al, 2018).

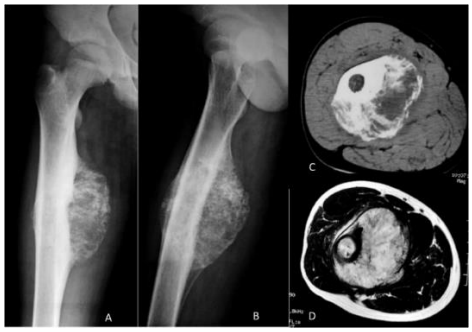

Fig. 10: Radiography of High-Grade Surface Osteosarcoma. Source: Zhiping Deng et al. 2020

1.1.3.5. Imaging and Diagnosis

In order to diagnose osteosarcoma quickly and efficiently, a preoperative imaging protocol has been developed in the recent past (A. Misaghi et al., 2018). This section will list all the technologies used according to the chronological order of the protocol and according to the increasing suspicion of osteosarcoma lesion (Hogendoorn PCW et al., 2010; Xin Zhao et al., 2021; Stefan S. Bielack et al., 2016).

In general, combining the advantages of different techniques can effectively guide the prognosis and choice of clinical procedures for treating patients. However, it is necessary to take into consideration the costs associated with the method used, the availability of technologies in hospitals, and the patient's accessibility to treatment.

1.1.3.5.1. X-Radiation

High spatial resolution radiographs are an effective, simple, and fast tool for locating and morphologically characterizing a tumour ((Xin Zhao et al., 2021; Stefan S. Bielack et al., 2016)

As a widely available technology, this examination is relatively accessible to most patients, so it is considered as the preferred tool for screening and preliminary diagnosis of lesions (Joel D. Howell, 1996).

However, radiographic examination does not allow visualization of small bony lesions and surrounding soft tissues (Xin Zhao et al., 2021). Therefore, analysing tumour invasion turns out to be particularly difficult.

1.1.3.5.2. Computed Tomography

Computed tomography is a multiplanar imaging technique that is used to visualise three-dimensionally the extent of internal and external tumour invasion, but also to detect the micro mineralized bone formation of tumours, which is not visible on X-rays (A. Misaghi et al., 2018; Stefan S. Bielack et al., 2016).

This methodology is recommended in order to rule out the development of lung metastases due to the sensitivity (75%) and specificity (almost 100%) of the technology used (Hogendoorn PCW et al., 2010, cited in Xin Zhao et al., 2021). However, computed tomography cannot determine all pulmonary nodules detected during surgery, and there is a high possibility of false-positive results (especially when the lesion size is <5 mm) (Xin Zhao et al., 2021).

1.1.3.5.3. Magnetic Resonance Imaging

Magnetic resonance imaging is an important tool for determining tumour stage and tumour grade thus for preoperative planning of osteosarcoma surgical treatment (Xin Zhao et al., 2021; A. Misaghi et al., 2018; Hogendoorn PCW et al., 2010).

Magnetic resonance imaging of the entire affected bone is also important to assess the presence or absence of *jump metastasis* which are small, non-adjacent lesion that is usually located in the proximal intramedullary canal of the affected bone (Xin Zhao et al., 2021).

However, Hogendoorn PCW et al. (2010) support that magnetic resonance imaging is not a suitable for visualizing periosteal reaction and Codman's triangles of the bones, which are instead visible by Computed tomography analysis.

1.1.3.5.4. Biopsy

Since currently available imaging techniques cannot support the diagnosis of benign outcomes, tissue biopsy is the current gold standard for the diagnosis of osteosarcoma (Xin Zhao et al., 2021; Hogendoorn PCW et al., 2010). The biopsy must be performed after a complete medical history, as it is an invasive methodology that reveals the specific type and grade of the tumour. (Zile Singh Kundu, 2020). Performing a tissue biopsy offers some advantages, including allowing intuitive analysis and observation of the tissues of the lesion, enabling a more accurate understanding of the course and development of the lesion and the processes involved (Xin Zhao et al., 2021). Disadvantages of this method include invasiveness, the possibility of incurring infection (particularly for long tissues), examination timing, and, most importantly, the alteration of haemostasis after the biopsy procedure (Zile Singh Kundu, 2020).

1.1.3.5.5. Non-Routine Technologies

Recently, other imaging technologies not yet used in routine imaging protocols have been developed. These technologies include positron emission technology scanning (Cao Q et al., 2013; Xiaojuan Zhang et al., 2018; Winfried Brenner et al., 2003) and dynamic magnetic resonance imaging (Farghaly R et al. 2017; Tadahiko Kubo et al., 2016; Wilburn E. Reddick et al., 2001; Reham Farghaly et al., 2016). Researchers are working to determine their possible role in future diagnosis, monitoring response to treatment, and detecting recurrence.

1.1.3.6. Treatments

The tumour's grade is the most important factor in treatment decision-making (https://www.cancer.net/cancer-types/osteosarcoma-childhood-and-adolescence/introduction). Available treatments are divided into conventional and unconventional. The current management of osteosarcoma treatment includes preoperative (neoadjuvant) chemotherapy followed by surgical removal of the detectable tumour mass (including metastases) and postoperative (adjuvant) chemotherapy (Anja Luetke et al., 2013) (Anja Luetke et al., 2013). Furthermore, thanks to the strong development of imaging techniques, it has been possible to refine the tumour surgical resection technique allowing the preservation of uninvolved tissues

and avoiding limb amputation in 80% of osteosarcoma cases (A. Misaghi et al., 2018; Bacci G et al., 2001; Ferrari S et al., 2001; Ferrari S et al., 2009).

In previous decades, limb amputation was considered an optimal solution to fight osteosarcoma; however, comparison of local recurrence rates between amputation and conventional surgery showing no significant difference in survival (Anja Luetke et al., 2013).

Additionally, the incidence of local recurrence in conventional surgery is closely related to the surgical margins achieved, as the appropriate thickness of tissue to be severed during surgery is generally not defined (Errani C et al., 2011), However, this surgical treatment remains essential for healing.

Recently, most chemotherapy regimens applied for osteosarcoma have been based around four drugs: high-dose methotrexate (HDMTX) with leucovorin rescue, doxorubicin (DOXO), cisplatin, and ifosfamide (Zhao et al., 2021).

Experimental chemotherapy regimens have greatly improved survival rates, and several chemotherapy protocols that included multiagent regimens leading toward neoadjuvant and adjuvant multi-agent chemotherapy at the same time have been studied over the past three decades (Anja Luetke et al., 2013).

The preoperative chemotherapeutic treatment offers an opportunity to allow time for planning limb salvage surgery and subsequent treatments to surgery. Subsequent subsections will discuss the roles and benefits of each drug used in today's chemotherapy and the potential use of docetaxel as an anti-chemotherapy drug.

1.1.3.6.1. DOXO

DOXO came into use for treatment of osteosarcoma in the early 1970s and it is an anthracycline topoisomerase inhibitor isolated from cultures *Streptomyces peucetius* var. *caesius* (https://labeling.pfizer.com/ShowLabeling.aspx?id=530#section-1). The chemical name of DOXO hydrochloride is 5,12-Naphthacenedione, 10-[(3-amino-2,3,6-trideoxy-α-L-lyxo-hexopyranosyl)oxy]-7,8,9,10-tetrahydro-6,8,11-trihydroxy-8-(hydroxylacetyl)-1-methoxy-, hydrochloride (8S-cis). The chemical structure of DOXO hydrochloride is shown in Fig. 11.

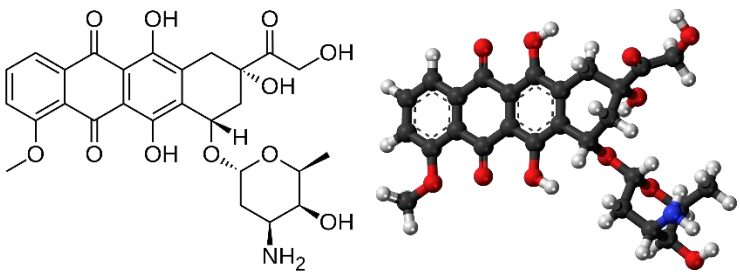

Fig. 11: Skeletal formula of doxorubicin. Source: https://en.wikipedia.org/wiki/Doxorubicin

There are two mechanisms by which DOXO acts in the cancer cell: intercalation in the cellular DNA with subsequent disruption of DNA repair mediated by topoisomerase-II (through the TOP2A, MLH1, MSH2, TP53

and ERCC2 genes) or alternatively, an oxidation of DOXO to semiquinone (an unstable metabolite) that is converted back to DOXO in a process that releases reactive oxygen species that can lead to lipid peroxidation and membrane damage, DNA damage, and oxidative stress so as to trigger apoptotic pathways of cell death (Thorn et al. , 2011).

However, DOXO shows mechanisms of cardiotoxicity. These mechanisms are still controversial, but there are two predominant theories on the causes of cardiotoxicity: iron-bound free radicals or the formation of the metabolite Doxorubicinol with subsequent alteration of mitochondrial activity. Both mechanisms can lead to the disruption of cellular respiration and subsequent apoptosis due to the release of cytochrome-C (Thorn et al., 2011). Despite this, DOXO has been declared the most effective agent for the treatment of osteosarcoma.

1.1.3.6.2. Cisplatin

(SP-4-2)-diamminedichloridoplatinum(II), shown in the Fig. 12, was discovered in 1845 and used for medical purpose in 1978.

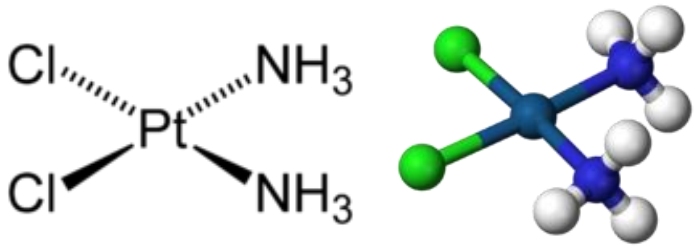

Fig. 12: Skeletal formula of Cisplatin. Source: https://en.wikipedia.org/wiki/Cisplatin

It exerts its cytotoxic action by platination of DNA; In fact, the principle of action involves exerting its cytotoxicity upon cancer cells through the formation of DNA adducts that include mono-, inter, and intrastrand cisplatin DNA cross-links that arrest the cell cycle at S, G1 or G2-M thus induces apoptosis (Aldossary S. et al., 2019). However, there are several studies in the literature that testify to drug resistance of osteosarcoma cells which will be discussed in the section num. 1.1.3.6.5 (Kartalou et al., 2001; Stewart et al., 2007; Fanelli M et al., 2020).

Generally, Cisplatin is contraindicated in patients with myelosuppression, in patients with renal dysfunction or with hearing impairment and in dehydrated patients (https://go.drugbank.com/drugs/DB01181).

In fact, Platinum compounds share several adverse effects that can be categorized into acute toxicity and delayed toxicity (https://www.aimac.it/farmaci-tumoure/chemioterapici/cisplatino). The latter includes: Peripheral neuropathy (distal symmetric), impaired liver and kidney function, hearing loss, and haemolytic anaemia.

1.1.3.6.3. Ifosfamide

N,3-Bis(2-chloroethyl)-1,3,2-oxazaphosphinan-2-amide 2-oxide (Fig. 13) is a drug for chemotherapy approved in 1987 in the United States.

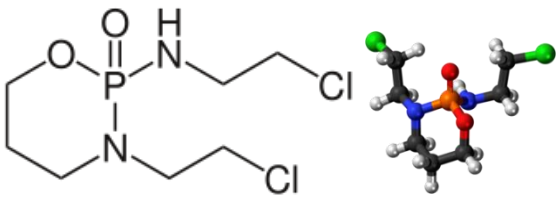

Fig. 13: Skeletal formula of Ifosfamide. Source: https://en.wikipedia.org/wiki/Ifosfamide

Ifosfamide is a cell-cycle non-specific drug that is activated mainly by hydrolysis of the first four carbons, forming Ifosfamide aldehyde, which decomposes into nitrogenous phosphorus amide and acrolein (Zhang et al., 2017). The cytotoxic effect of Ifosfamide affects DNA cross-linking by slowing down the G2 phase of the cell cycle, with no risk of long-term cardiotoxicity (Cancer Treatment and Research Steven T. Rosen, M.D., Series Editor Robert H. Lurie Comprehensive Cancer Center Northwestern University Medical School, 2009). Ifosfamide may be administered in combination with etoposide (VP-16), which is thought to augment the efficacy of the alkylating agent through a synergistic interaction (Cancer Treatment and Research Steven T. Rosen, M.D., Series Editor Robert H. Lurie Comprehensive Cancer Center Northwestern University Medical School, 2009), that increases patient survival compared to data obtained with DOXO treatment (https://www.humanitas.it/enciclopedia/principi-attivi/antineoplastici-antitumourali/leucovorin/). The main problem with etoposide is the toxicity on the central nervous system and the temporary reduction of blood cell production by the bone marrow (https://www.aimac.it/farmaci-tumoure/chemioterapici/ifosfamide#potenziali).

1.1.3.6.4. HDMTX with leucovorin rescue

HDMTX was discover in 1947 and used in 1956 as antimetabolites drug for metastatic osteosarcoma cancer due to its ability to counteract the synthesis of folic acid. The chemical name of HDMTX is (2S)-2-[(4-{[(2,4-Diaminopteridin-6-yl) methyl] (methyl)amino}benzoyl)amino]pentanedioic acid. The chemical structure of HDMTX is shown in Fig. 14.

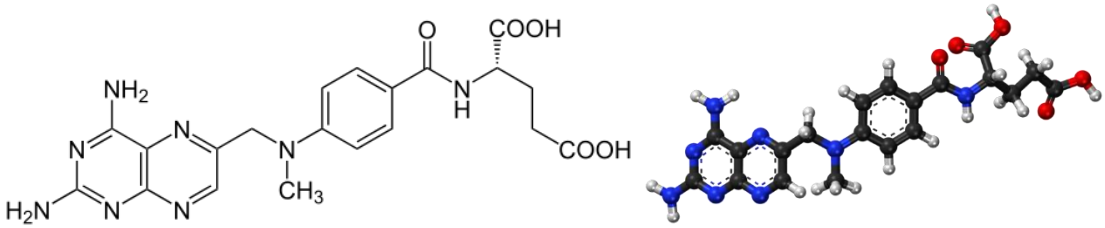

Fig. 14: Skeletal formula of HDMTX. Source: https://en.wikipedia.org/wiki/Methotrexate

Methotrexate binds stoichiometrically and irreversibly to dihydrofolate reductase, thereby inhibiting the formation of tetrahydrofolate from dihydrofolate and interfering with the biosynthesis of purines and pyrimidines (hence thymidylate), leading to cell death and preventing DNA synthesis and cell growth (Henghe Tian et al., 2007). This is possible due to the internalisation of HDMTX in cells via three different pathways: Folate receptors, proton-coupled folate transporter, and reduced folate carrier (Louise Marchandet et al., 2021).

Since HDMTX is administered in high doses and is highly toxic, leucovorin (5-formyl tetrahydrofolate) is provided as an antidote after completion of the drug's therapeutic cycle. In fact, within the cell, leucovorin is converted to 5,10-methyl tetrahydrofolate and 5-methyl tetrahydrofolate, thus replenishing the product eliminated by methotrexate (Cancer Treatment and Research Steven T. Rosen, M.D., Series Editor Robert H. Lurie Comprehensive Cancer Center Northwestern University Medical School, 2009).

Regarding the efficacy of HDMTX, there are several works in the literature demonstrating a controversial and noninfluential role of HDTMX when administered in a two- or three-drug regimen (Krailo M. et al, 1987; Bramwell VH et al., 1992; Souhami RL et al., 1997).

Prerequisites for HDTMX therapy include normal renal and hepatic function in order to avoid any fluid collections (pleural, pericardial, and peritoneal effusions) which may cause a delay in methotrexate excretion by sequestering methotrexate in the fluid collection and are contraindicated in treatment with HDTMX (Cancer Treatment and Research Steven T. Rosen, M.D., Series Editor Robert H. Lurie Comprehensive Cancer Center Northwestern University Medical School, 2009).

1.1.3.6.5. Docetaxel (DTX)

DTX is a second-line chemotherapy drug approved by the Food and Drug Administration and the European Medicines Agency EMA in 1995. The chemical name of DTX is 1,7β,10β-trihydroxy-9-oxo-5β,20-epoxytax-11-ene-2α,4,13α-triyl 4-acetate 2-benzoate 13-{(2R,3S)-3-[(tert-butoxycarbonyl) amino]-2-hydroxy-3-phenylpropanoate} and the chemical structure of DTX is shown in Fig. 15.

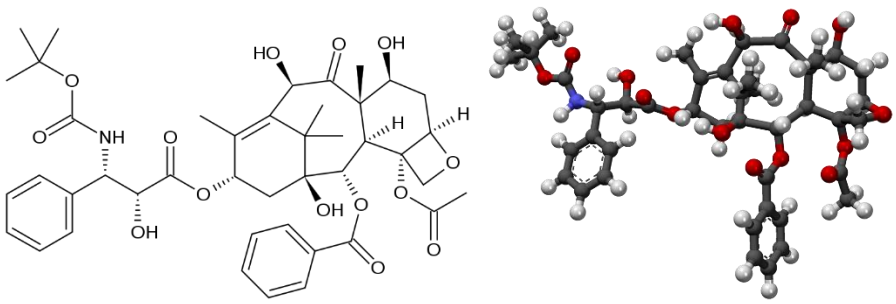

Fig. 15: Skeletal formula of DTX. Source: https://en.wikipedia.org/wiki/Docetaxel

DTX is a non-cytotoxic precursor derived from the needles of Taxus specimens that has been chemically modified to yield a Taxol type antitumour agent (Cancer Treatment and Research Steven T. Rosen, M.D., Series Editor Robert H. Lurie Comprehensive Cancer Center Northwestern University Medical School, 2009). The prolonged and long-term action of DTX promotes stable polymerisation of microtubules and inhibition of depolymerisation, thus significantly reducing the number of free microtubules, inhibiting spindle separation at the two poles, blocking G- and M-phases and ultimately inhibiting mitosis and proliferation of cancer cells (K J Pienta, 2001).

Since docetaxel works on dividing cells, it can also affect non-tumour cells, such as blood cells (https://www.pfizermedicalinformation.com/en-us/docetaxel-0/contradictions).

For this reason, DTX should not be used in patients with neutrophil counts below 1500 cells/mm^3 or with severe liver problems (https://www.ema.europa.eu/en/documents/product-information/taxotere-epar-product-information_it.pdf). These observations indicate that such approaches may be useful in the treatment of metastatic and relapsed/refractory Osteosarcoma, and Osteosarcoma that is unresponsive to first line treatment.

1.1.3.6.6. Efficiency of current chemotherapy treatment: is everything known?

The current chemotherapeutic treatment of osteosarcoma involves the combined use of HDMTX with leucovorin rescue, DOXO and cisplatin (a regimen often referred to as MAP), but there is still no consensus on their optimal combination, particularly on the role of HDTMX and ifosfamide (Anja Luetke et al., 2013; Steven T. Rosen et al., 2009). In contrast, the toxicity of cisplatin is known and has been discussed in several works in the literature that involved two- or multi-drug intra-arterial regimens (M. Sears et al., 2022; Printezi et al., 2022; Dasari et al., 2022). The most prominent cytotoxic effect is early or late heart failure due to doxorubicin toxicity (Thorn et al., 2011).

Anja Luetke et al. (2013) also discussed the role of second-line chemotherapy and showed that it shows a good anti-chemotherapy response when correlated with first-line chemotherapy on relapsed and metastasised osteosarcoma.

Other chemotherapeutic agents such as cyclophosphamide and dactinomycin have mostly been abandoned, as they have not proven as effective as the above drugs (Anja Luetke et al., 2013; Nathalie Gaspar et al., 2020).

1.1.3.6.7. Chemotherapy drug resistance

In 35-45% of osteosarcoma cases, osteosarcoma cells tend to develop drug resistance against chemotherapy treatment (Louise Marchandet et al., 2021; Anja Luetke et al., 2013).

The drug resistance offered by osteosarcoma cells is one of the biological processes underlying the failure of conventional chemotherapeutic strategy (Hattinger et al., 2021). Therefore, understanding the mechanisms

of drug resistance is important to overcome the barriers offered by osteosarcoma cells. The various mechanisms of chemoresistance in osteosarcoma include: decreased intracellular drug accumulation, drug inactivation, increased DNA repair, modulation of signalling pathways, autophagy-related resistance, altered expression of cell cycle-related genes or even involvement of the microenvironment (Louise Marchandet et al., 2021).

According to Louise Marchandet et al. (2021), decreased drug accumulation is one of the main mechanisms used by cancer cells to cope with the cytotoxic effects of chemotherapeutic agents. For that, tumour cells can alter drug transport by reducing the number of folate transporters on their surface or by decreasing the speed of drug transport by genetically altering RFC proteins (Louise Marchandet et al., 2021).

To the mechanisms just mentioned, it is possible to add upregulation of drug efflux through pumps associated with proteins belonging to the ATP-binding cassette family of efflux transporters, which are closely related to multidrug resistance and reduced DOXO accumulation according to Louise Marchandet et al. (2021).

Furthermore, alterations in the structure or overexpression of target enzymes can alter drug transport by decreasing their affinity due to mutations in the target enzymes (an example is the upregulation of DHFR linked to the absence or defects in the p53 protein) (Louise Marchandet et al., 2021).

However, there are other mechanisms of drug resistance. As stated in paragraph no. 1.1.3.6.4, DOXO and Cisplatin form reactive oxygen species that can interact with cellular DNA inducing oxidative stress (Thorn et al., 2011). To restore low levels of reactive oxygen species, cells have protective detoxification mechanisms consisting of detoxification enzymes (e.g., glutahtione-S-transferase P1-1) that are responsible for drug inactivation and thus responsible for the degree of resistance offered by cancer cells to the drug used (Louise Marchandet et al., 2021).

Furthermore, it is widely known that chemotherapeutic agents cause DNA damage and lead to cell death. However, cancer cells can sometimes resist chemotherapeutic treatment by enhancing the DNA repair pathway through the potential of the BER mechanism and upregulation of the apurinic endonuclease enzyme APE-1 (Louise Marchandet et al., 2021).

Regarding the hallmarks discussed in paragraph num. 1.1.2.2., osteosarcoma cells exhibit alterations in the TP53 gene and in anti-apoptotic and pro-apoptotic proteins (Bcl-2 and Bax, respectively) that will obviate the mechanisms of senescence and apoptosis (DeChant, M.J et al., 2003).

Cell surface receptors in osteosarcoma cells are often disturbed, showing overexpression of several kinases belonging to the ErbB/HER family that lead to activation (via receptor phosphorylation) of the phosphoionositol 3-kinase-protein kinase and MAPK signalling pathways, which lead to survival and proliferation of cancer cells following chemotherapeutic treatment, respectively (Louise Marchandet et al, 2021).

It has also been found that osteosarcoma tumour cells often exploit the autophagy pathway (Degenhardt, K. et al., 2006) through overexpression of High Mobility Group Box1 (a nuclear chromatin-binding protein) and alterations in the HSP90AA1 gene (encoding the heat shock protein HSP 90-alpha) that promote chemotherapy resistance and survival by bringing the cell into a more stable form (Louise Marchandet et al., 2021).

Finally, the multi-drug resistance of osteosarcoma may be influenced by the tumour microenvironment due to the presence of cancer stem cells, which are able to develop subpopulations that are resistant to chemotherapeutic agents (Senthebane, D.A et al., 2017).

Furthermore, the acidic pH of the tumour microenvironment is able to reduce the sensitivity of tumour cells to drugs such as DOXO, HDMTX and Cisplatin (Cheng Z. et al., 2016; Louise Marchandet et al., 2021).

1.1.3.6.8. Radiotherapy

Although osteosarcoma is considered a radioresistant tumour (Anja Luetke et al., 2013), radiotherapy may be an option as a treatment for local tumour control, preservation of limb function, and induction of symptom relief in all those cases where osteosarcoma is unresectable or has been incompletely resected (Errani C et al., 2011; Machak GN et al., 2003, cited in Anja Luetke et al., 2013).

1.1.3.7. Non-Conventional therapeutic Treatments

Supplemental therapeutic approaches such as chemoembolization or angio-embolization, thermal ablation, radiofrequency ablation, and cryotherapy are experimental (Zhao et al et al., 2021; Anja Luetke et al. 2013). However, the unconventional treatments that are becoming more popular among researchers are gene therapy and immunotherapy.

1.1.3.7.1. Immunotherapy

Immunotherapy is an adjuvant therapeutic approach implemented in advanced, metastatic, and recurrent osteosarcoma and aimed at regularizing an organism's immune function through cytokines to enable tumour cell killing (Juan Martin-Liberal et al., 2017; Zhao et al., 2021).

Currently, interleukin-2 has been tested for the postoperative treatment of osteosarcoma because it activates effector T cells (which contribute to the anti-tumour-mediated effect in the body) and enhances the function of natural killer cells (which act as the body's first line of natural defence against tumours) (Zhao et al., 2021; Cristina Meazza et al., 2017). The results provided by Cristina Meazza et al. (2017) show significantly enhanced immunogenicity of tumour cells. However, this approach still requires clinical studies.

1.1.3.7.1. Gene therapy

Since genetic mutation is the main cause of osteosarcoma, gene therapy can be a key tool by which normal genes or genes with therapeutic effects are introduced into human target cells through vectors to correct gene defects (Zhao et al., 2021).

Osteosarcoma gene therapy mainly focuses on tumour suppressor genes, suicide genes, combination gene therapy, antisense genes, immune genes and anti-angiogenic genes (Zhao et al., 2021; Jack A. Roth and Richard J. Cristiano, 1997). However, gene therapy is still in the experimental stage and thus far from real clinical application.

1.1.3.8. Human Osteosarcoma cell lines: a brief comparison to human Osteoblasts

There are several cell lines of human osteosarcoma. In this thesis, only Saos-2 and U2OS cell topologies will be discussed. Both cell types have epithelial morphology; however, they were derived from different malignant bone tumours of different donors.

SAOS-2 was isolated in 1973 from the bone of an 11-year-old, white, female osteosarcoma patient treated with RTG, HDMTX, DOXO, vincristine, cytoxan, and aramycin-C (https://www.atcc.org/products/htb-85). This cell type appears with a polygonal morphology.

U2OS was derived in 1964 from a moderately differentiated sarcoma of the tibia of a 15-year-old, white, female osteosarcoma patient (https://www.atcc.org/products/htb-85). U2OS cells show a spindle or triangle shape.

Regardless of whether they are sub-confluent or confluent cells in suspension, the morphology of the osteosarcoma cells just described is different from that of osteoblasts, which show an elongated shape when attached to the substrate that is six times larger than osteosarcoma cells. According to Christoph Pautke et al. (2004), cell growth of osteosarcoma cells in cell culture is not restricted to monolayers, as these cells do not show any contact inhibition mechanism; therefore, these cancer cells show a significantly higher proliferative capacity (2 to 3 times) than fibroblasts.

Through an immunohistochemical comparison between osteosarcoma cell lines and normal osteoblasts, Christoph Pautke et al. (2004) were able to state that the osteosarcoma cell lines had very heterogeneous labelling profiles which differed significantly from that of normal osteoblasts (Tab. 2). This resulted in a different production of extracellular matrix. Although osteosarcoma cells share some osteoblastic characteristics, their chromosomal alterations lead to abnormal molecular and cellular functions.

Markers	SAOS-2	U2OS	Human Osteoblasts
Osteocalcin	+	-	±
Bone sialoprotein	+	+	+
Decorin	+	-	±
Procollagen-I	+	± (50%)	+
Collagen type III	-	+	+
Osteoprotegerin	-	+	+
MMP-9	+	+	-
Collagen type X	+	+	-
Molecules related to Cartilage	-	+	-

Tab. 2: Summary of results obtained from immunohistochemical analysis of osteosarcoma cells and normal osteoblasts. A '+' sign defines the expression of the factor, while a '-' sign indicates the opposite. The sign "±" denotes results dependent on other features. Source: Christoph Pautke et al., 2004

At first glance, the work of Christoph Pautke et al. (2004) shows how human osteoblasts change their labelling profile according to cell density (e.g., positive labelling for Decorin and Osteocalcin if cells are confluent).

Saos-2 cells showed the most mature osteoblastic phenotype, with positive results for alkaline phosphatase activity and other markers, also showing receptors for 1,25-dihydroxyvitamin D3 and parathyroid hormone and producing cyclic AMP in response to parathyroid hormone treatment (Christoph Pautke et al., 2004).

According to the literature, the U2OS cell line secretes a platelet like derived growth factor (PDGF)-like protein, expresses insulin-like growth factor (IGF) receptors and respond to the addition of IGF-I and II with an increase in DNA synthesis (Heldin, C. H. et al., 1986; Raile, K. et al., 1994; all cited in Christoph Pautke et al., 2004). Moreover, these cells were negative for almost all osteoblastic markers but positive for cartilage markers (like collagen II, IX and X). Therefore, the U2OS cell line is not classified as osteoblastic, but also as fibroblastic (Christoph Pautke et al., 2004).

1.2. Nanotheranostics

1.2.1. General Features and Statistics

In recent decades, the translation from conventional medicine to '4P medicine' (that is predictive, preventive, personalised and participatory) is becoming increasingly popular among researchers and this can be done through different systems, including theranostics systems (Simona Mura and Patrick Couvreur, 2012).

Multifunctional or theranostics platforms are particles that combine therapeutic potential with diagnostic potential to personalise patient treatment and achieve better quality of pharmacotherapy (Sonali et al., 2018; Tang et al., 2019a, 2019b; Liao et al., 2020). This category also includes NPs that simultaneously have imaging and treatment roles, such as quantum dots (QDs) and carbon dots (CQDs).

The role of theranostics is interesting on several levels, especially in the field of oncology where it allows the *in vivo* and non-invasive quantification of targets belonging to tumour cells and the subsequent delivery of a therapeutic counterpart to the same regions (Miller C et al., 2022).

Thus, the application of theranostics with the support of nanotechnology opens new horizons in the management of cancer according to its three dimensions: diagnosis, treatment and response monitoring (Caldorera-Moore et al., 2011; Vinhas et al., 2015; Sonali et al., 2018; Cui & Wang, 2016).

Furthermore, the non-invasive monitoring of particle accumulation at the target site allows for early feedback on treatment efficacy, making it possible to select patients who will respond positively to treatment (characterised by high nanomedicine accumulation) from others who would need a different treatment option (Simona Mura and Patrick Couvreur, 2012).

Consequently, thanks to the characteristics of nanotheranostics systems, it will be possible to achieve maximum therapeutic efficacy, the best safety profile and improved disease management without waiting for traditional end points such as tumour shrinkage. (Simona Mura and Patrick Couvreur, 2012).

The first theranostics paper dates to 1940 and dealt with the use of radioiodine for the diagnosis and management of thyroid gland tumours (Rudolf A. Werner et al., 2021). From its inception to the present, theranostics has experienced exponential growth in the number of articles published in PubMed, as shown in Fig. 16 (Miller C et al., 2022). The most common reason for this trend has been found to be the side effects associated to the traditional chemotherapeutic therapies and the development of theranostic systems that are increasingly selective against target tumour sites (S. Jeelani et al., 2014).

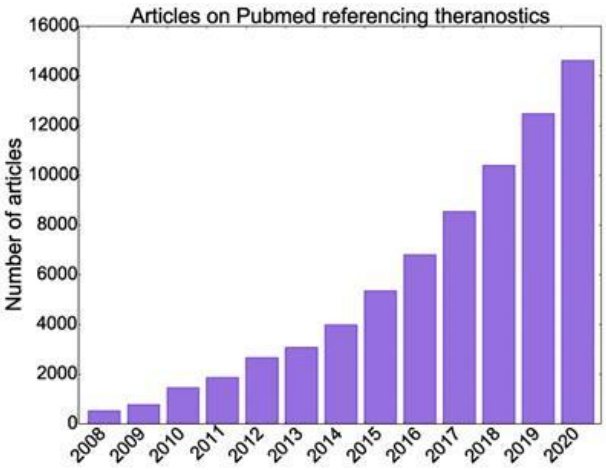

Fig. 16: Number of articles published on PubMed containing the words "theranostics" or "theragnostics" from 2006 to 2020. Source: Miller C et al., 2022

An ideal nanotheranostic system should circulate in the body for a long time, exhibit high specificity and tissue penetration, and should have sufficient pharmacological release for the intended treatment (Sonali et al., 2018).

In this context, the holistic compression of the organism is crucial, but also the complete compression of the chemical-physical properties of NPs, including their interactions with the organism's components (Vishwakarma et al., 2010; S. Jeelani et al., 2014; Simona Mura and Patrick Couvreur, 2012).

Although effective nanotheranostic systems for cancer treatment have been developed over time, there are several reasons why these agents have not yet been introduced into clinical practice (Simona Mura and Patrick Couvreur, 2012; Sonali et al., 2018). A major difficulty is the integration of multiple technologies (imaging and processing) within a single carrier (S. Jeelani et al., 2014). In addition, some nano-fabrication methods use toxic raw materials or generate by-products that are toxic to the organism (Murty et al., 2013). Furthermore, in the interest of nanomedicine development, there is no standard characterisation protocol for NPs, especially from a technical/regulatory perspective (Neuberger et al., 2005; Oberdörster et al., 2005). Furthermore, many current characterisation techniques are still limiting, such as the methodologies used to characterise the biodistribution of NPs in vivo (Neuberger et al., 2005; Oberdörster et al., 2005).

1.2.2. Combining Nanomedicine with Nanotechnology

The US National Institute of Health has described nanomedicine as the ability to manipulate matter at the nanoscale for simultaneous medical applications such as diagnostics, medical imaging, treatments, nanotheranostics, vaccines and regenerative medicine of biological systems (Markman JL et al., 2013).

In the last 25 years, 50 different nanomedicines have received Food Drug Administration (FDA) approval and are currently used in clinical practice (Ventola, 2017).

The first anti-cancer nanodrug was approved in 1995 by the FDA and was a stealth formulation of doxorubicin (DOXO) called Doxil (DOXO HCl liposome injection) that consists of DOXO encapsulated within pegylated nanocapsules of unilamellar liposomes (https://www.accessdata.fda.gov/drugsatfda_docs/label/1999/50718s06lbl.pdf#:~:text=DESCRIPTION%20Doxil%C2%AE%28doxorubicin%20%20HCl%20liposome%20injection%29%20is%20,relative%20to%20those%20of%20the%20%20unencapsulated%20drug). To date, Doxil is marketed.

The second nano-drug approved by the FDA is Abraxene in 2005 and is an NPs consisting of an albumin-bound formulation of Placlitaxel (https://www.ema.europa.eu/en/documents/product-information/abraxane-epar-product-information_it.pdf).

Here, Paclitaxel is the anticancer drug that acts by arresting the division of tumour cells, while the albumin dissolves the Placlitaxel to cross the walls of tumour blood vessels (Evelina Miel et al., 2009).

Therefore, nanotechnology is a platform that has generated considerable interest in the manipulation of nanomedicines at the nanoscale and is being applied to the production of nanocarriers between 10 and 1000 nm in size for bioimaging and drug delivery due to the various advantages offered over macroscale and conventional drug products in terms of toxicity profiles (Sonali et al., 2018). One of the main advantages belonging to NPs is their ability to circulate longer in the bloodstream than standard chemotherapeutics, increasing the chances of absorption by tumour blood vessels (Penet et al. 2014).

Nanoparticles essentially consist of a core that can be used for encapsulation and delivery of one or more drugs, or for therapeutic imaging (via quantum dots, iron oxides or gold NPs) or gene therapy (Andrea Tautzenberger, Anna Kovtun and Anita Ignatius, 2012). Instead, the surface of the NPs dictates how it interfaces with the biological environment. Example, NPs with stealthing properties have been surface-modified through the presence of hydrophilic polymers (Polyethylene glycol (PEG) or Polyvinylpyrrolidone (PVP)) or through biomimetic coatings in order not to trigger an immune response from the host organism (Narges Hadjesfandiari and Anilkumar Parambath, 2018).

Furthermore, as some fluorophores can be masked if they are embedded in the NPs core, the surface of NPs can also be exploited to achieve imaging properties through binding with imaging agents such as QDs, antibodies, peptides or fluorescent probes. This will make it possible to track the distribution of nanoparticles in the body and to mark specific cellular sites (Lara K. Bogart et al., 2014).

There are several possible classifications for NPs. Generally, NPs can be massive, if they present a solid matrix and the drug is finely dispersed in it; or they can be nanocapsules, where the core is hollow and the drug is encapsulated in the matrix forming the shell; or they can be nanocomplexes if a drug is used that presents a net charge (such as RNA or miRNAs) that can be complexed with another charged material (Saurabh Bhatia, Natural Polymer Drug Delivery Systems: Nanoparticles, Plants, and Algae, , Springer Cham, 2016, 1st edition).

The subdivision of NPs that can be used for nanotheranostics can also be made according to their chemical composition (Panoraia I. Siafaka et al., 2020), which include inorganic NPs (gold NPs, iron oxides, QDs, CQDs,

silicon-based NPs and Molecular beacons), polymeric, conjugated, viral and smart NPs. For the purposes of the discussion, QDs and CQDs will be dealt with in detail in sections 1.2.3 and 1.2.4, respectively.

1.2.2.1. Iron Oxide NPs

Due to their size (1-100 nm), iron oxide NPs have superparamagnetic behaviour when magnetised, so NPs do not retain magnetisation after removing the external magnetic field due to the presence of a single magnetic domain (Attarad Ali et al., 2016). Thus, by applying an external magnetic field, the domains of the NPs will all orient themselves in the same direction as the external field, and once the field is removed, the domains will return to the relaxed condition without hindering each other (Attarad Ali et al., 2016). This does not occur in the material in bulk form, which exhibited ferromagnetic behaviour as it retained magnetisation despite the magnetic field having been removed (Amyn S. Teja and Pei-Yoong Koh, 2008).

These NPs can be surface functionalised with polymers to stabilise NPs in solution (to prevent aggregation and precipitation) and for various biomedical applications, including drug transport (Seyed Mohammadali Dadfar et al., 2019). One of the main applications of these NPs is their use as a negative contrast agent in nuclear magnetic resonance as they change the timing of relaxation due to spin-spin interactions in cancerous tissue (Fangyuan Li et al., 2019).

Generally, tumours have a higher cell density than healthy tissue, so they have different relaxation times (T1 and T2) than surrounding tissue. However, if the tumour is in the early stages of growth, it is not always possible to discriminate between the two zones (Rafael Torres Martin de Rosales et al. 2011). Therefore, the use of Iron Oxide NPs can lead towards an early diagnosis of the tumour.

Another interesting application is the hyperthermia therapy by exploiting the heating of the NPs (60 °C) caused by an alternating magnetic field that induces a continuous mutation of the magnetising vector (Hui S Huang and James F Hainfeld, 2013). If the NPs are conducted inside the tumour site via magnetic drag (Chengyin Fu and Nuggehalli M. Ravindra, 2012), the heat generated by the NPs will not be exchanged with the outside due to the vascular disorder of the tumour, leading to cell apoptosis (Hui S Huang and James F Hainfeld, 2013).

The work of Jeon et al. (2016) and Nigam and Bahadur (2018) demonstrated, on superficial tumours, the efficacy of magnetic entrainment and heat development mechanisms by oxide-based NPs complexed with Placlitaxel and DOXO, respectively, while also demonstrating enhanced drug accumulation within the tumour (without exploiting the EPR effect).

However, the use of iron oxide NPs is limited due to their poor biodegradability and the need to administer a high dose to have a significant hypothermic effect (Joan Estelrich and Maria Antònia Busquets, 2018).

Finally, it has been shown by Creagh et al. (2000) that cancer cells exhibit heat resistance mechanisms, whereby they are able to adapt to such conditions.

1.2.2.2. Gold NPs

Gold-based metal NPs are colloidal suspensions of gold NPs in monodisperse water that are inert and easy to synthesise (Xue Bai et al., 2020). According to Burrows et al. (2017), gold is very reactive in the presence of thiol groups, so NPs can be surface functionalised in a variety of ways and can be simultaneously detected by conductivity or fluorescence measurements. In addition, gold NPs have a negative charge that can be used for electrostatic reactions to confer greater stability to NPs in the body, as they are affected by pH, temperature and salt concentration conditions (N. D. Burrows et al., 2017).

This type of particle can have different shapes, including spherical, rod, hollow, nanocage or nanostar (D. K. Awasthi, Gyanendra Awasthi and Kritika Verma, 2020).

Applications of gold NPs include drug delivery, photoacoustic imaging, photothermal therapy, radiotherapy and bioactive tagging (Negar Sedghi Aminabad, Masoud Farshbaf and Abolfazl Akbarzadeh, 2019).

Like iron oxide NPs, gold NPs exhibit differences in terms of properties compared to its bulk form. Indeed, at the nanoscale, gold NPs have fewer electrons than a macrometric substrate, so the surface plasmon, which is produced by exciting gold, remains confined (Xue Bai et al., 2020).

So, by exciting the surface with a light radiation at a specific wavelength, a few electrons will be promoted to a higher energy level, and if NPs are excited, they will oscillate around the nucleus due to the pullback force of the nucleus, inducing the phenomenon of surface plasmon resonance (Xue Bai et al., 2020). The NPs will oscillate according to the wavelength of the absorbed radiation; therefore, the suspension will emit a colour complementary to the absorbed wavelength (N. D. Burrows et al., 2017).

Generally, the intensity of the emitted light depends on the size and shape of the NPs, so they can modulate the wavelength at which surface plasmon resonance phenomenon occurs (D. K. Awasthi, Gyanendra Awasthi and Kritika Verma, 2020). In fact, for larger sizes, the absorption peak shifts to longer wavelengths (red and infrared).

In nanorods, radiation can hit both the long and short sides, so they can have two absorption wavelengths and two surface plasmons, making them very versatile (Rozanova Nadejda and Zhang JinZhong, 2009).

Nanostars, on the other hand, show a shift toward the infrared due to their own non-uniform morphology (Seyyed Mojtaba Mousavi et al., 2020).

The problems arising from gold NPs are several, including the possibility of inducing a change in skin colour for high dosages, non-biodegradability with short-term nonspecific accumulation (Jaber Beik et al., 2019).

1.2.2.3. Molecular Beacons

Molecular beacons are highly specific molecular probes that have a hairpin shape. They have a stem consisting of a DNA double helix with a fluorophore and quencher located in the base of the stem, and a DNA single helix loop that is larger in size than the stem (25-30 base pairs) and will have base sequences complementary to other target base sequences (G. Goel et al., 2005).

The single helix has a higher free energy than the stem; therefore, it appears to be less stable than the stem and will favour thermodynamic free energy minimization reactions aimed at creating a more stable bond, thus creating a double helix with complementary base sequences (Kemin Wang et al., 2009).

In closed configuration, the fluorophore and the quencher are close together; therefore, the fluorescence emission of the fluorophore is completely captured by the quencher due to the Fret effect because the quencher has an absorption spectrum almost totally superimposed on the emission spectrum of the fluorophore (Weihong Tan et al., 2004). The reverse happens when the molecular beacons are in an open configuration, allowing the presence of a target DNA sequences to be identified. Gold or iron oxide-based NPs can be used as a quencher. Thus, this tool is particularly useful for quantitative studies of genomic and proteomic information in biomedical studies, disease diagnosis and drug discovery (Weihong Tan et al., 2004) The disadvantages of this technique certainly include cost (Haiyan Dong et al., 2016).

1.2.2.4. Silica-Based Nanomaterials (SNP)

SNPs have an inert symmetrical solid matrix with several characteristics, such as size (generally from 5 to 1000 nm), unique optical properties, high specific surface area, low density, adsorption capacity, ability to encapsulate drugs and biomolecules, biocompatibility, and low toxicity (Ahmad Bitar et al., 2012).

Indeed, by engineering the surface charge and modify the affinity of SNPs, it will also be possible to control their biological behaviour, such as cellular uptake, biodistribution, and some immunostimulatory activities (Yannan Yang, Min Zhang, Hao Song, and Chengzhong Yu, 2020). In addition, the presence of silanol groups on the surface allows them to create bonds with ligands or other biomolecules to further enhance the therapeutic efficacy of drugs and reduce side effects (Juan L. Vivero-Escoto et al., 2010).

One particular type of SNPs are the mesoporous silica nanoparticles (MSNs), which are particularly used for tumour-targeted drug delivery applications (Yannan Yang MPhil and Chengzhong Yu, 2015).

MSNs contain a porous honeycomb structure of silica with a high surface area rich in reactive silanol groups that can conjugate with almost all types of groups for active targeting purposes (Chitra Rajani et al., 2020).

There are mainly three types of MSNs: ordered MSNs, hollow or rattle MSNs, and core/shell MSNs (Charu Bharti et al., 2015).

Ordered MSNs possess a uniform pore size and an orderly arranged pore structure (Yu-Shen Lin et al., 2005).

Hollow MSNs are preferred over ordered MSNs because of the higher drug loading and easy surface functionalization (Feng Chen et al., 2014).

The cylindrical pore size and particle size can be finely tuned in a very wide range (from 2 nm to 1 μm) that allow the high payload of NPs, precisely control the housing of host molecules and control their release profile (Yannan Yang MPhil and Chengzhong Yu, 2015).

Therefore, intensive research has been conducted to use SNPs in various biomedical applications, using SNPs as protectors of contrast agents or as carriers for drug delivery (Ahmad Bitar et al., 2012).

The main disadvantages of SNPs and MSNs are the poor scalability of the synthesis process and the inability to incorporate some drugs at an adequate concertation within the pores, which will critically affect the total concentration of nanoparticles to be administered to achieve an effective therapeutic effect (Nerea Iturrioz-Rodríguez, Miguel A Correa-Duarte and Mónica L Fanarraga, 2019).

Recently, researchers have been investigating the possibility of exploiting the silica chemistry of SNPs as biomodulators to manipulate cancer cell death patterns, dendritic cell maturation, macrophage phenotype, and tumor microenvironment, either in combination with pharmacological molecules or alone (Yannan Yang, Min Zhang, Hao Song, and Chengzhong Yu, 2020). In addition, asymmetric SNPs have attracted considerable success in the recent past. According to Xiaomin Li et al. (2014), asymmetric SNPs confer significantly better hemocompatibility and uptake for immune cells than symmetric mesoporous SNPs, thus conferring significant advantages for future biomedical applications.

1.2.2.5. Polymeric NPs

In the case of polymeric NPs, the physico-chemical properties at the nanoscale are identical to those at the macroscale. According to Mahmoud Elsabahy and Karen L. Wooley (2012), this type of NPs allows for a different mode of transport and drug delivery, but also a different target recognition capability, resulting in different clearance kinetics of NPs and drugs in reference to the NPs mentioned above.

Polymeric NPs are highly biocompatible, biodegradable, and can encapsulate and bind a high amount of drug, releasing it in a controlled manner over time due to the drug diffusion mechanism (Mahmoud Elsabahy and Karen L. Wooley, 2012; Avnesh Kumari et al., 2009). For these reasons, they are widely used as drug carrier systems for biomedical applications.

Polymeric NPs have also some benefits in terms of reproducibility as they are not always easy to manufacture and are not always monodisperse (Nagavarma B. V. N. et al, 2012). Furthermore, drug-loaded particles are always subject to the drug burst release mechanism often attributed to the drug fraction adsorbed or weakly bound to the nanoparticle surface (Carina I.C. Crucho and Maria Teresa Barros, 2017).

Generally, polymeric NPs are subdivided according to the polymer that constitutes them: preformed polymers, lipid nanoparticles, and particles obtained from monomers (Nagavarma B. V. N. et al., 2012).

NPs obtained from preformed polymers only involve the preparation of the synthetic or natural polymer in the form of a particle containing the drug. Usually, emulsion, nanoprecipitation and salting-out techniques are used to prepare preformed NPs with massive structure, which are structurally stabilised by the presence of surfactants and have the drug finely dispersed in the core (Pegi Ahlin Grabnar & Julijana Kristl, 2011). These types of processes may use potentially toxic solvents that can affect the bioactivity of the encapsulated molecules and are generally not scalable techniques (Nagavarma B. V. N. et al, 2012).

The ionic cross-linking method is a technique that involves the addition of an oppositely charged ionic cross-linking agent to the polymer (e.g., tripolyphosphate ions or calcium ions) and allows it to work under mild

conditions (i.e., without solvents and without the use of surfactants), preserving the bioactivity of the encapsulated biomolecules (Cunli Pan et al., 2019). However, according to M.C. García et al. (2017), the choice of polymers is limited to those that are natural (such as chitosan, alginate) and with a net charge; moreover, only water-soluble drugs can be used, and attention must be paid to pH conditions that can affect the chemical structure of the polymers. Furthermore, only large, polydisperse particles can be obtained due to their high tendency to aggregate (M.C. García et al., 2017).

Polymeric NPs can also be obtained by *in situ* polymerisation of monomers within an emulsion or at the solvent/water interface of an emulsion or by polymer precipitation (Nagavarma B. V. N. et al., 2012).

However, there is a limited choice of solvents and polymers that can be used due to toxicity issues arising from the use of catalysts/monomers and residual solvents that can trigger reactions between monomers and drugs that induce inactivation of the biomolecules to be encapsulated (Nagavarma B. V. N. et al., 2012).

Polymeric NPs also include those of a lipidic nature.

Lipids are organic compounds that are abundant in nature and widely used in research because they are amphiphilic and biocompatible (Otto Liideritz et al., 1973). Depending on the type of lipid selected, it is possible to create massive structures (solid lipid particles), hollow structures (liposomes), or stealth liposome particles (Shuang Cai et al. 2011).

The latter particles possess the ability to circulate long-term without being recognised by the body's immune system due to the inclusion of a hydrophilic polymer (PVP or PEG) on the surface of the nanoparticle (Narges Hadjesfandiari and Anilkumar Parambath, 2018).

Liposomes are hollow lipid structures that allow the simultaneous encapsulation of hydrophilic molecules in the core of NPs and hydrophobic molecules within the phospholipid bilayer of the shell (Diana Guimaraes et al., 2021). Generally, these NPs have a spherical, energy-stable shape and controllable size and can be easily internalised by cells because the shell structure is like cell membranes (Diana Guimaraes et al., 2021). The addition of cholesterol during synthesis is intended to reduce the H-bond interactions formed between the phospholipid tails, making the liposomal membrane more deformable and extrudable in order to reassemble the liposomes (via thermal or mechanical deformation cycles) from structures with multiple lipid bilayers towards structures with a single lipid bilayer (Pooria Nakhae et al., 2021). According to Maja Leitgeba et al. (2020), liposomes are distinguishable into unilamellar, which show a single lipid bilayer of 5-6 nm, multilamellar, which exhibit multiple concentric lamellae, and oligolamellar, which show multiple lamellae contained in a larger vesicle.

Liposomes are generally obtained by a film hydration method (Amarnath Sharma and Uma S. Sharma, 1997). The main disadvantage of these NPs is the lack of long-term energy stability, which leads to the formation of liposomal aggregates or the release of NP content in an uncontrolled manner (Diana Guimaraes et al., 2021).

As far as solid lipid particles, they exhibit greater stability than other lipid NPs since they are produced from lipids that are solid at room temperature (Van-An Duong et al., 2020). These lipids are first dissolved through a hot homogenisation technique and then subsequently assembled by extrusion (Van-An Duong et al., 2020). Notably, these particles do not have a multivesicular core but have a solid internal component in which hydrophilic drugs can be encapsulated (Shuang Cai et al. 2011; Van-An Duong et al., 2020). However, attention must be paid to the rather high temperature of hot homogenisation techniques, as they could affect the bioactivity of the encapsulated molecules. Therefore, the process temperature makes this method of nanoparticle production not very versatile.

1.2.2.6. Conjugated NPs

In the previous paragraphs, it was pointed out that the distribution profile of free drug in chemotherapy was not entirely adequate and efficient for the proposed treatment. To improve the distribution profile, it is possible to conjugate drug molecules or proteins to a polymer chain by imposing a certain spatial distribution on the bound molecule, resulting in folded nanostructures that tend to aggregate (Iriny Ekladious et al., 2019). This has made it possible to change the way polymer chains and drugs are distributed (Andreas Wicki et al., 2015).

1.2.2.7. Viral Nanoparticles

Following the extraction of the genetic content encapsulated within the viral membrane, the capsid of a virus is loaded with appropriate genetic material (DNA or RNA) with which it will be possible to transfect cells due to the extremely high ability of viruses to penetrate cell membranes, including the nuclear membrane (Andreas Wicki et al., 2015).

1.2.2.8. Smart nanoparticles for cancer diagnosis and treatment

Smart particles show a specific response if they are interrogated or stimulated from outside the organism (ultrasound, light, magnetic field) or within the biological environment of the target site (pH change or by particular enzymes) (An et al., 2019). The word "smart" refers to the ability of the polymer (which coats or forms the core of the NPs) or the ability of the bond (by which I bind a drug to the NPs) to be sensitive to specific conditions by changing its stability in favour of drug release at the target site (Fig. 17) (Byung Kook Lee, Yeon Hee Yun, Kinam Park, 2015). Below, the type of smart NPs that are sensitive to stimuli within the body will be discussed in detail. However, it is possible to create multi-stimuli sensitive NPs that combine sensitivity to multiple different stimuli within the NPs (B. Sahoo, et al., 2013).

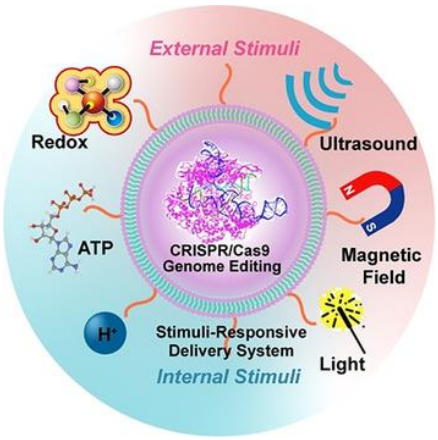

Fig. 17: Overview of internal and external stimuli that can influence the behaviour of smart-NPs. Source: Weiqi Cai et al. 2020

1.2.2.8.1. pH-Sensitive NPs

As demonstrated by Salime Bazban-Shotorbani et al. (2017), NPs can exploit pH condition as an internal stimulus for cancer treatment as it changes between healthy and pathological sites as well as between one body district and another (e.g. stomach and intestine), but also in different compartments of the individual cell (e.g. endosomes have an acidic pH and it is different from cytoplasmic pH) (Fig. 18).

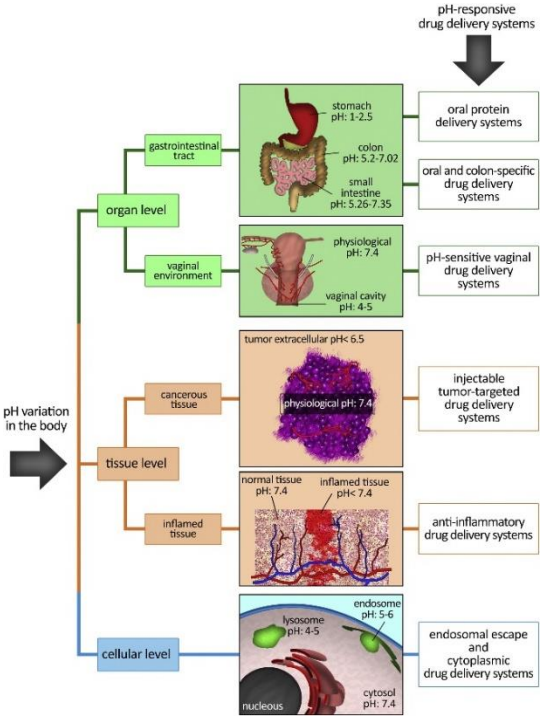

Fig. 18: Overview of different pH conditions in different districts of the body; Source: Salime Bazban-Shotorbani et al., 2017

To exploit the pH as an internal stimulus for drug release, polymers that acquire or give up protons under specific pH conditions can be used; thus, we can use polyacids that in the presence of low pH accept protons leading towards greater polymer stability. In the case of high pH, the polymer gives up protons and tends to

destabilise (F.Reyes-Ortega, 2014; (Fabrice Ofridam,Mohamad Tarhini et al., 2021). The opposite behaviour can be exploited through polybases.

Furthermore, there are polymers that have bonds with pH-sensitive groups (such as ortho ester, acetal, hydrazone) that protonate at acidic pH conditions, whereby the bond destabilises by breaking (Fabrice Ofridam,Mohamad Tarhini et al., 2021).

There are several works in the literature concerning the development of smart and pH-sensitive NPs.

For example, Longlong Chang et al., (2012) worked to create an NPs for oral administration consisting of methoxy poly(ethylene glycol)-block-(polycaprolactone-graft-poly(methacrylic acid)) (mPEG-b-(PCL-g-PMAA)) that encapsulate Ibuprofen. The authors have demonstrated that the exposed carboxyl groups of Poly(methacrylic acid) (PMAA) behave like a polyacid, thus in the stomach (pH 3), the PMAA chains form a protective layer around the core of the NPs limiting the release of ibuprofen, thus helping to protect and slow down drug release in low pH environments (about 50 % of ibuprofen is released at pH 3 in the first 12 h). Once the NPs reach the gut (pH 7. 4), the PMAA chains elongate, and the drug is released, achieving an accelerated organ-specific release. Furthermore, by adjusting the ratio of MAA in the block copolymer, pH sensitivity can be regulated; in fact, more presence of MAA monomers increases ibuprofen release to 95 % at pH 7.4.

A similar mechanism of action was also obtained in the work of M.A. Quadir et al. (2014), where they used an NPs obtained from a copolymer made of PEG-polybasic polypeptide (which was poly(γ-propargyl-Lglutamate) for the release of DOXO at acidic pH. In fact, DOXO release at pH 7.4 amounts to about 20 %, whereas at acidic pH the NPs rapidly disassemble and release their contents almost completely.

An example of NPs binding a drug via a pH-sensitive bond is that provided by M. Prabaharan et al. (2009), in which the core of gold NPs binds DOXO via hydrazone groups, which tend to hydrolyse at acidic pH. This mechanism totally inactivates drug release in the blood and maximises it in an acidic pH context. Moreover, the kinetics of drug release in this case will not be defined by drug diffusion but will be defined by the hydrolysis of the pH-sensitive bond. However, this strategy involves chemically binding the drug to the substrate, so there is a risk of inactivating the drug due to the treatment used (M. Prabaharan et al., 2009).

1.2.2.8.2. Enzyme-sensitive NPs

Enzyme-sensitive carriers exploit the different concentration of enzymes between pathological and normal conditions to disrupt their structure or induce the breaking of sensitive bonds through the presence in the NPs of a certain sequence degradable by a specific target enzyme (Thomas L. Andresen, David H. Thompson and Thomas Kaasgaard, 2010). However, the same enzymes can also be present in other organs, so undesired degradation (and, thus, release) can take place in non-target tissues/organs.

A typical enzyme over-expressed at tumour sites are metal protease enzymes (Sahitya K Denduluri et al. 2016). This type of enzyme was used by L. Dong et al. (2010) as a tool for the release of DOXO contained

within an electrostatic complex of artificial DNA and gelatin (complex A). DOXO is inserted into artificial DNA due to its ability to intercalate within double helices (Thorn et al., 2011).

Gelatin is a substrate for metal protease enzymes, so to avoid enzymatic degradation in the liver, L. Dong et al. (2010) created a pH-sensitive coating on complex A via an alginate-PEG copolymer by exploiting the charge interactions of the materials (complex B). Thus, drug release is due to dual stimulation, maximising release at the tumour site, minimising drug release in the liver and inducing accelerated release in the presence of target site-specific enzymes. The results of the in vivo studies showed that free DOXO has poor targeting capacity, while NPs reduce cardiotoxicity, but complex A is completely degraded by the liver, while complex B will ferry the tumour and release effectively and selectively, increasing animal survival (L. Dong et al., 2010).

1.2.2.8.3. Redox-sensitive NPs

Various oxidative states are present between the intracellular and extracellular environment that cause a redox potential (Michael P. Gamcsik et al., 2012).

The peptide pair that is most responsible for creating the redox potential is Glutanione-Glutanione Disulfide (GSH-GSSG) and their ratio is indicative of the oxidative state of the environment considered. GSH is usually significantly more concentrated inside the cell (2-10 mM) than outside the cell (2-20 μM) as it is responsible for protecting the cell from oxidative stress (Ondrej Zitka et al., 2012).

In tumours, the concentration of GSH is very high inside the cells due to the strong oxidative stresses to which it is subjected; in fact, GSH oxidises (becoming GSSG) and reduces the oxidative species by inhibiting its activity (Michael P. Gamcsik et al., 2012).

Thus, it is possible to exploit GSH overexpression in cancer cells to accelerate drug release in response to intracellular conditions through the creation of NPs that contain a disulfide bond in the main or side chain or through a crosslinker (Yongli Shi et al., 2022). As demonstrated by Yongli Shi et al. (2022), this type of bond will be stable in the extracellular environment because they are poorly oxidising, conversely to the intracellular environment where GSH will reduce the disulphide bond causing the NPs to break (with subsequent release of the drug into the cytoplasm) and become GSSG.

1.2.3. Quantum Dots

QDs are approximately zero-dimensional (5-10 nm) single crystals made up of a combination of transition metals (such as Cadmium (Cd), Sulphur (S), Lead (Pb), Zinc (Zn), Selenium (Se), Tellurium (Te)), which are used in various fields of applications (such as quantum dot light-emitting diodes, in bioimaging, drug carriers, electrical applications) due to their special optical and electronic properties (Debasis Bera et al., 2010).

Semiconductors change their properties depending on the size at which they are used; in fact, when used in nanoscale dimensions, electrons are confined within the nanocrystal and are close to the nucleus compared

to semiconductors in bulk form; therefore, they fluoresce in narrow fields when exposed to a certain wavelength (Alexander L. Efros and Louis E. Brus, 2021).

Optical properties are easily controlled by composition and size, resulting in a wide range of colours (Nair et al. 2017).

To understand the mechanisms intrinsic to QDs, a physical-quantum approach through band theory is required (Jasieniak, Califano and Watkins, 2011). Due to the small size of the QDs, the energy levels of the different bands will be quantised and directly related to the size of the dots, which allows the optical properties to be adjusted in relation to the diameter of the quantum dot due to quantum confinement effect (Debasis Bera et al., 2010; Alexander L. Efros and Louis E. Brus, 2021). According to Jasieniak, Califano and Watkins (2011), in the unexcited state, the electrons of QDs are distributed close to the nucleus (around the valence band) and partly in the higher energy band (conduction band), which can directly interact with the atoms in the nucleus to define the chemical properties of the atom. The conduction and valence bands are separated by an energy gap and, according to quantum confinement theory, as the size of the QDs decreases, the band gap increases due to the increased intensity of the attraction forces between electrons and core atoms (Sotirios Baskoutas and Andreas F. Terzisa, 2006; Reshma, V. G et al., 2019). When sufficient energy is provided to the QDs, the electron leaves a hole in the valence band where it was originally located (creating a gap) and temporarily switches to the conduction band. This produces an electron-hole pair known as an exciton (Reshma, V. G et al., 2019; Debasis Bera et al., 2010).Subsequently, the hole and electron recombine, emitting a photon of energy equal to the gap between the two bands, giving rise to the fluorescence phenomenon (Reshma, V. G et al., 2019; Freeman and Willner, 2012; Jasieniak, Califano and Watkins, 2011). Thus, the choice of QD size allows the energy of the photon emitted by the QDs and the emitted wavelength to change (Jasieniak, Califano and Watkins, 2011), according to Eq. 1:

$$E = \frac{h\,c}{\lambda} \qquad \text{(Eq.1)}$$

To summarise, for the same composition, as the size of the QD varies, the emission wavelength and thus the emitted colour will vary; therefore, the greater the energy emitted by the photon, the shorter the wavelength emitted by the QD (Reshma, V. G. and Mohanan, P. V., 2019). On the other hand, larger particles (lower band gap) emit photons of lower energy and fluorescence towards the infrared region (Fig. 19).

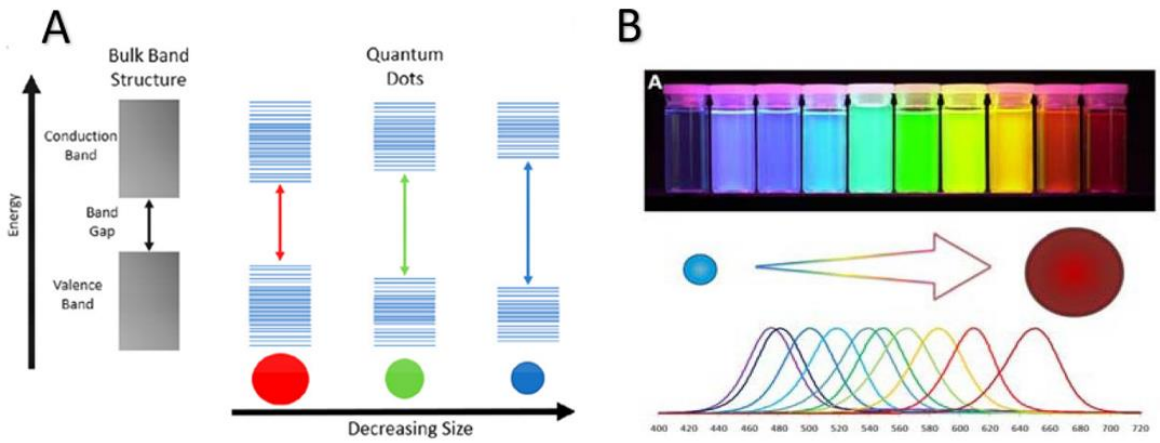

*Fig. 19: **A.** Band Theory of semiconductor materials, Quantum Confinement Effect and light emission mechanism. Source: Reshma, V. G. and Mohanan, P. V., 2019;*
***B.** Unique photo-physical properties of QD probes: narrow size-tuneable light emission profile enables precise control over the probe colour via varying the nanoparticle size. Source: Pavel Zrazhevskiy, Mark Senawb and Xiaohu Gao, 2009*

For the same size, changing the composition material will modify the emission wavelength because the band gap energies will be different depending on the semiconductor used (Thomas C. Wareign et al., 2021). Hence, QDs have the advantages of emitting precise, narrow-field, and modulable fluorescence due to their nanometric size, making them extremely efficient fluorophores or fluorescence tracers in comparison to other organic fluorophores for in vitro staining of cells in real time (Fig. 20) (Warren C.W. Chan et al., 2002). In fact, QDs have the property of reducing image bleaching, improving brightness and have a large multiplexing capacity (Warren C.W. Chan et al., 2002).

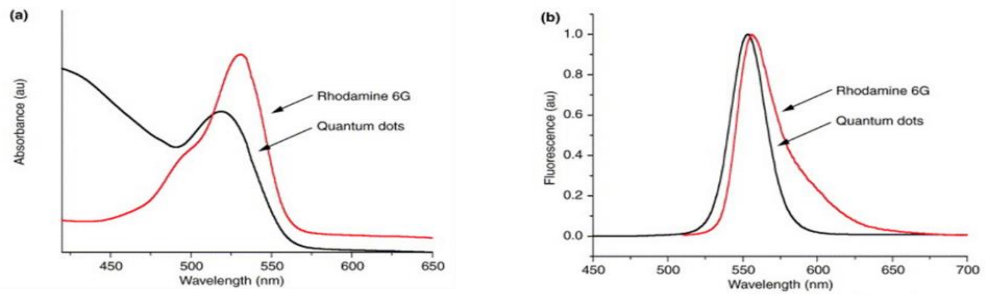

*Fig. 20: Comparison of **(a)** the excitation and **(b)** the emission profiles between rhodamine 6G (red) and CdSe QDs (black). The QD emission spectrum is nearly symmetric and much narrower in peak width. By contrast, the organic dye rhodamine 6G has a broad and asymmetric emission peak and is excited only in a narrow wavelength range; Source: Warren C.W. Chan et al. (2002)*

Indeed, QDs emit twenty times more intense fluorescence and are up to a hundred times more stable to photochemical degradation than organic fluorophores due to their high quantum yield of over 50% (which is a measure of photon emission efficiency defined by the ratio of the number of photons emitted to the number of photons absorbed) (Thomas C. Wareing et al., 2021).

An example is provided by the work of Kaul Z. et al. (2003) who captured immunofluorescence images on human foetal fibroblasts (WI-38) by comparing the photo-stability between Alexa 488 and Cd/Se QDs coated with an additional Zn/S semiconductor shell and conjugated with streptavidin (final size of ~15-20 nm).
The images in Fig. 21 were acquired continuously under the confocal microscope and show that the labelling signals of Alexa 488 started to fade and became undetectable after 6 min due to photobleaching, whereas the QD signals showed no noticeable change for the entire illumination period of 9 min, showing no decrease in detection efficiency (Kaul Z. et al., 2003).

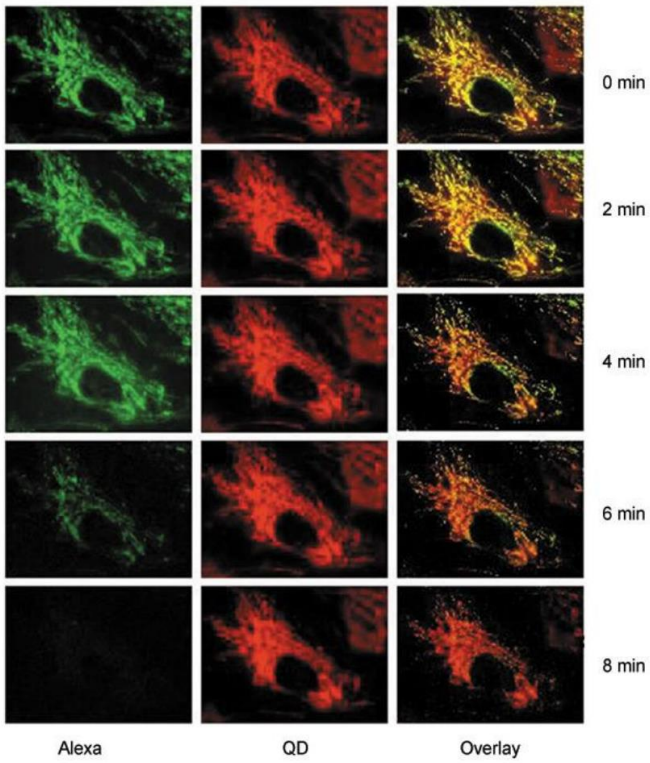

Fig. 21: Immunofluorescence images of mortalin to compare the photostability between Alexa 488 and quantum dots in cells. Source: Kaul Z. et al., 2003

Another advantage of QDs is that they allow multi-imaging since they show narrow and symmetrical emission spectra; therefore, it is possible to combine the use of QDs with another fluorophore or other types of QDs when they both show two non-overlapping and non-interfering emission spectra. In this way, the two fluorescence absorption can be easily discriminated (Timothy Jamieson et al., 2007).
However, it must be emphasised that cell viability decreases as a function of QDs concentration and UV exposure time (Tsung-Rong Kuo et al., 2011).
QDs have a problem related to their toxicity to humans and to the environment; so, for this reason, they are only used in preclinical imaging or in *in vitro* tests. According to Chiu et al. (2016), their toxicity is due not only to the use of organic metals but also to the synthesis process. Indeed, the materials can be immunogenic

and contribute to dangerous immune reactions; moreover, the cores can release free radicals that are extremely toxic to cells.

Instead, the synthesis process has an inherent toxicity due to the persistence of traces of hydrophobic organic solvent molecules on the surface of QDs, e.g. trioctylphosphine (TOP) and trioctylphosphine oxide (TOPO) (Sarita Kango et al., 2015; Robert E. Bailey et al., 2004).

Generally, the fabrication of QDs always starts with the injection of the organometallic reagents into a hot coordination fluid (300 °C), such as TOP or TOPO; subsequently, the temperature is gradually lowered (to around 200 °C) to facilitate the nucleation phase of the organometallic precursor crystals, and then the crystals are grown to the desired size at a constant temperature (Robert E. Bailey et al., 2004). This type of fabrication is very easy and fast; however, it is possible to incur the formation of surface defects in QDs that can cause energy 'losses' that affect the quality of light emission (Sarita Kango et al., 2015).

Alternatively, to stabilise the size and shape of QDs without dynamically changing the temperature during the synthesis process, another organometallic precursor can be injected, which will grow on the surface of the previously obtained crystal (B.O. Dabbousi et al., 1997; Hao Zhou et al., 2019). In this way, core-shell QDs are obtained that have two layers of different semiconductor material. Examples of typical configurations are CdS/ZnS, CdSe/ZnS and CdSe/CdS (D. Vasudevan et al., 2015) In addition, these outer shells will provide greater protection from environmental changes, photo-oxidative degradation, without affecting the fluorescence properties of the QDs core (D. Vasudevan et al., 2015).

For instance, the work of Derfus et al. (2004) and Hao Zhou et al. (2019) showed that covering the CdSe QDs with a ZnS shell enables better cytocompatibility of the NPs, without modifying or altering the fluorescence properties of CdSe (Fig. 22). In these reported cases, functionalisation acts as a protection against the oxidative environment, but does not eliminate the core toxic effect under UV light.

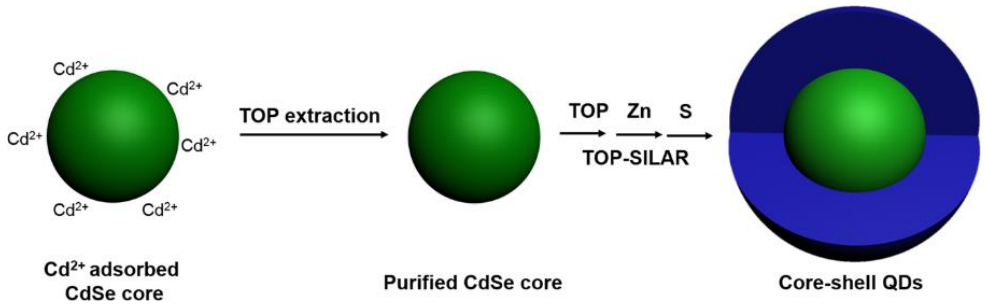

Fig. 22: Illustration of the manufacture of QD CdSe with a ZnS shell; Source: Junjie Hao et al., 2019

These types of synthesis processes are highly efficient and extremely reproducible.

Another possible alternative is the use of QDs doped with metal ions such as manganese, copper, cobalt, nickel or Cd (and others) to enhance the fluorescence properties of NPs and avoid self-quenching (Peng Wu and Xiu-Ping Yan, 2013).

Research has also focused on the development of QD by water-based synthesis method to achieve a hydrophilic surface during the synthesis process with easier, cheaper and reproducible procedures (Mohammadreza Alizadeh-Ghodsi et al., 2019; Wang, Z. and Tang, M., 2021).

This type of synthesis involves mixing metal salts (such as cadmium salts with sodium selenide/telenide) and thiol compounds as capping reagents (Fatemeh Karimi et al., 2019). However, this process is characterised by time-consuming reactions and a lower quantitative yield than those prepared through organic synthesis; moreover, the particles obtained do not possess the high crystallinity observed in organically prepared QDs (Wang, Z. and Tang, M., 2021).

Since QDs needs be suspended and used in contact with aqueous media, they need to be stabilised in water through surface modification to have a hydrophilic and biocompatible surface, hence a *core/shell* structure (that is different from core-shell mentioned before) (Pavel Zrazhevskiy, Mark Senawb and Xiaohu Gao, 2009). According to Pavel Zrazhevskiy, Mark Senawb and Xiaohu Gao (2009), several interactions can be exploited to obtain a core/shell structure: one possible solution involves on replacing the native hydrophobic surface ligands with hydrophilic ligands by direct anchoring to the QDs surface. Alternatively, hydrophilic chains can be sandwiched between the hydrophobic chains and the QD surface; moreover, QDs can be coated with amphiphilic molecules (such as polymers or lipids) through hydrophobic interactions.

After creating a hydrophilic coating, it is possible to exploit the high surface-to-volume ratio to create conjugations (covalent, non-covalent or electrostatic) with biologically active compounds to target specific cell sites (Pavel Zrazhevskiy, Mark Senawb and Xiaohu Gao, 2009). Weibo Cai et al. (2006) exploited the thiol groups of the arginine-glycine-aspartic acid (RGD) peptide sequence to covalently conjugate them to the terminal maleimide groups of the hydrophilic PEG chains previously deposited on the surface of CdTe QDs. The PEG spacer also ensures the maintenance of the 3D conformation of the bioactive molecule. Comparing the *ex-vivo* and *in-vivo* results obtained from functionalised and non-functionalised NPs, Weibo Cai et al. (2016) show that only the type of QDs functionalised with RGD and PEG penetrate U87MG tumour cells to a greater extent, making the tumour area visible. However, this type of NPs has a non-specific distribution in other non-target organs, such as liver and kidney.

Some papers in the literature also demonstrate the usefulness of QDs for real-time imaging of ligand-receptor interaction kinetics on tumour cells, through which certain cellular processes could be monitored (Tang Hailing et al., 2022).

1.2.4. Carbon-based Dots

1.2.4.1. General Features

CDs were discovered in 2004 by Xu et al. (2004) and their development was aided by their intrinsic properties of high biocompatibility, chemical inertness, solubility and their modulable optical characteristics depending on their size, shape, composition, internal structure and surface chemistry, proving to be a viable alternative to QDs in biomedical applications (Pradip Jana and Abhimanyu Dev, 2022).

Moreover, CDs can emit fluorescence in the near-infrared (NIR) spectral region which is the emission region that has the greatest depth of penetration into tissues making them suitable for biomedical applications (Mohammad Jafar Molaei, 2019).

Finally, CDs have a greater ecological impact than QDs because they are made from organic chemical precursors or biomass (CQDs), obtaining a structure consisting of carbon characterized by the presence of surface functional groups that enhance the properties of carbon dots (Bruno Peixoto de Oliveira and Flávia Oliveira Monteiro da Silva Abreu, 2021; Li, X. et al., 2015).

From the perspective of optical properties, CDs show excellent absorption properties at low wavelengths (230-320 nm), due to the π - π* transition of C = C bonds and the n-π* transitions of C=O bonds, respectively (Zhu, S. et al., 2015)

It has been said that the CDs have been particularly successful due to their photoluminescence properties.

However, the photoluminescence mechanisms underlying CDs are still unknown (Li, X. et al., 2015; Thomas C. Wareing et al., 2021), in fact quantum confinement has not been fully defined for this class of materials (Zheng, X.T. et al. 2015; Liu et al., 2019).

In addition, although the possibility of CDs having an emission spectrum dependent on the excitation wavelength is widely discussed in the literature (Mohammad Jafar Molaei, 2019; Nair et al. 2017), several papers show that the only parameter capable of changing the emission is the size (and shape) of the NPs (Chiu et al. 2016; Iannazzo et al. 2017).

From a structural point of view, CDs can be distinguished into graphene quantum dots (GQDs) and amorphous quantum dots (ACQDs). To date, the difference between GQDs and CDs is not very clear and sometimes GQDs are considered a type of CDs, just as graphene is a type of carbon (Aumber Abbas et al., 2018).

Another possible classification for CDs is according to the derivation material.

1.2.4.1.2. GQDs

GQDs are crystalline structures available in different morphologies, consisting mainly of sp^2 hybrid carbon (Aumber Abbas et al., 2018). Generally, GQDs are made by cutting out graphene lattices (characterized by less than 10 stacked layers) to zero size (Aumber Abbas et al., 2018).

Although the mechanisms of photoluminescence of GDQs are still controversial, it is thought to consist of the quantum confinement effect of conjugated π-domains (characteristic of the graphene core), or from the surface and edge state (characteristic of the chemical groups surrounding the core), or even a synergistic effect of both (Thomas C. Wareing et al., 2021).

In addition, the orientation of the edges of the structure affects the emission spectrum of the GQDs (Sk M. A. et al, 2014): the armchair edge widens the band gap of the GQDs by sizes 1.27 nm and 2.06 nm inducing them to an emission in the blue (450.5 and 678.2 nm); zigzag-edged GQDs have traps located in the edges that reduce the conduction band energy, leading toward an emission over the entire visible light spectrum (551 and 872 nm). Moreover, oxidation of GQDs by the -OH or -COOH functional groups shifts the emission peaks toward the red due to band gap reduction (Sk M. A. et al., 2014).

1.2.4.1.3. ACQDs

ACQDs are quasi-spherical carbon nanoparticles in the size range of 2-10 nm, consisting of graphite and turbostratic carbon mixture in different ratios, thus more sp^3 hybrid carbon, higher oxygen abundance and less carbon than GQDs (Aumber Abbas et al., 2018).

The fluorescence of this type of NPs is widely discussed in the literature and is divided into those who argue that it comes from surface defects (which are energy traps capable of absorbing and releasing light, thus shifting the emission to red), those who support that photoluminescence becomes from energy transfer between the core and the CD surface (the core has hybrid sp^2 domains immersed in an amorphous hybrid sp^3 matrix), and those who say that phosphorescence comes from aromatic carbonyls on the surface of CDs (Thomas C. Wareing et al, 2021).

1.2.4.2. CDs synthesis

CD synthesis methods can be divided into two categories: top-down and bottom-up.

Top-down methods refer to the cleavage of bluk materials into smaller materials through methods such as chemical oxidation, discharge, electrochemical oxidation and ultrasound (Inderbir Singh et al., 2018). Impure products, low yield, and the use of aggressive and ecologically unclean chemicals plague top-down methods, so generally bottom-up methods are preferred (Liam Joseph Desmond et al., 2021).

Bottom-up methods create CDs from smaller building blocks; therefore, these technologies have great dimensional and morphological control of the NPs produced (which is critical in biomedical applications), high yield, lower overall costs, and are more eco-friendly than top-down methodologies (Inderbir Singh et al., 2018; Liam Joseph Desmond et al., 2021).

However, these technologies are characterized by a long production time (Liam Joseph Desmond et al., 2021).

Typical bottom-up methods for the synthesis of CDs are hydrothermal treatment, ultrasonic treatment, thermal decomposition, pyrolysis, carbonization, microwave synthesis, and solvothermal methods (Inderbir Singh et al., 2018).

Tab. 3 shows the different synthesis processes that can be used to manufacture CDs and their advantages and disadvantages. The properties that these different methods affect are mainly the surface functional groups of the particles, which can make them water-soluble or suitable for further functionalization.

Method (top-down/bottom-up)	Procedure	Advantages	Disadvantages
Arc discharge method (top-down)[44,45]	Two graphite rods in an open vessel are used as anode and cathode electrodes, respectively, with an arc of current voltage produced in between the two	This method produces MWCNTs, which in theory could be broken down further to produce CQDs	Nanotube soot contains a variety of impurities. The graphitic sheets in the soot have a greater oxidative stability than the nanotubes
Laser ablation (top-down)[36,49–53]	Toluene is used as the carbon source *via* laser irradiation technique. The size of CQDs is controlled using laser furnace	The size/photoluminescence properties of the CQDs can easily be controlled by changing the parameters such as irradiation time	This is not a green method; a low yield of CQDs is generated (4–10%). Low QY, poor control over sizes, modification is needed
Acidic oxidation (top-down)[29]	Carbon nanoparticles are oxidised by a mixture solution of HNO_3, H_2SO_4 and $NaClO_3$, then hydrothermally reacted with DMF, NaHS and NaHSe	The generated CQDs exhibit tuneable PL performance, high quantum yield and longer fluorescence lifetime than other CQDs	The heavily doped heteroatoms can affect the PL properties due to the electronegativity of N, S, and Se
Plasma induced pyrolysis (bottom-up)[54,55]	A negative electrode and a platinum disc are connected to a negative power supply to ignite and sustain the plasma. The CQDs are generated from here	The amphiphilicity of the CQDs make them dispersible in water/most organic solvents. This method can be used to produce CQDs from a wide range of carbon sources	Losses to the reactor walls in the form of tar as well as gas leakage to the atmosphere as this uses higher temperatures than conventional pyrolysis
Combustion/thermal routes (bottom-up)[56–58]	Combustion of a carbon source followed by functionalization with carboxyl groups through conjugation of acetic acid moieties under a high temperature	The obtained CQDs possess a uniform particle size and rich carboxyl groups on the surface. Facile, ease of scale-up production	Small polycyclic aromatic hydrocarbons (PAHs) are generated in soot formation; an environmental hazard
Hydrothermal/solvothermal synthesis (bottom-up)[59–61]	Small organic molecules/polymers are dissolved in water/organic solvent then transferred to a Teflon-lined stainless-steel autoclave at high temperature to form CQDs	Quantum yield of the CQDs can reach 80%, facile synthetic process, green method, many carbon sources can be used	Low quantum yield. Losses *via* the reactor wall can occur; gas is a side product. Poor control over size
Microwave pyrolysis (bottom-up)[41,62]	Combining a carbon source and a saccharide in water to form a transparent solution, in an inert environment, followed by heating in a microwave oven	A rapid synthesis route, great commercialization, simple and environmentally friendly method	The maximum QY reported is 34%, lower than those of other methods reported in the table

Tab. 3: Overview on the Synthesis Methods of Biomass Derived CDs; Source: Liam Joseph Desmond et al., 2021

Several chemical precursors for CDs generation have been identified, including ethylene diamine tetra acetic acid, phenylenediamine, thiourea, carbon nanotube and graphite (Siavash Iravani and Rajender S. Varm, 2019), but the main chemical precursors are mentioned in Tab. 4.

PRECURSORS	METHODS	REFERENCE
Ammonium Citrate	Hydrothermal	Fang et al., 2017
Ethylene Glycol	Microwave Pyrolisis	Jaiswal et al., 2012
Citric Acid	Hydrothermal	Schneider et al., 2017
Phytic Acid	Microwave Pyrolisis	Wang W. et al., 2013
Cetric Acid	Thermal Pyrolisis	Feng et al., 2016
Cetric Acid & bPEI25K	Microwave Pyrolisis	Pierrat et al. 2015
Glycerol & bPEI25k	Microwave Pyrolisis	C. Liu et al. 2012

Tab. 4: Chemical precursors for CD fabrication

Following the synthesis of CDs, several purification and filtration steps are generally required to obtain pure solutions of solid dots (Thomas C. Wareing et al., 2021). These processes can affect the timing and economy of the process, but also the purity and the final properties of the dots produced.

For example, Zhaofeng Wang et al. (2016) created through a bottom-up method sp^2 carbon sheets subsequently cleaved into GQDs by a top-down method (Zhaofeng Wang et al. 2016).

After dot synthesis, functionalisation of the CDs by surface modification or doping of heteroatoms is extremely important to regulate the properties of the dots (Pradip Jana and Abhimanyu Dev, 2022).

Doping makes it possible to change the size of the band gap, thus inducing higher quantum yields and changing the emission wavelength of CDs (Yongqiang Dong et al., 2013).

Indeed, doping CDs with highly electronegative atoms, such as nitrogen and sulphur, results in blue-shifted emission, whereas doping with low electronegative atoms, such as phosphorus and boron, leads to red-shifted emission (Thomas C. Wareing et al., 2021).

In terms of modifying the surface of QCDs, it is possible to functionalise the surface through the numerous functional groups present, creating bonds with various biomolecules.

In general, it is possible to exploit different types of covalent reactions (such as amide coupling, esterification, sulfonylation, copolymerisation, silanisation) that allow bonding with different biomolecules to achieve better control of the size, shape and physical properties of CDs, but also for active targeting (Fanyong Yan et al., 2018).

Non-covalent modifications are also possible by π-interaction with small aromatic molecules (99) or surface modifications via electrostatic interactions, exploiting the charge of surface functional groups (Fanyong Yan et al., 2018).

1.2.4.3. Biomass Derived Carbon Dots (CQDs)

Biomass carbon sources are environmentally friendly natural energy sources that can be converted to obtain higher value and useful materials, facilitating waste management even at a lower cost (Weixue Meng et al., 2019).

Biomass is rich in carbon (up to 40-50%) with an abundance of oxygen and nitrogen, so it can be used as a successful precursor for making CQDs (Liam Joseph Desmond et al., 2021).

As well as being more environmentally friendly and potentially less toxic, these dots generally have similar properties to chemical CDs: high biocompatibility, intense photoluminescence emission and optical properties, good conductivity, broadband optical absorption, high chemical stability, non-flashing, resistant to photobleaching, broad excitation wavelength and emission wavelength that can be tuned by changing the synthesis parameters, including size, shape, composition, internal structure and surface chemistry. (Thomas C. Wareing et al., 2021).

Furthermore, a wide variety of biomasses can be used to produce CQDs with different optical and physico-chemical properties (Manju Kurian and Anju Paul, 2021; Thomas C. Wareing et al., 2021; Liam Joseph Desmond et al., 2021).

Therefore, in the field of biomedicine, biomass selection must be carefully evaluated to achieve high process yields combined with excellent photostability and photoluminescence properties, while maintaining a uniform CQD size (Manju Kurian and Anju Paul, 2021; Liam Joseph Desmond et al., 2021).

1.2.4.3.1. Synthesis CQDs

Top-down or bottom-up approaches can also be used to produce CQDs. The processes for synthesising CQDs are discussed in detail in Tab. 5.

method	process	properties	advantages (Adv) and disadvantages (Dis)
hydrothermal bottom-up	uses heat and pressure in aqueous conditions to produce quantum dots in a cheap, convenient, and ecofriendly way; no passivation required for PL	papaya carbon source produced blue colored CDs with a 2–6 nm size and QY of 18.98%; peach extract produced blue nitrogen-doped with particle size of 8 nm and a QY of 15%	Adv: simple to operate, controllable and nontoxic Dis: poor control over size and presence of impurities.
pyrolysis	uses high temperatures to carbonize organic substances as a simple and ecofriendly way to produce CDs in inert atmospheric conditions	konjac flour as precursor produced nitrogen-doped CDs with quasi-spherical shape, average diameter of 3.37 nm and QY of 22%	Adv: simple and well-established method
bottom-up		CDs from marigold flower had a QY of 7.84% and blue fluorescence.	Dis: high temperatures; further passivation can be needed
microwave	uses microwave heating to carbonize organic substances to produce CDs	casein dots had high QY of 18.7% and size of 7 nm	Adv: most effective and least time-consuming methods; high efficiency and homogeneous heating
bottom-up	QY and quality of this method can be improved by utilizing short duration heating	CDs from rose petals had high QY of 13.45% and size range of 4–6 nm	Dis: poor control over size, microwave radiation is harmful to human beings.
extraction method	uses simple centrifugation and filtration to extract CDs made in nature	dots extracted from Nescafe' were strongly photoluminescent with a size of 4.4 nm and were well-dispersed in water and with QY about 5.5%	Adv: no complicated treatment method; synthesis process is avoided and is low cost
neither		beer extracted dots had an average size of 2.5 nm, were highly soluble, and had excellent fluorescence properties; QY of approximately 7.39%	Dis: poor control over properties.
ultrasonic synthesis top-down	causes biomass to go through dehydration, polymerization and carbonization; CDs are fully synthesized after a short single nuclear burst	food waste dots showed a high degree of solubility in water, a narrow band of PL emission (400–470 nm), a size of 4 nm and excellent photostability	Adv: process is simple, easy to control, and promotes crystal structure Dis: transformations of the dots, poor size control, and a long reaction time
chemical oxidation top-down	oxidants (such as H_2O_2 and H_2SO_4/HNO_3) are used to stimulate the carbonization of biomass materials; the process also introduces oxygen-containing functional groups, such as −OH, −COOH, which increases hydrophilicity	biowaste synthesized dots had an average particle size of 5–6 nm and the QY < 2%	Adv: very hydrophilic and variable emission, and effective and facile method suitable for large scale; process is easily modified, and surface state is tunable Dis: harsh chemical may be used and biotoxicity of the products is increased

Tab. 5: Overview on the Synthesis Methods of Biomass Derived CQDs; Source: Thomas C. Wareing et al., 2021

In addition to these methods, there are other less common synthesis methods, and these are biogenic, solvothermal, oxidation, reflux, calcination, and microwave hydrothermal (Thomas C. Wareing et al., 2021). Even for this topology of CDs, filtration and purification processes to obtain pure solutions or solid dots are still required to obtain pure end products with excellent properties.

Although the methods listed above are widely used in the literature, there is a method of synthesising CQDs from biomass that is experiencing widespread success and is referred to as the 'bottom-up pyrolysis-carbonisation method' (Meng, W. et al., 2019).

This method incorporates two methods (pyrolysis and hydrothermal carbonisation) into a simple two-step method that has clear evidence of success in generating CQDs from biomass material (Malavika, J. P. et al., 2022).

Pyrolysis is a process that requires heat and occurs when organic matter is heated in the absence of oxygen, inducing the decomposition of the fuel source (in this case biomass) into a substance called char (carbon and ash) and volatile matter (bio-oil) (Meng, W. et al., 2019).

Hydrothermal carbonisation is a thermochemical conversion technique that can convert char into energy and chemicals without pre-drying and convert char into CQDs without pre-treatment (Wang, T. et al., 2018).

The particle size of CQDs prepared by bottom-up pyrolysis-carbonisation method is generally between 0.4 and 6 nm and the quantum yield is between 3% and 25% (Malavika, J. P. et al., 2022).

In general, the synthesis of CQDs for biomedical purposes can be done with an infinite number of naturally occurring biomasses (Tab. 6), however, for the purposes of this thesis, only a review of the most successful work in the literature using chitin or ground coffee as a starting biomass will be made.

Source	Synthesis Method	Applications	Reference
Banana peel	Hydrothermal	Bio-imaging	R. Atchudan et al., 2020
Cassava peels	Hydrothermal	Bio-imaging	Permono Adi Putro et al., 2019
Chicken egg shell membrane	Hydrothermal	Probe for DNA recognition	Srikrishna Pramanik et al., 2018
Chickpea peel	Pyrolysis	Bio-imaging	Regina C. So et al., 2017
Citrus fruit peels	Sand bath assisted	Biological labels for cellular imaging	K.K. Gudimella et al., 2020
Duck breasts	Roasting	Bio-imaging	S. Cong et al., 2019
Garlic	Hydrothermal	Cellular Imaging and Free Radical Scavenging	Shaojing Zhao et al., 2015
Milk	Hydrothermal	Drug delivery	Yuan, Y. et al., 2017
Orange peels	Hydrothermal	Bio-imaging	P. Surendran et al., 2020
Stem of banana plant	Hydrothermal	Probes for imaging	S.A.A. Vandarkuzhali et al., 2017
Peanut shells	Hydrothermal	Bio-sensing	Jing Zhu et al. 2019
Rice husk	Hydrothermal	Bio-imaging	Zhaofeng Wang et al., 2015
Shrimps	Hydrothermal	Drug delivery	D'Souza, S. L. et al., 2016
Shark cartilage	Hydrothermal	Bio-imaging	Kim, K. W. et al., 2020
Silkworm cocoon	Pyrolysis	Anti-inflammatory bioactivity	X. Wang et al., 2020
Sugarcane bagasse	Hydrothermal	Bio-imaging	Fengyi Du et al., 2014
Waste tea leaves	Hydrothermal	Bio-sensing	Jing Zhu et al. 2019

Tab. 6: Biomass used to create CQDs for biomedical purposes

1.2.4.3.2. CQDs derived from coffee grounds

Coffee grounds are rich in carbon and nitrogen, so they can be used as a source of high-quality carbon to produce CQDs (Junzhe Chen et al., 2021).

There are some papers in the literature related to the use of coffee grounds as a primary resource for the manufacture of CQDs, and in this section, some papers will be given as examples.

Pin-Che Hsu et al. (2012) developed an approach for the preparation of CQDs from coffee grounds through four steps, including dehydration, polymerisation, carbonisation and passivation, which resulted in CQDs with an average diameter of 5 ± 2 nm and a quantum yield of 3.8%. X-ray diffraction analysis (XRD) and Energy Dispersive X-ray Analysis (EDX) confirm that the CQDs obtained consist of carbon atoms, while FTIR measurements reveal the existence of carboxylate and hydroxyl groups on their surface (Pin-Che Hsu et al., 2012). The photoluminescence of the CQDs obtained by Pin-Che Hsu et al. (2012) is due to the presence of numerous emission traps on their surface, thus showing broad emission spectra ranging from blue (400 nm) to red (600 nm), with a dependence on excitation wavelengths. The strongest photoluminescence occurred at 440 nm when excited at 365 nm, not changing its intensity as a function of pH and under continuous excitation of an Xe lamp for 6 hours (Pin-Che Hsu et al., 2012).

Process yield data are not reported. Subsequently, Pin-Che Hsu et al. (2012) used LLC-PK1 cells as a sample to test the imaging capabilities of CQDs (1.2 mg/mL CQDs for 24 h).

Following excitation at a wavelength of 375 nm, it was possible to localise the CQDs in the cell membrane and cytoplasm of LLC-PK1 cells, thus leading to the hypothesis of internalisation via an endocytosis mechanism (Fig. 23) (Pin-Che Hsu et al., 2012).

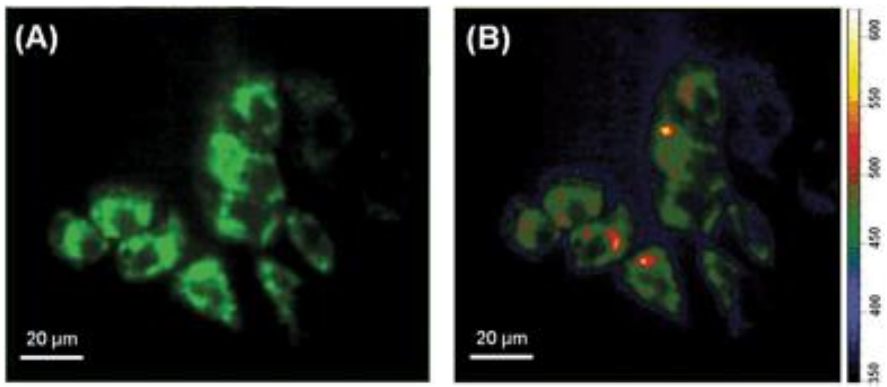

*Fig. 23: **A.** Location of CQDs; **B.** their photoluminescence intensity in LLC-PK1 cells. Excitation wavelength is 375 nm; Source: Pin-Che Hsu et al., 2012.*

Woo Tae Honga and Hyun Kyoung Yang (2021) prepared water-soluble CQDs by hydrothermal synthesis at 220 °C for 20 h using wasted coffee grounds as a carbon precursor, nitric acid and iron nitrate. The structures obtained showed a uniform, spherical, honeycomb-crystallised reticular morphology with a size between 0.5-4.0 nm, with a process yield of 19.7 % (Woo Tae Honga and Hyun Kyoung Yang, 2021).

The highest absorption band of the CQDs obtained by Woo Tae Honga and Hyun Kyoung Yang (2021) was observed at 270 nm, while the main emission and excitation wavelengths were recorded at 411 nm and 334 nm, respectively, due to the presence of sp^2 domain in the carbon structure of the CQDs. The quantum yield was not reported.

The hydrothermal carbonisation treatment was also exploited by Junzhe Chen et al. (2021) to obtain CQDs derived from coffee grounds of about 4 nm. The obtained CQDs showed strong emission at a wavelength of 460 nm, with an optimum excitation of 370 nm due to an enrichment of surface functional groups (-OH, -NH2) confirmed by FTIR analysis (Junzhe Chen et al., 2021). However, the quantum yield and process yield of the quantum dots were not reported in this work.

To transform coffee grounds into CQDs precursors, H. Xu, L. Xie and M. Hakkarainen (2017) used an efficient and eco-friendly route, following the microwave-assisted hydrothermal strategy for 2 h at 180 °C and a pressure of 40 bar. The product obtained were carbon sheets that were subsequently oxidised in 10 % HNO3 under sonication at 45 °C for 0.5 h, and subsequently cut and exfoliated under magnetic stirring at 90 °C for 0.5 h to obtain CQDs (H. Xu, L. Xie and M. Hakkarainen, 2017). Interesting are the explanations offered by H. Xu, L. Xie and M. Hakkarainen (2017) regarding the variable size of the obtained CQDs (between 6 and 80 nm): from the HRTEM and Atomic Force Microscope (AFM) analyses (which show a clear gap between the height and diameter of the QDs), the authors hypothesise the presence of a mechanism of assembly of nanometric graphene oxide sheets for the creation of the CQDs. FTIR and XPS results also confirm the coexistence of sp^2 and sp^3 carbons and showed numerous surface traps and oxygen functional groups in CQDs that provide excellent water solubility and excitation-dependent emission (H. Xu, L. Xie and M. Hakkarainen, 2017). It should be noted that a process yield of 96 % has been claimed, however the quantum yield is not shown (H. Xu, L. Xie and M. Hakkarainen, 2017).

1.2.4.3.3. Chitin-derived CQDs

Chitin is a naturally abundant amine polysaccharide, which is biodegradable and biocompatible as it has a high nitrogen content given by N-acetyl-D-glucos-2-amine units, making it chemically and thermally stable (Hui Su, Jiake Wang, and Lifeng Yan, 2019). Since chitin is a low-cost, non-toxic, environmentally friendly and carbon-rich material, it is possible to use it as biomass to obtain CQDs. However, there are few articles in the literature that make use of chitin as biomass to derive CQDs and these will be mentioned below.

The first article where the use of chitin as biomass to produce CQDs appeared was by Yu. A. Shchipunov, O. N. Khlebnikov, and V. E. Silantiev (2014), where they obtained crystalline NPs with a size of 4-8 nm by hydrothermal treatment under mild conditions (at 160°C for 15 h) of chitin isolated from shrimps. Absorbance spectra of CQDs showed a narrow absorption band at 282 nm, while illumination of the solution with a UV lamp at a wavelength of 365 nm revealed the presence of blue luminescence.

The emission wavelength appears to be dependent on the excitation conditions, showing a gradual shift of the emission peak from 440 to 540 nm and a return of the peak to 440 nm with a further increase in the excitation wavelength from 500 to 600 nm. This mechanism, however, was not explained by the authors, calling for further studies. The quantum yield result is not reported by Yu. A. Shchipunov, O. N. Khlebnikov, and V. E. Silantiev (2014), while the process yield was 50 %.

M. F. Gomes et al. (2019) also used a hydrothermal carbonization treatment (at 200 °C for 6 h) to obtain amorphous CQDs derived from chitin biomass with a size of 2-3 nm (Fig. 24 B) and rich in nitrogen in the form of amine groups. CQDs emit bright blue luminescence when subjected to ultraviolet irradiation (365 nm) (M. F. Gomes et al., 2019).

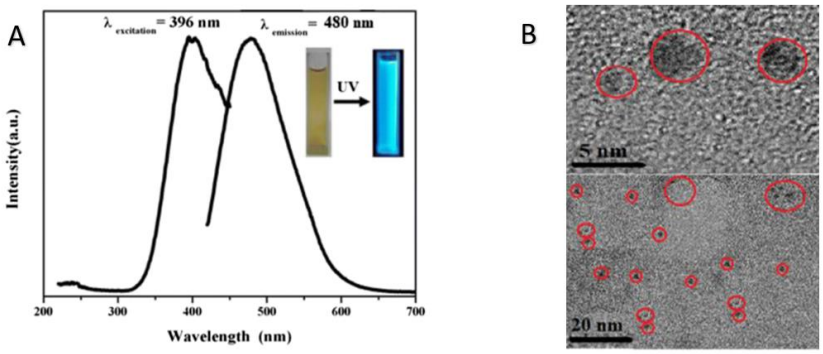

*Fig. 24: **A.** Fluorescence spectra; **B.** TEM images of the CQDs; Source: M. F. Gomes et al., 2019*

The behaviour of the UV-vis absorption spectrum for the CQDs shows a strong peak at 344.1 nm attributed to the sp^2 transitions of the C=C, whereas the maximum excitation and emission wavelengths were 396 nm and 480 nm, respectively, and almost totally overlapped each other (M. F. Gomes et al., 2019) (Fig. 24 A). The process yield of the CQDs produced by M. F. Gomes et al. (2019) was not received, nor was the behaviour of emission wavelengths compared to excitation wavelengths. The quantum yield was 17.1 %.

Hui Su, Jiake Wang, and Lifeng Yan (2019) also obtained CQDs by hydrothermal treatment of chitin that was previously dissolved at low temperature in a homogeneous aqueous solution of potassium hydroxide/urea at different concentrations (0.01, 0.03, 0.05 and 0.07 g/mL). From this process, small organic acids and degradation liquids can be formed simultaneously, from which fluorescent CQDs with sizes between 1-10 nm can be obtained by freeze-drying (Hui Su, Jiake Wang, and Lifeng Yan, 2019). According to Hui Su, Jiake Wang, and Lifeng Yan (2019), the starting chitin concentration has no significant influence on the fluorescent quantum yield (5-6 %) and CQDs productivity (between 3-4 %). FTIRs of the CQDs show the presence of surface amine groups and hydrophilic functional groups (such as carboxyl and hydroxyl groups), which result in good water solubility of the CQDs. The XPS spectra of the CQDs confirm this as they show strong peaks corresponding to C 1s, O 1s and N 1s, also showing different types of carbon binding with oxygen and nitrogen.

Analyses on the optical properties of the CQDs conducted by Hui Su, Jiake Wang, and Lifeng Yan (2019) showed several properties: the UV-vis absorption spectra of the CQDs peaked at 285 and 360 nm, while the peak of the emission spectrum at an excitation wavelength of 360 nm is located at 460 nm, allowing the CQDs solution to emit a bright blue colour (Fig. 25a). However, the authors showed that as the excitation wavelength increases, the position of the emission peak tends to shift towards longer wavelengths, thus exhibiting excitation-dependent emission behaviour (Fig. 25b). Furthermore, the solution of CQDs has a pH-independent fluorescence intensity for a wide range (3-7), whereas for low or high pH, surface functional groups may undergo protonation or deprotonation, resulting in a change in fluorescence intensity.

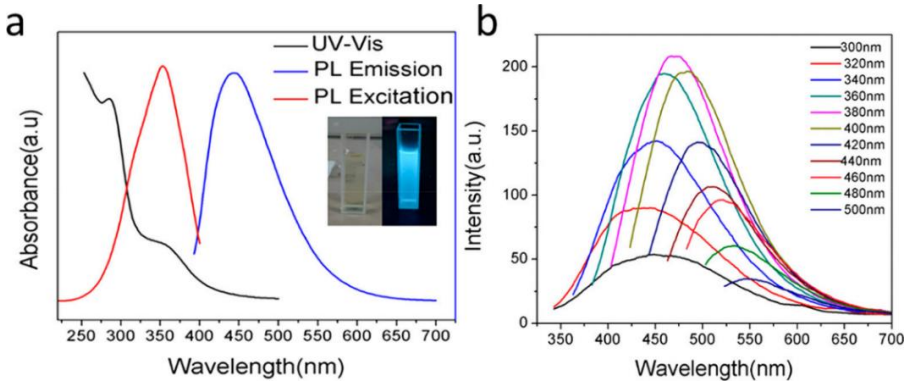

*Fig. 25: **a.** UV–vis absorption, photoluminescence emission, and excitation spectra of CQDs; **b.** Photoluminescence emission spectra of CQDs at different excitation wavelengths changing from 300 to 500 nm. Source: Hui Su, Jiake Wang, and Lifeng Yan, 2019*

There are also works in the literature where chitin based CQDs were doped with nitrogen, oxygen and sulphur, as reported in the works of Mi Feng et al. (2022) and Qiwen Jiang et al. (2020), where the authors prepared doped, photoluminescent CQDs using a deep eutectic solvent treatment of quaternary ammonium salt and sulphonic acid at 150 °C for 5 h. It is also important to emphasise that Mi Feng et al. (2022) obtained a photoluminescence of CQDs that can be shifted from blue to red by changing the composition of the solvent used and reducing the temperature. Different sizes and surface amine and hydroxyl groups were mainly responsible for the red shift of the photoluminescence emission properties . Process yield and quantum yied were 9.9 % and 8.9 %, respectively .

Qiwen Jiang et al. (2020) also demonstrated the synthesis of nitrogen doped CQDs by hydrothermal treatment at 240 °C for 10 h. As indicated in the results, the nitrogen-doped CQDs exhibited a spheroidal morphology with an average diameter of 4.21 nm, a process yield of 17.6 % and a quantum yield of 25.8 % due to the increased nitrogen content in the CQDs (+ 9.89 % nitrogen content) which allowed the formation of multiple nitrogen-containing functional groups. The UV-Vis absorption spectrum showed absorption peaks at 213 nm and 272 nm, while the fluorescence spectra of the CQDs showed narrow peaks and excitation-dependent emission. Furthermore, the CQDs showed bright blue fluorescence when exposed to a 365 nm UV lamp and the emitted radiation had an intensity independent of the pH of the solution in which the CQDs were dispersed.

1.2.4.4. Bioimaging applications of CQDs

Sheng-Tao Yang et al. (2009) fabricated PEG-functionalised oligomeric CQDs with custom-made methodology using carbon soot as precursors.

The chemical-physical characterisation results suggested that the CQDs obtained by Sheng-Tao Yang et al. (2009) had an average diameter of 4-5 nm and were highly fluorescent in aqueous solution (quantum yield of about 20% at 440 nm excitation). Subsequently, the produced CQDs were evaluated for their optical and cytotoxicity performance in vitro (on MCF-7 human breast cancer cells and HT-29 human colorectal adenocarcinoma cells) and in vivo (on murine tumours) with reference to commercially supplied PEG_{1500N} particles and the literature data of CdSe/ZnS QDs. In this work, the high biocompatibility had been demonstrated for both concentrations used (8 and 40 mg carbon core equivalent/kg body weight) and the high fluorescent compared with CdSe/ZnS QDs (Fig. 26 A). Histological analyses also showed that the organ structures of the exposed mice were normal, showing no steatosis, necrosis or hydropic degeneration in the exposed liver sections (Fig. 26 B). Indeed, the amounts of CQDs in the liver and spleen were relatively much higher than those in other organs, but still low in terms of absolute population (20 µg and 2 µg in the liver and spleen, respectively, Fig. 26 C).

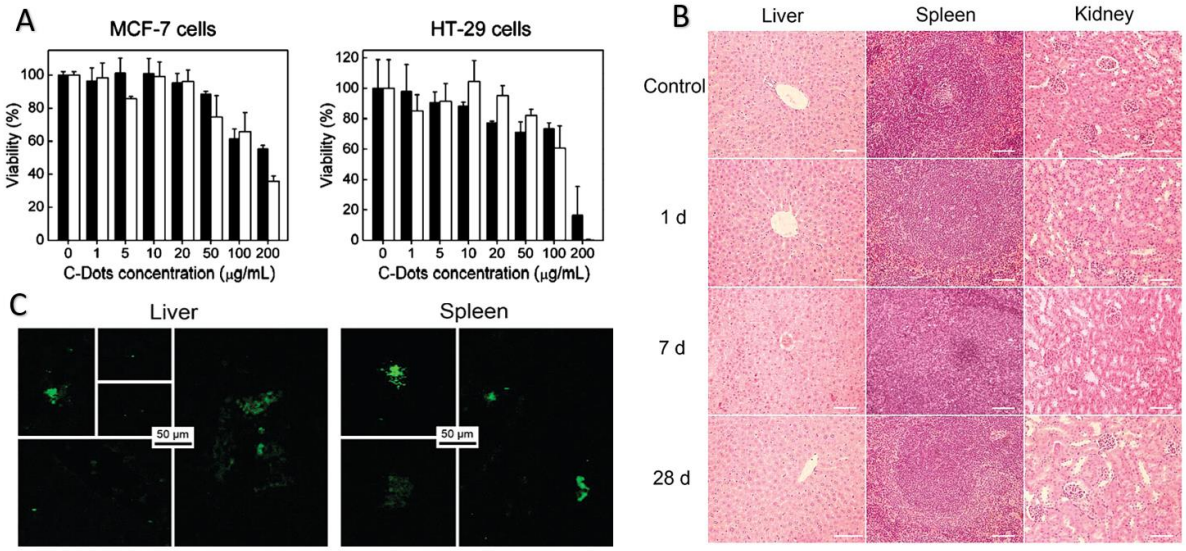

*Fig. 26: **A.** Cytotoxicity evaluations of CQDs (black) and PEG1500N (white). Data presented as mean ± SD.*
***B.** Results from histopathological analyses of liver, spleen, and kidneys.*
***C.** Fluorescence images (two-photon excitation at 800 nm) of sliced liver and spleen harvested from mice 6 h after intravenous exposure to CQDs. Source: Sheng-Tao Yang et al., 2009*

Yunhua Yang et al. (2011) produced highly amino-functionalised CQDs (CNPs) by hydrothermal carbonisation of chitosan at a moderate temperature (180 °C) without any external surface passivation agent or further modification. Produced CQDs were monodisperse and had a narrow size distribution of 4-7 nm in diameter, showing a process yield of 7.8%. The optical properties of the CQDs showed a strong UV-vis absorption characteristic centred at 288 nm (Fig. 27 a), while fluorescence measurements showed the

excitation-dependent emission phenomenon (Fig. 27 b), due to the recombination of excitons trapped by the defects due to the abundance of surface functional groups containing nitrogen, oxygen and carbon.

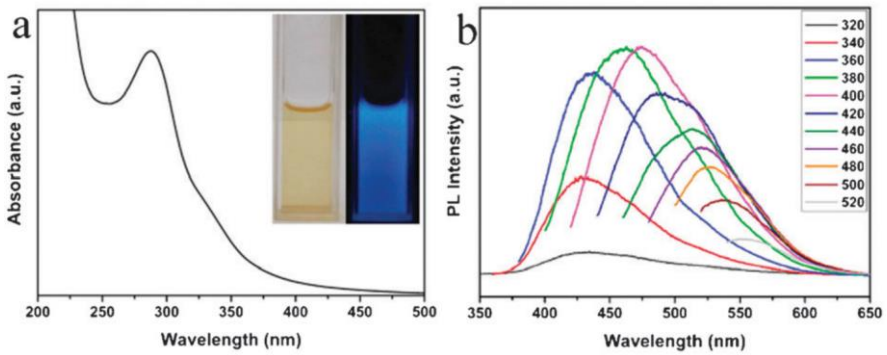

*Fig. 27:**a.** Absorption spectra of the CNPs (inset: photograph of the samples excited by daylight and a 365 UV lamp). **b.** Emission spectra of the CNPs at different excitation wavelengths as indicated. Source: Yunhua Yang et al., 2011*

In addition, the authors demonstrated excellent photostability of the CQDs, as the fluorescence intensity did not change after continuous excitation under a 150 W Xe lamp for several hours and even after immersion in a solution at pH neutral or below 7. The quantum yield of the CQDs was 43 % when excited at 360 nm, much higher than most CQDs reported in the literature.

Subsequently, the CQDs produced were applied to the bioimaging of A549 human lung adenocarcinoma cells, demonstrating low cytotoxicity and excellent biocompatibility; thus, these CQDs can be used in high concentration for imaging or other biomedical applications. Using in-vitro confocal microscopy, photoluminescent spots could be observed in the cell membrane and cytoplasmic area of the cell (Fig. 28), but they were very weak in the nucleus region, indicating that the CQDs easily penetrated the cell but not the nuclei, causing no genetic alterations. The results further confirmed the low cytotoxicity of CQDs.

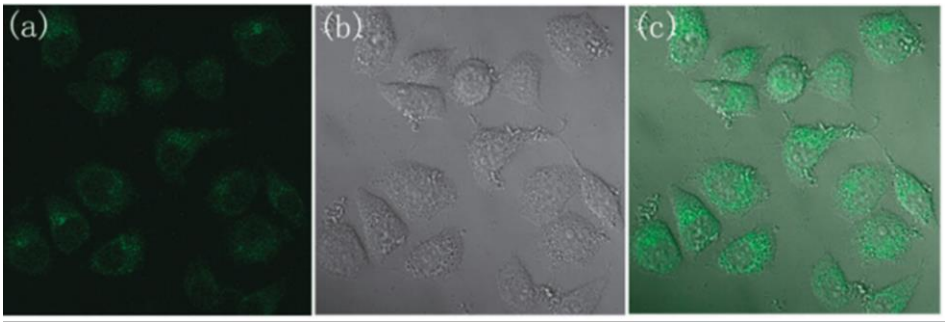

*Fig. 28: **a.** Confocal fluorescence microphotograph of A549 cells labelled with the CNPs at 37 °C for 24 h. (λex: 405 nm). **b.** Bright-field microphotograph of the cells. **c.** An overlay image of A and B. Source: Yunhua Yang et al., 2011.*

Chengkun Jiang et al. (2014) reported the discovery of photoluminescent CQDs in commercial Nescafe instant coffee. Following their extraction in hot water (90 °C) and by centrifugation and a column chromatographic

separation, TEM analysis revealed that the CQDs have an average size of 4.4 nm and were found to be water-soluble and strongly photoluminescent under ultraviolet light excitation with a quantum yield (QY) of 5.5%. The overall yield of the CQDs was about 2% and the physico-chemical characterisation of the CQDs showed an amorphous structure with high C, O and N contents and a high abundance of surface groups, such as -OH and -COOH. In Fig. 29 A, the UV-vis spectra of the extracted CQDs consisted of two peaks between 250 nm and 360 nm, while the photoluminescence of the CQDs appeared to have a strong emission at 465 nm when excited with a wavelength of 390 nm and an excitation-dependent emission behaviour with excellent pH stability over a wide pH range (between 2 and 11). However, after excitation in the NIR region, the photoluminescence spectra of the CQDs showed variable emission peaks between 460 nm and 475 nm but not excitation-dependent (Fig. 29 B).

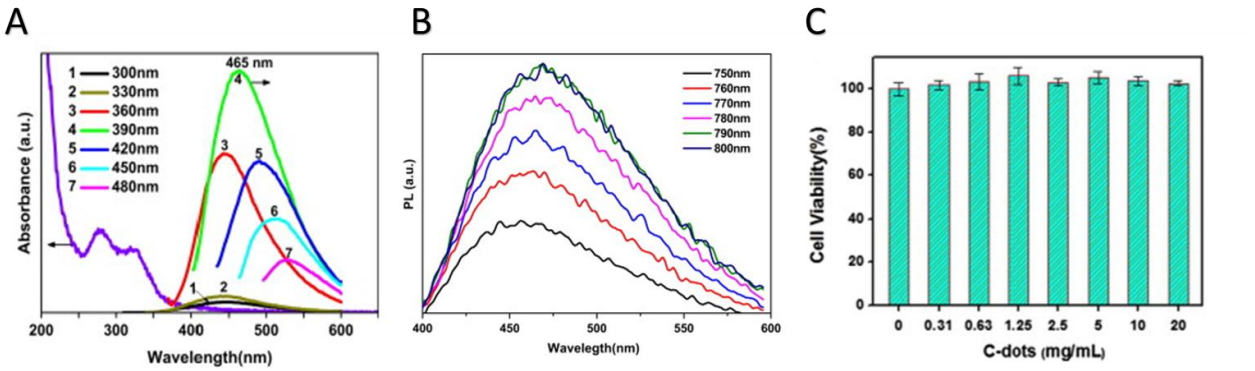

*Fig. 29 : **a.** UV–vis absorption and PL emission spectra of CQDs; **b.** Photoluminescence emission spectra of CQDs excited in the NIR region; **c.** Cytotoxicity of CQDs seeded in CHO cells; Source: Chengkun Jiang et al., 2014*

The cytotoxicity study carried out on CHO cells and human hepatocellular carcinoma cells revealed that CQDs caused no toxicity to the cells up to a maximum concentration of 20 mg/mL for an exposure time of 24 h, and that CQDs can be used for labelling carcinoma cells in vitro through a simple incubation method (Fig. 29 C). Finally, the authors investigated the possibility of using coffee CQDs for fluorescent imaging of small animals by feeding guppy fish a food mixed with CQDs, as shown in Fig 30.A strong photoluminescence of the CQDs-food mixture was observed compared to the control (fish food); moreover, the tested fish remained alive during the observation period for up to four weeks, revealing that the obtained CQDs had low biotoxicity. Thus, these CQDs might have potential for in vivo imaging in small animals.

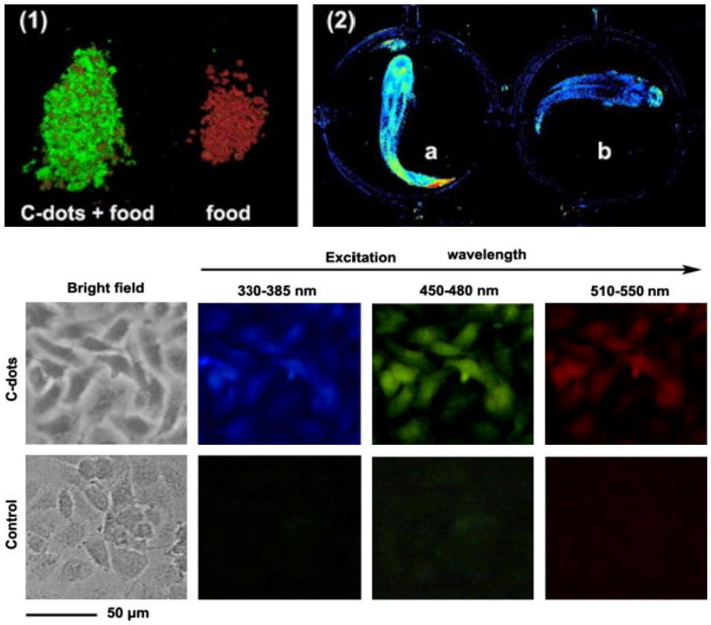

Fig. 30: ***(1).*** *Unmixed fluorescence images of fish food and CQDs-food mixture;* ***(2).*** *Fish treated with CQDs -food mixture (2a) and its control (2b);* ***(3).*** *Bright field and fluorescence microscope images of human hepatocellular carcinoma cells incubated with CQDfor 24 h. Exposure time was 400 ms; Source: Chengkun Jiang et al., 2014*

1.2.4.5. Limitations

CQDs also have disadvantages. According to Thomas C. Wareing et al. (2021) and Liam Joseph Desmond et al. (2021), the main disadvantages are their low quantum yield (less than 30 %) compared to that of QDs (between 40 and 90 %) and the very low process yield of CQDs, which is between 0.12 and 30 %. In this context, it must be emphasised that most studies in the literature do not report the value of the process yield and, if it is present, the discussion of the results obtained is generally omitted. Therefore, further research is needed to develop standard protocols for synthesising CD in an environmentally friendly manner and with very high yields.

To date, only heteroatom doping strategies in the structure of CQDs or surface passivation treatments of CQDs have been developed to improve quantum yields (Wareing et al., 2021; Cao et al. 2013).

Furthermore, it is emphasised that there are not many works in the literature showing a comparison of cytocompatibility between CQDs and QDs or CDs. Finally, the biomedical applications of CQDs are still limited.

Despite these drawbacks, CQDs show considerable potential to solve the challenges arising from the application of QDs, especially in nanomedicine applications in combination with therapeutic counterparts, due to their optical properties, their biocompatibility and the possibility of modifying their surface to acquire active targeting mechanisms (Pradip Jana and Abhimanyu Dev, 2022).

1.2.5. Tumour Recognition by Nanoparticles

Nanoparticles used in cancer treatment can selectively recognise a tumour according to two different mechanisms of action involving passive or active targeting (Mohamed F. Attia et al., 2019).

1.2.5.1. Passive Targeting

As stated in the previous paragraphs, the tumour is formed by cancerous cells that can proliferate indefinitely and can call upon blood and lymph vessels to receive the nourishment necessary to sustain tumour growth. The development of vessels through angiogenesis occurs rapidly and in a disorganised manner (Hanahan and Weinberg, 2011). In fact, in accordance with the findings of Y. Matsumura and H. Maeda (1986), tumours are formed by highly vascularised vessels that are heterogeneous in size and architecture, showing larger and thinner fenestrations than in healthy tissue (Fig. 31).

Therefore, the particles can recognise and passively accumulate within the tumour mass due to their small size (100-300 nm), but also due to a greater permeability of the cancerous tissue to circulating macromolecules compared to healthy tissue, and due to a greater retention of macromolecules in tumours caused by the poor efficiency of the lymphatic system present in the tumour tissue (H. Maeda et al., 1999; H. Maeda et al, 2012). This set of effects resulting from the nature of the tumour is called the EPR effect.

However, murine models used in the laboratory are extremely simple, expensive and do not accurately reproduce the human tumour microenvironment and the rate of tumour development due to the high growth rate of murine tumours, which will significantly alter the pharmacokinetics of drug carriers, accentuating the efficacy of the EPR effect and mitigating their toxicity (F. Danhier, 2016). This could explain the large differences that occur in the therapeutic efficacy of a given drug between preclinical and clinical studies (Shi et al., 2017).

The tumour microenvironment in human tumours has some important differences compared to murine tumours, such as heterogeneity in terms of fenestrations in the tumour endothelium, extent of hypoxic regions, pericyte and basement membrane (BM) coverage, and also in terms of higher extracellular matrix density (F. Danhier, 2016). It is important to emphasise that not all tumours show the EPR effect as it strongly depends on tumour characteristics such as tumour stage, anatomical location of the tumour and composition of the tumour microenvironment (H. Maeda et al., 1999; H. Maeda et al, 2012).

The EPR effect also differs according to tumour type, as argued in the work of Yokoi et al. (2015) where they studied the passive accumulation of liposomal DOXO in brain metastases in different murine organs (murine breast cancer (4T1) vs murine lung cancer (3LL)). Yokoi et al. (2015) were able to demonstrate that the ability of NPs to penetrate through vessels is completely different, showing a passive accumulation of NPs exclusively in the 4T1 tumour resulting in improved survival rates after 30 days. The same authors showed that the intensity of the EPR effect also depends on the location of the tumour and thus on the composition

of the tumour microenvironment, or rather on which primary cells have generated the tumour. In particular, collagen was identified as a matrix protein that influences extravasation (Giovana Onzi et al., 2021).

Indeed, Yokoi et al (2015) show that the 3LL tumour shows no EPR effect due to a high presence of type IV collagen around the blood vessel. As MMP9 metalloproteases are not expressed in the tumour microenvironment, the matrix cannot be degraded; therefore, the collagen remains intact and particles cannot pass through the tumour fenestrations (Danny C. LeBert et al., 2015).

On the other hand, the 4T1 tumour shows the EPR effect as the collagen present is not dense and is distributed loosely around the vessels due to the presence of MMP9 in the tumour microenvironment, facilitating extravasation (Yokoi et al, 2015).

In addition, the size of tumour windows varies over time, so particle characteristics are also crucial: if particles are injected systemically, the particle size must not be smaller than 50 nm so that they are not subject to rapid renal clearance (Muthupandian Saravanan and Hamed Barabadi, Cancer Nanotheranostics: Volume 2, 1st edition 2022 edition, Springer-Verlag GmbH), but they should not be larger than the pore size of the endothelial junction in the tumour environment (300-400 nm) as they would be eliminated by the mononuclear phagocytic system and accumulate non-specifically in various organs such as spleen and liver (Y. Nakamura et al, 2016; Uma Prabhakar et al., 2013; H. Maeda et al., 2012).

These nano dimensions enhance the circulation time of anticancer drugs in vivo and improve uptake from tumour blood vessels to tissues (Y. Nakamura et al., 2016). In addition, H. Maeda et al (2012) also demonstrate that low molecular weight NPs (Mw < 40 kDa) have poor tumour selectivity, consequently they do not provide sufficient therapeutic benefit.

To summarise, nanoparticle accumulation in tumours is not governed by the EPR effect alone, but by a combination of factors.

Although there are several works in the literature on nanoparticles exploiting the EPR effect as a mechanism of action for pharmacological cancer treatments, there are several controversial statements in recent research papers on this mechanism in humans (Chen et al., 2017). The latter argue that the EPR effect is extremely heterogeneous in humans and is a phenomenon that is mainly exploitable in rodents, which is why the development of some nanomedicines in cancer therapy is failing and has no clinical application (F. Danhier, 2016). Other researchers have sparked a debate on the efficacy of the EPR effect in solid tumours, showing that the average tumour uptake of nanoparticles is only 0.7% compared to the injected dose (Wilhelm et al., 2016; F. Danhier, 2016; Simona Mura and Patrick Couvreur, 2012), also demonstrating an inter-patient variability of the EPR effect and, therefore, the need to develop alternative mechanisms to have an effective tumour targeting and to overcome the biological barriers present in the human body.

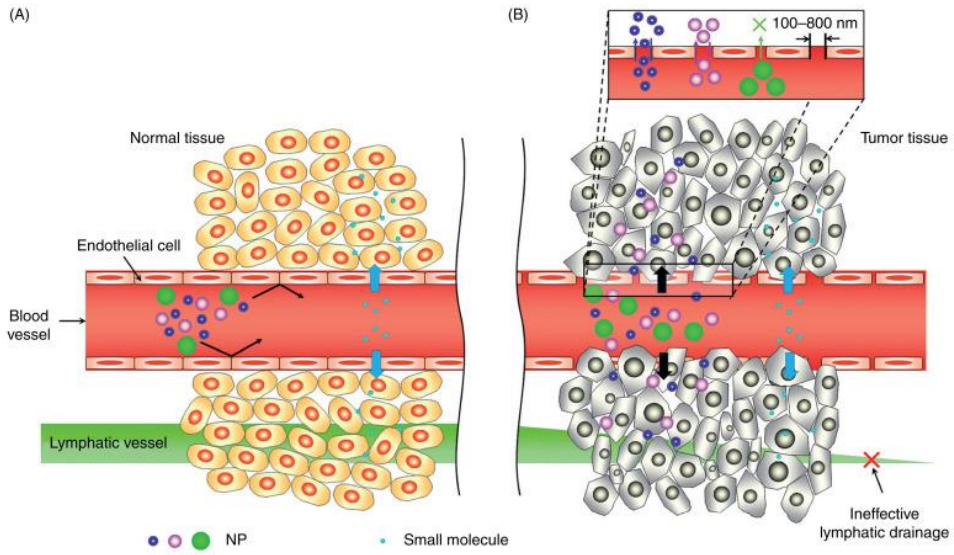

*Fig. 31: Schematic showing differential uptake of NPs and small molecules based on their size across (**A**) normal and (**B**) cancerous tissues. Source: Neda Alasvand et al., 2017*

1.2.5.2. Active Targeting

To enhance the accumulation and the therapeutic efficacy of NPs for cancer treatment, the versatile active targeting strategies can be employed, which allows the selective interaction of the particles with target cancer cells receptors by surface modification of the NPs with a ligand specific (Fig. 32) (Cai et al., 2016; Simona Mura and Patrick Couvreur, 2012). Ligands can be bound to the surface of NPs via covalent and non-covalent conjugations, electrostatic interactions or by exploiting reactions with surface functional groups (Pavel Zrazhevskiy, Mark Senawb and Xiaohu Gao, 2009). Generally, ligands used for active targeting are peptides, antibodies, polysaccharides and other biological molecules (Chin S. Kue et al., 2016). Active targeting is possible due to the high surface-to-volume ratio of NPs, which allows the loading of imaging probes and targeting ligands in the case of cancer therapies (Loverde et al. 2012).

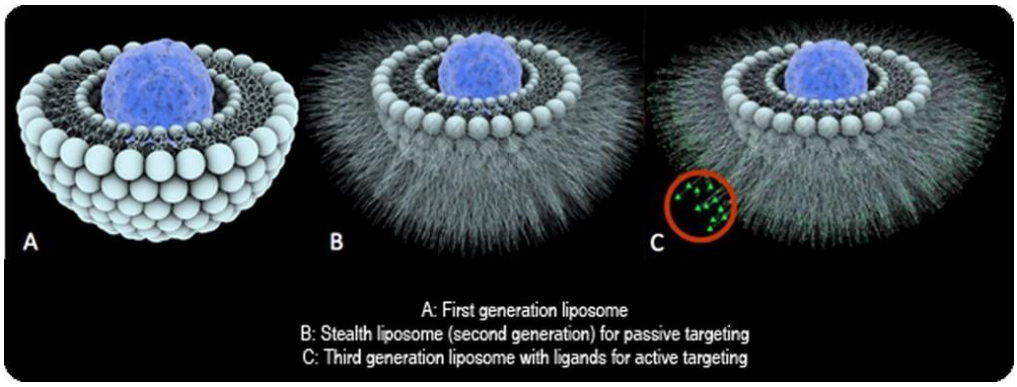

Fig. 32: generational evolution of NPs by tumour targeting; Source: http://reflexions.ulg.ac.be/upload/docs/image/png/2013-03/en-trois-sortes-liposomes.png

Active targeting, however, requires passive targeting to accumulate the particles at the tumour site and subsequently selectively recognise the tumour cells (Simona Mura and Patrick Couvreur, 2012).

The idea of exploiting cell membrane receptors is caused by their fundamental role in controlling cell behaviour and their over-expression on the surface of cancer cells; therefore, there is a higher probability that NPs interact with the target cell than with the healthy cell (Cheng et al., 2008, Bhowmick et al., 2004).

Generally, receptors are on the cell membrane in an inactive state, so ligand-receptor binding activates the receptor on the cell membrane, leading to several pathways: internalisation of the receptor, conformational changes that expose the dimerization domain, formation of homo- and hetero-dimers of receptors, and activation of signalling pathways downstream of the membrane (Kai W. Wucherpfennig et al., 2010).

The result is the facilitated penetration of NPs through the cell membrane of cancer cells, allowing the release of the encapsulated drug exclusively within the cytoplasm or nucleus of the cancer cells, maximising the therapeutic efficacy of the treatment and minimising the side effect of the treatment by not affecting healthy cells (N. Schleich et al., 2015; Cai et al., 2016).

Examples of target receptors used in works in the literature and showing extremely strong affinity to trigger receptor endocytosis are CD44 and HER2 (Zhe Yang et al., 2016; Lilly Y. W. Bourguignon et al., 1997). However, the expression of receptors, proteins, antibodies or surface peptides depending on the cell type (Masood and Farha, 2016).

However, active targeting is specific for a certain type of target cells present in the tumour microenvironment, but it will not be possible to target all cell types present in the microenvironment that do not exhibit the target receptor (N. Schleich et al., 2015; Masood and Farha, 2016; Hanahan and Weinberg, 2011).

1.2.6. Designing NPs to bypass biological barriers and treat cancer

As illustrated in Fig. 33, NPs must have a specific design to bypass the biological barriers that arise during their administration (E. Blanco et al., 2015).

The first biological barrier is offered by the endothelial reticulum system, which allows the recognition of particles as foreign elements in the body through the action of macrophages and circulating phagocytic cells, resulting in non-specific distribution of particles in non-target organs (Yiming Zhou and Zhifei Dai, 2018). There are also haemoreological limitations, which are mainly related to the shape and size of the NPs (Susmita Aryal et al., 2019). Once arrived at the target site, NPs can be restricted by the high pressure of tumour interstitial fluids and by the internalisation mechanisms present in the cell membrane of cells (E. Blanco et al., 2015).

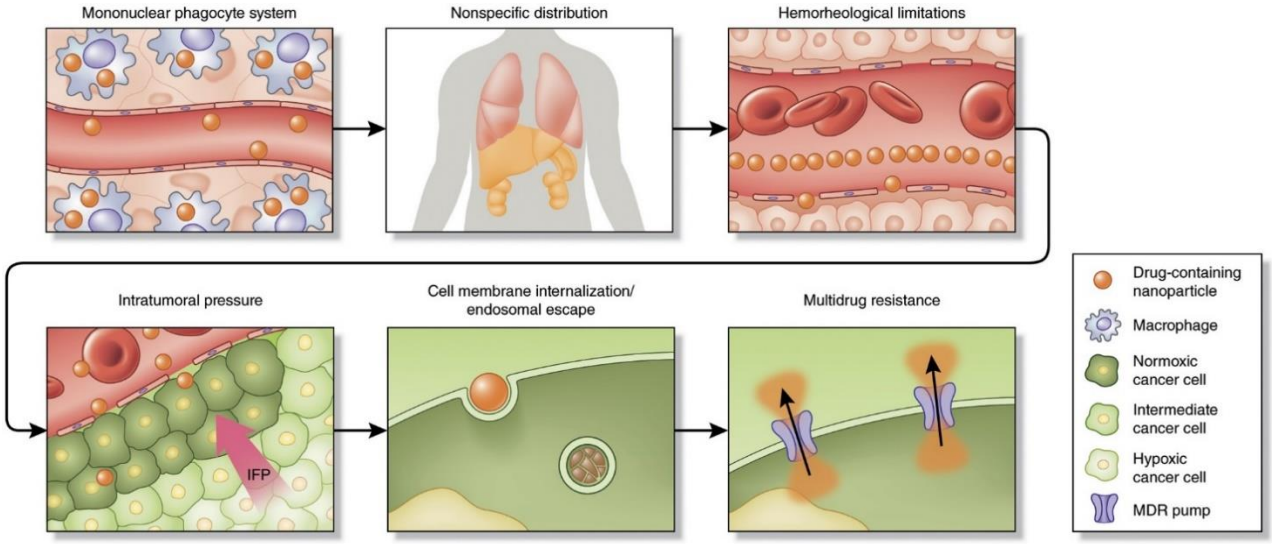

Fig. 33: Biological barriers against cancer treatment by NPs; Source: E. Blanco et al., 2015

1.2.6.1. Mononuclear Phagocyte System

The reticulo endothelial system consists of macrophages and monocytes (that are in abundance in the liver and spleen) with a useful role in phagocytosis and elimination of substances foreign to the body as soon as they come into contact with the blood (Nikita Lomis et al., 2016). The activation of circulating macrophages and the subsequent phagocytosis and transport to non-specific organs is possible through the process of opsonisation of NPs surfaces (Nikita Lomis et al., 2016). Regarding the liver, this has particular macrophages called Kupfer cells and are recognised as the main non-specific accumulation point of NPs (Evaldas Sadauskas et al., 2007).

Various ways for avoiding the adsorption of plasma proteins on the surface of NPs have been discussed in the literature. A first mechanism is the creation of stealth NPs by PEGylation to hysterically repel blood proteins and obviate recognition by macrophages (Shyh-Dar Li and Leaf Huang, 2009).

However, the organism can develop PEG-specific antibodies following repeated administration of these particles such that the NPs can still be recognised (Qi Yang and Samuel K. Lai, 2015). Thus, the role of biomimetic coatings through cell membrane components of stealth cells, such as erythrocytes, has been discussed in the literature, as they are easy to harvest (via a blood draw and subsequent implosion or explosion of the cell via osmotic treatment with hypertonic or hypotonic solutions) and possess limited clearance, thus being able to remain in circulation for a long time (Wenyuan Zhang et al., 2021).

Moreover, erythrocyte membranes are very simple, thus not requiring complex purification mechanisms, and are scalable due to the ability to self-assemble the lipid component of the cell membrane around a more rigid surface following simultaneous extrusion of the components (Wenyuan Zhang et al., 2021).

An example of this type of biomimetic coating is offered in the work of C. Hu et al. (2011) where the in vivo half-life time of spherical poly(lactic-co-glycolic acid) (PLGA) NPs (diameter approx. 75 nm) coated with PEG or lipid shells extracted from erythrocyte membranes (diameter approx. 8 nm) was studied and compared.

From this study the half-life time of lipid shell NPs was 39.6 h, whereas pegylated NPs after 15.6 h were filtered almost exclusively by the liver (50 %). Thus, particles with a lipid shell circulate for a longer time, thus allowing for greater selectivity towards other organs (such as the spleen, lungs and heart), including the target organs, resulting in a possibly better survival rate if a nanomedicine is inserted into the NPs core (C. Hu et al., 2011).

A similar example is also offered by Ji-Gang Piao et al. (2014) where they coated non-spherical inorganic NPs (gold nanocages) with a lipid shell from erythrocyte membranes. The results of the in vivo studies show a higher survival rate in the case of NPs with a lipid shell compared to those coated with PVP, due to the greater stealth properties offered by the erythrocyte membranes. Furthermore, the gold nanocages system is particularly interesting as they show controlled drug release in vitro through NIR photothermal effects indicative of potential applications in combinatorial chemo-photothermal therapy (Moon G. D. et al., 2011).

As an alternative to erythrocytes, platelets can be used to coat NPs as they are circulating cells that can reach and accumulate at tumour sites and can also recognise circulating tumour cells (Nicole M et al., 2020)

The role of platelets towards circulating tumour cells is widely discussed in the literature and there are works demonstrating that P-Selectin (over-expressed on the platelet membrane) specifically binds to tumour CD44 receptors (over-regulated on the tumour cell surface) to secrete TGFβ1, which activates the TGFβ/Smad pathway and the NF-κB pathway to induce the epithelial-mesenchymal transition, making tumour cells less visible to the immune system, thus favouring spread to other tissues (Labelle M. et al, 2011).

Therefore, coating NPs with a shell of purified platelets may be important in the recognition of circulating tumour cells and tumour sites and to minimise immunogenicity in vivo and prolong the circulation time, thus allowing NPs to infiltrate within the tumour mass and release the drug to reduce and eliminate the cancer (Shalvi Sinai Kunde and Sarika Wairkar, 2021).

In the literature there is a work by Q. Hu et al. (2015) where platelet membrane envelope was deposited on a nano gel vehicle obtained by single emulsion and cross-linked by an acid-degradable cross-linker. These NPs were loaded with two anticancer drugs, which are apoptosis-inducing ligand (TRAIL) and DOXO.

TRAIL induces apoptosis of cancer cells by binding to death receptors (DR4, DR5) on the cell surface (Xun Yuan et al., 2018). The obtained core-shell structures had an average diameter of 120.9 nm and a zeta potential of -21.3 mV and they showed an accumulation at the tumour site due to the combination of the EPR effect and active targeting based on the affinity between platelets and CD44 receptors over-expressed on tumour cells (Labelle M. et al., 2011; Q. Hu et al., 2015). The results of in vivo studies conducted by Q. Hu et al. (2015) showed that NPs containing the two drugs and coated with platelet membranes tend to infiltrate and accumulate more at the tumour site leading to a statistically different reduction in tumour mass compared to the control groups (free TRAIL-DOXO, TRAIL-Platelets, DOXO-Platelets or only the nano vehicle). In addition, there was a significant reduction in the number of metastases (visible nodules) compared to the control groups (Q. Hu et al., 2015).

Minjun Xuan et al. (2015) and Yu Zhang et al. (2018) discovered another possible biocoating that originates from macrophage membranes to allow a greater ability to infiltrate and transport drugs within the tumour mass. However, isolating macrophages is not as easy as in previous cases, but their use as a coating allows NPs to be unrecognised by other macrophages in the liver and spleen; therefore, it allows their non-specific distribution to be avoided to promote a greater therapeutic effect at the target site. This work demonstrated the importance of this alternative using mesoporous silica nanocapsules loaded with DOXO and subsequently coated with macrophage membranes. The capsules just described show a significant reduction in tumour volume compared to free DOXO, blank NPs and capsules containing DOXO and coated with PEG (Minjun Xuan et al., 2015).

Finally, there is work in the literature by Ze Chen et al. (2016) where PLGA NPs are coated by membranes belonging to tumour cells to take advantage of the cells' homing ability to accumulate at the tumour site (avoiding non-specific accumulation in the kidney and liver). Moreover, these self-assembled membranes have PEG chains on the surface to allow the nanocapsule to avoid being recognised by the biological barriers just discussed. Furthermore, PLGA capsules encapsulate a fluorophore (indocyanine green) that is used for therapeutic and imaging purposes due to photoacoustic effects. The NPs obtained by Ze Chen et al. (2016) had a final spherical size of 200.4 nm and show a long residence time in tumours allowing real time imaging with high spatial resolution and deep penetration, also improving the photothermal therapy. So, this type of biomimetic coating can open a versatile strategy for safe and effective cancer therapy.

1.2.6.2. Aspecific distribution

The main limitation of nano-therapeutic administration is the inability to reach therapeutic levels at disease sites due to non-specific absorption in healthy organs. Indeed, NPs injected systemically will enter the venous circulation, and then pass into the lungs to be convoluted into the arterial circulation and thus into the other organs up to the kidneys and then back to the venous circulation. The lungs are the first filter for NPs and the first organ of non-target accumulation, but the main accumulation of NPs occurs in the spleen, liver and kidney (E. Blanco et al., 2015).

So, NPs are distributed between target and non-target organs; therefore, to maximise NPs accumulation in the target, accumulation in non-target organs must be minimised. As illustrated in Fig. 34, the chemical-physical and morphological characteristics of NPs determine how NPs are going to be distributed in different body districts, according to Susmita Aryal et al. (2019).

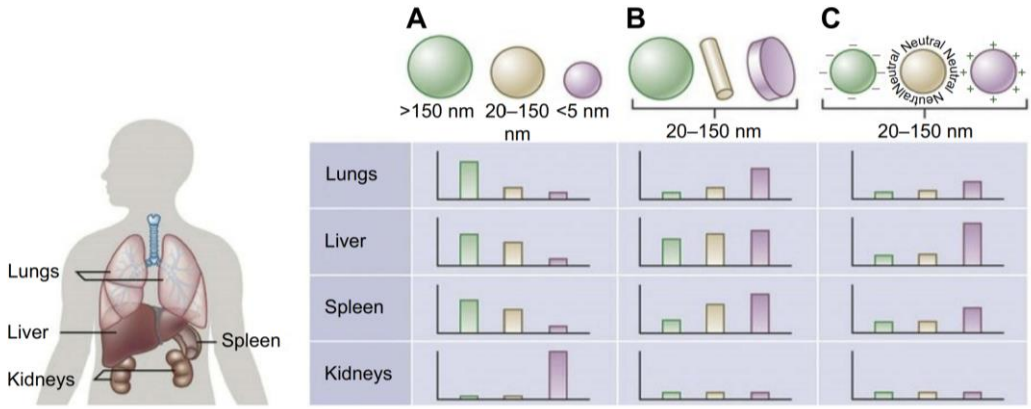

Fig. 34: Physical-chemical and morphological characteristics of NPs determine the biodistribution of NPs in different body districts; Source: Susmita Aryal et al., 2019.

In fact, according to Susmita Aryal et al. (2019), spherical NPs with size greater than 150 nm will be filtered by the lungs and will be more recognized by macrophages in the liver and spleen because of their size. In contrast, spherical particles with sizes smaller than 20 nm will be filtered totally by the kidneys. Nanoparticle charge influences opsonization, circulation time, and interaction with macrophages: NPs with positive surface charge are more prone to sequestration by macrophages in the liver, lungs, and spleen, while NPs with neutral and slightly negative charge have longer circulation times and less accumulation in the aforementioned organs.

Furthermore, strongly cationic NPs interact more favorably with cell membranes, enhancing intracellular uptake, but are toxic when in high concentrations (Jiaqi Lin and Alfredo Alexander-Katz, 2013).

Finally, the shape of NPs alters circulating lifetimes, interactions with membranes, and uptake by macrophages (P. Decuzzi et al., 2009; Randa Zein, Wissam Sharrouf and Kim Selting, 2020). For example, discoidal or rods NPs tend to accumulate more in the lungs, but also in the liver and spleen in slightly smaller amounts (Randa Zein, Wissam Sharrouf and Kim Selting, 2020).

1.2.6.3. Haemoreological Limitations

During the circulation of NPs, rheological limitations of the blood are also present, the effect of which depends on the shape and size of the NPs (P. Decuzzi et al., 2009).

In order to reach a certain target tissue, NPs must marginalize in the vessel border in order to interact with endothelium cells and to be internalised (E. Blanco et al., 2015). According to P. Decuzzi et al. (2009), NPs geometries are exploited to promote margination and increase accumulation at tumour sites of NPs. In fact, usually spherical particles with smaller dimensions remain in the centre of the vessel, whereas spherical larger NPs and larger rods have a greater tendency to marginalise due to collisions with other molecules in the blood vessel (Randa Zein, Wissam Sharrouf and Kim Selting, 2020).

R. Xu er al. (2016) fabricated a porous silicon-based discoidal carrier with a diameter of 2.5 μm and a thickness of 700 nm and a pores size of 40-80 nm that allows loading of polymeric DOXO. This carrier is exploited for tumour targeting in pulmonary vessels and is used as a generator of NPs due to the polymer's ability to self-assemble into an NP once it exits the pore (R. Xu er al., 2016). These NPs will be able to directly target the lung tumour, resulting in an enhanced therapeutic effect. The result of the *in vivo* studies show that half of the tested animals survive after 240 days due to the treatment used, whereas the mice treated with the control or untreated NPs show no survival rate after 120 days (R. Xu er al., 2016).

1.2.6.4. Intra-Tumour Pressure

When NPs arrive close to the tumour mass, they are subjected to high pressure due to the high proliferation rate, the accumulation of waste products that create an oxidative environment, but also by dysregulated vascularisation, by the heterogeneous composition of the tumour and, above all, by the presence of a dense extracellular matrix (Hanahan and Weinberg, 2011).

These assumptions mean that the intra-tumour pressure is greater in intensity than that of the surrounding tissues, as a result there will be greater resistance to NPs entering the tumour microenvironment, pushing them towards the nearest blood vessels (E. Blanco et al., 2015).

An effective way to overcome tumour pressure is the one proposed by Hao Zhou et al. (2016) where they created a co-delivery of enzymes that degrade the extracellular matrix of the tumour to normalise the pressure and improve particle penetration.

Therefore, the use of pegylated PLG NPs functionalised with recombinant human hyaluronidase PH20 enzymes may represent an effective degradative treatment against hyaluronic acid present in the tumour extracellular matrix. In fact, NPs lacking the PH20 enzyme on the surface tend to accumulate in the tumour site in significantly lower amounts (Hao Zhou et al., 2016).

However, when degrading the tumour extracellular matrix, there is a risk of making more room for tumour cells, which is more likely to trigger metastasis formation (Juliane Winkler et al., 2020).

For this reason, this type of proposed treatment has been shelved over time.

1.2.6.5. Cell Membrane

The last step in the circulation for NPs is their cellular internalisation across the cell membrane (E. Blanco et al., 2015). To increase the interaction between NPs and cell membranes, it is possible to use the strategy of active targeting of the NPs' surface through ligands or proteins (such as Albumins) that allow a specific interaction with cell receptors present in membranes resulting in the activation of precise internalisation pathways (Cai et al., 2016; Simona Mura and Patrick Couvreur, 2012).

When the particle penetrates inside the cell, it is incorporated by endosomes and polysomes to be degraded. This mechanism is absolutely to be avoided to allow drug release within the cellular environment (E. Blanco et al., 2015).

Therefore, it is necessary to break the endosomal barrier, and this is possible by exploiting the intrinsic properties of the materials from which the NP is made (Fig. 35) (Samuel A. Smith et al., 2018). Since endosomes have the same nature as the cell membrane, we can use lipid NPs (liposomes) that are able to fuse with the endosome membranes, with subsequent rupture of the formed capsule (Hidetaka Akita et al., 2009).

Another mechanism discussed by Nancy M. Funhoff et al. (2004) is the use of materials that release ions as a degradation product caused by the acidic environment of the endosome, or materials that attract ions from outside. To restore the ionic concentration balance inside the vesicle, water will penetrate the endosome and cause its rupture by osmosis, resulting in the release of the particles (which will be intact) (Nancy M. Funhoff et al., 2004).

A similar mechanism can be used if the polymers used to form the NPs can absorb water under the specific pH conditions of the endosomes, leading towards a simultaneous increase in the size of the NPs and size reduction of the endosome (Atsushi Tamura, Motoi Oishi and Yukio Nagasaki, 2009). The final result is the rupture of the endosome capsule as the NPs have become larger than the endosome can contain.

Finally, surfactant-coated particles can be used to destabilise the endosome membrane due to their ability to insert into the lipid bilayer of the membrane (Anthony J. Convertine et al., 2008). Subsequently, NPs escape intact into the cellular environment.

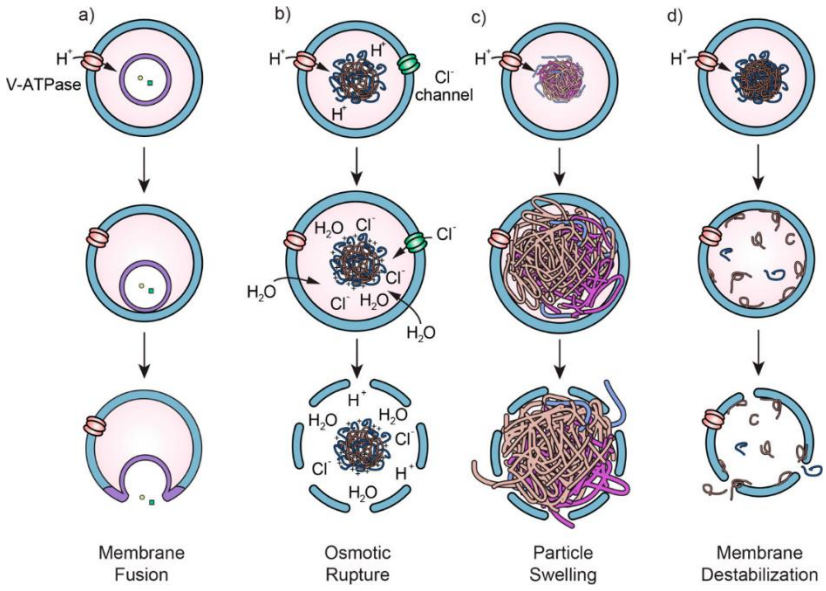

Fig 35: Mechanisms of endosome disruption by NPs; Source: Samuel A. Smith et al., 2018

1.3 Layer-by-Layer Assembly

1.3.1 General features

The layer-by-layer (LbL) assembly method, first proposed by Decher et al. in 1991, is one of the fastest growing bottom-up strategies for the generation of films with controllable thickness (1-500 nm) that can provide physico-chemical functionalisation of substrates without appreciably affecting the size and without changing the bulk properties of the material. Chemico-physical modification of the surface makes it possible to improve the optical, electrical, mechanical properties and the interaction with the surrounding environment of a substrate. For these reasons, LbL is a particularly attractive procedure for numerous application fields, including catalysis, optics, energy, and biomedicine (Joseph J. Richardson, Mattias Björnmalm, Frank Caruso, 2016).

The scheme of the LbL film deposition process appears to be very simple and versatile as it is based on the alternating exposure of a charged substrate to positively and negatively charged polyelectrolyte (PE) solutions, interspersed with rinsing steps to remove the PE excess and prevent cross-contamination of PE solutions (Jason Lipton et al., 2020). These steps allow the formation of a film with the easiest architecture (A/B), however, the steps can be repeated alternately until the desired multilayer structure of type $(A/B)_n$ is achieved.

As just mentioned, PE are essentially the building blocks of LbL. PEs are natural or synthetic macromolecules that, once dissolved in a polar solvent (e.g. water), have many charged groups covalently bonded to them (J. Lyklema, Fundamentals of Interface and Colloid Science, Elsevier, 2005, Volume IV). In general, PE can have different types of such groups:

- Cationic polyelectrolytes: these are macromolecules that assume a positive charge on the chain because of the dissociation of OH^- ions, according to the reaction:

$$R - NH - R + H_2O \rightleftarrows R - NH_2^+ - R + OH^-$$

- Anionic polyelectrolytes: macromolecules that hydrolyse, releasing H^+ ions and consequently assuming a net negative charge on the chain, according to the reaction:

$$R - COOH + H_2O \rightleftarrows R - COO^- + H^+$$

- Polyampholites: macromolecules with both cationic and anionic groups on the chain.

Compared to polymers without charge, the special properties of PEs are their excellent solubility in water, their propensity to swell and their ability to bind and encapsulate large quantities of macromolecules (J. Lyklema, Fundamentals of Interface and Colloid Science, Elsevier, 2005, Volume IV). A distinction is usually made between weak and strong PEs. According to C. Pedeste et al. (2015), weak PEs are polymers with weakly acidic or basic groups that are protonated or deprotonated depending on the pH of the surrounding medium

(thus depending on their dissociation constant), resulting in a pH-dependent charge density. In contrast, the charge density of strong PEs is not affected by pH.

In general, the formation of multilayers from PE is enabled by various interactions, including donor/acceptor interaction, hydrogen bonds, covalent bonds, and the formation of stereocomplexes with specific interactions. However, the driving force of the entire process is the electrostatic substrate/polyelectrolyte and polyelectrolyte/polyelectrolyte interaction (Jason Lipton et al., 2020; Guzmán E. et al., 2020).

Deposition substrates can take different shapes and sizes and can be of different natures, including polymers, colloids, biomacromolecules, organic or inorganic molecules and ions (Joseph J. Richardson, Mattias Björnmalm, Frank Caruso, 2016).

The deposition materials are also numerous and can have nanometric or macroscopic dimensions, even materials characterised by surfaces with complex nanometric patterns. The major disadvantages of this technology are the operator dependence of the process and the relatively long timescales to achieve complete deposition of a layer (Ana Mateos-Maroto et al., 2021).

As the scalability and reproducibility of the process are also limiting, several automated systems for LbL have been developed in the literature; however, they are still a long way from clinical application (Ana Mateos-Maroto et al., 2021; Joseph J. Richardson, Mattias Björnmalm, Frank Caruso, 2016).

1.3.2. LbL Technologies

The LbL technologies available in the literature can be condensed into five broad categories: immersion, spin, spray, electromagnetic and fluidic assembly.

Immersive LbL assembly is the most popular method and is typically performed by manually immersing a planar or particulate substrate in a solution of the desired PE for ~15 minutes, followed by two to three washing steps to remove unbound material (Fig. 36) (Guzmán E. et al., 2017; Abubakar Musa Yola et al., 2021). Immersive assembly results in more homogeneous, thinner, and interpenetrated films than non-LbL assembly technologies; however, the main problem with this type of assembly is the high waste production since the solutions used will have to be replaced with new ones to avoid cross-contamination (Abubakar Musa Yola et al., 2021; Joseph J. Richardson, Mattias Björnmalm, Frank Caruso, 2016).

Although automation reduces manual involvement, it does not substantially reduce overall assembly time, which is why some researchers have focused on combining faster deposition kinetics with automated systems, including roll-to-roll technology. To reduce PE assembly time and enable the deposition of materials with low surface charge and/or small contact area, solutions doped with organic solvents (e.g. dimethylformamide) can be used to eliminate rinsing and drying steps and replace them with dehumidification and evaporation processes (Joseph J. Richardson, Mattias Björnmalm, Frank Caruso, 2016).

It has been said that particles can also be coated. In this case, there is a step of particle collation by centrifugation between the deposition and washing steps, which is labour-intensive and generally difficult to

automate (Yan Yan, Mattias Björnmalm, and Frank Caruso, 2014). This step can lead to aggregation of NPs, so it should be avoided (Joseph J. Richardson, Mattias Björnmalm, Frank Caruso, 2016). A solution to this problem could be the saturation method through ζ-Potential measurements (D.V. Voldkin et al., 2004; M. Adamczak et al., 2012; M. Müller et al., 2003). This method involves the deposition of a layer with an optimal thickness when the ζ-potential of the NPs have reached a value close to or higher than the ζ-potential of the PE solution used (M. Adamczak et al., 2012). This technique achieves a shell thickness similar to those obtained by centrifugal assembly but is about three times faster (Joseph J. Richardson, Mattias Björnmalm, Frank Caruso, 2016). Alternatively, aggregation can be avoided by introducing sonication steps between deposition (Yan Yan, Mattias Björnmalm, and Frank Caruso, 2014).

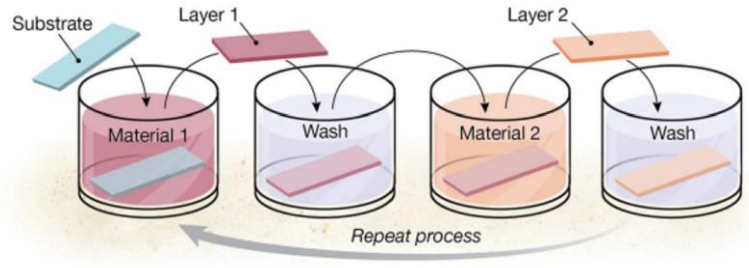

Fig. 36: Layer-by-layer immersive; Source: Joseph J. Richardson, Mattias Björnmalm, Frank Caruso, 2016

Spin assembly uses spin substrates to deposit layers by casting PE solutions and to remove excess coating material (Fig. 37) (Steven Vozar et al. 2009). According to Joseph J. Richardson et al. (2016), centrifuge assembly typically produces thinner, more organized, and more layered multilayers than immersive assembly, and the process can be much faster (~30 s) due to the forces that govern the process: electrostatic interactions, which cause adsorption and rearrangement of polymers, and centrifugal, air shear and viscous forces, which cause desorption of weakly bonded polymers and dehydration of the films resulting in better chain organization and smoother interface (Abubakar Musa Yola et al., 2021). The thickness of polymer films assembled by spin is mainly related to spin speed. At higher velocities, thinner films will be produced (Steven Vozar et al. 2009). However, standard spin coaters are generally designed for flat surfaces and are not suitable for complex shapes or rough surfaces because of the high shear forces involved in film assembly (Joseph J. Richardson, Mattias Björnmalm, Frank Caruso, 2016).

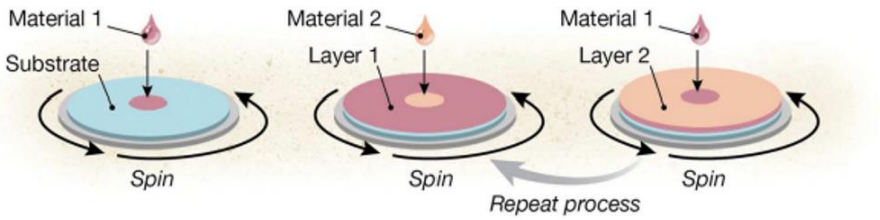

Fig. 37: Layer-by-layer Spin-Coating; Source: Joseph J. Richardson, Mattias Björnmalm, Frank Caruso, 2016

LbL spray assembly is another category of assembly, in which films are assembled by aerosolizing polymer solutions and spraying them (in vacuum or not) sequentially onto three-dimensional substrates (Fig. 38) (Abubakar Musa Yola et al., 2021). The resulting films are usually well-organized with distinct layers and can coat large or nonplanar substrates. In contrast, coating of complex substrates is poorly appreciable (Joseph J. Richardson, Mattias Björnmalm, Frank Caruso, 2016). In spray assembly, the film thickness is affected by the concentration of the suspension, spray flow rate, spray duration, resting time, whether the substrate is washed or not, and whether the solution is sprayed vertically or horizontally (Abubakar Musa Yola et al., 2021). This control derives from the main forces governing the atomisation assembly process, which are the mass movement in the atomisation and the random movement in the liquid film (Joseph J. Richardson, Mattias Björnmalm, Frank Caruso, 2016).

Spray assembly is much faster than immersive assembly (up to ~6 s per layer divided by 3 s for each deposition step and 3 s for washing), so it is widely used in various applications because it offers fast assembly times and is suitable for both automation and scalability (Deng et al., 2013; Morton et al. 2013). However, spray LbL assembly produces films that may not be homogeneous because of gravity drainage and due to irregular droplets sprayed (Joseph J. Richardson, Mattias Björnmalm, Frank Caruso, 2016). Furthermore, substrate washing steps generally produce thicker films than the unwashed substrate, due to the rearrangement of polymers during washing (Joseph J. Richardson, Mattias Björnmalm, Frank Caruso, 2016).

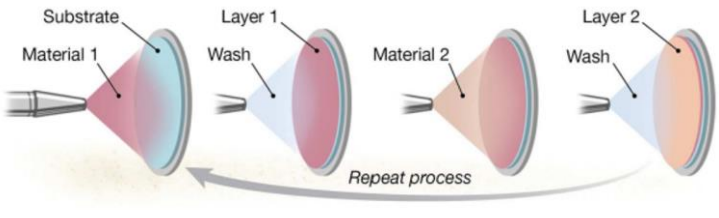

Fig. 38: Layer-by-layer Spray; Source: Joseph J. Richardson, Mattias Björnmalm, Frank Caruso, 2016

Electromagnetic assembly uses electric or magnetic fields created by immersion of electrodes in PE solution, which can be inverted according to the polarity of the layer to be deposited (Fig. 39) (Abubakar Musa Yola et

al., 2021). This method allows the deposition of films on planar substrates or on (immobilized) magnetic particles by pH changes in the solution or by current-induced redox reactions (Joseph J. Richardson, Mattias Björnmalm, Frank Caruso, 2016). In addition, ions, polymers, and colloids can also be encapsulated in short timescales. Following each deposition step, a washing step is required in an identical way to immersive technology. Generally, electromagnetically assembled films are thicker and denser than those prepared by other LbL assembly methods, however, deposition times are shorter than the immersive gold standard, as they are ~1.5 nm/s (Joseph J. Richardson, Mattias Björnmalm, Frank Caruso, 2016). This is true for planar substrates, while the deposition times for particulate substrates are a few tens of minutes (Yan Yan, Mattias Björnmalm, and Frank Caruso, 2014). Although electromagnetic assembly is a viable alternative, it requires special equipment and expertise to use.

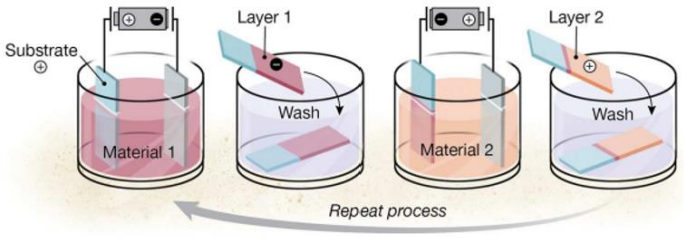

Fig. 39: Layer-by-layer Electromagnetic; Source: Joseph J. Richardson, Mattias Björnmalm, Frank Caruso, 2016

Finally, fluidic assembly is an alternative that is gaining wide acceptance among researchers. This technology provides assembly solutions through microfluidic channels allowing the creation of region-specific patterning (Abubakar Musa Yola et al., 2021). In addition, thanks to the size of the devices is relatively small, the method allows production to be increased to an industrial level, while also enabling significantly lower reagent consumption (Fig. 40) (Joseph J. Richardson, Mattias Björnmalm, Frank Caruso, 2016).

This technology allows not only the deposition of polymers, but also larger cargoes, such as gold nanoparticles or liposomes. In addition, there are several studies where researchers have used this technology to assemble NPs, such as emulsions and lipid particles (Chaitanya Kantak et al. 2011).

In general, the coating can be deposited through two ways: by coating the channel wall, or by placing the substrate in a channel perfusion chamber and moving the deposition material using pressure or vacuum within the channels. The parameters that control the thickness of the deposited layers are polymer concentration, contact time and flow rate. Generally, assembly times are between 5-10 min for a thickness of 1.5 nm. In addition, it is possible to exploit capillary forces that allow for significantly faster material deposition (1.2 nm thickness in less than 2 min) (Joseph J. Richardson, Mattias Björnmalm, Frank Caruso, 2016).

However, this latter alternative is not suitable for larger volumes or when dynamic flow rate control is needed. Moreover, creating and understanding how to manage a microfluidic system properly and competently is not easy (Guzmán E. et al., 2017).

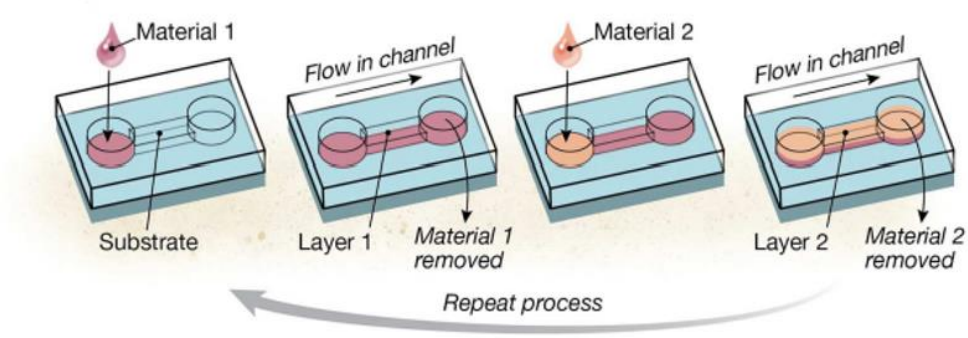

Fig. 40: Layer-by-layer Fluidic; Source: Joseph J. Richardson, Mattias Björnmalm, Frank Caruso, 2016

To summarise, the strong progress of the LbL method in recent years is very promising, opening exciting avenues for the design of engineered multifunctional nanomaterials for numerous technological and biomedical fields. The characteristics of the different LbL technologies can be summarised by Tab. 7.

LbL Assembly Techonology	**Substrate size**	**Time per layer**	**Layer thickness (nm)**	**Automated**	**Layer structure**
Immersive	10 mm – 1 mm	10 s – 12 h	1-15	Yes	Interpenetrated
Spin	1-100 mm	10 s – 5 min	1-2	Yes	Stratified
Spray	10 nm – 10 m	1 s – 24 h	1-15	Yes	Stratified
Electromagnetic	10 nm – 100 mm	1 s – 20 min	1-20,000	No	Stratified
Fluidic	100 nm – 100 mm	10 s – 45 min	1-3	Yes	Not Reported

Tab. 7: Features of LbL Assembly Technologies; Source: Joseph J. Richardson, Mattias Björnmalm, Frank Caruso, 2016

1.3.3. Parameters modifying physico-chemical properties of LbL multilayers

Over the past two decades, several researchers have focused their attention on the mechanisms regulating the growth mechanisms of LbL coatings. Indeed, it is known that there is no single regular growth mechanism for all polyelectrolyte systems (Fig. 41). PE films can grow linearly or non-linearly and can undergo a transition between both types of growth, depending on the strength of the intermolecular interactions of the polyelectrolytes, thus depending on the combination of polyelectrolyte pairs and the experimental deposition conditions (Ana Mateos-Maroto et al., 2021).

In linear growth, both the mass and thickness of the film increase with the number of layers deposited, and the resulting thickness is the sum of the characteristic chain lengths of the two PEs. Non-linearly growth systems include those films whose mass and thickness increase with the number of layers deposited faster than in the case of linear systems (Guzmán E. et al., 2020). Although the mechanism underlying the non-linearly growth regime is still not entirely clear, film roughness (Guzmán E. et al., 2012) and the diffusion of PE chains from the entire film during deposition (Elbert DL et al., 1999) are indicated as the main sources of this growth.

The influence of PE charge density on the assembly of multilayer systems has also been studied and explored. In fact, the use of strong PE generally leads to coatings with linear growth and less thickness due to their high charge that is independent from the pH of the solution in which they are solubilised (Kyleen E. Swords et al., 2011; Abubakar Musa Yola et al., 2021). On the other hand, due to the presence of functional groups that are not completely dissociated in their chain, the use of weak PEs leads to the creation of less tightly assembled films that allow for a greater interpenetration of chains between one coating and another (Kyleen E. Swords et al., 2011; Abubakar Musa Yola et al., 2021). Consequently, the formation of coacervates in the interfacial region, and their subsequent precipitation, can justify an increase in thickness beyond that expected for a linear polymer layer (Ana Mateos-Maroto et al., 2021).

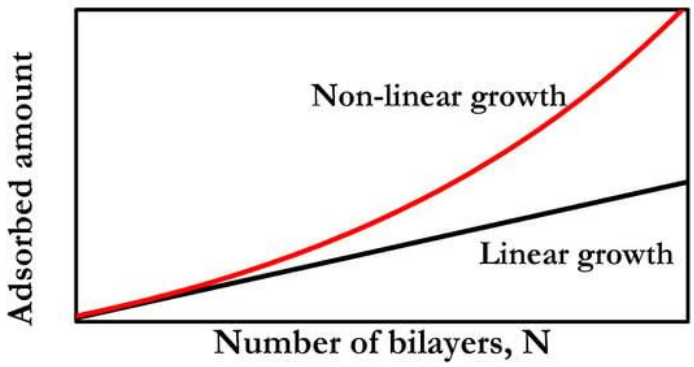

Fig. 41: LbL growth mechanisms; Source: Eduardo Guzmán et al., 2020.

As an example, Tab. 8 shows the growth mechanism of some PE pairs in the literature.

Materials	Growth Type	Reference
PAH – PSS	Linear	Ladam G. et al., 2000
PEI - PAA	Linear	Yang Y-H et al., 2011
PAH – PAA	Linear	Johansson E. et al., 2009
CHI - ALG	Linear	Yuan W. et al., 2007
PLL – HA	Non Linear	Jourdainne L. et al., 2009
PLL – PGA	Non Linear	Itoh K. et al., 2008
CHI - PAA	Non Linear	Guzmán E. et al., 2011
CHI - HA	Non Linear	Salomakki M. et al., 2009
PDADMAC-PSS	Non Linear	Guzmán E. et al., 2009

Tab. 8: Combination of PE multilayers and their growth type

The mechanism of PE deposition on oppositely charged surfaces is driven by the phenomena of charge compensation and charge overcompensation. Due to steric factors, the deposition of PEs does not initially lead towards neutralisation of the surface but induces the deposition of excess charge chains that protrude towards the bulk solution (Eduardo Guzmán et al., 2020). This mechanism ensures the neutralisation of the unconcentrated charges of the substrate and the overcompensation of the initial surface charge, also allowing the hindrance of the adsorption of additional molecules due to the electrostatic repulsive interactions induced by the presence of the charged chains that are oriented to the bulk solution (Eduardo Guzmán et al., 2020). This phenomenon will allow the alternating deposition of oppositely charged layers.

Generally, the deposition process involves the compensation of the excess of charges of the inner layers during successive depositions to avoid film instability and to fulfil the boundary conditions of electroneutrality. This compensation can be intrinsic if there is a perfect match between the charges of the monomers in the adjacent layers, leading to the formation of multilayers with a significant degree of ionic cross-linking between the polymer chains. However, there is usually no perfect correspondence between the charges in the adjacent layers, and the presence of counter-ions (from the bulk) is mandatory to guarantee the electroneutrality of the multilayers, inducing extrinsic compensation and the formation of multilayer structures with a wide range of different stoichiometries (Ana Mateos-Maroto et al., 2022).

In this context, the counter-ions distribution profile will be crucial as it will affect the osmotic stress within the multilayer, regulate the roughness of the layers and define the structural and chemical-physical properties of each layer (Eduardo Guzmán et al., 2020).

However, there are many other parameters that control the physico-chemical characteristics of the deposited layers. Some parameters that can influence coating growth are the physico-chemical properties of the template, including charge density and surface roughness as they govern the interactions between the substrate and the deposited layers. This is particularly important when it comes to the deposition of the

initial layers (pre-layers), as these will be the layers that guarantee the stability of the final multilayer structure (Regine v. Klitzing, 2006; Eduardo Guzmán et al., 2020).

Another parameter that can influence layer deposition is the concentration of PE solutions. Indeed, LbL fabrication requires the use of solutions with enough concentration to allow the deposition of stable layers and to ensure charge reversal (Eduardo Guzmán et al., 2017). However, according to Shen et al. (2012) using too high a concentration of PE in solution drastically affects the growth mechanism of multilayers, inducing the formation of thicker layers. A good solution to this problem would be to use the Saturation Method described above.

The chemical nature of PEs and substrates is an important factor to consider, especially regarding their hydrophilic/hydrophobic nature, the flexibility of PE chains, their charge density and molecular weight (Eduardo Guzmán et al., 2017). These characteristics will also define the surface topography of the substrates, imparting hydrophilic or hydrophobic or superhydrophobic (anti-fouling) properties to the generated surface (Nan Zhao et al., 2005). In terms of charge density, the PE solution must be lower than a certain threshold because it could cause the removal of the previously deposited layer, resulting in the formation of inter-polyelectrolyte complexes in solution (Ana Mateos-Maroto et al., 2021).

A similar effect is caused by the assembly of low molecular weight PEs (Ana Mateos-Maroto et al., 2021). However, as the molecular mass of PEs increases, the adhesion of PEs increases due to their weight and leads towards multiple layering (Eduardo Guzmán et al., 2020).

Equally important are the polarity of the solvent, the pH of the solution and the assembly temperature. Most films obtained by the LbL method are generally obtained from aqueous solutions of polyelectrolytes, minimising the toxicity associated with the use of organic solvents. However, in some cases it may be necessary to use organic solvents with different polarities to adjust the interactions between PEs with dispersion forces and hydrogen bonds, modifying the conformations of the PEs and consequently the structure and properties of the films obtained (Eduardo Guzmán et al., 2020).

The pH plays a key role in the deposition of the layers and must be chosen particularly carefully, especially for weak PEs. Changes in pH induce changes in the ionic balance and, consequently, affect the degree of ionisation of the PE chains and the effective charge of the PE (C. Pedeste et al., 2015).

The impact of temperature is also important, as an increase in the intensity of this parameter may allow for greater solubilisation of the PEs to be deposited and may induce a transition in the growth mechanism of the layers (from linear to non-linear) due to increased mobility of the chains within the multilayer (Eduardo Guzmán et al., 2020).

According to Eduardo Guzmán et al., 2020, the fundamental parameter governing LbL assembly is ionic strength since ions can order or disorder water around other molecules; thus, they are able to modify enthalpic and entropic equilibrium. In fact, an excessive presence of counter-ions can cause the possible

shielding of charges along PE chains and, consequently, can cause less inter- and intra-chain repulsion between PE of the same nature.

This leads to a worsening of the solubility of the polyelectrolyte, a change in the degree of swelling and hydration of the multilayers, resulting in changes in the properties and in the structure of the multilayers, leading to increased deposition or to the deconstruction of the multilayers.

In general, most PE multilayers have a relatively high-water content (between 20 and 80 % of the total weight of the films), which allows the encapsulation and release of active compounds from the assembled LbL materials (Eduardo Guzmán et al., 2009). Generally, the water content of the films strongly depends on the thickness of the multilayer and the densification of the deposited material (Eduardo Guzmán et al., 2009, Stephan T. Dubas and Joseph B. Schlenoff, 2001).

Equally important are the methodological aspects during layer deposition, i.e., the contact time between the solution and the multilayer, the immersion speed, the rinsing and drying steps between the adsorption of adjacent layers (Joseph J. Richardson, Mattias Björnmalm, Frank Caruso, 2016).

Indeed, it is strictly necessary to optimise these parameters to obtain lamellar and homogeneous layers.

The adsorption time and immersion speed must be optimised (not too long) to avoid a weakening of the multilayer structure caused by the internal reorganisation of the PE chains and their inter-diffusion (Eduardo Guzmán et al., 2020).

Rinsing between the deposition of adjacent layers allows the removal of excess deposited material that is weakly adsorbed onto the surface. This step is crucial to avoid the formation and precipitation of inter-polyelectrolyte complexes in solution (which would be thermodynamically favoured). It must be considered that the introduction of rinsing steps in the assembly process can lead to the removal of PE material due to the weak intensity of the electrostatic interactions between the formed layers. Furthermore, a considerable number of templates can be lost if the rinsing process is not appropriately optimised. On the other hand, the drying of the deposited film between two consecutive deposition steps is important to adjust the physico-chemical properties of the deposited PE multilayers (Joseph J. Richardson, Mattias Björnmalm, Frank Caruso, 2016).

From the perspective of physico-chemical properties of LbL multilayers, the porosity and permeability of multilayers play a key role in controlling the exchange of material between the inner region and surrounding environment (Ana Mateos-Maroto et al., 2021). In general, rigid multilayers present a high density, so they have a low amount of retained water due to the low presence of pores in the deposited layers (Eduardo Guzmán et al., 2020). However, the porosity of the obtained materials can be reversibly adjusted by changing the ionic strength, pH, temperature, light, ultrasound, magnetic field, or mechanical deformation (Paula T. Hammond, 2011).

1.3.4. Fabrication of Polyelectrolyte-Based Capsules for Biomedical Applications

Due to its versatility, simplicity, and the possibility to precisely control the function and structure of the layer, the LbL technique has been proposed as a valuable approach in the therapeutic field, especially for the surface engineering of materials for tissue engineering applications (L. Pastorino et al., 2016). Moreover, as the assembly usually takes place under mild conditions (in aqueous solution at room temperature and non-aggressive pH), LbL can involve the simultaneous use and encapsulation of molecules of different nature and properties, such as polymers, DNA, polynucleotides, bioactive molecules, cells, and nanoparticles (Eduardo Guzmán et al., 2017).

The deposited layers will enable their protection, giving them greater stability and control over their release in time and space (L. Pastorino et al., 2016). The release of the encapsulated compound can be the result of a partial destruction of their structure by a specific external or internal stimulus within the body (smart NPs), but it can also be as a function of capsule erosion and free diffusion of molecules from the internal cores or as a function of dissolution in a particular solvent (Jayanta Kumar Patra et al., 2018).

There are numerous works in the literature dealing with the LbL of NPs for biomedical purposes; however, most of them do not involve the encapsulation of bioactive molecules. Researchers have paid attention to sacrificial templates or to cores consisting of imaging NPs (such as QDs or gold NPs) on which multilayers of natural or synthetic chemistry have been deposited. Generally, in the literature, the adsorption of synthetic polymers is preferred over natural polymers for LbL purposes because they are more stable and have physico-chemical and mechanical properties that are easier to manipulate depending on their composition (Bogdan C. Simionescu & Daniela Ivanov, 2015). However, their inertness is a double-edged sword, as their degradation in the body is not without toxicity, also due to their long residence time (Maria Ratajska and Stefan Boryniec, 1998). Natural polymers represent a possible solution to this problem; however, they have higher degradation kinetics than their synthetic counterparts (Maria Ratajska and Stefan Boryniec, 1998). Moreover, their extraction from animals and plants is not always easy. Furthermore, there are not many studies reporting on their use in the literature.

As far as encapsulation is concerned, it generally takes place by dissolution of the template and subsequent immersion of the samples in a drug solution, which will tend to penetrate the multilayer nanocapsules (lacking their core) by diffusive mechanism. To the best of my knowledge, there are no papers presenting the encapsulation of bioactive molecules by previous dissolution of these in the PE solution that will subsequently be deposited on the substrate. Moreover, the encapsulation and release of two or more drugs has been little studied by researchers, who have focused their efforts on the chemical-physical characterisation of particles coated with different materials. Therefore, NPs only incorporate drugs in the NP core and are usually coated by up to two layers. This is particularly true in the case of drug codelivery. Finally, few works present *in vitro* cellular tests of these NPs, let alone *in vivo* ones. Among the various systems that have been developed by

researchers, nanotheranostics systems consisting of a core of QDs subsequently coated with PE pairs are particularly interesting.

In this context, M. Adamczak et al. (2012) developed PE multilayer capsules with CdTe QDs as cores. The deposition PEs were either PAH-PSS or poly-l-lysine-poly-d-glutamic (PLL-PGA) pairs to create seven deposition layers on CdTe according to the saturation method. The size of the complexes obtained by M. Adamczak et al. (2012) was less than 100 nm and the ζ-potentials had charge variations from 42 mV to -40 mV for the PLL/PGA pair and from 52 mV to -49 mV for the PAH/PSS pair. To assess the cytotoxicity of the capsules, their influence on the proliferation of the B-lymphoblastoid cell line (B-LCL) was examined (Fig. 42). The encapsulation of CdTe QDs in the layers of PLL/PGA reduced their cytotoxicity, whereas capsules prepared with synthetic PAH/PSS showed no such effect (M. Adamczak et al, 2012). In addition, the non-specific binding of nanocapsules to P-blood mononuclear cells was assessed by flow cytometry, showing that CdTe-labelled PLL/PGA capsules did not bind to blood cells, allowing them to be considered for biomedical purposes (M. Adamczak et al., 2012).

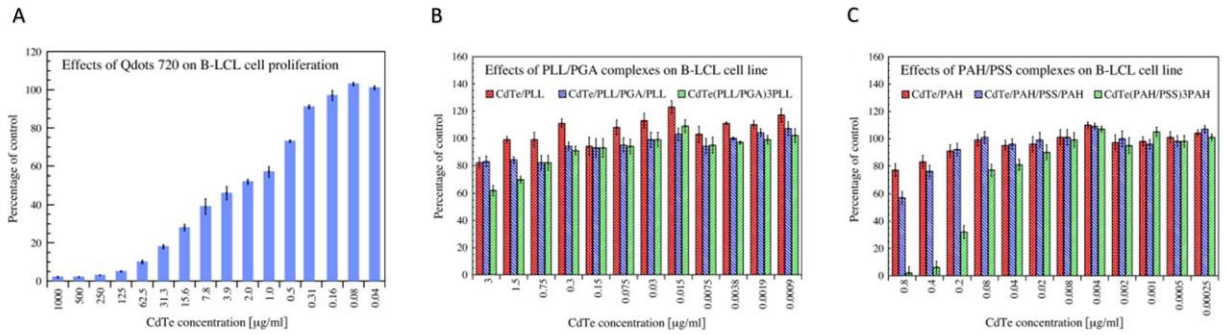

Fig. 42: Results of cytotoxicity test for free-CdTe (A), CdTe-labeled capsules with 1, 3 and 7 layers of PLL-PGA (B) or PAH-PSS (C);. Source: M. Adamczak et al., 2012

Similar work was done by Gulnara A Gaynanova et al. (2019) where they deposited five layers of the CH-PAA pair on a CdSe core previously stabilised in CH (Fig. 43).

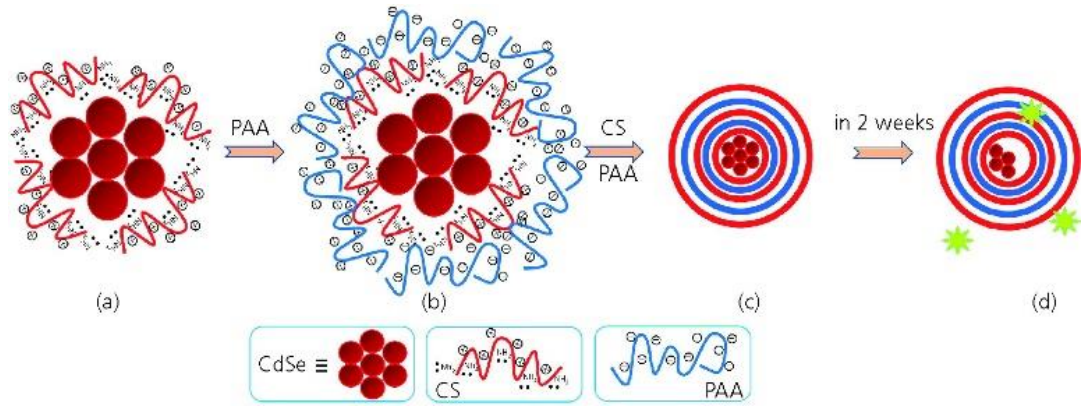

Fig. 43: Fabrication of NPs with CdSe and CS-PAA; Source: Gulnara A Gaynanova et al., 2019.

The results of Gulnara A Gaynanova et al. (2019) showed the change in ζ-potentials from -50 to + 50 mV and the hydrodynamic diameter of the final capsules was 93 nm with PDI of 0.508. Encapsulation of QDs in a polymer matrix increased their stability in water and significantly reduced their cell toxicity (Gulnara A Gaynanova et al., 2019). However, in vitro tests of the produced capsules have not been reported. Furthermore, in this work, a gradual release of QDs from the polymer matrix was observed after one month. The release was very slow, which reduces toxic effects on human cells.

A very interesting work is also done by M. Adamczak et al. (2013) where they encapsulated hydrophobic CdSe/ZnS QDs inside PLL-PGA nanocapsules. To encapsulate hydrophobic QDs, it is necessary to create a mixture of linseed oil and chloroform subsequently stabilized with lecithin. Then, the emulsion was used for the LbL adsorption of PEs according to the saturation method. Interesting is the absence of rinse phases between depositions. The results showed that the ζ-potential of the emulsion was -47.6 mV and during deposition varied between 43.5 mV and -41.56 mV. Regarding diameters, the average core size was 100 nm and the size of the multilayer nanocapsule was 130 nm. The cytotoxicity of the capsules was evaluated on mouse embryonic fibroblasts (NIH 3T3). Emulsion containing only QDs and capsules with a single layer were toxic to NIH 3T3 cells, whereas cells seeded with NPs that had one or two bilayers showed proliferation like the control (Fig. 44). So, the nanocapsules produced had eliminated the potential toxic effects of hydrophobic QDs, demonstrating potential as carriers for the release of poorly water-soluble drugs.

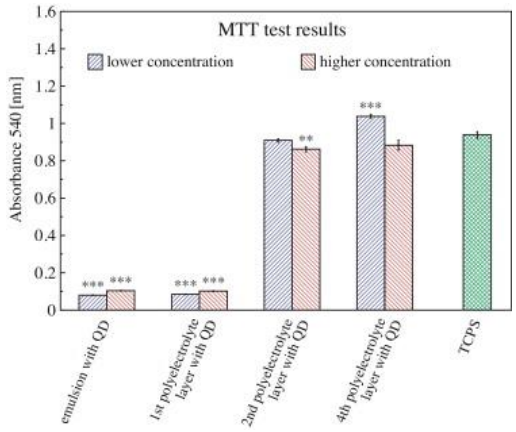

Fig. 44: Results of the MTT viability test of NIH 3T3 mouse embryonic fibroblasts cultured for 24 h; Source: M. Adamczak et al., 2013.

QDs can also be used as deposition layers. This type of strategy was implemented by Hong Xia et al. (2004) to fabricate two types of NPs with an iron oxide core (Fe_3O_4) with a size of 8.5 nm and a surface charge of -25.7 mV. The first model involved the deposition of PAH-PSS for a total of 27 layers and a final CdTe layer. In contrast, the second model involved CdTe deposition for every 3 bilayers deposited, for a total of 16 layers deposited.

In the case of the Fe_3O_4/PEn/CdTe nanocapsules, they showed the reversal of the ζ potential (from +7.5 mV to -41.5 mV) during the deposition of the layers, and the last CdTe layer had a potential of -38.1 mV (Fig.

45A). The Fe3O4/(PE3/CdTe)$_n$ particles also showed charge reversal however they assumed slightly lower negative values when the QDs were deposited (Fig. 45B). The final sizes of the two types of NPs are not reported. In addition, the results demonstrate an absence of cross-interference between magnetic cores and QDs due to the distance and layers between them. Moreover, nanocomposites could be easily picked up by an external magnetic field; therefore, their application in biomedicine for site-specific in vivo transport, biolabelling, bioseparation, immunoassay and diagnostics is promising (Hong Xia et al., 2004).

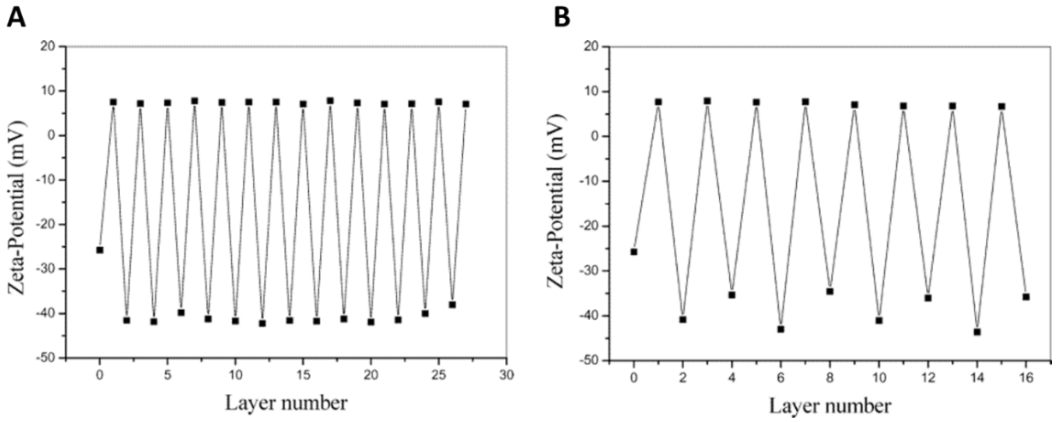

Fig. 45: ζ -potential of the magnetic luminescent nanocomposites Fe3O4/PEn/CdTe (A) and Fe3O4/(PE3/CdTe)n (B); Source: Hong Xia et al., 2004

Chai F. et al. (2016) studied the encapsulation and release of DOXO through its precipitation in PLGA NPs that were subsequently alternatively coated with CH and alginate (ALG). The NPs produced were spherical and uniform (200 nm) and showed a charge reversal between 36.4 mV and -48.0 mV during layer deposition. I*n vitro* studies demonstrated an undesirable initial release of PLGA NPs loaded with DOXO and without layers. Subsequently, the burst release was reduced from 55.12% to 5.78% using the LbL technique (Fig. 46). In fact, the halved release time of DOXO had increased from 0.78 to 61.58 hours with the presence of the layers. Furthermore, DOXO release increased more than 40% by decreasing pH from 7.4 to 5.0, demonstrating how the coatings are pH sensitive.

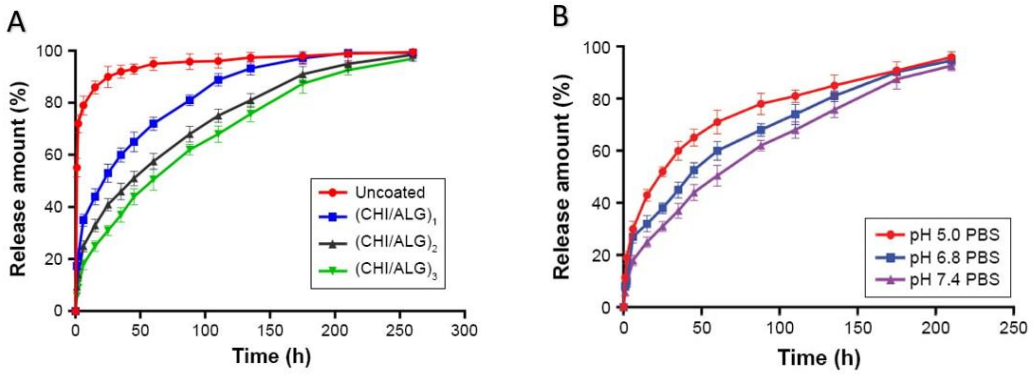

Fig. 46: Release profiles of DOXO from PLGA NPs and NPs with different number of coatings (A) and release profiles of DOXO from NPs with seven layers in solution with different pH (B); Source: Chai F. et al., 2016

In addition, multilayer NPs with a DOXO concertation of 5 mg/kg were tested on tumour mice (Fig. 47), showing a higher tumour inhibition rate (83.17%) than PLGA NPs containing DOXO and free DOXO in solution (with same concentration). Thus, the NPs created represent a novel and effective approach to minimize initial burst release, allowing drug release in a controlled manner while reducing toxicity (Chai F. et al., 2016).

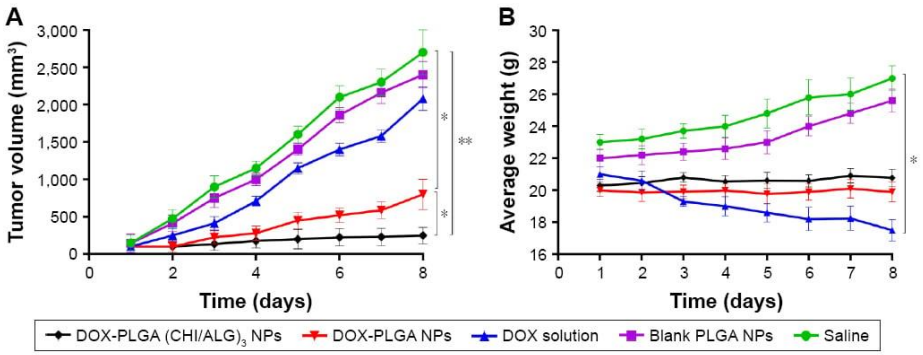

Fig. 47: In vivo antitumour efficacy of free DOXO, DOXO-containing PLGA NPs, DOX-PLGA (CHI-ALG)$_3$ NPs, white PLGA NPs and saline on S180 tumour-bearing mice following i.v. administration (dose =5 mg/kg) (A); Changes in body weight of tumour-bearing mice with time after i.v. administration (dose =5 mg/kg) (B); Source: Chai F. et al., 2016

Yunyun Chen et al. (2021) designed and synthesised porous silica carriers (pSiO2) that encapsulate CDs, DOXO and gold NPs. Biocompatible HA/ALG/CH (HCA) multilayers were deposited on the pSiO2 templates to seal the pores where the drug was loaded (Fig. 48). This type of particle was created to achieve synergy between the components.

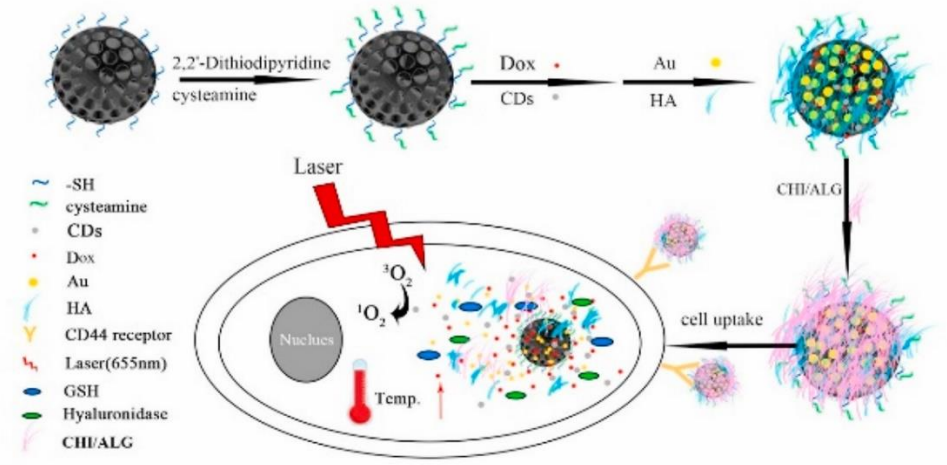

Fig. 48: Fabrication of pSiO2 with their components; Source: Yunyun Chen et al., 2021

The diameter of $pSiO_2$ was 280 nm with a divergent pore structure. The final dimensions of the multilayer NPs were not reported. The ζ-potential of bare silica is approximately -25.6 mV due to the presence of silanol

groups; however, the coating did not show a charge reversal, but a further charge decreases to -40.7 mV. The NPs were not able to enhance synergistic chemotherapy, photothermal therapy and photodynamic therapy on HCT-116 tumour cells. However, these particles are interesting because they showed DOXO release triggered by pH/redox/enzymes (Fig. 49B). Furthermore, cytotoxicity assays on normal human liver cells (7702) without light radiation and without DOXO showed high cytotoxicity (Fig. 49A) (Yunyun Chen et al., 2021).

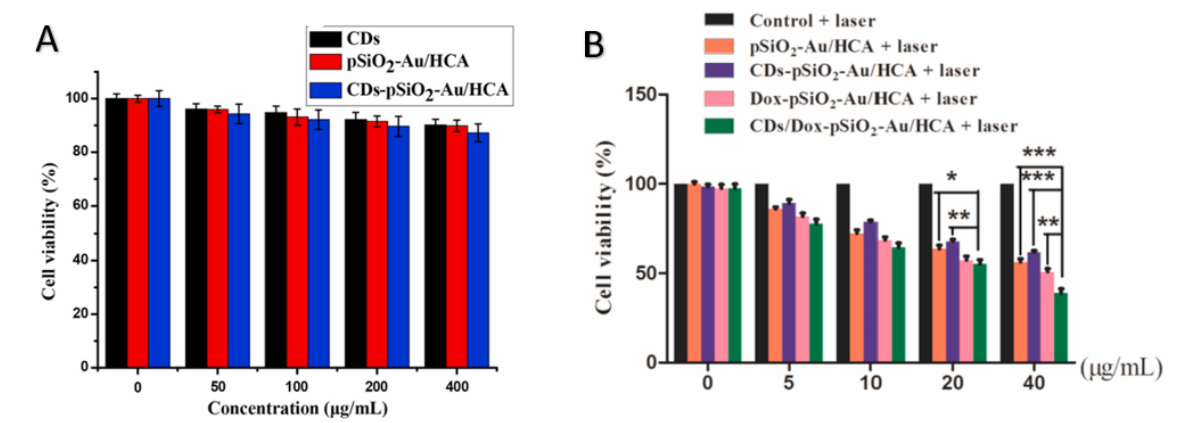

Fig. 49: Cytotoxicity of CD, pSiO2-Au/HCA and CD-pSiO2-Au/HCA for HCT-116 cells without light radiation on normal human liver cells (7702) (A) Cytotoxicity of pSiO2-Au/HCA, CDs-pSiO2-Au/HCA, Dox-pSiO2-Au/HCA and CDs/DOXO-pSiO2-Au/HCA on HCT-116 cells with light radiation (650 nm, 200 mW, 10 min) (B); Source: Yunyun Chen et al., 2021

One material used as a removable template for subsequent drug encapsulation is calcium carbonate (CaCO3). Its attractive properties, such as biocompatibility, biodegradability, chemical inertness, low cellular cytotoxicity, and cost-effectiveness, make calcium carbonate-based carriers one of the most widely used sacrificial templates for LbL assembly (L. Pastorino et al., 2016).

As example, Daria Kalenichenko et al. (2021) designed three microcapsule templates functionalized with DOXO or QDs. The first model involved co-precipitation of DOXO simultaneously with $CaCO_3$ formation (Fig 50A). Subsequently, the obtained core was coated by PAH-PSS with four bilayers. The second model involved the formation of the $CaCO_3$ core to be subsequently coated with as many bilayers and then dissolved in ethylenediaminetetraacetic acid at physiological pH, allowing encapsulation of DOXO following immersion of the particles in a drug solution (Fig 50B). The third method consisted of a $CaCO_3$ core subsequently coated with PAH-PSS for four bilayers, replacing the layer number four with a layer of QD CdSe/ZnS (Fig 50C).

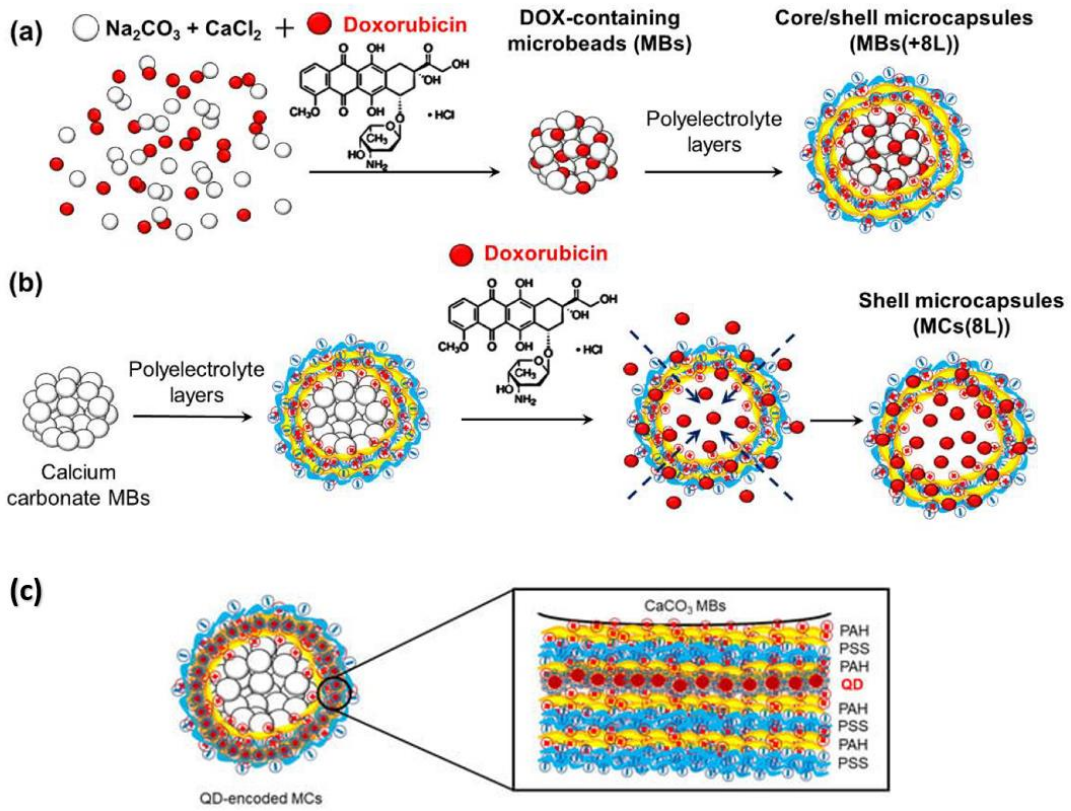

Fig.50: Schematic diagram of the preparation of doxorubicin-containing microcapsules with coprecipitation method (a), spontaneous loading (b) and with QDs (c); Source: Daria Kalenichenko et al., 2021

The original $CaCO_3$ cores had a surface charge of -17.2 mV and a spherical size of 2.5 µm. The PE shell were nanometer-sized for the three types analysed. As for model No. 1, the coating was characterized by a charge reversal from -32.6 to +16.2 mV. The efficiency of drug encapsulation through this preparation step was 73.1 ± 0.6 %. On the other hand, the second model involved first LbL deposition of PEs and then subsequent core dissolution. Deposition of the PEs was characterized by a charge inversion from +21.3 mV to -20.4 mV, and subsequent core dissolution did not significantly change the average size and surface charge of the capsules . The final step involved immersing the particles in the drug solution. This step achieved a DOXO encapsulation efficiency of 65.6 ± 0.1 %. Finally, the third model encapsulated negative QDs creating particles characterized by a bright fluorescence signal, as demonstrated by fluorescence microscopy. DOXO release from the two systems was analysed under different conditions as shown in Fig. 51. For both types, DOXO releases at pH 6 and 7.4 was no more than 70 % after 48 h, however, the release was accelerated under more acidic pH conditions. Furthermore, both types exhibited a burst release of drug within the first two hours, and this was particularly intense for particles in the first model. The authors explain that the increased release is due to diffusion of the drug from the core to the outermost layers during shell assembly. In all cases, the release rate decreased after three hours of incubation, suggesting that DOXO is released from the core of the carrier. Subsequently, the release was further slowed. The slower release of the second carrier at pH is

also due to weaker ionization of DOXO in the medium at pH 6 . However, *in vitro* and *in vivo* cellular studies of these particles are not reported, probably due to their excessive size (Daria Kalenichenko et al., 2021).

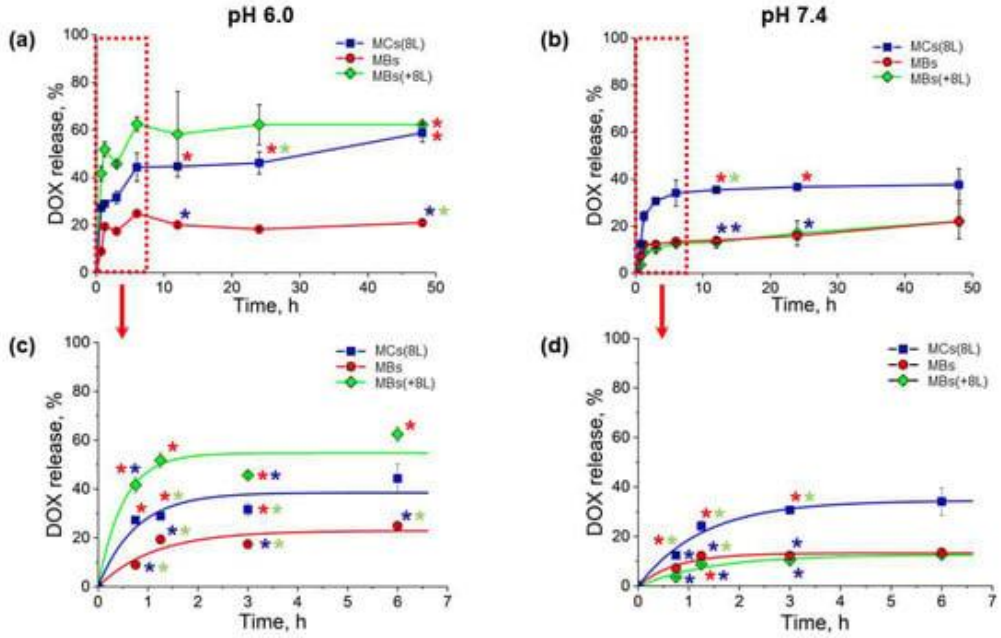

Fig. 51: Profiles of doxorubicin release from microcapsules at (a) pH 6.0 and (b) pH 7.4 during 48 h and profiles of the initial drug release during the first 6 h of incubation at (c) pH 6.0 and (d) pH 7.4; Source: Daria Kalenichenko et al., 2021

Despite the many advantages of using such carriers, micrometer size can become a limitation (L. Pastorino et al., 2016). Therefore, the development of calcium phosphate (CaP) nanocarriers may be a viable alternative to CaCO3 particles, especially in the treatment of osteosarcoma, due to its biocompatibility, biodegradability, (acid) pH reactivity and due to their ability to encapsulate a variety of drugs in the matrix (Mahmood Barani et al., 2021). Iuliia S. Elizarova et al. (2016) developed a system for the continuous and fast large-scale manufacture of CaP capsules coated with nine layers, obviating the problems related to material loss during washing and centrifugation. In this study, Iuliia S. Elizarova et al. (2016) produced a CaP core through a tubular flow-type reactor and then deposited the PE via a second pumping circuit (Fig. 52). Both configurations had a flow rate of 10 ml/min.

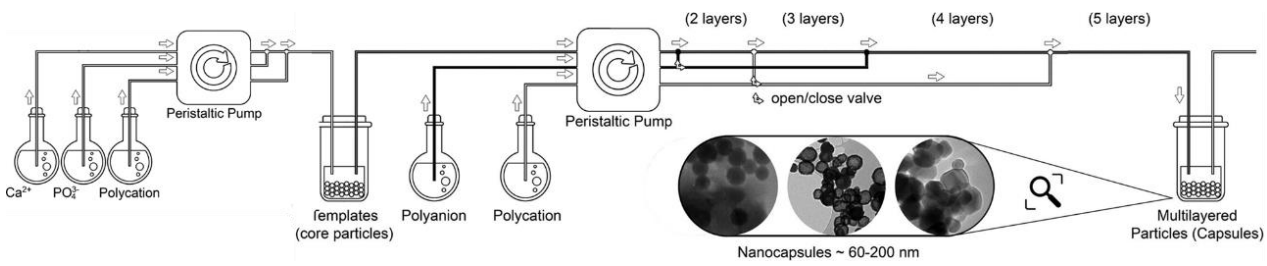

Fig. 52: Schematic layout of continuous production; Source: Iuliia S. Elizarova et al., 2016

In addition, two different PE pairs were deposed in this work, which are lambda carrageenan/ε-poly-lysine and PSS/PDADMAC. The particles created in each deposition step were stable, as all had a zeta potential greater than ±25 mV. Moreover, they show a charge reversal from -30 mV to +40 mV for both PE pairs used. Furthermore, for both PE pairs, the size of the NPs ranged from 60 to 200 nm and had a spherical and homogeneous morphology. Interestingly, the number of particles produced was 130 mg of NPs at nine layers per hour (Iuliia S. Elizarova et al., 2016).

A potential problem found by Iuliia S. Elizarova et al. (2016) was related to the presence of an excess of polyelectrolyte in the tube that could affect the deposition on the substrates. However, according to the authors, polymers and polyelectrolytes have a high-affinity adsorption isotherm so the polymer first adsorbs on the surface of the NPs and then remains in solution. Therefore, to solve this problem, it was essential to carefully control the polymer concentration used during deposition so as not to incur cross-complication of the PE with that of opposite charge. After reaching the required number of PE layers, the CaP cores were easily removed by dissolution in hydrochloric or acetic acid (Iuliia S. Elizarova et al., 2016).

However, the encapsulation of drugs or bioactive molecules following core dissolution has not been studied. Moreover, it could be interesting to exploit this strategy to encapsulate different components for biomedical purposes and subsequently test their bioactivity on in vitro cell tests. In fact, this type of configuration would reduce production time and enable large-scale production of NPs, making this technology accessible for future clinical applications. The works just reported are the most successful and useful for the purposes of the proposed thesis. Other works worth mentioning are included in Tab. 9.

PE	Number of layers	Final size (nm)	ζ-Potential (mV)	Drug-Compounds incapsulated	EE (%)	Reference
CH-ALG	4	350	-32/+36	DTX	97	Singh et al., 2015
CH-Dextran	5	110	-28/+40	Placlitaxel	98	Yu and Pishko, 2011
PLL-PLA	1	127	-9/+26	DOXO	18.7	Lim et al., 2017
PAH-PSS	7.5	128	-20/+40	Ibuprofen	72	Santos et al., 2015
PLGA-PLLA	2	34,700	Not Reported	DOXO - Paclitaxel	45.3 - 90.1	Wei Li Lee et al., 2015
Gelatin/QDs-CS	1	269	-40.8/+23.5	Celecoxib - Rapamycin	93.7 - 94.0	Ahmed S AbdElhamid et al., 2018
Poly-l-arginine/Dextran sulfate	2.5	250	Not Reported	Gemcitabine or Clodronate	45 or 25.1	Marina V. Novoselova et al., 2020
PEI-HA/DOXO	2	23	-24.1/+4.96	CDs/DOXO/CD44	6.3	Na Gao et al., 2017

Tab. 9: LbL application in Nanomedicine

In conclusion, numerous nanotheranostics systems have been developed in recent years for the diagnosis and treatment of cancer. It is evident that nanotheranostics systems improve the drug delivery profile by minimising the accumulation of NPs in non-target organs. However, the biology of the tumour is critical and needs to be thoroughly investigated for efficient results. For this and many other reasons, most nanostructured approaches have not yet been translated into clinical trials. However, nanotheranostics is expected to play a key role in future cancer diagnostics and treatment.

1.4. Aim and Objectives of the work

The main goal of this project was to use immersive LbL technology to create nanometre-sized theranostics systems using CQDs as imaging probes and chemotherapeutic drugs to treat cancer cells, by releasing the drug payload in a controlled timely manner. The corresponding objectives (OBJ) were:

OBJ1: Synthesis and evaluation of the chemical, physical and optical properties of chitin-derived CQDs using the two-step bottom-up method derived from pyrolysis and hydrothermal carbonisation

OBJ2: Evaluation of the cytocompatibility of chitin derived CQDs on Neo-dermal fibroblasts.

OBJ3: Production and optimisation of a nanoteranostic system consisting of a calcium phosphate (CaP) core containing Doxorubicin (DOXO) stabilised by PAH deposition through a pumping system and subsequently functionalised with DOXO and CQDs through their encapsulation with LbL.

OBJ4: LbL as a strategy to coat a core of CHBOCQDs and to encapsulate DOXO and DTX in the nanolayers of the NPs to create a nanotheranostic drug codelivery system.

OBJ5: Characterisation of NPs produced through chemical-physical, morphological and in silico analyses, with a focus on the layers' ability to encapsulate and release drug molecules and CQDs.

OBJ6: Evaluation of the cytotoxicity of different types of NPs produced on osteosarcoma cells (Saos-2 and U2OS cells) to verify the efficacy of the intended treatment and the internalisation of NPs by cancer cells.

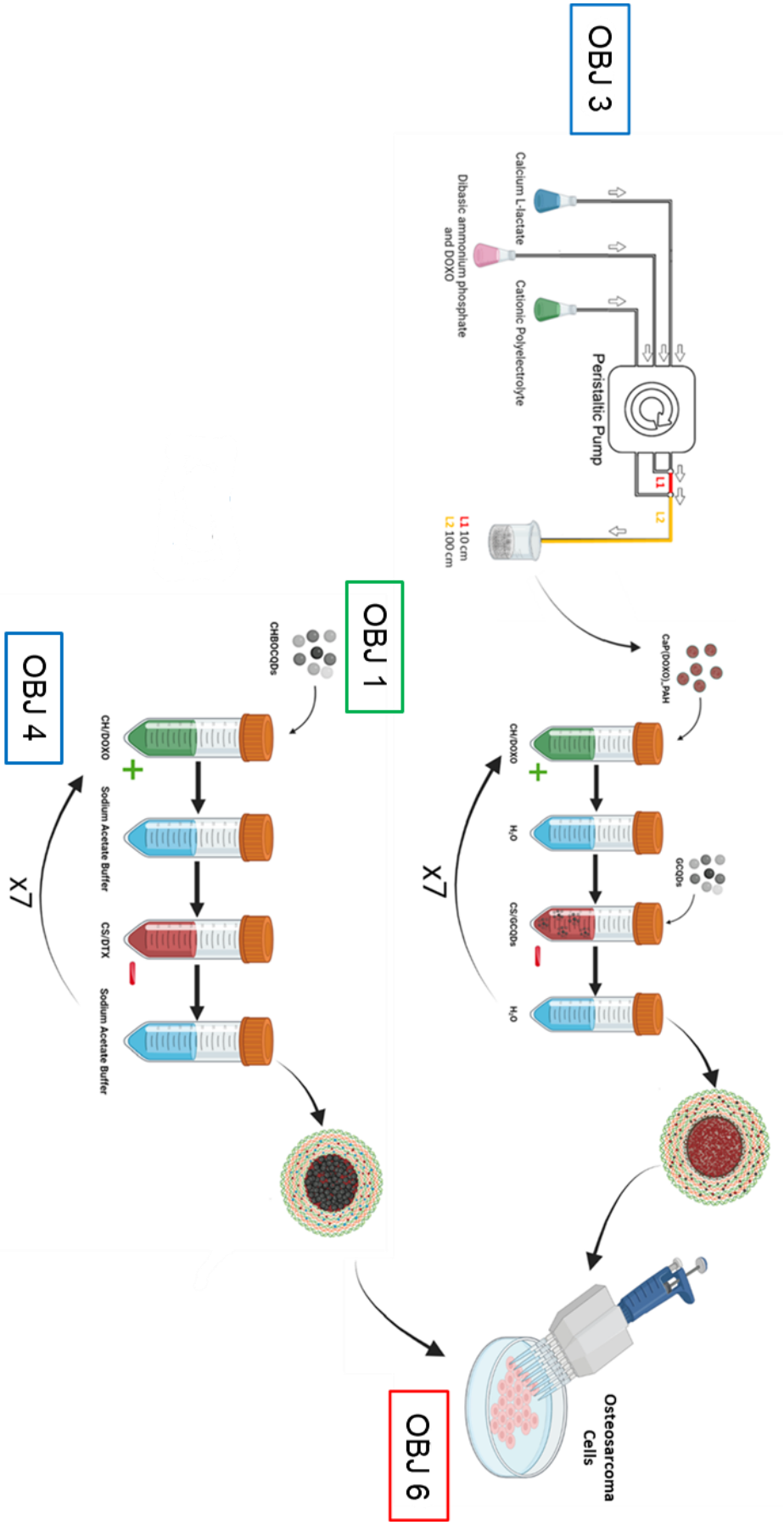

Aim of Work Scheme

Chapter 2: Manufacturing protocols and Characterisation

2.1 Materials

2.1.1 General materials

All the regents, if not differently stated, were purchased from Sigma Aldrich (UK).

For the system consisting of calcium phosphate, Calcium L-lactate hydrate (> 98.0 %), Dibasic ammonium phosphate (purum p.a., >98.0 %), Poly(allylamine hydrochloride) (PAH) (Mw ~ 15 000 Da), Chitosan (CH) (Low Mw, Deacetylation Degree 75%) and Doxorubicin hydrochloride (DOXO; Apollo Scientific Ltd) (98.0-102.0% HPLC) were purchased. The materials used for LbL deposition were CH, Chondroitin Sulfate A sodium salt from bovine trachea (CS), DOXO and Docetaxel (DTX) (purity > 99.0 %, purchased from Apollo Scientific Ltd). Both drugs were dissolved in a solution of Dulbecco's phosphate-buffered saline (PBS; Sigma Life Science) and Dimethyl sulfoxide (DMSO) (Hybri-Max™, sterile-filtered, BioReagent, suitable for hybridoma, ≥99.7%).

The proof-of-concept test for the insoluble CQDs in water involved the use of linseed oil, the phosphatidylcholine (lecithin from egg yolk, type VI-E, ≥99%), 1,3-Dioxane and Ethyl alcohol (>99.98%).

The three systems created involve the use of 3 different types of in-house CQDs that will be used as cores or will be encapsulated in the deposited layers. To produce the CQDs, the biomasses of chitin and ground coffee were used as precursors.

Other materials used included Hydrochloric acid (HCl) (reagent grade 37%), (Sigma-Aldrich, UK), Sodium acetate (mw: 82.03 g/mol) and Glacial acetic acid (100%) (Mw: 60.05 g/mol) to make sodium acetate buffer, Sodium chloride (tablets) (NaCl), deionized water (dH_2O), Cellulose membrane in dialysis tube (typical cut-off of Mw = 14,000 Da) and 0.22 μm filter papers.

2.2 Manufacturing Methods

2.2.1 CQDs synthesis

2.2.1.1 Synthesis of CQDs from coffee ground products (GCQDs)

CQDs derived from ground coffee were kindly provided by Thomas C. Wareing (PhD student in Newcastle University). These were produced using a two-step reaction: HTC with an acid catalyst followed by oxidation**.**

2.2.1.2 Synthesis of hydrophobic CQDs from Char products (CHCQDs)

CQDs were prepared by bottom-up method consisted in two-step process called "pyrolysis-carbonization method". The purpose of this process was to convert biomass wastes to char (via pyrolysis) and then to CQDs (via HTC) and it is shown in Fig. 53.

The first step involves a pyrolysis treatment using chitin biomasses as carbon sources (65 g). The biomasses were first treated in a tube furnace at 700 °C for 2 h in a N_2 atmosphere. During the pyrolysis reaction, char and bio-oil products are formed. Char products were transferred to a Teflon-lined stainless-steel autoclave and incubated at 200 °C for 2 h in distilled water (dH_2O) to obtain CQDs solution derived from chitin char.

Then, a purification step using 0.22 µm filter papers and a Buchner funnel were carried out to remove excess solid. Then, sequential centrifuging at 400rpm for 20 minutes were performed.

Finally, the obtained CQDs were frozen at -20 °C and then subjected to a freeze-drying process (Christ freeze-dryer) for 48 hours at -51 °C. CQDs were stored at 4°C protected from light.

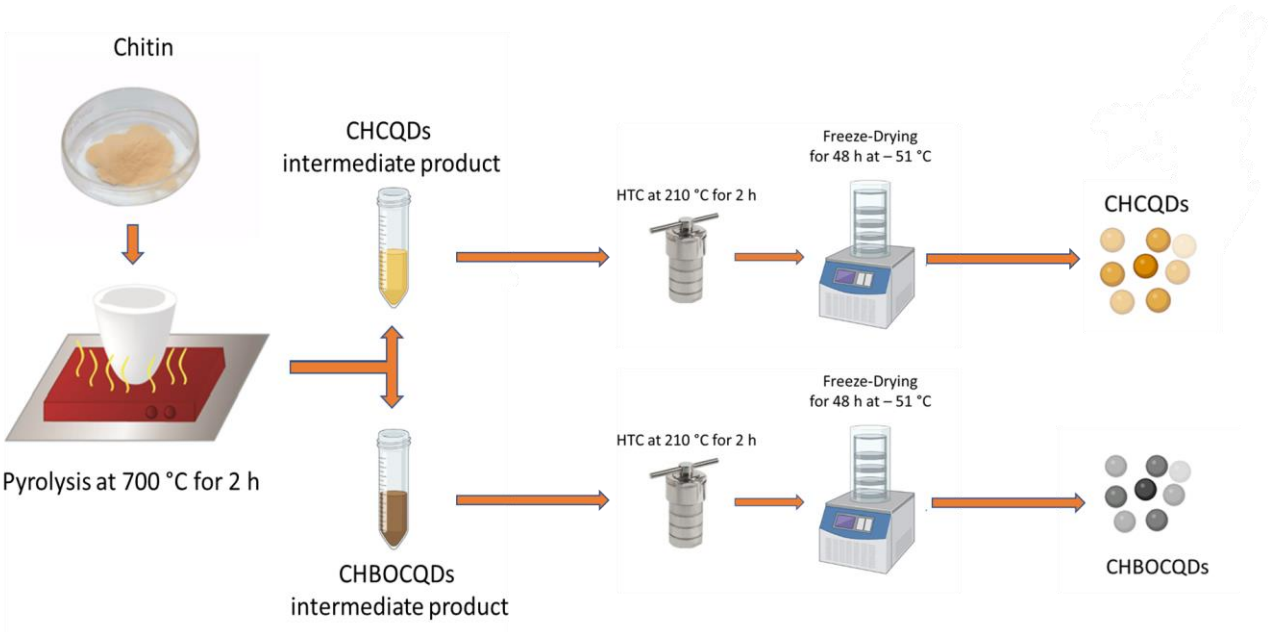

Fig. 53: Synthesis of CQDs from Chitin.

2.2.1.3 Synthesis of hydrophilic CQDs from Bio-Oil products (CHBOCQDs)

The approach described in the paragraph 2.2.2 is unchanged (Fig. 53). In this case, the Bio-Oil side product formed as a result of the pyrolysis process is transferred separately to a Teflon-lined stainless-steel autoclave. The process continues in the same manner with the same parameters until a CQDs solution derived from chitin BioOil is obtained. Again, purification and freeze-drying steps are required and are performed exactly as described in the paragraph just cited. Then, CQDs were stored at 4°C protected from light.

2.2.2. Preparation of LbL nanoparticles

2.2.2.1 DOXO-containing calcium phosphate nanoparticles synthesis and their stabilization by polymer coating

To fabricate NPs template core, the methodology described by Urch et al. (2008) and Elizarova et al. (2016) was followed by making appropriate changes. Using a P-3 peristaltic pump (Pharmacia Fine Chemicals) and a process of continuous and rapid mixing of aqueous solutions, calcium phosphate NPs containing DOXO were created which will then be coated with a cationic polyelectrolyte (PAH or CH).

Briefly, 40 mL of aqueous solutions of Calcium L-lactate hydrate (24 mM, pH 10) and Dibasic ammonium phosphate (15 mM, pH 10) were separately prepared to achieve the formation of the calcium phosphate core. A DOXO solution was prepared in PBS:DMSO (1:1 % v/v) with a concentration of 10 mM and 135 µL of it was added to the dibasic ammonium phosphate to obtain the formation of a drug-containing core.

Moreover, 40 mL of PAH (pH 10) or CH (pH 5) was prepared in dH_2O as an aqueous solution of cationic polyelectrolyte. Different concentrations of the polyelectrolyte solution were tested (0.5, 1, 2.5 and 5 mg/mL) as to identify the saturation point related to the deposition of the polyelectrolyte on the surface of the calcium phosphate NPs. Then, each solution was pumped with a flow rate of 10 mL/min into the corresponding silicon tubes (diameter of 3 mm).

The generation of the core (at first) and outer coating (subsequently) is ensured by the outlet configuration of the channels from the peristaltic pump (Fig. 54): a first 10-cm-long tube is present where calcium phosphate NPs encapsulating DOXO will be formed; then the newly formed core will be conveyed into a second 100-cm-long tube where the polyelectrolyte will be adsorbed on the calcium phosphate surface.

The resulting NPs were collected in a conical flask without filtering, stirred for 24h and collected again to be dialyzed against dH_2O using dialysis membranes for 12 h.

The NPs were then centrifuged at a speed of 4400 rpm for 20 min in Centrifuge 5701 (Eppendof), the supernatant was removed and replaced with an equivalent volume of dH_2O. The resulting system was sonicated in Ultrasonic Cleaner 1510 (Branson) for 2 min. The final product was suspended once again in NaCl and stored at 4°C or freeze-dried for further tests. From here on, these types of NPs will be named CaP.

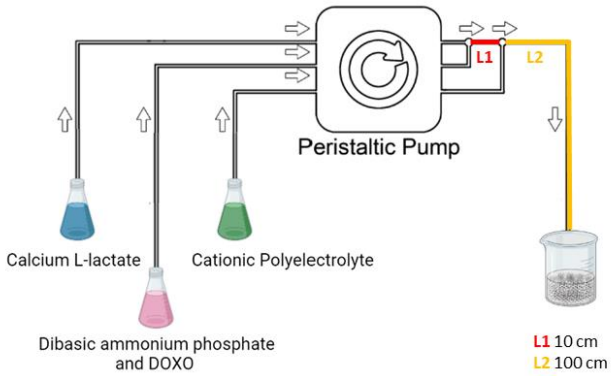

Fig. 54: DOXO-containing calcium phosphate nanoparticles synthesis and their stabilization by polymer coating

2.2.2.2 Deposition of aqueous solutions of polyelectrolytes on CaP NPs

The LbL-assembly procedure (shown in Fig. 55) was conducted changing the polyelectrolytes concentrations (1, 2.5 and 5 mg/mL) to recognize the saturation point of polyelectrolyte deposition on the NPs surface. CH and CS were used as deposition polyelectrolytes.

CH was prepared in a solution of dH_2O where 1 % (v/v) of acetic acid was previously added, whereas CS was dissolved only in dH_2O. The washing steps were carried out in dH_2O solution. Finally, the pH of all aqueous solutions was adjusted to 6 adding NaOH and HCl (respectively 0.25M and 0.1M).

Since the starting CaPs were positively charged, 10 mg of freeze-dried NPs were dissolved in 10 mL of CS solution, then sonicated for 15s. Then, the NPs solution was shaken at 95 rpm for 15 min by Orbital shaker SSM1 (Cole Parmer/Stuart).

Next, a first centrifuge of 10 minutes at 4400 rpm was carried out and it were followed by two washing steps in dH_2O to remove the excess polyelectrolyte.

For the first washing step, the supernatant is taken and replaced with 10 mL of dH2O; then, the NPs were sonicated for 15s and they were shaken again for 10 min at 95 rpm. Following, a second centrifuge of 5 minutes at 4400 rpm was carried out. For the second washing step, the washing procedure is repeated by replacing the supernatant with 3 mL of dH20, sonicating the NPs for 15s and then being shaken again for 3 min at 95 rpm. Finally, the NPs are centrifuged again at 4400 rpm for 10 min, so that the deposition of the next CH layer can begin in the same manner as previously stated.

Before the last centrifugation step, 100 µL of functionalized NPs was removed in order to measure the corresponding ζ-potential.

This process was repeated until 7 layers (opposite in charge) were created consecutively. After the LbL procedure the obtained product was freeze-dried and then kept in vacuum desiccator for further test.

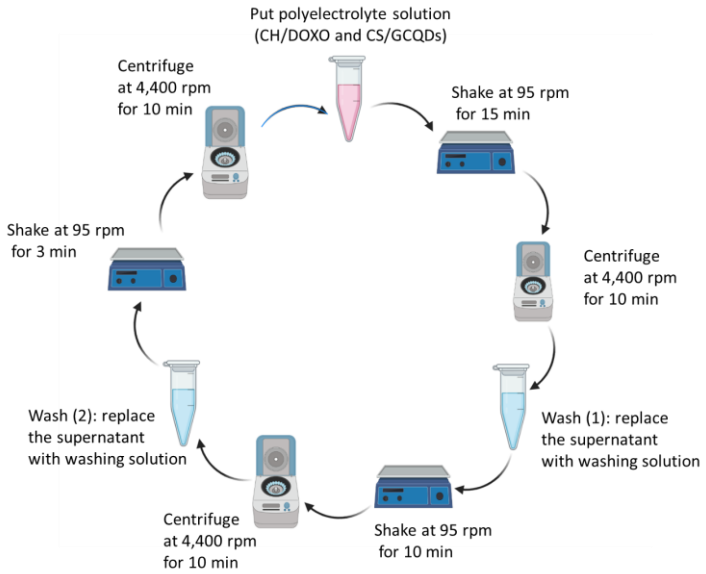

Fig. 55: LbL protocol for CaP.

2.2.2.3 Deposition of CQDs and DOXO on CaP NPs by LbL assembly in aqueous solutions

The procedure of LbL is the same as previously stated in the paragraph 2.2.5 with changes only occurred in the preparation of the starting solutions.

DOXO solution was prepared in PBS:DMSO (1:1) with a concentration of 10 mM. Then, an aliquot of 34 µL of DOXO solution was added for every 10 mL of cationic polyelectrolyte solution to create a CH/DOXO solution in order to incorporate the drug within the positive layers.

Similarly, GCQDs were added to CS aqueous solution, resulting in a concentration of CQDs in water of 0.33 mg/mL. In this way, a solution of CS/CQDs was obtained and the CQDs will be integrated into the negative layer of the NPs.

The last layer deposited will be CH and will not contain any drug or CQDs to avoid their burst release effect.

The polyelectrolyte concentrations tested were different (1, 2.5 mg/mL and 5 mg/mL) to recognize the saturation point of polyelectrolyte deposition on the NP surface.

As in the previous paragraph 2.2.5, an aliquot of 100 µL of functionalized NPs was removed in order to measure the corresponding ζ-potential before the last centrifugation step.

Following the deposition of 7 layers, the obtained NPs were freeze-dried, then were stored in vacuum desiccator to perform appropriate future analysis.

2.2.2.4. Deposition of polyelectrolyte solutions in sodium acetate buffer on CaP NPs

Except for the preparation of starting solutions, the polyelectrolytes (CH and CS) and LbL deposition process are identical to those described in the paragraph 2.2.5. Indeed, CS and CH were dissolved in 0.1 M sodium acetate buffer at pH 5.

Then, different concentrations of polyelectrolyte (1, 2.5, 5 mg/mL) were tested, and 7 consecutive layers were created so as to identify the saturation point of polyelectrolyte deposition on the NP surface. As in the previous section 2.2.5, the ζ-potential was evaluated for each of the 7 layers deposited.

After freeze-drying the NPs with 7 layers, they were stored in vacuum desiccator for further test.

2.2.2.5 Deposition of CQDs and DOXO on CaP NPs by LbL assembly with sodium acetate buffer

Similar procedure reported in par. 2.2.6 was followed with the only difference being related to the dissolution of polyelectrolytes and CQDs in sodium acetate buffer (pH 5, 0.1 M). The DOXO solution was added with the same amounts to the CH solution. Also, the polyelectrolyte concentrations tested were different (1 mg/mL, 2.5 mg/mL, 5 mg/mL) to recognize the saturation point of polyelectrolyte deposition on the NP surface. The last of the 7 layers created will be CH that did not encapsulate drugs and CQDs in order to avoid burst release phenomenon.

As in the previous paragraph 2.2.5, each of the 7 deposited layers was characterized in terms of ζ-potential.

The freeze-dried NPs were stored in vacuum desiccator for further test.

2.2.2.6 Deposition of polyelectrolyte solutions in sodium acetate buffer on CHBOCQDs.

The LbL assembly protocol (shown in Fig. 56) was conducted using a concentration of 1 mg/mL of the polyelectrolytes (CH and CS) dissolved in sodium acetate buffer (0.1 M, pH 5).

The washing steps were carried out in sodium acetate buffer (0.1 M, pH 5).

A concentration of 0.2 mg/mL negatively charged quantum dots CHBOCQDs dissolved in 1 mL of sodium acetate buffer was used as the core.

Following a centrifugation of the CQDs solution at 10000 rpm for 10 min, the supernatant was replaced by 1 mL of CH solution to stabilize the quantum dots core by deposition of a polymer coating.

Then, the NPs solution was shaken at 80 rpm for 15 min using an orbital shaker.

In order to remove the excess polyelectrolyte, a first centrifuge of 10 min at 10000 rpm was carried out and it was followed by two washing steps, replacing the supernatant with 1 mL of sodium acetate buffer.

For the first washing step, the NPs were shaken again for 10 min at 80 rpm as to perform the second centrifugation for 5 min at 10000 rpm.

For the second washing step, the same procedure was repeated by shaking the NPs again for 3 min at 80 rpm. Finally, the NPs were again centrifuged at 10000 rpm for 10 min, so that the deposition of the next CS layer started.

Before the last centrifugation step, 100 µL of functionalized NPs were taken to measure the corresponding ζ-potential. This process was repeated until 7 layers were created consecutively.

As a final step, the coated NPs were freeze-dried, and they were stored in vacuum desiccator to perform appropriate future analysis.

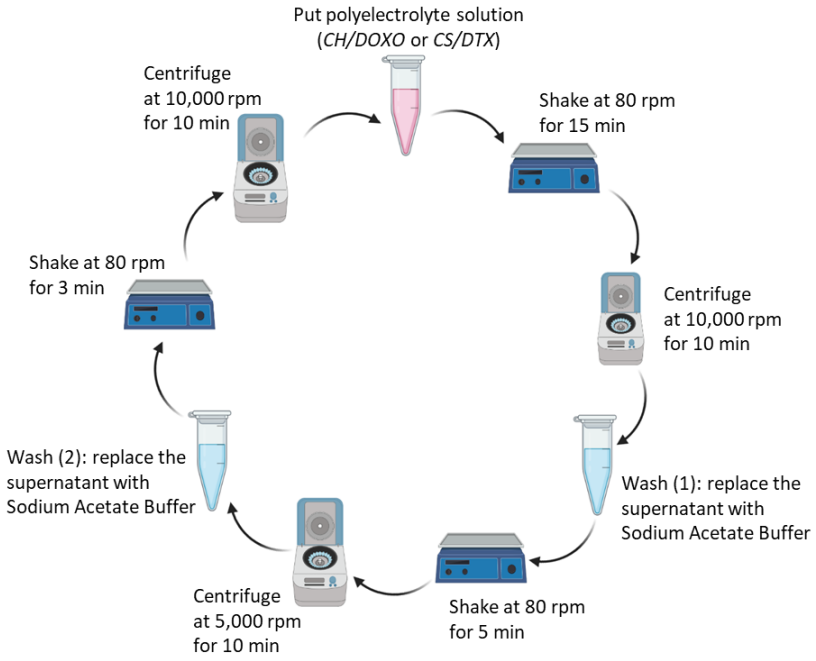

Fig. 56: LbL protocol for CHBOCQDs.

2.2.2.7 Deposition of DOXO and DTX on CHBOCQDs NPs by LbL assembly with sodium acetate buffer solutions

DOXO and DTX solutions were prepared separately in PBS:DMSO (1:1) with a concentration of 10 mM and 600 µM, respectively.

Next, an aliquot of 34 µL of DOXO solution was added for every 10 mL of cationic polyelectrolyte solution to create a CH/DOXO solution in order to incorporate the drug on the nucleus and within the positive layers.

Using the same quantities, DTX solution was added to CS so as to create a CS/DTX solution and incorporate the drug within the negative layers.

The last layer deposited will be CH and will not contain any drug in order to avoid their burst release phenomenon. The procedure of layer deposition was similar to the one reported in par. 2.2.9 and it was repeated until 7 layers were created consecutively. After the LbL procedure, the obtained products were freeze-dried and then kept in vacuum desiccator for further test.

2.2.2.8 Deposition of polyelectrolyte solutions in sodium acetate buffer on CHCQDs.

As a proof of concept, the fabrication of NPs with a hydrophobic core of CQDs was conducted following the work reported in the literature by M. Adamczaka et al. (2013). The protocol involves two phases: the creation of emulsions and the subsequent deposition of polyelectrolytes to create the nanocapsules, as shown in Fig. 57.

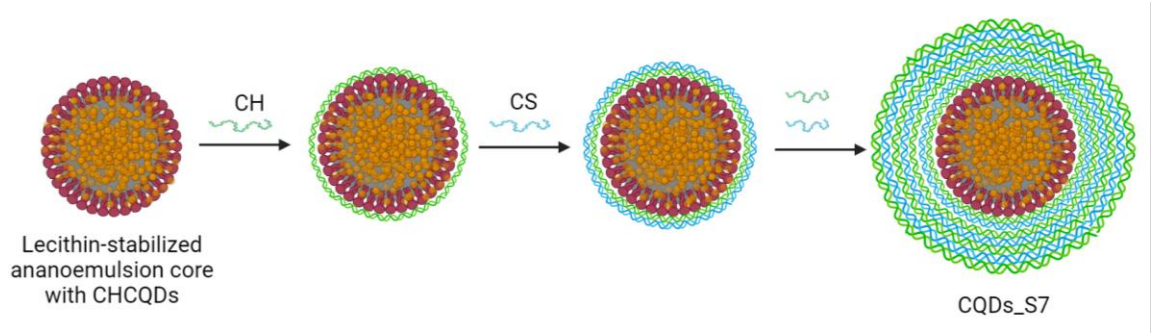

Fig. 57: Scheme of the multilayer nanocapsules formation using LbL of polyelectrolytes on the liquid emulsion core.

The first phase was done using the spontaneous emulsion technique, also known as the "Ouzo effect" where the rapid diffusion of water-soluble solvent into the aqueous phase causes oil supersaturation and liquid-liquid nucleation of emulsion droplets (M. Adamczaka et al., 2012) (M. Adamczaka et al., 2013).

First, a solution of CHCQDs dissolved Dioxane:Linseed oil (1:1) with a concentration of 2 mg/mL was prepared. This solution was the oil phase. Separately, 2 mL of ethanol containing 0.05 M of the phospholipid Lecithin was prepared and, subsequently, 0.1 mL of the oil phase was added to this solution. The resulting solution

was stirred with a magnetic stirrer at 350 rpm for several hours until a clear monophasic organic solution was obtained.

The next step involved dropwise addition of 0.1 ml of the organic phase to 10 ml of water during continuous stirring at 350 rpm until a turbid solution was obtained. At this point, an O/W emulsion containing 0.05 vol% oil phase was obtained. These oil cores will have a negative charge.

The second protocol phase involved the deposition of 7 layers of polyelectrolyte on the oil cores by the LbL technique. To do this, 0.1 mL of the O/W emulsion was added to 10 mL of cationic polyelectrolyte solution (CH), previously dissolved in sodium acetate buffer (0.1 M, pH 5) in a concentration of 1 mg/mL.

This solution was stirred for 15 min at 350 rpm. To remove all the excess polyelectrolyte on the surface of the NPs, the solution was centrifuged at 13000 rpm for 5 min, the supernatant was replaced with the wash solution (0.1 M sodium acetate buffer at pH 5) and it was stirred for 10 min at 350 rpm. Next, the solution was again centrifuged at 13000 rpm for 5 min to begin the deposition of the second polyanion (CS) layer in the same way as just described. To do this, CS was previously dissolved in sodium acetate buffer (0.1 M, pH 5) in a concentration of 1 mg/mL. The procedure was repeated to obtain a nanocapsules shell composed of 7 consecutive polyelectrolyte layers. Each layer was characterized in terms of ζ-potential by taking an aliquot of 100 µL from the corresponding solution before the last centrifuge.

To perform appropriate future analysis, the obtained NPs were stored in NaCl solution at 4 °C.

2.3 CQDs Characterisation methods

2.3.1 Physico-chemical analysis

2.3.1.1 Fourier Transformed Infrared spectroscopy (FTIR-ATR)

Infrared spectroscopy was performed with a Spectrum Two PE instrument equipped with a horizontal attenuated total reflectance (ATR) crystal (ZnSe) (PerkinElmer Inc., USA) to evaluate the surface functional groups of the CQDs created. The analysed samples, in powder form, were placed directly on the ATR crystal, so that the spectra were collected in absorbance mode and recorded in the wavelength range 4000-550 cm^{-1}. Each spectrum was the result of averaging 16 scans with a resolution of 2 cm^{-1}.

2.3.1.2 X-ray photoelectron spectroscopy (XPS)

Freeze-dried CQDs were subjected to an XPS analysis to quantitatively assess the elemental composition of the surface of the biomaterials. Samples were examined by a scanning microprobe Kratos Axis UltraDLD XPS spectrometer (EPSRC Harwell XPS Service Cardiff, UK), equipped with a monochromatised AlKα X-ray radiation source. The base pressure in analysis chamber was 10−9 mbar. Samples were analysed in High

Power mode with an X-ray take-off angle of 45° (scanned size∼1400 × 200 µm). For each specimen, survey scans (Fixed Analyser Transmission mode, binding energy (BE) range 0–1200 eV, pass energy 117.4 eV) and high-resolution spectra (FAT mode, pass energy 29.35 eV) were acquired of C1s. Atomic concentration (At.%) on the survey scan was performed using the built-in CasaXPS software package and in order to detect the Binding Energy (BE) representing the chemical binding states of the each elements within the films, the XPS spectra for the chemical elements detected from the films were subjected to peak deconvolution using the same software.

2.3.1.3 ζ-Potential measurements

A Zetasizer Nano ZS Instrument (Malvern Panalytical Ltd) was used to measure the CQDs surface charge. The samples were diluted 1:10 in dH_2O. The values shown in the Results section will be the result of the average of three measurements where each measurement was obtained after a maximum of 100 runs. The experiments were performed in triplicates.

2.3.1.4 UV-Vis analysis

A double-beam UV-Vis spectrophotometer (Cintra 10e, GBC) was used to investigate the absorbance pattern of CQDs aqueous solutions excited on a whole wavelength range (200-600 nm).

2.3.1.5 Fluorescence measurement

A Cary Eclipse PL spectrophotometer (Varian CA, USA) excited the CHCQDs solution on a wavelength range from 300 nm to 380 nm. The emission was then analysed and plotted on a range from 300 nm to 650 nm.

2.3.2 Morphological analysis

2.3.2.1 High-resolution transmission electron microscopy (HRTEM)

High-resolution transmission electron microscopy (HRTEM) micrographs of the prepared nanopowders were recorded with a JEOL 2100F field emission cannon transmission electron microscope (FEG TEM) operating at 200 keV. Samples were prepared for HRTEM analysis by dispersing the nanopowders of dots on a holey carbon grid.

2.3.3 Cytotoxicity Evaluation

2.3.3.1 Cell cultures

Neo-dermal fibroblast cells were grown in Dulbecco's Modified Eagle's Medium (DMEM) with 10% fetal bovine serum (FBS) and 5000 U/mL penicillin/streptomycin. Culture materials were purchased from Sigma Life Science. Cells were maintained at 37 °C with 5 % CO_2 in a humidified incubator.

2.3.3.2 PrestoBlue

The metabolic activity of fibroblast cells was estimated using PrestoBlue™ assay.

Briefly, neo- dermal fibroblast cells were seeded in a 96-well plate (5000 cells/well) and allowed to grow for 24 h. Next day, media was removed and replaced with fresh media containing CQDs in different concentration (50, 200, 500, 1000 µg/mL). The formulations were incubated for 48 h, then culture medium was removed, and samples were washed with pre-warmed PBS at 37 °C in order to assess the metabolic activity of cells using PrestoBlue solution.

PrestoBlue™ reagent (Thermo Scientific, USA) was warmed up and diluted in DMEM (1:10) protected from light. 200 µL of solution was added to each well and incubated for 2.30 h at 37°C, 5% CO_2. Then, 100 µL of each well solution was transferred to a white bottom 96-well plate and a FLUOstar Omega MicroPlate Reader (BMG Labtech) was used to measure the fluorescence (560 nm excitation and 590 nm emission).

The obtained values were corrected subtracting the average fluorescence of control wells with only PrestoBlue solution. Results are shown in viability (%) vs concentrations of CQDs types (ug/mL). Percent viability was obtained by relating the value in fluorescence of each sample with the average fluorescence value of the control cells (which have not been treated).

2.3.3.3 Live/Dead

Live/Dead assay (LIVE/DEAD® Cell Imaging Kit, Life Technologies, Thermo Fisher Scientific, UK) is used to measure cell viability. It is a two-colour fluorescence test that simultaneously determines the population of live cells (green) and dead cells population (red).

The cell types, number of cells, timings, types and concentrations of the CQDs tested in the paragraph 2.3.3.2 are unchanged. Instead of using 96-well plate, 48-well plate were used.

Live/Dead assay was used according to the manufacturer's instructions. Each cell culture condition was washed thrice with PBS before incubation with staining. In brief, 4 µM ethidium homodimer-1 and 10 µM Calcein dilute in PBS, were incubated in the dark with the cell-seeded for 30 min at 37 °C. Live/Dead images were taken by a EVOS M5000 (Thermo Fisher).

2.4 NPs Characterisation methods

2.4.1 Physico-chemical analysis

2.4.1.1 Fourier Transformed Infrared spectroscopy (FTIR-ATR)

Infrared spectroscopy analysis was conducted using the same equipment and parameters described in the section 2.3.1.1 in order to evaluate the surface functional groups of the NPs created. The different types of NPs analyzed are shown in Tab. 10. The analyzed samples were all in powder form.

CORE	LAYERS	STATUS
CaP	None	Pre-Dialysis
CaP	None	Post-Dialysis
CaP	PAH	Pre-Dialysis
CaP	PAH	Post-Dialysis
CHBOCQDs	CH/DOXO	Layered

Tab. 10: Samples analysed by FTIR-ATR.

2.4.1.2 ζ-Potential

A Zetasizer Nano ZS Instrument (Malvern Panalytical Ltd) was used to measure the surface charge of the NPs during the formation of each layer and to assess the stability of the charge several days later.
The characterization was conducted in the same way as stated in the paragraph 2.3.1.2.
The experiments were performed in triplicates.

2.4.1.3 Process Yield (Y)

To measure the amount of formulation produced (%) referring to the amount of formulation components, the following equation was used:

$$Y\ (\%) = \frac{(weight\ of\ the\ formulation)}{(weight\ of\ polymers + weight\ of\ drug + weight\ of\ other\ components)}\ x100 \qquad \text{(Eq.2)}$$

Produced formulations were measured following freeze-drying of solutions containing the NPs covered by polyelectrolytes.

2.4.1.4 Effectiveness of Encapsulation of drugs in the core of CaPs

Most calcium phosphates are sparingly soluble in water, but all dissolve in acids (Tung, M.S.,1998; J.F. De Rooij et al., 1984). For this reason, the DOXO encapsulated in the core of CaP NPs was extracted through two steps. The first step involves the use of a solvent that will solubilize both the polymers and the drug. Therefore, 1 mg of lyophilized CaP NPs (containing DOXO in their cores) were dissolved in 3 mL of HCl and they were stirred at 120 °C until the acid is completely evaporated and a pellet consisting of drug and polymers will be obtained. The second step was to disperse the pellet in a second solvent (Ethanol/Water 3:1) soluble exclusively to the drug. After stirring the solution for 5 h, the solvent was withdrawn, centrifuged at 13000 rpm for 10 min and 100 µL of eluate for each sample was transferred into a 96-well plate.

Afterwards, the optical density of the solution was measured at 480 nm using and a FLUOstar Omega MicroPlate Reader (BMG Labtech). The effective absorbance was calculated by subtracting the average absorbance of the wells containing the blank (Ethanol/Water 3:1) to each standard and each sample.

For each absorbance value, the corresponding DOXO concentration in µg/mL was calculated (referring to the previously obtained calibration curve). Finally, to obtain the total µg of drug encapsulated within the CaP cores, Eq. 2 is used (where the drug supplied is a known amount):

$$EE\ (\%) = \frac{(amount\ of\ drug\ in\ nanoparticles)}{(amount\ of\ drug\ supplied)}\ 100 \qquad \text{(Eq.3)}$$

The experiment was done in triplicate.

2.4.1.5 Effectiveness of Encapsulation of drugs in layers

The effectiveness of encapsulation of the two drugs by the layers was evaluated by an indirect method for the NPs tabulated in Tab. 11.

CORE	LAYERS
CaP + DOXO	6 layers without DOXO and GCQDS
CaP + DOXO	6 layers with DOXO
CaP + DOXO	6 layers with DOXO and GCQDS
CHBOCQDs + CH/DOXO	none
CHBOCQDs + CH/DOXO	6 layers without DOXO and DTX
CHBOCQDs + CH/DOXO	6 layers with DOXO
CHBOCQDs + CH/DOXO	6 layers with DOXO and DTX

Tab. 11: Samples analysed to test the effectiveness of drug encapsulation

During the formation of each layer and following each centrifugation related to the NPs washing steps, the supernatant was recovered and 100 µL of this solution was transferred into a 96-multiwell in triplicate.
Thereafter, the samples were analysed in absorbance using a FLUOstar Omega MicroPlate Reader (BMG Labtech), measuring separately the absorbance of the unencapsulated DOXO (at 480 nm) and the absorbance of the unencapsulated DTX (at 230 nm) from the newly deposited layers on the NPs surface.
The effective absorbance was calculated by subtracting the average absorbance of the wells containing the blank (washing solutions or the drug-free deposition solutions) to each standard and each sample.
For each absorbance value, the corresponding DOXO and DTX concentration in µg/mL were calculated (referring to the previously obtained calibration curves).
Finally, to obtain the total µg of drug encapsulated within layers, Eq. 3 is used (where the drug supplied is a known amount):

$$EE\ (\%) = \frac{(amount\ of\ drug\ in\ supplied) - (amount\ of\ drug\ NOT\ in\ nanoparticles)}{(amount\ of\ drug\ supplied)}\ 100 \qquad \text{(Eq.4)}$$

The experiment was done in triplicate.
Following freeze-drying of the samples, it was possible to match the amount of drug encapsulated by the Nps layers to the actual weight of the NPs produced.

2.4.1.6 Drug Release Studies

For the determination of drug release profiles, 0.4 mg of NPs were accurately weighted, dispersed in 1 mL Phosphate Buffer Saline (PBS) and incubated at 37 °C for up to 28 days. PBS was used as release medium. The NPs on which the drug release study was done are tabulated in Tab. 11.
The amount of drug released was measured every 7 days. In order to characterize the initial burst effect, the measurement was taken after 10 min and up to 6 h soaking during the first day of incubation.
At each step, 60 µL of supernatant (replaced at each withdrawal with an equal number of µL of PBS) was taken from each sample and mixed with PBS in a 1:10 ratio in a final volume of 600 µL.
Next, the obtained solution was centrifuged at 13000 rpm for 10 min and the supernatant was taken and transferred to a new eppendorf.
Finally, the optical density of the solution was measured separately at 480 nm for DOXO and at 230 nm for DTX using a Plate Reader. For each time step analyzed, the effective absorbance was calculated by subtracting the average absorbance of the wells containing the blank (PBS) to each standard and to each sample. Through the two different calibration curves of DOXO in PBS and DTX in PBS, the concentration of DOXO and DTX released at each time step (µg/mL) were obtained; multiplying the concentration by the volume of the supernatant (1 mL), the µg of DOXO and DTX released were obtained.

Since the release was cumulative the amounts of each drug obtained at each time step were added to the amounts obtained at the previous time steps (Eq. 4). The percent release for each time step was calculated by dividing by the amount of DOXO or DTX encapsulated within the NPs.

$$\%M_{rel} = \frac{Mrel(\mathrm{t}-1) + M(t)}{(Weight\ of\ encapsulated\ drug)} \times 100 \qquad \text{(Eq.5)}$$

The experiment was done in triplicate for each type of NP tested.

2.4.2. Morphological analysis

2.4.2.1. Dynamic Light Scattering (DLS)

The average size analysis of the hydrodynamic diameter of NPs and their size distribution analysis was performed using a Zetasizer Nano-S90 (Malvern Instruments, Malvern, UK). In addition, the Polydispersity Index (PDI) of each solution tested was evaluated.

A dilute solution (1:10) of samples with only one layer or with 7 layers deposited on the core surface were used for NPs size analysis. The values shown in the results section will be the outcome of the average of three measurements. The graphs corresponding to these values are shown as Size Distribution by Number (%) vs Size (d. nm). Each measurement was obtained after a maximum of 14 runs.

2.4.2.2. Transmittance Electron Microscopy (TEM)

To analyse the morphology and the size of NPs with a single layer and with 7 layers deposited on the corresponding core, the TEM analysis was performed on a Philips CM 100 Compustage (FEI) transmission electron microscope (Philips) at HV = 100.0 kV, and digital images were capture using an AMT CCD camera (Deben) with a range of magnification up to 130,000x. To do this, a small drop of NPs solution was deposited on a copper grid (Agar Scientific); then, images were captured upon evaporation of the solution.

2.4.3. Cytotoxicity Evaluation

2.4.3.1. Cell cultures

Saos-2 and U-2 OS osteosarcoma cancer cells and neo-dermal fibroblast cells were grown in Dulbecco's Modified Eagle's Medium (DMEM) with 10% fetal bovine serum (FBS) and 5000 U/mL penicillin/streptomycin. Culture materials were purchased from Sigma Life Science. Cells were maintained at 37 °C with 5 % CO_2 in a humidified incubator.

2.4.3.2. PrestoBlue

The metabolic activity of cancer cells was estimated using PrestoBlue assay. Briefly, U2OS and Saos-2 osteosarcoma cancer cells were seeded in a 96-well plate (7000 cells/well) and allowed to grow for 24 h.
Next day, media was removed and replaced with fresh media containing NPs or free drugs in different concentration (Tab. 12).

SAMPLE	CONCENTRATION (µ g/mL)
CHBOCQDs + 7 layers without drugs (CQDs_7L)	0.5, 1, 5, 10, 100
CHBOCQDs + 7 layers with DOXO (CQDs_7D)	0.5, 1, 5, 10, 100
CHBOCQDs + 7 layers with DOXO and DTX (CQDs_7DD)	0.5, 1, 5, 10, 100
CaP + 7 layers without drugs (CaP_7D)	100, 250, 500
CaP + 7 layers with DOXO and GCQDs (CaP_7DC)	5, 10, 100, 250, 500
Free DOXO	0.5, 1, 5, 10, 100, 250, 500
Free DTX	0.5, 1, 5, 10, 100, 250, 500
Free DOXO/DTX	0.5, 1, 5, 10, 100, 250, 500

Tab. 12: Samples analysed to test the drug release.

The formulations were incubated for 24 h, then culture medium was removed and samples were washed with pre-warmed PBS at 37 °C in order to assess the metabolic activity of cells using PrestoBlue solution.
Subsequently, the experiment was conducted in the manner stated in paragraph 2.3.3.1.
Final results are shown in viability (%) vs concentration of different types of NPs and drugs tested (ug/mL). Percent viability was obtained by relating the value in fluorescence of each sample with the average fluorescence value of the control cells (which did not undergo any treatment).

2.4.3.3. Live/dead assay

Live/Dead assay (LIVE/DEAD® Cell Imaging Kit, Life Technologies, Thermo Fisher Scientific, UK) is used to measure cell viability. The cell types, number of cells, well plate type, timings, types and concentrations of the NPs and drugs tested in the paragraph 2.4.3.1 are unchanged.
The experiment was carried out according to the methods outlined in Section 2.3.3.2.

2.4.3.4. Immunostaining assay

Immunostaining was used to determine the number of nuclei (using 4', 6- diamidino-2-phenylindole (DAPI)) and to assess the coarse morphology of the cells by staining their actin filaments (using rhodamine-phalloidin). Specifically, this staining was applied to U2OS and Saos-2 cells following NPs cultures for 24 h in

96-well plate (7000 cells/well). The NPs tested in different concentrations were exclusively for CaP_7L and CaP_7DC. The concentrations of the tested NPs solutions are given in Tab. 12.

After one day of cell culture with the NPs, the culture medium was removed, the samples were washed three times in PBS and were fixed in 50 µL of in 4 % (w/v) Paraformaldehyde (PFA) (pre-warmed) overnight. The next day, cells were permeabilised using 0.1 % (v/v) Tween20® (Sigma, Life Science) in PBS for three washes. Then, an ActinRed solution was made (2 drops of phalloidintetramethylrhodamine B isothiocyanate (Sigma) per mL of PBS). 50 µL of ActinRed solution is placed in each sample for 20 min at room temperature, protected from light. Residue of phalloidin-rhodamine was removed by washing samples with 0.1 % PBS/Tween20® solution three times. Following this, samples were immersed in DAPI solution (1 drop of DAPI solution in each well) for 10 minutes at room temperature protected from light. Then, samples were washed other three times with 0.1% PBS and were imaged using a EVOS M5000 (Thermo Fisher).

2.4.3.5. Transmittance Electron Microscopy (TEM)

Uptake of NPs by Saos-2 cells was verified by TEM analysis. Through this method it is also possible to make morphological assessment and to localize cellular structures (organelles and internal structure). The equipment used is described in section 2.4.2.2.

Only the CaP_7DC Nps were tested with Saos-2 cells with a concentration of 500 µg/mL in culture medium. 5000 cells were adhered for 24 h on a 24-well plate having Corning™ Transwell™ Multiple Well Plate with Permeable Polyester Membrane Inserts (Thermo Scientific™). Then, NPs were seeded for 24 h with the cells. Following removal of the culture medium and washing in PBS (three times), the cells were fixed on the membranes using a pre-warmed solution of 2% glutaraldehyde (TAAB Laboratory Equipment) in sodium cacodylate buffer at 4 °C.

After various dehydration steps, the cell layer was embedded in resin, and cut in ultrathin sections using a diamond knife on a Leica EM UC7 ultra microtome (Leica Microsystems). The sections were stretched with chloroform to eliminate compression, mounted on Pioloform-filmed copper grids (Agar Scientific) and ready to be visualized.

2.4.4. Computational approach on drug kinetics release from multilayer capsules: an innovative and preliminary study

The data obtained from in vitro drug release experiments (DOXO and DTX) related to CQDs_7DD NPs were compared with results obtained from a mathematical model implemented for drug release from NPs.

The mathematical model was implemented from work previously reported in the literature by Barchiesi et al. (2022).

To solve the mathematical problem of the following equations (Eq. 4-7), a finite method was employed by using COMSOL Multiphysics software (COMSOL Multiphysics, 2019).

The proposed model is mainly based on the analysis of diffusion mechanisms as predominant in the kinetic drug release profile. In addition to this mechanism, the model will also simulate the progressive degradation of the layers due to PBS as the surrounding environment. This phenomenon will cause a subsequent release of both drugs contained in the layers, proportional to the volume of material removed. The decrease in radial diameter of the NPs will be simulated symmetrically and through a linear law from a given instant t_0:

$$R(t)= R(t_0) - v\,t \quad \text{for } t \geq t_0 \qquad \text{(Eq. 6)}$$

Initially, the CQDs_7DD multilayer spherical system (involving n concentric enveloping layers Ω_1, Ω_2, Ω_n) is considered as a core-shell system consisting of a spherical core Ω_0 of radius R_0 and a single enveloping shell Ω_1 of radius R_1 with the latter simulates the presence of the multiple layers present on the surface of the NPs core. The coordinate system has origin located at the centre of the NP and the r-axis oriented with the positive direction outward (Fig. 58).

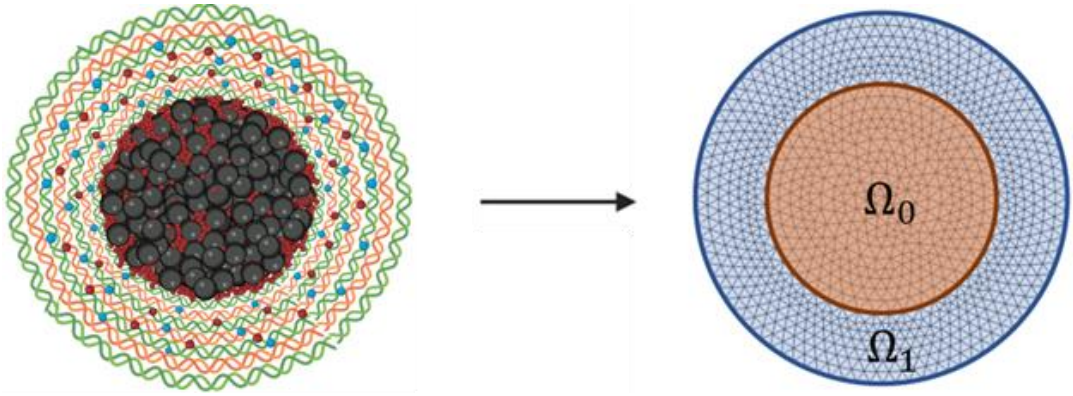

Fig. 58: Schematic figure of CQDs_7DD (A) and its modelling by COMSOL Multiphysics (B).

The release mechanism of the drug encapsulated in the NPs core reproduced by the mathematical model simulates the nonlinear dissolution of the drug in the PBS solution (which will infiltrate between the layers and into the core) and the subsequent diffusion of the drug with diffusion coefficient (D_0 is the diffusion coefficient in the core). The drug dissolution and diffusion dynamics in Ω_0 is defined by the resulting nonlinear partial differential equations:

$$\frac{\partial b_0}{\partial t} = -\beta b_0^a (S - c_0)$$

$$\frac{\partial c_0}{\partial t} = \nabla(D_0 \nabla c_0) + \beta b_0^a (S - c_0) \;\; in\; \Omega_0 \quad \text{(Eq. 7-8)}$$

Where the $b_0(x, t)$ concentration is related to undissolved drugs within the core and $c_0(x, t)$ concentration is the dissolved drug. β is the specific dissolution rate of drugs and S is the solubility of drugs in PBS.

Representing the bound and unbound phase concentrations in Ω_1 shell by $b_1(\boldsymbol{x}, t)$ and $c_1(\boldsymbol{x}, t)$, the dynamics of the drug in Ω_1 can be represented by the equations below:

$$\frac{\partial c_1}{\partial t} = \nabla(D_1 \nabla c_1) - kc_1$$
$$\frac{\partial b_1}{\partial t} = kc_1 \ \ in\ \Omega_1 \quad \text{(Eq. 9-10)}$$

where D_1 is the diffusion coefficient in the coating shell.

As initial conditions, the drugs are homogeneously distributed initially, and their release will be hindered by the resistance offered by the layers. In addition, continuity of normal flux and concentration are considered as initial and boundary conditions. At the outer surface, it was imposed a perfect sink condition, in order to mimic the *in vitro* experiments conditions where the NPs are immersed in a large environment fluid.

The drug release profile is determined cumulatively can be defined through the Eq. 4.

2.4.5. Statistical analysis

Tests were performed at least in triplicate for each sample. Results are presented as means ± standard deviations. Statistical significance was evaluated by analysis of variance (ANOVA), followed by Turkey's multiple comparison test using levels of statistical significance of $p < 0.05$ (*), $p < 0.01$ (**), $p < 0.001$ (***), and $p < 0.0001$ (****).

CHAPTER 3: Results and Discussion

3.1. CQDs characterisation

3.1.1. Physico-chemical characterisation of chitin-derived CQDs

Hydrothermal pyrolysis-carbonisation (HTC) method has been used for the synthesis of CQDs from chitin biomass waste by first converting biomass to char (pyrolysis) and then to CQDs (HTC). A side product formed in the pyrolysis reaction, bio-oil, was never considered useful for the synthesis of CQDs and considered a waste product (Li Y. et al., 2016). However, in this thesis, the use of bio-oil as a synthesiser of CQDs was investigated when used in the HTC step in the same way as char produced by pyrolysis. This would allow an increase in the overall yield of the two-stage process, a previous disadvantage of this process. Moreover, the use of bio-oil for the synthesis of CQDs would make the overall process more environmentally friendly due to less waste production.

Pyrolysis is a process that takes place when organic matter is decomposed at temperatures above 200°C in the absence of oxygen to produce a substance called char (carbon and ash) and volatile matter, which includes condensable vapours called pyrolysis oil (also known as bio-oil) at room temperature and non-condensable (permanent) gases such as carbon monoxide, carbon dioxide, hydrogen and light molecular weight hydrocarbons such as methane, collectively called synthesis gas (syngas or producer gas).Bio-oil is acidic, viscous, dark-brown aqueous liquid rich in soluble (acids, esters, etc.) and water-insoluble (pyrolytic lignin) compounds. In addition, bio-oil has a high oxygen content, resulting in non-volatility and a tendency to polymerise when exposed to air (Kumar S., 2013).

Direct comparison by FTIR-ATR (Fig. 59) analysis between char and bio-oil obtained from the same pyrolysis of a waste biomass.

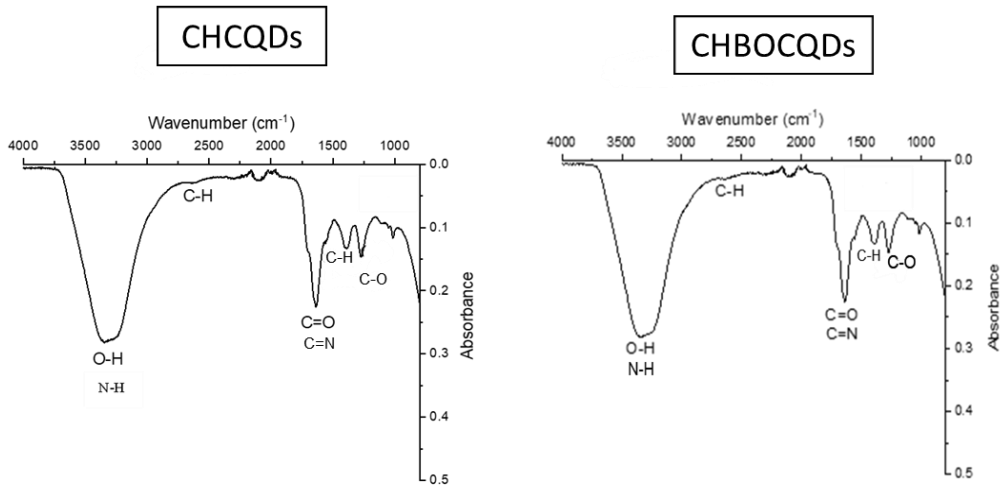

Fig. 59: FTIR-ATR of char (A) and biooil (B) product after pyrolysis of Chitin

Particularly, the FTIR-ATR results of char and bio-oil generated after the pyrolysis reactions on chitin showed identical analytical spectra, with significant peaks at ~3200 cm^{-1} (O-H and N-H), ~1600-1700 cm^{-1} (C=O), ~1600 cm^{-1} (C=N) and ~1300-2600 cm^{-1} (C-H), indicating the presence of these surface chemical groups in the char and bio-oil samples. The similarity of these two products confirmed that the bio-oil samples are suitable for the HTC phase. It is important to note that nitrogen is present in a significant composition in the char and bio-oil. This is because the pyrolysis of the biomass material was done in an inert atmosphere by nitrogen efflux.

HTC is a thermochemical conversion technique that can transform char and bio-oil into CQDs without pre-drying. By comparing the FTIR-ATR analysis performed on the CQDs obtained from the HTC reactions and comparing the results obtained with the spectra in the literature, it was evident that not only the char-derived CQDs were successfully synthesised as expected, but also that the bio-oil-based HTC reaction successfully synthesised CQDs (Fig. 60). The surface structure and composition of the CQDs from both reactions were characterised by same bonds in the same regions, which are O-H/N-H (~ 3200 cm^{-1}), C-H (~2900 cm^{-1}), C=O (~1600 cm^{-1}), C=C (~ 1300 cm^{-1}) and C-O (~ 1100 cm^{-1}). Importantly, they all contained C=C bonds indicating a π-π* electronic transition and C=O bonds indicating an n-π* transition, which are key features of CQDs and confirm the optical results (Dager, A. et al., 2019). CQDs mainly had C=C, C=O and C-H peaks, which are negative moieties, indicating the charge of CQDs would be negative. This will be confirmed by measuring the zetapotential of these samples.

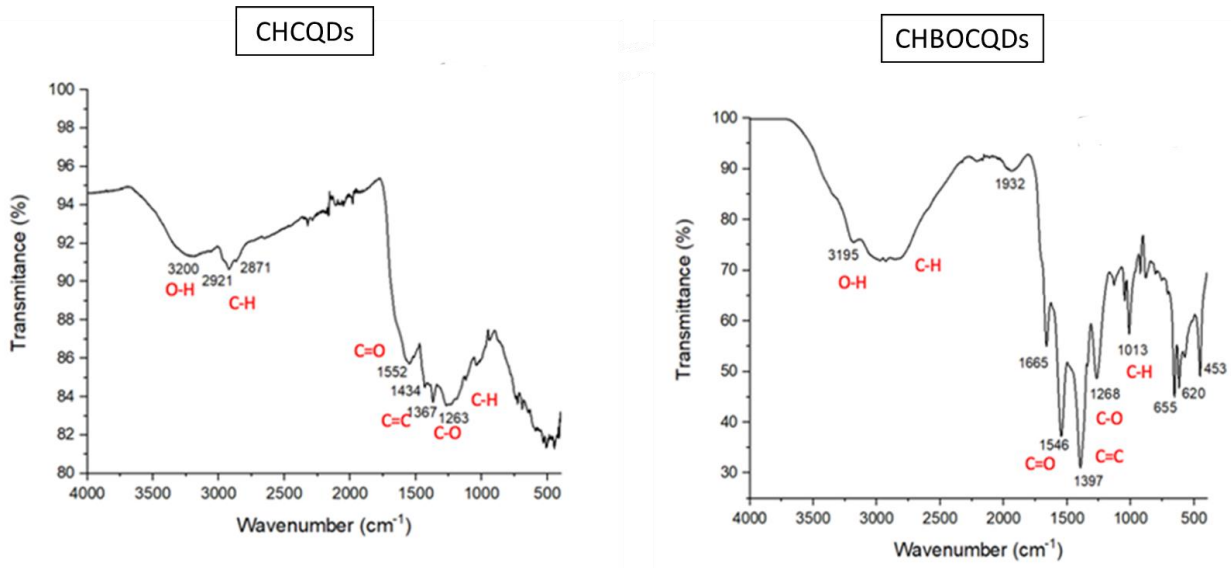

Fig. 60: FTIR-ATR analysis of CHCQDs (left) and CHBOCQDs (right)

These samples were compared directly with XPS readings to validate the composition of these structures obtained by FTIR-ATR (Fig. 61).

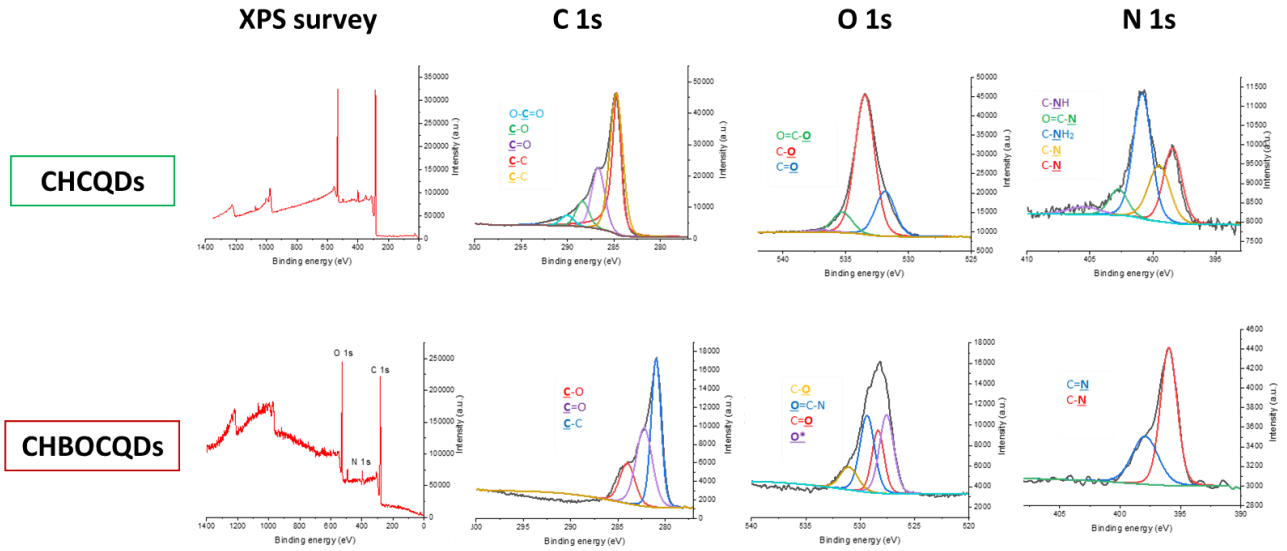

Fig. 61: XPS element analysis of CHCQDs (up) and CHBOCQDs (down)

The presence of C=C and C=O have been confirmed in all the XPS high resolution spectra of the samples with traces of nitrogen detected in all samples (in the survey spectra), due to the inert atmosphere of pyrolysis step.

Subsequently, CHBOOCQDs and CHCQDs were characterised by ζ-Potential analysis. Both types of CQDs showed negative charges, which were -15.6 ± 3.3 mV for CHBOCQDs and -19.7 ± 1.4 mV for CHCQDS.

Furthermore, a negative potential indicates that the surface of the CQDs has negative charge moieties, which are essential to ensure the dispersion of CQDs in aqueous solvents (Dager, A. et al., 2019).

However, the solubility of bio-oil-derived CQDs was much higher than that of char-derived CQDs (Fig. 62), which will be more advantageous for CQD applications that require CQDs to be dissolved in solutions.

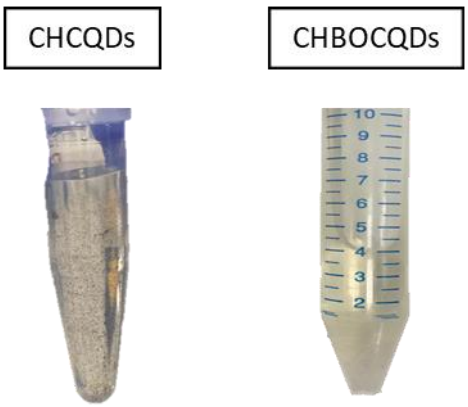

Fig. 62: CHCQDs (left) and CHBOCQDs (right) dissolution in water.

The investigation of the optical properties of the synthesised QCs were obtained by using UV-Vis absorption and photoluminescence spectra. The latter also made it possible to determine the quantum yield.

These analyses provide unequivocal confirmation of the success of the synthesis of CQDs (Nguyen, H.A. et al. 2020).

Initially, the fluorescence of the samples was examined by a UV lamp with 12" UV light at 365 nm. As can be seen in Fig. 63, the intense blue light indicates the high presence of CQDs in the solution, which were small and emitted a high amount of energetic light, according to the quantum confinement effect.

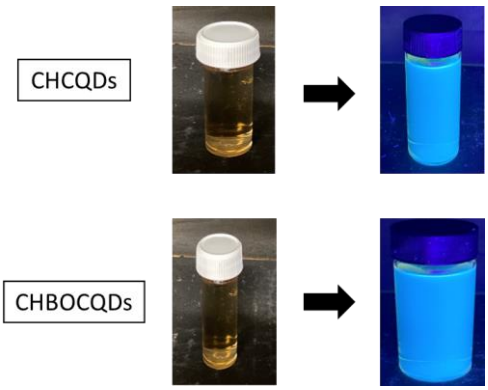

Fig. 63: The two prepared CQD samples (left) and their corresponding image while held under the UV lamp (right)

The next test was to determine the absorbance of light by the dots. This is done using UV-Vis spectroscopy. The UV-Vis absorption spectra of both CQDs variants showed almost identical absorption which were 280 nm for CHCQDs and 290 nm for CHBOCQDs (Fig. 64), giving a blue colour. The absorption peak appearing in these CQD samples between 230-280 nm and 300-330 nm were indicative of the presence of π-π* electronic transitions of C=C bonds belonging to an aromatic ring and the n-π* transition of C=O bonds, respectively (Alas, M. O. et al. 2020).

Therefore, since the samples appeared blue under the UV lamp and had an absorbance peak in the 300 nm region of the UV-Vis spectrum, this indicated that the solutions had CQDs, as reported by Alas, M. O. et al. (2020). This is very important for the type obtained from Bio-Oil, which confirmed the novelty of this reaction.

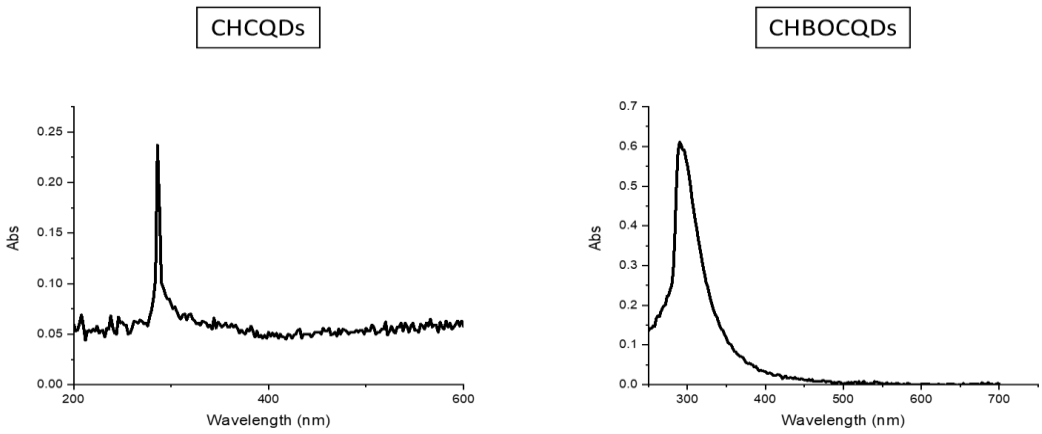

Fig. 64: UV-Vis spectra of CHCQDs (right) and CHBOCQDs (left).

The photoluminescence spectra of CHCQDs and CHBOCQDs were recorded to obtain the Quantum Yield of char and bio-oil derived CQDs (Fig. 65). For the CHCQDs, a strong peak was detected centred at 360 nm, a consequence of excitations at 300 nm. As the wavelengths increase, the emission intensity decreases and shifts towards the red end of the spectrum, showing excitation-dependent emission. This could be due to the size distribution of the nanoparticles (Yuan et al. 2014). However, the spectrum is not uniform, but has secondary peaks at different emission wavelengths.

On the other hand, CHBOCQDs showed excitation-independent behaviour. Indeed, for excitations from 310 nm to 360 nm, the emission peak was centred in 400 nm. In addition, two peaks with maximum intensity were present and were in response to excitation wavelengths of 310 and 320 nm. For higher excitation wavelengths up to 360 nm, the peak remained centred at an emission wavelength of 400 nm but decreased in intensity.

Exciting the CHBOCQDs with wavelengths above 360 nm, a slight excitation-dependent behaviour was observed, shown by a continuous decrease in fluorescence intensity and a shift of the emission wavelength towards the red. The comparison of the emission graphs of CHCQDs and CHBOCQDs fully confirmed the success of bio-oil in the synthesis of CQDs. Indeed, the two types of CH-derived CQDs emitted fluorescence in the same region (at 400-500 nm) but showing different optical behaviour.

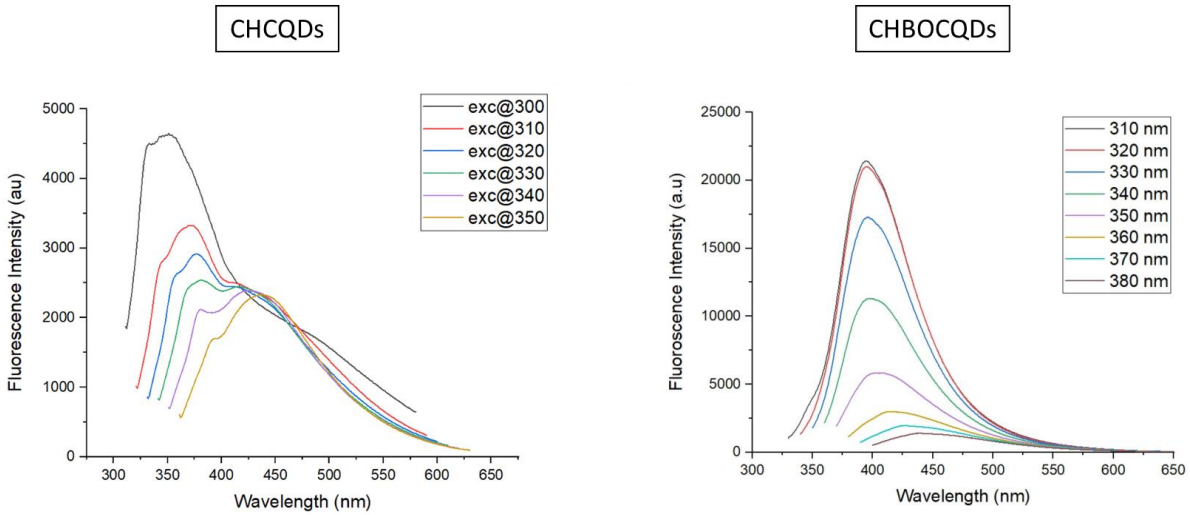

Fig. 65: Emission spectra of the CHCQDs (right) and CHBOCQDs (left) at different excitation wavelengths.

In general, absorption capacities agreed with what was found when examining the fluorescence properties. Indeed, the spectra showed intense peaks centred on 360 or 400 nm as a result of excitations in the UV-A range (300-380 nm). The causes of the excitation-dependent or excitation-independent emission can depend on a multitude of factors. Moreover, the mechanisms underlying fluorescence are not yet fully known. As a hypothesis, the fluorescent emission may be due to the quantum confinement effect, or to chemical and

structural defects on the surface (carboxyl and amide groups have been associated with green emission, hydroxyls with blue emission) and the edges of carbon-based nanoparticles (Wareing TC et al. 2021).

The quantum yield of CHBOCQDs was determined as 18 % and that of CHCQDs as 8 %. Compared to previous research on biomass-derived CHCQDs, these numbers are encouraging as no surface modifications were required to achieve such a consistently high yield, a recurring problem in char-derived CQDs. In fact, average quantum yield values derived from biomass and following passivation or atomic doping treatments are generally between 7 and 36 %. (Zhou, J. et al. 2012; Prasannan, A. et al. 2013). To improve the quantum yield, surface passivation and interatomic doping methods can usually be applied; however, this was not studied in this thesis.

Finally, the yield of the process after the two production steps was evaluated. CHBOCQDs had a process yield of 25.9 %, while CHCQDs had a yield of 23.9 %. Thus, more CQDs were produced through the production process using bio-oil. In total, there was a process yield of 49.9 %, which was very high compared to the works in the literature.

3.1.2. Morphological characterisation

After successfully determining the optical properties and composition of the derived CQDs, the final step was to determine the morphology of the CQDs, obtained using HRTEM (Fig. 66). Both types were visible at HRTEM, further demonstrating the success of the HTC reaction in Bio-Oil samples. Furthermore, all dots appeared to be between 0.5 and 10 nm. However, clear particle aggregates of larger size were present in the captured images.

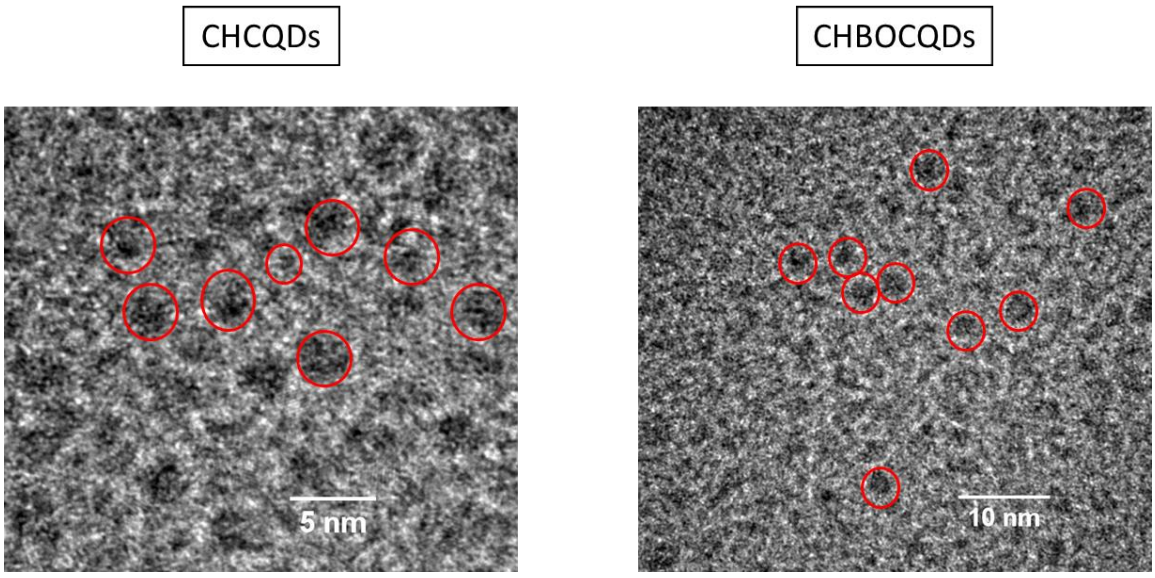

Fig. 66: HRTEM of CHCQDs (left) or CHBOCQDs (right).

3.1.3. Cytocompatibility of CHBOCQDs

CQDs obtained from chitin were evaluated by PrestoBlue assay on Neo-dermal fibroblasts after 48 h of seeding at different concentrations. Due to the insolubility of CHCQDs, the biocompatibility of only CHBOCQDs was studied.

The PrestoBlue assay (Fig. 67) shows that CHBOCQDs showed no significant alteration in metabolic activity compared to the untreated control for NPs concentrations below 500 µg/mL (cell viability were between 102.8 ± 9.3 % for 50 µg/mL and 90.7 ± 4.1 % for 500 µg/mL). For the highest concentration of 1000 µg/mL, a decrease in cell viability can be observed (58.1 ± 0.9 %) with a statistically significant difference between 200 µg/mL (p-value 0.0004) and 500 µg/mL (p-value 0.0012).

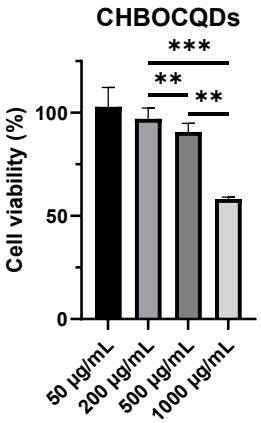

Fig. 67: PrestoBlue assay of Neo-dermal Fibroblast seeded with CHBOCQDs at different concentrations.

To qualitatively and visually verify the results obtained from the PrestoBlue assay, a Live/Dead assay was conducted on Neo-dermal Fibroblast cells treated with the same NPs and concentrations as in the cytotoxicity assay. For both phenotypes tested, the Live/Dead images show increasing red staining as the particle concentration increases, thus not showing results consistent with the PrestoBlue assay, even if qualitative (Fig. 68). However, the images confirmed the high biocompatibility of the tested NPs also because the concentrations of 500 and 1000 µg/mL were extreme for clinical application.

Furthermore, it was found that cells with low metabolic activity had visually fewer adherent cells than control. This is possible because the apoptotic cells no longer had the adhesion receptors for the substrate, which consequently floated in the seeding solution. Therefore, these cells were removed during the PBS wash steps before staining. The cells treated with concentration of 50 µg/mL showed diffuse and homogeneously distributed cells throughout the substrate. It is interesting to note that as the concentration increases, the cell morphology changes completely, reducing to small red dots compared to the counterparts at lower concentrations that show a more diffuse green colouration.

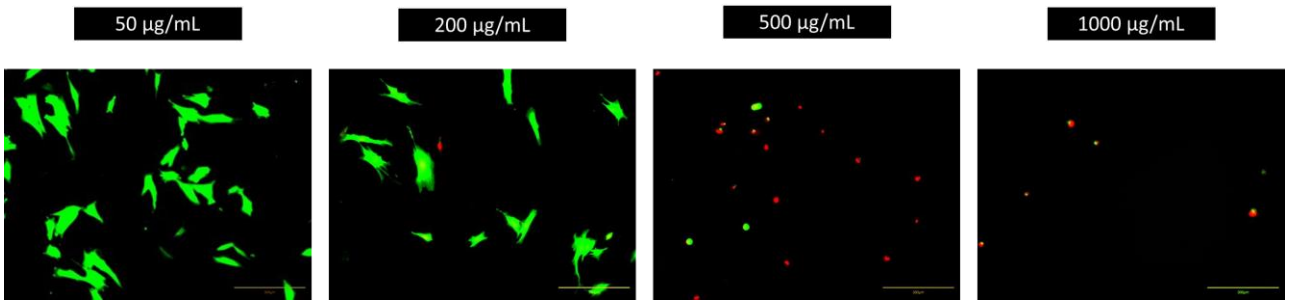

Fig. 68: Live/Dead images with CHBOCQDs at different concentrations.

These results showed that dots can be passively internalised by cells despite their negative charge and that they can escape from endosomes due to their negative charge (Dehua Pei and Marina Buyanova, 2019). However, due to their negative charge, they can be internalised in small percentages (Gratton SE et al. 2008). CHBOCQDs also caused cytotoxicity, but this depends essentially on the high concentration tested and the number of cells used in seeding (Esfandiari N. et al. 2019).

3.2. NPs characterisation

3.2.1. Material Selection

The choice of materials was made based on the planned engineering specifications, which were to form particles consisting predominantly of natural components that could be recognised by the host organism and that could enable the formation of NPs in the 100 nm size range (Humaira Idrees et al., 2020).

CH is a linear polysaccharide (amino-sugar) abundant in nature and consists of numerous N-acetyl-D-glucosamine units with acetylated amine groups that make it a cationic PE. CH is a bioactive material as it can mediate cell adhesion thanks to amino groups in the chain that make it biomimetic with respect to laminin (an adhesive protein that enables the adhesion of nervous system cells with the extracellular matrix) (Andrea Lončarević et al., 2017). Furthermore, CH is also biodegradable due to the digestive action of lysozymes present in the human body. Finally, CH is also known for its antibacterial effects. CH's benefits towards osteoblasts are also well known as it can increase their proliferation by significantly increasing the activity of alkaline phosphatase and increasing the expression of bone morphogenetic protein-2 mRNA (Parisa Maleki Dana et al., 2020).

Furthermore, Parisa Maleki Dana et al. 2020 reported that pure CH and combinations of CH with other compounds are effective against certain cancer cell lines, including osteosarcoma cells, exerting anti-tumour roles such as inhibition of proliferation, induction of apoptosis exerting anti-oxidative activities and suppressing metastasis through the involvement of mitochondrial pathways, inhibition of Exh2 expression (as evidenced by the reduction of membrane potential), cytochrome c release and G0/G1 cell cycle arrest.

CS is a sulphated glycosaminoglycan, composed of an alternating chain of sugars. Cells do not have specific receptors that recognise this compound; however, it has a negatively charged structure that is adapted for interactions with proteins or PEs of opposite charge. Thus, it is normally found associated with proteins, forming a proteoglycan. For this reason, CS was selected as the polyanion. Moreover, CS is not bioactive, but has a highly biomimetic structure.

Finally, PAH is a highly water-soluble synthetic cationic polymer prepared by the polymerisation of allylamine. Due to its biocompatibility and chemical inertness, it is widely used in LbL technology for biomedical applications. However, the physicochemical properties of PAH are highly dependent on pH and ionic strength, and the presence of primary amines along the polymer backbone makes PAH highly cytotoxic.

DOXO is used as a first-line chemotherapeutic drug for the treatment of osteosarcoma due to its mechanisms of action that allow intercalation of the drug into the cellular DNA resulting in the disruption of DNA repair mediated by topoisomerase-II and, simultaneously, allow the production of reactive oxygen species that can lead to lipid peroxidation and cell membrane damage of cancer cells. For these reasons, it will be encapsulated within NPs.

DTX is a second-line chemotherapeutic drug inserted into NPs to act on the mechanics of the cancer cell, promoting stable microtubule polymerisation and inhibition of depolymerisation, thus significantly reducing

the number of free microtubules. Thus, the main effect is the inhibition of the G and M phases of the cell cycle, i.e. mitosis and proliferation of cancer cells.

3.2.2. CaP synthesis

3.2.2.1. Physico-chemical analysis

CaPs particles coated or uncoated with a cationic polymer (PAH or CS) were synthesised via a pump system. First, the calcium phosphate was formed during a crystallisation time of 5 s and, subsequently, the CaPs were stabilised in colloidal form by functionalisation with the cationic polymer for a further 15 s to obtain a precipitate of NPs, as stated by H. Urch et al. (2009). The times were calculated based on the flow rate and tube diameter. Following dialysis and freeze-drying, the colour of the NPs in the absence or presence of the coating was white, while the NPs encapsulating DOXO were reddish. Since the DOXO solution was red in colour, it was possible to observe the encapsulation of the drug within the core of the NPs.

The process yield (Y (%)) of CaP(DOXO)_PAH was 51.5 ± 7.6 % due to the production of 98 mg of functionalised NPs, emphasising the fair amount of particles obtained. However, much of the material was discarded or removed from the dialysis process. Furthermore, it is possible that some of the NPs were dispersed during freeze-drying due to the size of the holes in the parafilm, which were created manually.

The functional groups present on the surface of PAH-coated CaPs using a concentration of 1 mg/mL were identified through FTIR-ATR analysis (Fig. 69). In addition, as a control, unfunctionalized calcium phosphate NPs were prepared under the same conditions. This analysis made it possible to identify the fundamental role of dialysis, which was to remove excess carbonate ions from the NPs.

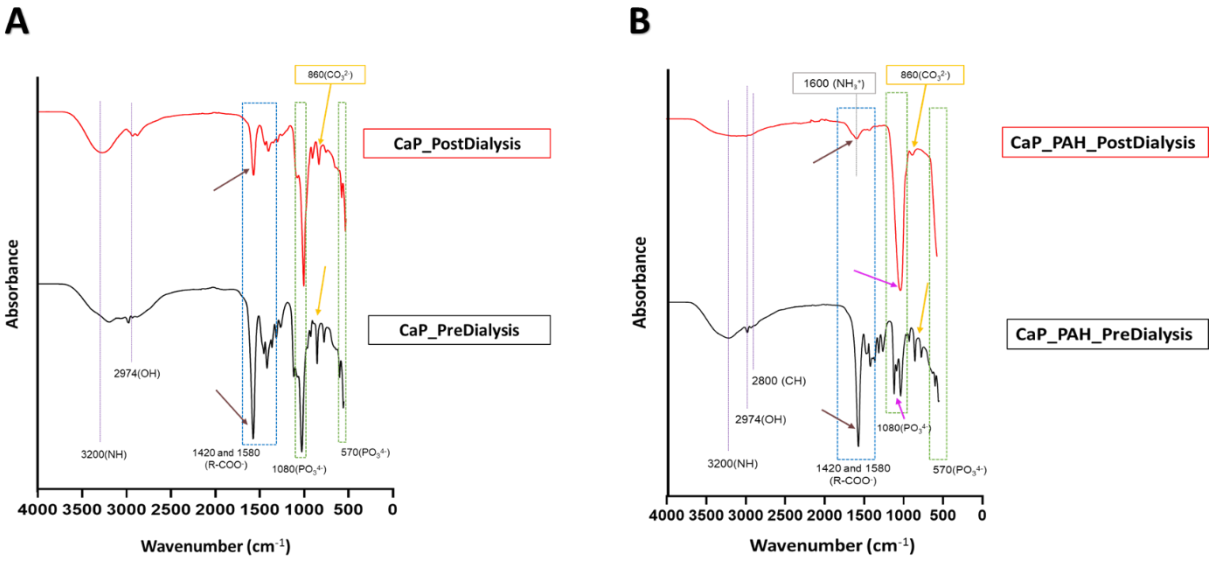

Fig. 69: FTIR-ATR of CaP (A) and CaP_PAH (B) before (black) and after (red) dialysis.

All samples showed carbonate bands (around 1427 and 1490 cm^{-1} and in 860 cm^{-1}) and phosphate bands (570 cm^{-1} and 1080 cm^{-1}). The region below 1000 cm^{-1} can be interpreted as reported by C. Rey et al. (2007) and Urch et al. (2009). The band at 570 cm^{-1} is due to apatite PO_4^{3-}, while the band at 864/868 cm^{-1} is characteristic of CO_3^{2-}. This type of carbonate was responsible for the surface aggregation of NPs. So, this formed the type B carbonate apatite, as also reported by C. Rey et al. (2007) and Urch et al. (2009).

For the CaP sample, the carbonate band at 1427-1590 cm^{-1} is more intense for the freshly precipitated sample than for the dialysed sample. The intensity of this peak decreased as a function of dialysis, which caused a desorption of excess carbonate anions to favour the creation of a hydrated layer from the bulk solution on the surface of the NPs. Thus, the dialysis phase was useful for the removal of carbonate residues.

For the CaP_PAH sample, the carbonate band at 1427-1490 cm^{-1} was very intense as soon as the NPs precipitated; however, following dialysis, the peak assumed a much lower intensity in support of the PAH polymer deposition on the surface of the CaPs (NH_3^+ deformation vibration and N-H bending groups between 1480 and 1600 cm^{-1}).

Furthermore, due to the deposition of PAH, the region below 1000 cm^{-1} showed a more homogenous and peak-free spectrum following dialysis, eliminating several peaks that were difficult to identify and of low intensity. This emphasised the stabilisation of the particles through the deposition of the polymer on the surface (Urch et al., 2009).

Following dialysis, the peaks of the phosphate groups showed no changes between the coated and uncoated sample. However, the freshly precipitated CaP_PAH showed a splitting of the peak at 1080 cm^{1} belonging to the phosphate group, which was not visible in the CaP sample under the same conditions. Furthermore, this peak showed a lower intensity in absorbance than the CaP sample. This was due to the deposition of the polymer on the surface of the NPs, as PAH had an amine group (C-N stretching) around 1020-1200 cm^{-1}. Following removal of excess polymer by dialysis and after stabilisation of the particles, the phosphate peak appeared again and with a similar intensity to the other samples. Finally, the smooth peaks present between 2950 and 3200 cm^{-1} were associated with the presence of water in the CaP sample, as the samples have not been freeze-dried.

On the other hand, the CaP_PAH samples have been freeze-dried and were analysed in powder form; therefore, this smooth peak can be associated with the deposition of the polymer on the CaP particle as it is rich in amine groups (N-H stretch 3400 cm^{-1}) and C-H stretch groups around 2800 cm^{-1} that made the particle positively charged. In addition, the amine peaks were present before and after dialysis in CaP_PAH sample.

However, the low intensity of the characteristic PAH peaks between 2950 and 3200 cm^{-1} was associated with the limitations of the technology used. In fact, FTIR-ATR allows the analysis of chemical bonds present on the surfaces of NPs from 100 nm to 1 µm. Therefore, FTIR-ATR has a detection range greater than the size of the NPs. An XPS analysis should be conducted to better characterise the outermost layers of the NPs. Otherwise, no significant differences were observed between the CaP and CaP_PAH samples.

Subsequently, the samples were characterised by ζ-Potential analysis. The charge of the solutions used was 40.1 ± 0.5 mV for CH and 35.4 ± 1.2 mV for PAH.

The ζ-Potential of the NPs was verified under the following conditions: precipitated NPs (Only Wash), dialyzed NPs (Before NaCl), NPs in stabilising solution (With NaCl), and 3 and 7 days after their synthesis (Day 3 and Day 7). The results are shown in Tab. 13.

	ζ-Potential ± Standard Deviation [mV]				
Materials	Only Wash	Before NaCl	With NaCl (15 mM)	Day 3	Day 7
CaP	-17.30 ± 0.64	+2.81 ± 0.00	-2,5 ± 0.21	-0.86 ± 0.17	1.86 ± 0.96
CaP_PAH 0.5 mg/mL	32.60 ± 1.19	12.93 ± 1.81	11,07 ± 0.25	9.91 ± 0.78	11.90 ± 0.40
CaP_PAH 1 mg/mL	16.80 ± 0.76	11.90 ± 0.81	13.40 ± 0.32	14.70 ± 0.40	18.38 ± 0.49
CaP_PAH 2.5 mg/mL	17.70 ± 0.40	12.90 ± 0.40	14.60 ± 0.27	13.50 ± 0.25	14.17 ± 0.75
CaP_PAH 5 mg/mL	14.10 ± 2.15	19.60 ± 0.84	13.30 ± 0.21	14.90 ± 0.20	16.10 ± 0.59
CaP_CH 1 mg/mL	11.95 ± 0.36	11.84 ± 2.57	9.57 ± 0.36	11.09 ± 1.71	10.21 ± 1.38
CaP(DOXO)_PAH 1 mg/mL	14.60 ± 0.46	15.60 ± 0.50	/	/	/

Tab. 13: ζ-Potential of the NPs under different conditions.

All particle combinations did not show ζ-Potential higher than +25 mV or less than -25 mV (a value that is often assumed to represent stable particles). So, a 12 h stirring process was necessary to provide better stability to the produced NPs. In agreement with the statements of H. Urch et al. (2009), CaPs showed a net negative charge following their precipitation, due to the presence of CO_3^{2-} groups on the surface of the NPs, as demonstrated by FTIR-ATRs in Fig. 69. This excess negative charge will be critical for the CaP_PAH system. The potential of the CaPs decayed around zero following dialysis, further demonstrating the filtration achieved by dialysis of the NPs, which allowed the removal of excess carbonate (the peak at between 1427-1490 cm^{-1} has a significantly lower intensity). Days later, the charge was stable around zero.

The NPs coated by the cationic polymers always showed positive charge, reflecting the deposition of the coating by electrostatic forces following the almost instantaneous precipitation of the negative CaPs. In general, the surface charge of the coated NPs did not vary significantly following dialysis. Furthermore, the 0.5 mg/mL concentration of PAH was considered as the saturation point of the surface even though the obtained ζ-Potential was significantly lower than the charge of the PAH solution. This was due to the fact that the ζ-Potential of the PAH-coated NPs did not vary significantly as the polymer concentration in solution increased. However, the precautionary concentration of 1 mg/mL PAH in solution was selected for future NPs productions because it was within the saturation values tested. The surface charge of the CaP_PAHs did not change significantly upon immersion of the NPs in NaCl, demonstrating the stability of the charge over days. The NPs encapsulating DOXO showed no difference in terms of charge compared to the CaP_PAH particles.

CH-coated CaPs exhibited very similar results to CaP_PAH in terms of ζ-Potential, both following dialysis and days after their synthesis.

Then, the amount of DOXO encapsulated within the CaP(DOXO)_PAH core was calculated. The results obtained by spectrophotometry showed an efficacy of DOXO encapsulation of 49.7 ± 3.9 % (486.92 ± 38.49 µg) compared with the amount of drug supplied for CaP synthesis (979.37 µg). So, each mg of CaP(DOXO)_PAH encapsulated 4.96 ± 0.39 µg of DOXO.

This result demonstrated that the structure of CaPs is porous which can encapsulate a large amount of drug that will be finely dispersed within the massive matrix of CaPs. In addition, the presence of the coating provided an obstacle to DOXO release during stirring and dialysis steps, allowing only the removal of weakly adsorbed molecules on the surface. Moreover, it cannot be excluded that during the stirring step some drug molecules present in the bulk solution may diffuse within the coating and core of the NPs.

There is a study in the literature by Chao Wu et al. (2017) where they obtained empty CaPs using a Polystyrene template that will be subsequently dissolved in tetrahydrofuran. In this case, DOXO was encapsulated by adsorption equilibrium method, showing an encapsulation efficiency of 80.4 ± 2.2 %. Although this value is significantly higher than that obtained from the CaP(DOXO)_PAHs, it is interesting to note that the core of the CaP(DOXO)_PAHs was not dissolved, still achieving drug encapsulation in high proportions. In addition, the manufacture of CaP(DOXO)_PAH did not involve the use of solvents that are potentially toxic to humans and the environment. As result, the fabrication method of CaP(DOXO)_PAHs appears to be innovative as well as user-friendly.

Moreover, the cumulative DOXO release profile by the CaP(DOXO)_PAH configuration was studied for 28 days, showing a DOXO release of 67.5 ± 2.5 % at day 1 and 91.1 ± 4.6 % at day 7 (Fig. 70A). The release profile was characterized by the burst release effect on day 1 probably due to the diffusion of the drug from the core to the outermost layer during the synthesis phase of NPs. In addition, another cause of accelerated drug release from the carrier may also be due to ionization of DOXO in the medium at pH 7.4 (Daria Kalenichenko et al., 2021).

After day one, drug release appeared to be controlled over time until it stabilized at day seven, suggesting that DOXO is released from the carrier core. From day 7 to day 28, the release profile is characterized by a plateau, indicating the absence of DOXO release. This phenomenon may be due to several aspects, including the possibility that DOXO molecules were trapped within the PEs or that the drug had failed to diffuse from within the core.

To best characterize the burst release, the rate of DOXO release was calculated by plotting the trend line for the first three time points. Next, the trend line (straight line y=mx+q) was calculated from which the slope (i.e., drug release rate) was obtained (Fig. 70B).

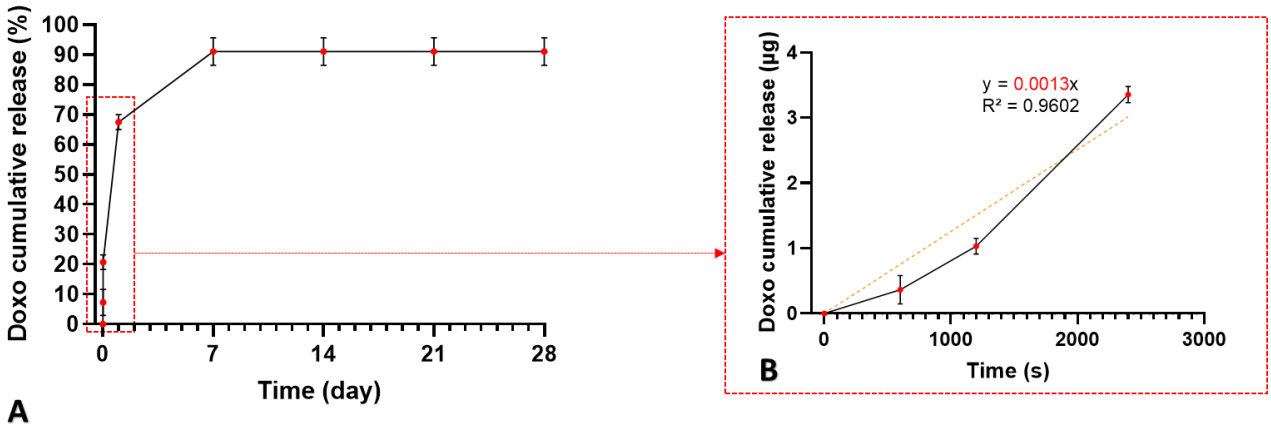

Fig. 70: Cumulative release of DOXO from CaP(DOXO)_PAH (A) and study of burst release rate (B).

3.2.2.2. Morphological characterisation

DLS analyses of the CaPs coated by the cationic polymer and those that encapsulated the drug are shown in Fig. 71.

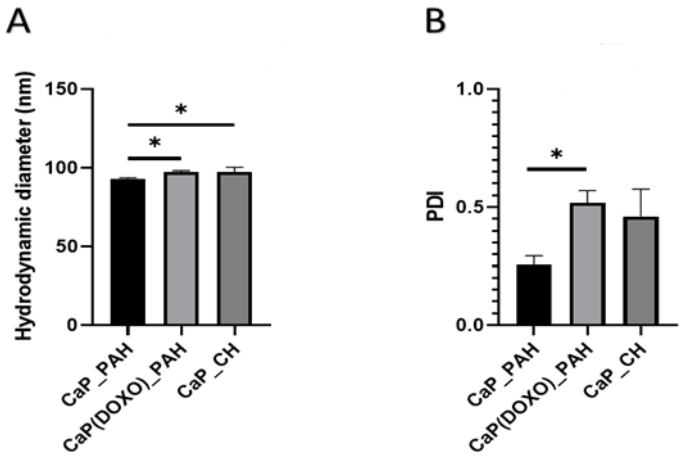

Fig. 71: DLS measurements: hydrodynamic diameter (A) and PDI (B) of CaP_PAH, CaP(DOXO)_PAH and CaP_CH.

The hydrodynamic diameter of CaP_PAH was 92.98 ± 0.64 nm and was associated with the lowest PDI among all the types obtained, which was 0.25 ± 0.04. The value obtained from the PDI indicates that the particles were quite homogeneous in size. This cannot be said for the CaP(DOXO)_PAH and CaP_CH types, as they had a PDI of 0.52 ± 0.05 and 0.42 ± 0.05, respectively.

As for CaP(DOXO)_PAH, their polydispersity was probably caused by the encapsulation of DOXO in the core of NPs, thus it could have modified the crystal structure of the particle leading toward the synthesis of nonhomogeneous particles, but with a hydrodynamic diameter of 97.48 ± 0.67 nm.

CaP(DOXO)_PAH size was statistically different from the CaP_PAH size ($p < 0.05$), so this result further supports the previous hypothesis.

On the other hand, CaP_CHs had a size of 97.55 ± 2.77 nm in diameter with a PDI of 0.42 ± 0.05. The PDI was slightly lower than that of CaP(DOXO)_PAH, however, the value taken was indicative of polydispersity. Furthermore, the PDI of CaP_CH was not statistically different from that obtained with CaP_PAH due to the high value of the standard deviation. However, the hydrodynamic diameter of these NPs was statistically different from that obtained with CaP_PAHs ($p < 0.05$). The explanation for this result could have been the different complexation of CH with negative CaPs compared with the more stable complexation of PAH with CaPs.

To better understand the results obtained, the above structures were observed by TEM analysis, as shown in Fig. 72.

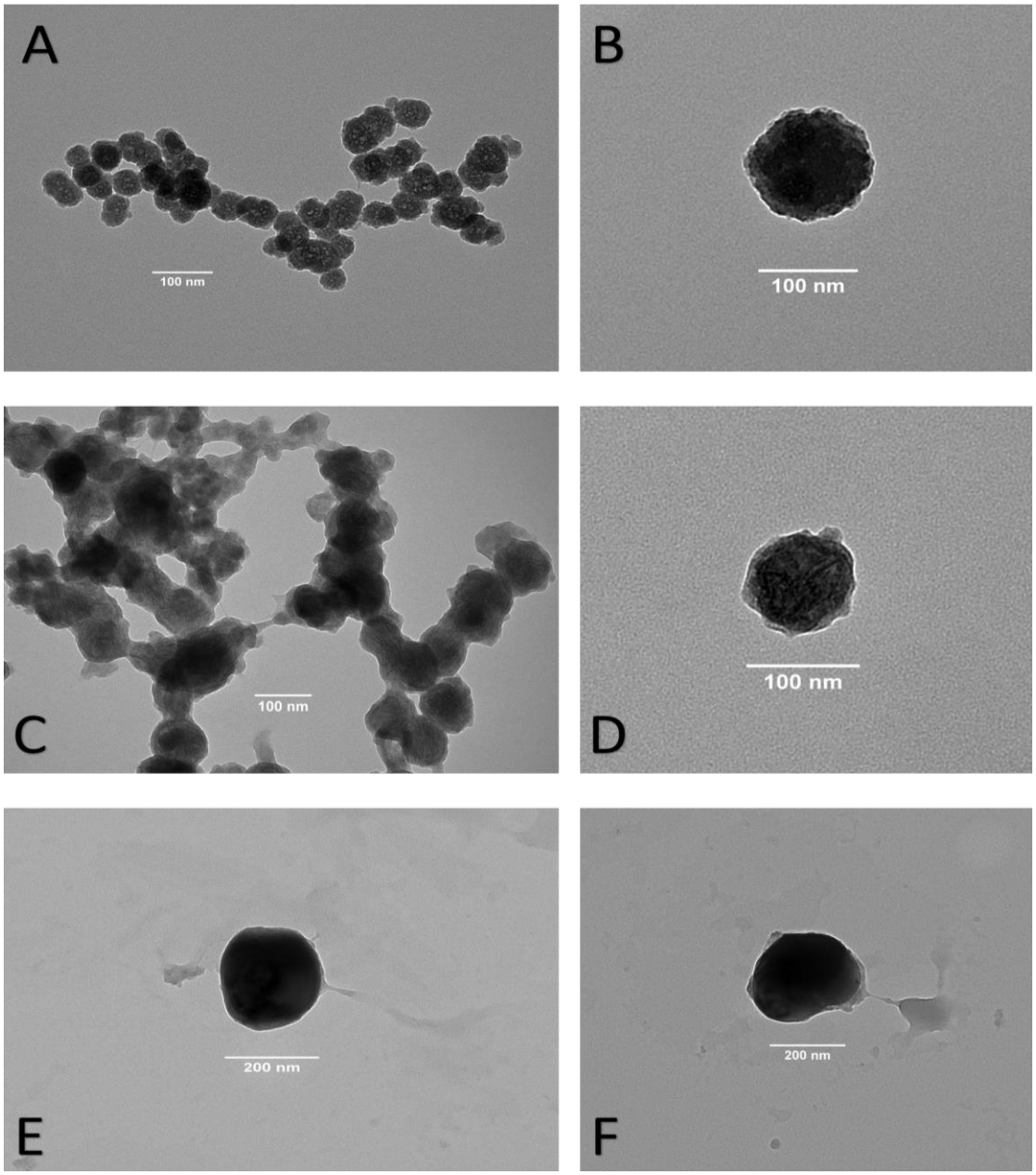

Fig. 72: TEM analysis of CaP_PAH (A-B), CaP(DOXO)_PAH (C-D) and CaP_CH (E-F).

Subsequently, the dimensions of the NPs were also calculated using ImageJ software. The results are shown in Fig. 73.

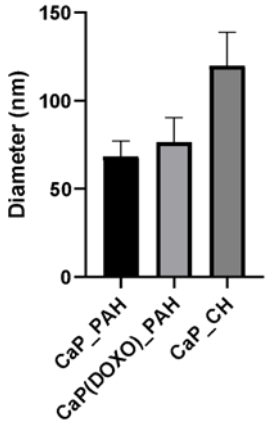

Fig. 73: TEM measurements of CaP_PAH, CaP(DOXO)_PAH and CaP_CH.

The sizes of NPs obtained by TEM analysis of CaP_PAHs (without and with DOXO) were smaller than the diameter obtained from DLS measurements and were 68.48 ± 8.81 nm and 76.60 ± 13.88 nm, respectively. This could be attributed to the DLS method because the intensity of scattered light is proportional to the sixth power of the size of the droplets in which NPs are dispersed, so the dynamic light scattering is overdependent on larger size fractions (Daria Kalenichenko et al., 2021). Another plausible explanation is that measurements made with ImageJ on images obtained through TEM are operator dependent.

An increase in the size of NPs can be seen as a function of DOXO encapsulation in the core. However, the measurements made on the CaP_PAH and CaP(DOXO)_PAH types through TEM are not statistically different due to the high standard deviations of the CaP(DOXO)_PAH samples. Thus, the high standard deviations of CaP(DOXO)_PAH are indicative of a marked polydispersity in size.

In terms of morphology, the PAH-coated NPs types showed a uniform, spherical and rough shape. The latter feature testified to the successful deposition of the cationic polymer.

Moreover, visually, CaP_PAH and CaP(DOXO)_PAH showed no differences in terms of the NPs amount present on the grid and in terms of morphology. On the other hand, the CaP_CH type had NPs with non-uniform, non-spherical morphologies, and sizes close to 130 nm. In addition, the amount of CaP_CH present on the copper grid was visibly lower than in the PAH-coated samples, although the microliters of NPs solution deposited on the grid were the same.

From this analysis, it was possible to deduce that the synthesis process of CaP_CH was not optimized. As mentioned above, CH definitely had a different interaction with CaPs than PAH, caused by several factors, including the nature of the polymer. Another factor may be the pH of the CH solution since it was half that of the ammonium phosphate and calcium lactate solutions. Therefore, a pH-shock may have occurred. This

may have caused a more random assembly of the coating and less control over the crystal structure of the calcium phosphates obtained by precipitation (Omar Mekmene et al., 2009; J. F. De Rooij et al., 1984). Furthermore, CaPs are soluble in acids, thus also in the sodium acetate buffer in which the CH was prepared, since it is weakly acidic solution (Amjad Z., Calcium Phosphates in Biological and Industrial Systems, 1998, Springer, Boston, MA). Therefore, this solubility toward the CH solution changed the structure and crystallinity of the CaPs, affecting the morphology of the NPs and the subsequent deposition of the polycations.

As a proof of concept, CaP_CH were synthesized by dissolving the polymer in a sodium acetate buffer solution at pH 6.5. The images obtained by TEM (Fig. 74) showed no morphological improvements over CaP_CHs obtained with a sodium acetate buffer solution at pH 5. This further supported the assumptions made earlier.

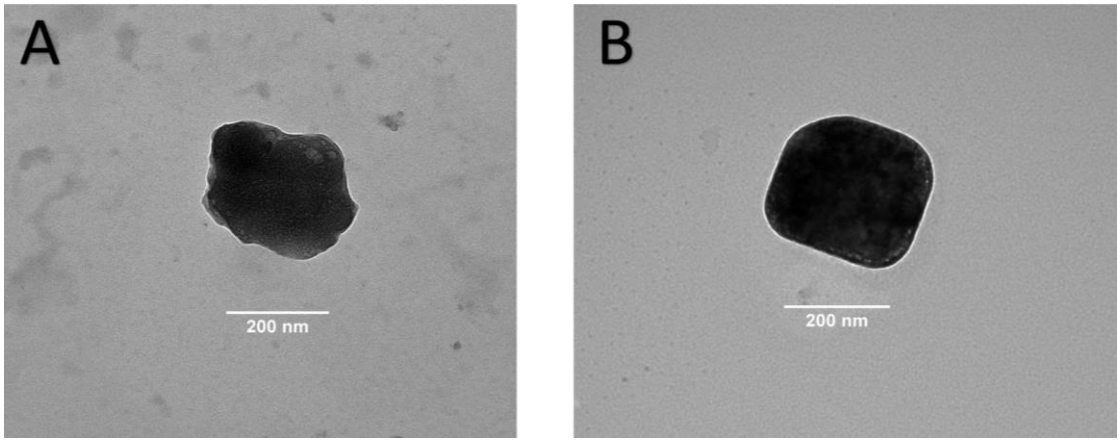

Fig. 74: CaP_CH synthesized by dissolving the polymer in a sodium acetate buffer solution at pH 6.5.

So, PAH deposition by dissolution of the polymer in aqueous solution at pH 10 did not change either the core morphology or the PE deposition, resulting in stable (poorly aggregated), spherical, homogeneous particles and, most importantly, particles less than 100 nm in size. Therefore, depending on the combination of the results obtained, the CaP_PAH and CaP(DOXO)_PAH types were selected as templates for subsequent LbL deposition.

3.2.3. CaP functionalisation

3.2.3.1. LbL with PEs solutions in sodium acetate buffer

To allow the surface functionalization of the NPs, the CaP_PAHs were subjected to a washing step in sodium acetate buffer. By measuring the ζ-Potential of the rinsed NPs, the increase in the surface charge of the CaP_PAHs was noted, obtaining a ζ-Potential of 37.1 ± 1.9 mV.

This may be due to a change in the orientation of the polymer chains due to the ionic strength of the buffer or it may be caused by an increased protonation of the PAH chains following the immersion of the NPs in the buffer solution at pH 5, since the pKa of PAH is 8.92 (Q. Ferreira et al., 2012).

From the TEM analysis, it was found that the core of the NPs had not changed morphology following their immersion in sodium acetate buffer for 15 min (Fig. 75). So, the polymer coating protected the CaP core from brief exposure to sodium acetate buffer.

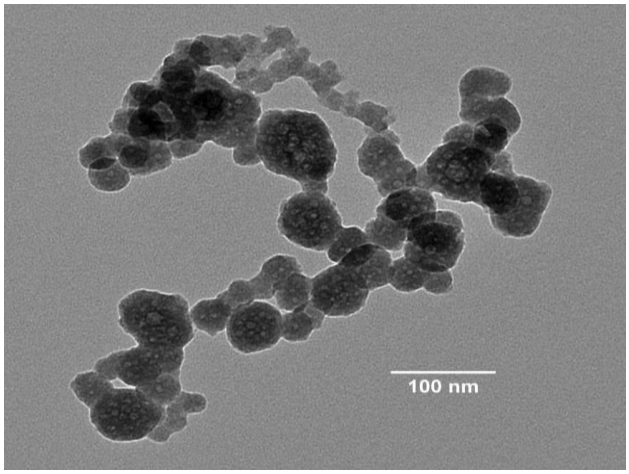

Fig. 75: TEM image of CaP_PAH in sodium acetate buffer for 15 min

Next, functionalization of CaP_PAH and CaP(DOXO)_PAH was conducted by alternating electrostatic deposition of CH and CS or CH/DOXO and CS/GCCQDs, according to the saturation method. The charge of the solutions used was found to be 40.1 ± 0.5 mV for CH and -20.1 ± 2.3 mV for CS.

The addition of the drug in the CH did not change the charge of the solution, since DOXO has a formal charge of zero. Addition of the CQDs to the CS solution slightly changed the ζ-potential, standing at -22.6 ± 2.6 mV. The pH of the solutions remained stable, as shown in Tab. 14.

Solution	**pH**	**Charge (mV)**
Sodium Acetate Buffer	5.00	/
CH in Sodium Acetate Buffer	5.02	40.1 ± 0.5
CH/DOXO in Sodium Acetate Buffer	5.00	39.3 ± 0.3
CS in Sodium Acetate Buffer	5.09	-20.1 ± 2.3
CS/GCCQDs in Sodium Acetate Buffer	4.96	– 22.6 ± 2.6

Tab. 14: pH and charge of PEs in sodium acetate buffer

In the first instance, deposition of CH and CS polyelectrolytes with concentration 1 mg/mL was tested for all layers (Fig. 76A). This type of particles will be named CaP_SAB_7L.

The LbL deposition was characterized by a charge inversion between 49.4 ± 0.6 mV and - 13.0 ± 1.2 mV, however, the saturation of negative layers had not been reached. Therefore, the concentration of CS was increased to 2.5 mg/mL (Fig. 76B). This system will be referred to as CaP_SAB_7L_125.

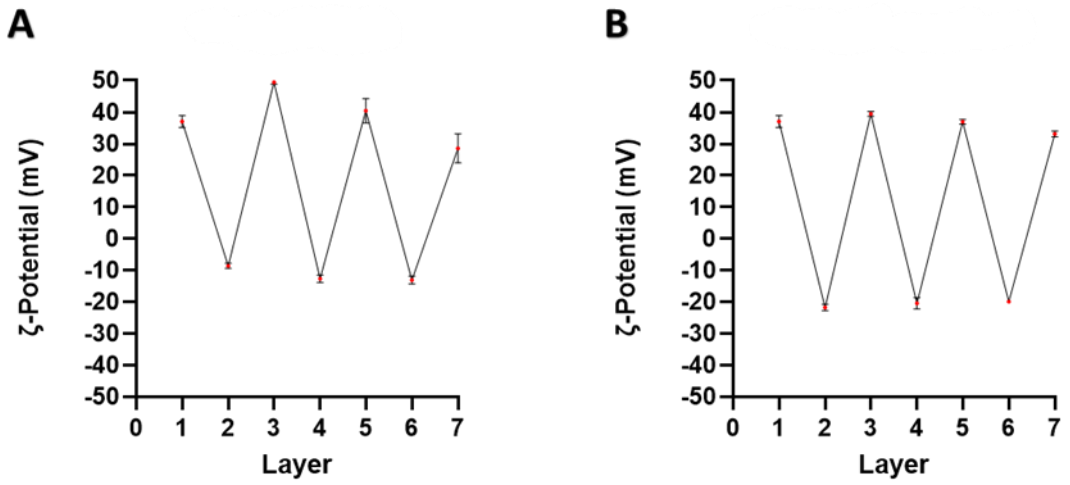

Fig. 76: ζ-potential graph of the LbL of CaP_SAB_7L and CaP_SAB_125 configurations.

Increasing the CS concentration resulted in a charge change between 39.5 ± 0.7 mV and - 20.4 ± 1.7 mV, achieving saturation of all deposited layers. During CH deposition, the NPs showed a positively charged layer with a ζ-Potential > +25 mV. This allowed the NPs to have sufficient surface charge to prevent surrounding similar templates, thus ensuring their stability and the possibility of obviating particle aggregation mechanisms (I.S. Elizarova et al., 2016). However, this was not possible when the CS was deposited in the NPs as they showed a surface charge > -25 mV. So, the deposition phase of the negative layers could exhibit the formation of particle aggregates due to the weak repulsive forces of the NPs.

Finally, the deposition of PEs in combination with the drug (DOXO) and CQDs was tested using 1 mg/mL as the concentration of CH/DOXO for all positive layers, while a concentration of 1 mg/mL was used for the CS/GCCQDs solution for the second layer and 2.5 mg/mL for layers num. 4 and 6 (Fig. 77). These particles will be named as CaP_SAB_7DC.

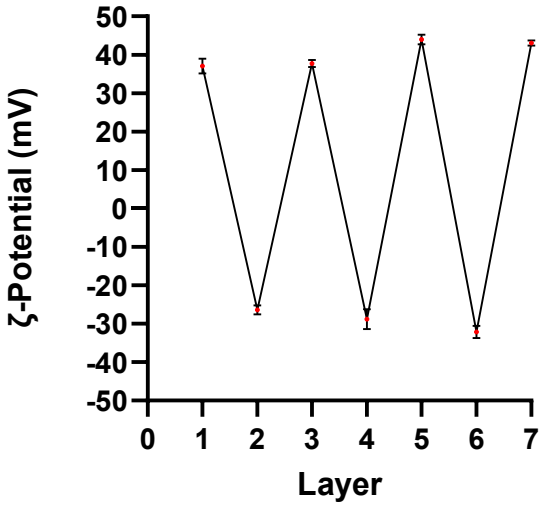

Fig. 77: ζ-potential graph of the LbL of CaP_SAB_7DC.

The phenomenon of overcompensation of layer charge occurred, showing intensity peaks between +44.00 ± 1.25 mV and -32.17 ± 1.59 mV. In addition, each deposited layer showed a surface charge higher than the charge of the deposition solution; therefore, the layers deposited in the NPs were saturated. Finally, all the layers exhibited values > +25 mV (for CH/DOXO layers) or < 25 mV (for CS/GCCQDs layers), so these NPs were particularly stable and obviated the aggregation mechanisms due to the intensity of the charges on the surfaces of the NPs for each deposited layer.

Compared with the CaP_SAB_125 configuration, the encapsulation of CQDs in the negative layers stabilized the polyelectrolyte deposition more, inducing an increase in surface charge and complete saturation of the layers. It is conceivable that the CQDs were in the intra-lattice porosities of the deposited layers, thus providing greater structural stability of the layer than in previous cases. In addition, CQDs also had a net negative charge; therefore, it is possible that they influenced the determination of the net charge of the deposited layer. On the other hand, the addition of DOXO did not affect the deposition of the positive and negative layers in any way, probably due to the small molecular size of the encapsulated drug and their neutral charge.

Next, DLS analysis of the CaP_SAB_7DC samples was performed. The hydrodynamic diameter of this particle type was 110.81 ± 5.91 nm and had a PDI of 0.74 ± 0.02. The increase in particle size testified the successful deposition of the PEs. Indeed, assuming that the growth of the PEs layers is uniform and linear, each deposited layer had a thickness of 2.21 nm. However, the PDI showed high polydispersity of NPs.

In addition, during the layer deposition steps, a progressive loss of materials was visually observed. This could have been due to the poorly optimized deposition method (J. J. Richardson, Bjornmalm and Caruso, 2015) or the infiltration of the sodium acetate buffer through the lattices of the PEs.

To understand the reason for such material loss, it was decided to visualize the CaP_SAB_7DC sample at TEM (Fig. 78).

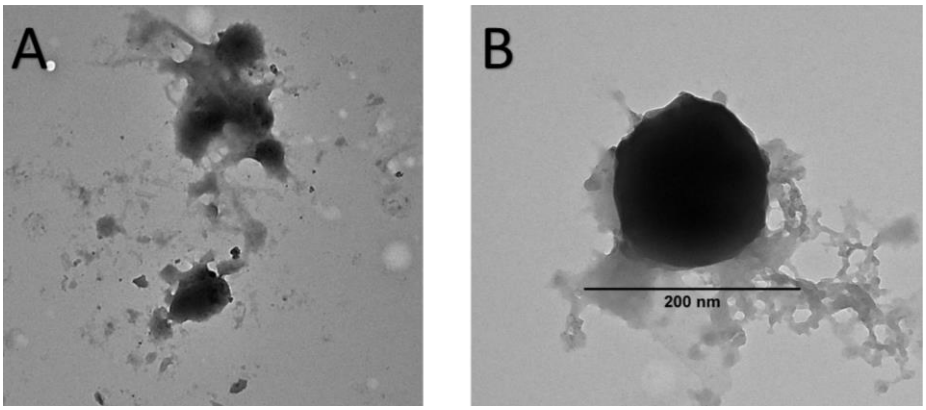

Fig. 78: TEM images of CaP_SAB_7DC

Thanks to TEM analysis, it was found that there was little presence of NPs on the copper grid. In addition, the grids were very dirty, hinting at the possibility of sample dissolution caused by the sodium acetate buffer.
The dimensions of the NPs analysed by TEM were consistent with those obtained from DLS analysis. In fact, a diameter of 139.52 ± 28.70 nm was obtained. In addition, the NPs showed different morphologies (not always spherical), justifying the PDI obtained by DLS analysis.
In addition, the NPs had an opaque black colour, no longer showing the roughness characteristic of CaP_PAH samples. This testified the encapsulation of the CQDs in the layers.
Because of the presence of residual material on the grid and because of the conformational changes to which the NPs were affected, it was decided to qualitatively evaluate the effect of sodium acetate buffer on CaP_SAB_7DC by dispersing the NPs in the buffer for 24 h, without imposing any other stimuli.
After 24 h and following sample collection, a significant decrease in quantity of the NPs could be visually noted (Fig. 79), suggesting that sodium acetate buffer infiltrated within the deposited layers and dissolved the CaP cores (Amjad Z., Calcium Phosphates in Biological and Industrial Systems, 1998, Springer, Boston, MA). So, the deposited coatings do not protect the core from contact with the sodium acetate buffer for long time of exposure. For this reason, this mode of LbL has been not considered anymore in this thesis.

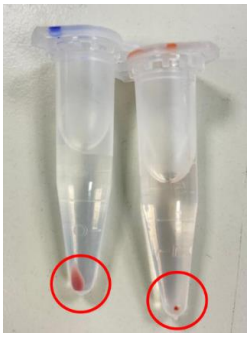

Fig. 79: CaP_SAB_7DC in sodium acetate buffer for 2 h (left) and for 24 h (right).

3.3.3.2. LbL with aqueous solutions of polyelectrolytes

As a solution to the problem induced using sodium acetate buffer, it was decided to use aqueous solution of the same PEs at pH 6. The choice of water as the dispersion solution of the PEs is due to the insolubility of CaPs in that solvent (Amjad Z., Calcium Phosphates in Biological and Industrial Systems, 1998, Springer, Boston, MA). Furthermore, the choice of this pH value is made in relation to the dissociation constants of the polymers used and with the intention of using a pH as close as possible to the physiological pH of the blood. In addition, the choice of this pH value is made in relation to the dissociation constants of the polymers used and with the intention of using a pH as close as possible to the pH sensitivity properties and different drug release profiles under neutral and acidic conditions, representing the physiological pH of blood and the internal pH of cancer cells. In fact, it is necessary for NPs to have a high stability in the physiological pH range, which would avoid non-specific drug release from the particle during circulation in the body (Asail Hendi et al., 2020). This will allow the entire drug mass to be distributed within the acidic cell environment.

Exactly as done in the previous paragraph, to begin the surface functionalization of the NPs, the CaP_PAHs were subjected to a washing step, this time in aqueous solution at pH 6.

By measuring the ζ-Potential of the rinsed NPs, a decrease in the surface charge of CaP_PAH was observed, with a ζ potential of 9.2 ± 0.2 mV. Next, functionalization of CaP_PAH and CaP(DOXO)_PAH was conducted according to the saturation method by electrostatic deposition of PEs dissolved in aqueous solution at pH 6. Tab. 15 shows the ζ-Potentials of the solutions and pH stability as a function of the addition of the drug or CQDs into the PE solution.

Solution	pH	Charge (mV)
H_2O	6.00	/
CH in H_2O	6.01	29.5 ± 2.0
CH/DOXO in H_2O	6.10	24.2 ± 1.8
CS in H_2O	6.03	-17.2 ± 1.9
CS/GCCQDs in H_2O	5.98	-19.5 ± 1.9

Tab. 15: pH and charge of PEs in aqueous solution at pH 6

First, the deposition of CH and CS polyelectrolytes with 1 mg/mL concentration was tested for all layers on the CaP_PAH templates (Fig. 80A). Then, layers of CH/DOXO with concentration 1 mg/mL were deposited, alternating with the deposition of CS (1 mg/mL) (Fig. 80B).

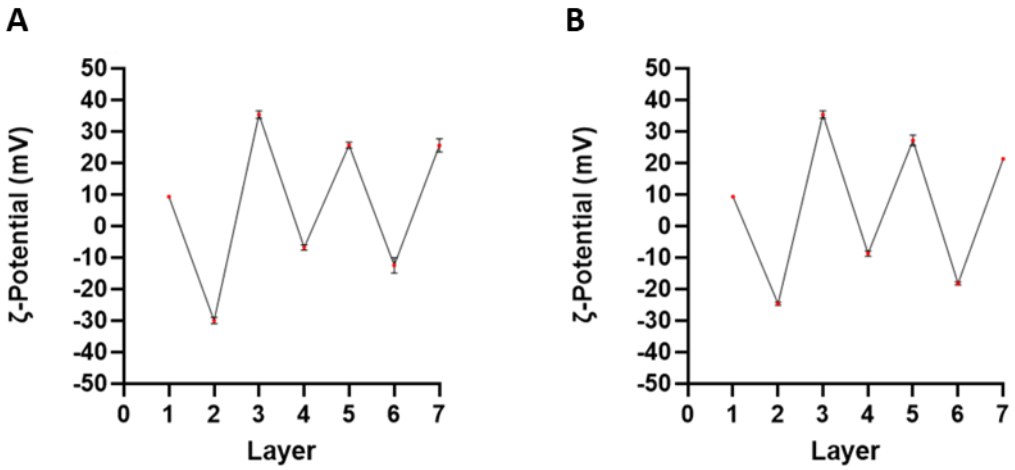

Fig. 80: ζ-potential graph of the LbL of CaP_PAH with CH-CS (A) and CH/DOXO-CS (B).

Finally, the effect of adding the GCCQDs within the anionic layers was also studied. The concentrations of polyelectrolytes remained constant (1 mg/mL). The result is shown in Fig. 81.

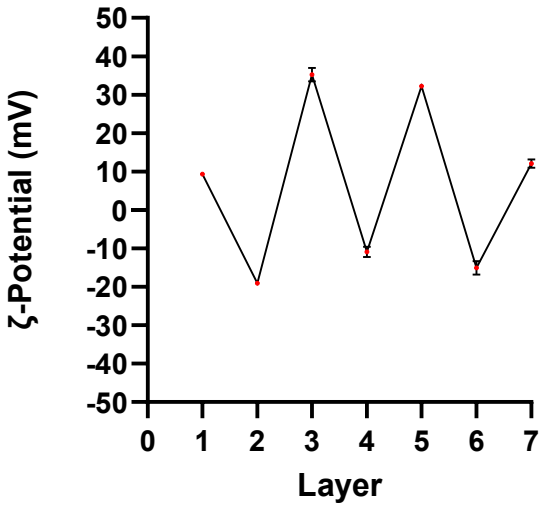

Fig. 81: ζ-potential graph of the LbL of CaP_PAH with CH/DOXO and CS/GCCQDs.

During the creation of multilayers, the deposition of each layer could be visually observed (Fig. 82). In fact, following the deposition of CH or CS the particles showed a white-like color, while after the deposition of CH/DOXO the NPs were characterized by a red-like color (Doxo solution was red). Finally, following the deposition of CH/GCCQDs the particles showed a brown color, given by the surface adsorption of CQDs (the solution of CQDs was brown).

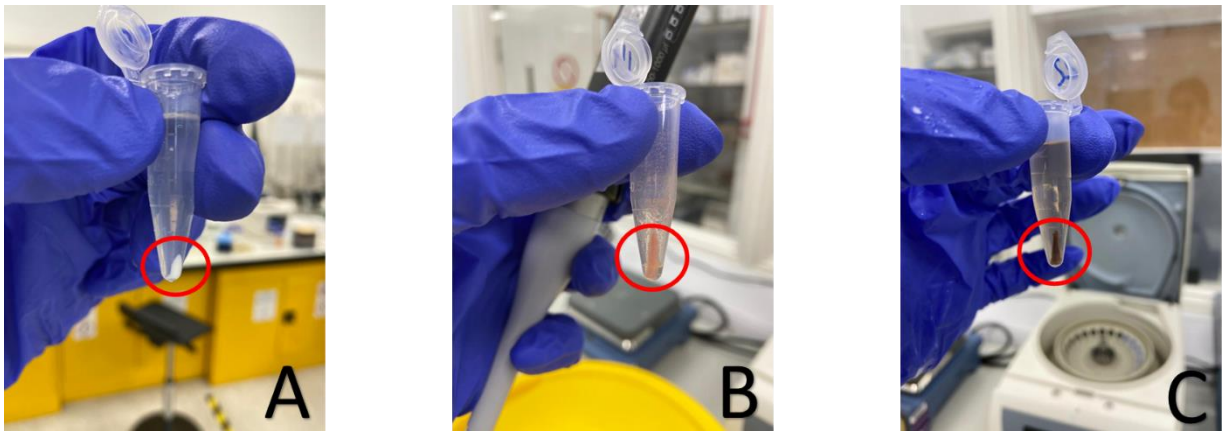

Fig. 82: NPs colour after deposition of CS or CH (A), CH/DOXO (B) and CS/DOXO (C).

In all cases studied, the phenomenon of charge reversal was noted, showing, however, similar nonhomogeneous trends for all configurations studied. Moreover, exactly as happened in the case of LbL with sodium acetate buffer, all CS layers did not show saturation, excluding the second layer belonging to all configurations. Moreover, the last polycation layer was not saturated in any configuration either. So, the saturation method had not been observed. The presence of DOXO and/or CQDs did not improve the deposition in terms of charge.

The lack of surface saturation is due to several factors. Previously, it was found that templates of CaP_PAH suspended in an aqueous solution had a ~31 % decrease in ζ-Potential. This could have been caused by a conformational change of the chains present in the first coating, leading toward a less accessible configuration with less exposure of the charged groups toward the deposition solution (Ana Mateos-Maroto et al. 2021; Guzmán E. et al., 2020). This could had affected the stability of the later deposited layers. However, in terms of charge, this does not seem to be the main cause of the lack of saturation of the subsequent layers. On the other hand, although water and sodium acetate buffer are polar, these can have different degrees of polarity, therefore, the interactions between PEs can be of a different nature (Guzmán E. et al., 2020). In addition, pH plays a key role in layer deposition. Indeed, variation in pH induce changes in the ionic balance and, consequently, affect the degree of ionization of PE chains and the effective charge of the PE (C. Pedeste et al., 2015). Finally, the ionic strength of the solutions is also definitely different and can change the enthalpic and entropic balance during layer deposition depending on the different distribution of ions caused by the diversity of solutions used (Guzmán E. et al., 2020).

Considering the aspects just discussed and the goal of achieving complete saturation of the layers, the concentration of the polyanion was increased to 2.5 mg/mL for CS layers numbers four and six (Fig. 83A). This configuration will be referred to as CaP_7L.

Finally, the insertion of DOXO (Fig. 83B) and then also CQDs (Fig. 84) into the layers deposited on the CaP(DOXO)_PAH particles was evaluated, maintaining the PE concentrations of the CaP_7L configuration. The configuration that includes the deposition of DOXO (CaP_7D) and CQDs will be called CaP_7DC.

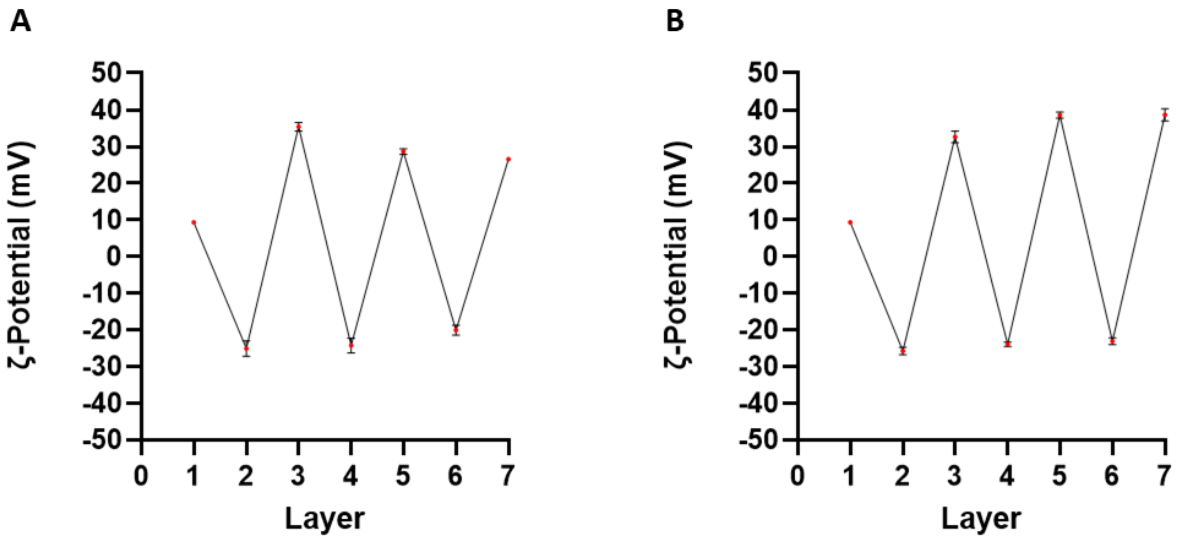

Fig. 83: ζ-potential graph of the LbL of CaP_PAH_7L (A) and CaP_PAH_7D (B).

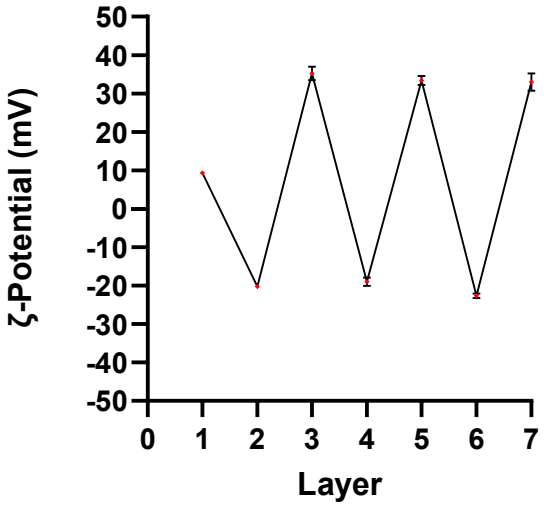

Fig. 84: ζ-potential graph of the LbL of CaP_PAH_7DC.

All types of NPs showed charge reversal and saturation of all layers. In the case of CaP_PAH_7L the ζ-Potential varied between +35.4 ± 1.1 mV and -28.6 ± 0.8 mV, while CaP_PAH_7Ds showed charge reversal between +32.6 ± 1.6 mV and -25.7 ± 1.0 mV. Finally, CaP_PAH_7DCs showed charge overcompensation between +35.2 ± 1.7 mV and -22.6 ± 0.6 mV.

Thus, the failure to saturate layer no. 4 in the configurations involving the deposition of PE with a concentration of 1 mg/mL was the main cause of the lack of saturation of the subsequent layers and the non-uniform course of the zeta potential graphs. This was mainly caused using CS with too low a concentration. Therefore, the use of a concentration of 2.5 mg/mL CS in aqueous solution for layers 4 and 6 achieved the desired results.

DOXO encapsulation did not significantly affect the surface charge of the layers; however, the inclusion of the CQDs provided a more homogeneous trend in terms of charge reversal, probably due to the higher negative charge of the CS/GCCQD solution, and thus the presence of the GCCQDs. The charge of the CH layers was always greater than 25 mV, while a charge of less than -25 mV was reached for almost all the CS layers. So, the NPs had sufficient charge to repel similar templates during the deposition steps, conferring stability to them.

To assess the effective encapsulation of GCQDs in the layers, the CaP_7DC particles were excited with a wavelength of 365 nm (Fig. 85). The NPs solution exhibited blue colour, indicating the actual presence of the dots within the structure.

Fig. 85: Excitation of CaP_PAH_7DC by a wavelength of 365 nm

Following the freeze-dry of the CaP_7L samples and the CaP_7DC particles, the Y (%) of synthesis processes were calculated and stood at 0.9 ± 0.2 % and 1.4 ± 0.2 %, respectively. The amount of particles obtained is significantly low and is mainly caused by a lack of optimisation of the centrifugation and NPs collection process. Indeed, during the centrifugation of the falcon tubes it was noted that the maximum speed of 4.4 rpm of the centrifuge used was not sufficient to totally collect the suspended samples, leading to a massive loss of template and indicating the need for a higher centrifugation speed. However, a higher speed could not be tested due to the absence of equipment suitable for the type of analysis proposed. Furthermore, a small amount of material may had been lost during freeze-drying due to the size of the holes created on the parafilm manually. However, it is pointed out that this possible explanation may have limited the Y(%) to small percentages.

By DLS measurements, CaP_7DC showed a hydrodynamic diameter of 104.67 ± 0.80 nm with a PDI of 0.45 ± 0.04, while the CaP_7L showed a size of 110.81 ± 5.91 nm with a PDI of 0.74 ± 0.02 (Fig. 86).

Although seven layers were deposited on the CaP templates, both types of NPs were just over 100 nm, demonstrating that the coating coatings were in the nanometric size. Assuming the growth mechanism during deposition to be linear, the thickness of each layer was ~3 nm for CaP_7L and ~2 nm for CaP_7DC.

Thus, the thickness value of the CaP_7DC layers allows us to assume that only CQDs with a diameter of less than 3 nm were actually encapsulated by the layers, while larger ones remained in solution. Indeed, morphological analysis of the GCQDs revealed the possibility of the creation of CQDs smaller than 2 nm,

which makes the reasoning consistent. However, further quantitative analysis of the effectiveness of the encapsulation of CQDs through flow-cytometry would be required to confirm this hypothesis.

In addition, the two types of NPs did not present a statistically significant difference in size.

However, the NPs presented a totally different PDI. Both values were objectively high, alluding to the possibility of a morphological difference of the particles, particularly for CaP_7L, which was statistically different from the CaP_7DC type. A possible explanation for this result is defined by the better inter-crosslinking of the deposited layers in the case of CaP_7DC due to the stabilising presence of CQDs in the negative layers.

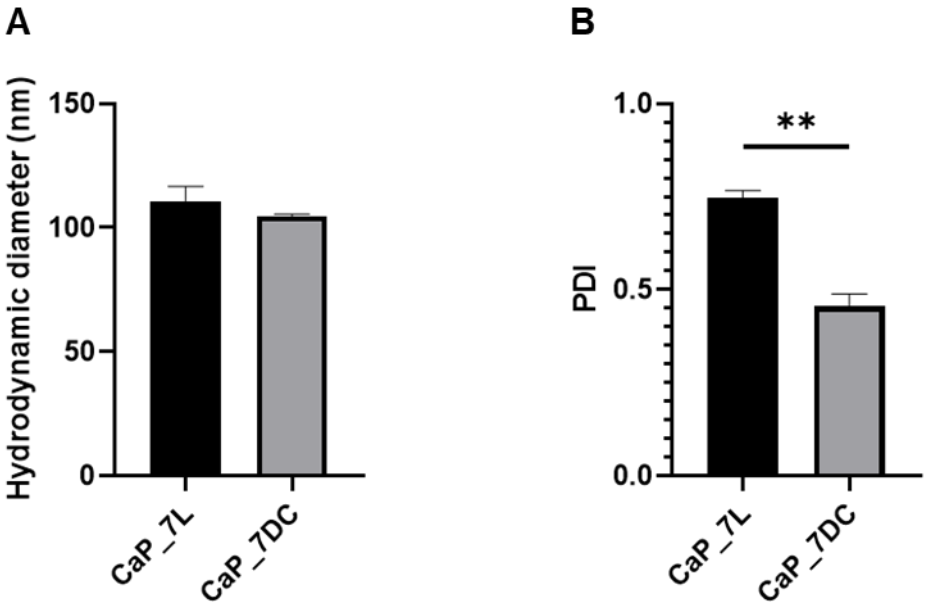

Fig. 86: DLS measurements: hydrodynamic diameter (A) and PDI (B) of CaP_7L and CaP_7DC.

To better understand the result provided by DLS analysis, CaP_7DC and CaP_7L were visualised by TEM analysis, as shown in Fig. 87.

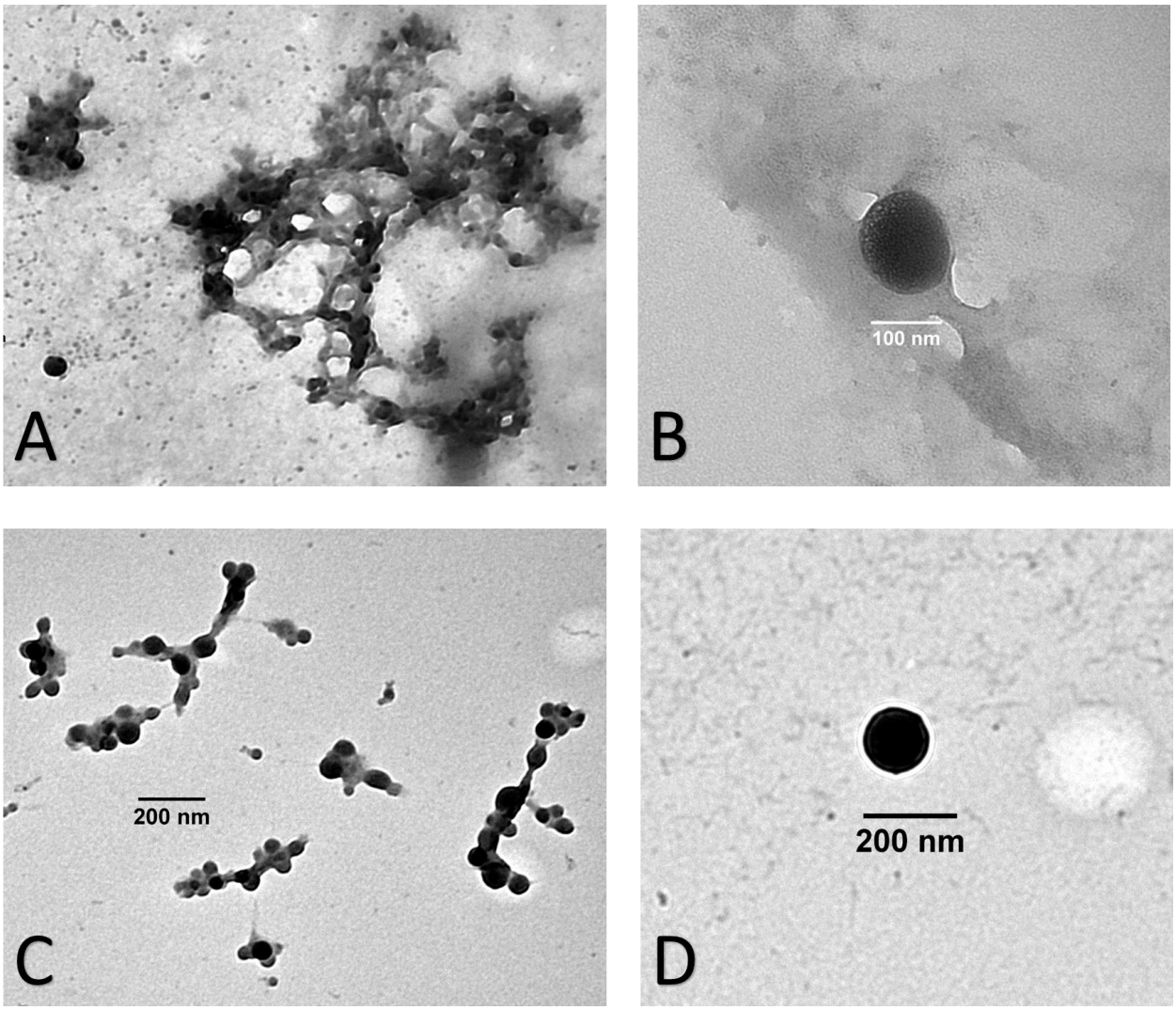

Fig. 87: TEM images of CaP_7L (A-B) and CaP_7DC (C-D).

For both types analysed, a higher presence of NPs could be observed compared to the test performed with CaP_SAB_7L. The particles that encapsulated the CQDs were opaquer than the particles without dots, which were rougher and more faded. This demonstrated the encapsulation of the CQDs by the deposited layers. In the case of CaP_7L, particle aggregates with a different colour could be seen (Fig. A). These aggregates could be due to the poorly efficient centrifugation process that induced the formation of inter-electrolyte complexes during the deposition of one layer and the next (Eduardo Guzmán et al., 2017). The presence of such entities was also appreciated in the CaP_7DC sample, but in smaller size and quantity. This could explain the PDIs obtained from the DLS analysis. Despite the presence of these aggregates, it was possible to note a very high presence of single NPs that presented a spherical and uniform morphology, with dimensions consistent with what was measured at DLS. In fact, the CaP_7L configuration had a size of 123.85 ± 25.37 nm, while the CaP_7DCs had a diameter of 115.79 ± 22.06 nm. Thus, the PDI values resulting from the DLS analysis were affected by the composition of the analysis solution. A serial filtering process through 0.2 µm syringe filters could partially solve this problem, however, the size of these particle aggregates was almost always

below 200 nm. It would be necessary to test a centrifugation speed higher than 4.4 rpm to verify the actual effect of this parameter in creating these aggregates.

Subsequently, the effectiveness of DOXO encapsulation by layers on the CaP_7D and CaP_7DC systems was evaluated (Fig. 88).

In addition, the amount of DOXO released from the core of the NPs during the synthesis process was assessed. For this purpose, six layers of PEs without CQDs and drug were deposited on the CaP(DOXO)_PAH and, for each step (of deposition and washing), the amount of DOXO released from the core of the NPs was quantified. Following the creation of the multilayers, a DOXO release of 45.7 ± 9.3 % (2.69 ± 0.54 µg) was found and this came exclusively from the NPs core. The result obtained indicated the presence of significant diffusion of the drug from the core to the outermost layer during synthesis of the NPs. This was mainly caused by the continuous stresses imposed on the NPs during the numerous stir steps of the deposition and washing solutions, but also due to the numerous centrifugations performed. In fact, the greatest percentage of DOXO release from the core was found following the deposition of the third layer.

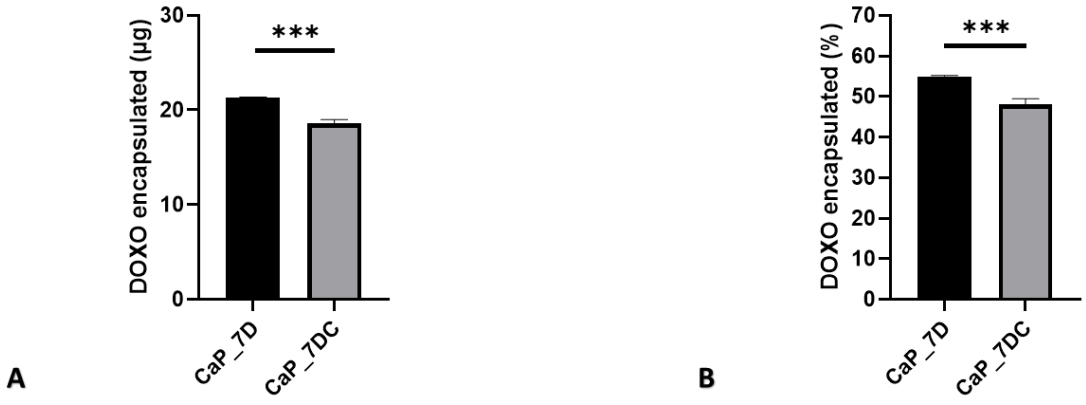

Fig. 88: Efficiency of DOXO encapsulation by layers of CaP_7D and CaP_7DC in different units: µg (A) and percentage (B).

Subsequently, the effectiveness of DOXO encapsulation in the layers of the different particles was evaluated. The effectiveness of DOXO encapsulation in the CaP_7D configuration was 54.9 ± 0.4 %, while CaP_7DC showed an encapsulation of 48.0 ± 1.5 %. There was a significant statistical difference ($p < 0.001$) in the encapsulation of DOXO by layers between the two configurations. This was due to the presence of CQDs in the layers, which could hinder the entrapment of drug molecules within the layers. Furthermore, the lower thickness of the layers in the CaP_7DC configuration certainly played a role in the encapsulation of the drug. In addition, the CQDs nay diffuse during layer deposition (M. Adamczak et al., 2012), as the drug in the CaP_1L6L configuration. Therefore, CQDs can interpenetrate the PEs lattices and can be trapped in the adjacent CH and CS layers, hindering drug encapsulation. Furthermore, due to their negative surface charge and spherical morphology, GCQQDs could favour the complexation of the oppositely charged layer, resulting in less thick CaP_7DC layers than CaP_7Ds. Indeed, the DLS analysis confirmed what has just been proposed;

however, further analysis would be required to better understand the interaction between the PEs, both in the presence and absence of CQDs. Quartz Crystal Microbalance analysis could be useful for this purpose. Interpolating the data obtained on the encapsulation efficiency of DOXO by the layers, the deposition steps allowed an average DOXO entrapment of 70.6 ± 1.1 % for CaP_7D, while for CaP_7DC it was 67.9 ± 1.0 %. Thus, the deposition steps allowed high drug encapsulation through layer deposition.

Furthermore, these data confirmed that the presence of CQDs hindered the entrapment of DOXO molecules by the layers as there is a statistically significant difference between the two encapsulation values obtained ($p < 0.01$). On the other hand, the washing steps removed a fair percentage of drug, especially in the case of CaP_7DC. In fact, two consecutive washing steps had removed 10.2 ± 1.1 % of drug trapped in the layer previously deposited on the CaP_7DC. In contrast, the CaP_7Ds showed a removal of 5.66 ± 1.31 % DOXO. For both types analysed, the first washing step always removed most of the drug that was weakly adsorbed on the surface, in agreement with the technique used (J. J. Richardson, Bjornmalm and Caruso, 2015). Thus, these data further confirmed what has been said about the effects caused by the presence of CQDs in the layers. In conclusion, adding up the amount of DOXO encapsulated in the NP core, CaP_7D encapsulates an amount of 26.22 ± 0.12 µg of DOXO, while CaP_7DC encapsulates a total of 23.53 ± 0.72 µg of DOXO. Finally, the DOXO release profiles from the CaP_7D and CaP_7DC systems in PBS solutions at 37 °C were studied (Fig. 89 A and C). Furthermore, to better characterise the burst release, the release rate of DOXO from the layers was calculated by plotting the trend line for the first three time points. Subsequently, the trend line (straight line y=mx+q) was calculated, then the slope (i.e. the drug release rate) was derived (Fig. 89 B and D).

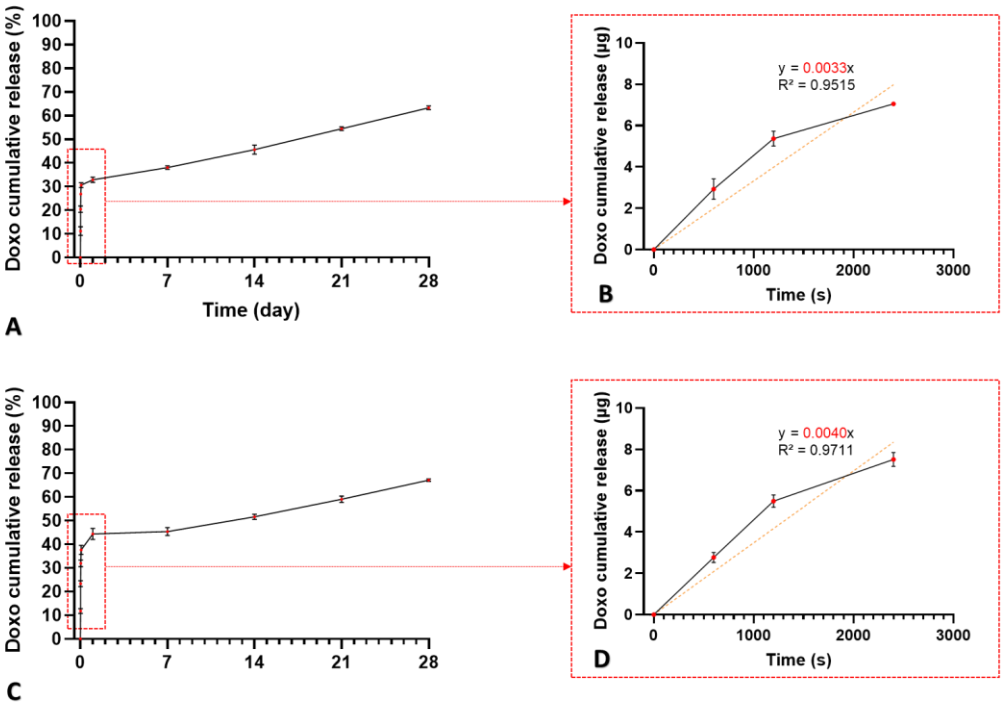

Fig. 89: Doxo cumulative release profiles and the study of burst release rate from CaP_7D (A-B) and CaP_7DC (C-D).

Although CaP_7D encapsulated the drug in the layers and core, and although the largest amount of drug was localised in the outermost shells of the NPs, the burst release was reduced from 67.4 ± 2.5 % to 32.8 ± 1.1 % compared to CaP(DOXO)_PAH by, moving the halved release time from 24 h to 21 days (54.4 ± 0.7 %) by using a LbL technique. A very similar argument applied to CaP_7DC; however, these showed a slightly more pronounced burst release than CaP_7D. In fact, after 24 h the amount of drug released was 44.3 ± 2.3 %, showing a halved release time of 14 days (51.6 ± 1.1 %).

Thus, the proposed systems showed controlled release over time due to the surface coatings present on the NPs. In addition, LbL ensured the stability of the drugs, preventing premature losses.

The degradation mechanisms of NPs cause drug release from NPs. Generally, biodegradable polymers can undergo hydrolytic degradation and erosion processes. The former process is chemical while erosion is a physical process of dissolution and diffusion. Since CH and CS are two hydrophilic components, the degradation mechanism will affect the entire mass as the aqueous solution will be able to penetrate the structure of the material leading to simultaneous surface and internal degradation (Lindsay N. Woodard e Melissa A. Grunlan, 2018). This type of degradation is characterised by the preservation of the shape and weight of the NPs, but the internal molecular weight decreases until the mechanical properties of the particles are driven to collapse. Usually, acid degradation products are generated inside and outside the NPs during bulk degradation. Products present on the surface will be readily removed from the NPs, while those in the interior will accumulate so the internal pH of the structure tends to decrease catalysing the hydrolysis of carbonyl bonds, accelerating drug release (Lindsay N. Woodard e Melissa A. Grunlan, 2018).

Furthermore, drug release is also influenced by its solubility and its localisation within the particle.

In fact, when NPs come into contact with aqueous body fluid (in this case PBS), it penetrates the system and dissolve the drug, starting with the outermost layers of the system and progressing to the innermost over time. The dissolved portion of the drug is then available for diffusion. Therefore, the dissolved and undissolved drug coexist within the matrix during drug release. Thus, upon penetration of water into the system, drug release initially occurs only from the outermost layers of the system (Juergen Siepmann and Florence Siepmann, 2011). Therefore, the drug from the adjacent, innermost layers will only be released when the excess drug in the outermost layer is completely exhausted (Juergen Siepmann and Florence Siepmann, 2011).

Although *in vitro* studies demonstrated controlled release, they still presented an undesirable initial drug release profile for both DOXO-loaded NPs. The burst release of CaP_7DC was more intense than that of CaP_7D, as shown by the values of the drug release rates obtained from the two systems, which were 0.004 and 0.0033, respectively. Both values obtained are significantly higher than that obtained with CaP(DOXO)_PAH (0.0013). This was due to a higher drug encapsulation in CaP_7D and CaP_7DC than in CaP(DOXO)_PAH. The amount released by the CaP_7DC system after 24 h was statistically different from that released by the system without CQDs ($p < 0.0001$).

Generally, burst release is a phenomenon due to a combination of many factors, including those relating to the conditions of the immersion environment (pH, ionic strength, nature of the solvent, etc.), physical stimuli or stimuli of a biochemical nature. For example, changes in the ionic strength present between the fabrication solution and PBS can induce reversible permeability changes on the NPs shell due to osmotic stress, increasing their swelling, thus promoting the release of counterions and DOXO from within the shells (Guzmán E. et al., 2017). In addition, the ionic force can induce desorption of the outermost layers, triggering an accelerated release of the encapsulated compounds. This can also occur over the long term (Ana Mateos-Maroto et al., 2022). The pH variations present between the fabrication solution and PBS are also crucial as they are closely related to the nature of the interactions present between the PEs. Furthermore, CH precipitates by forming a 'gel' at pH above 6.3. Thus, this mechanism could be an explanation for the initial burst release of the drug caused by the rearrangement of the CH polymer chains, and the subsequent controlled and slowed release of DOXO over time (Guzmán E. et al., 2017). The polarity and salinity of the dispersion solvent can also favour the release of a capsule load, either by modifying the porosity of the envelope or by initiating a process of surface erosion of the capsule that allows the release of the encapsulated compounds (Guzmán E. et al., 2020). Among the physical stimuli that most determine accelerated drug release is temperature. Indeed, an increase in temperature (from room temperature to 37 °C) causes the reorganisation of the layers and their partial dehydration, which changes the permeability and release profile (Ana Mateos-Maroto et al., 2021).

Furthermore, the use of mechanical deformation and tension can also be used to trigger release from LbL capsules, as it affects their stability, inducing capsule rupture. Therefore, the use of centrifuges and repeated ultrasound baths may have affected the drug release from the particles (Guzmán E. et al., 2017).

As for the statistically significant difference between the amount of DOXO released after 24 h by the CaP_7DC system compared to CaP_7D, this was probably caused by the presence of the dots within the layers. Due to the changes induced by changes in pH, ionic strength, salinity and temperature, the dots were able to diffuse through the deposited PEs lattices, thus creating an easier pathway for the drug molecules as they are smaller in size than the CQDs. However, the statistical difference in drug release between the two systems decreased as days passed until it was no longer present at day 28 (p-value= 0.0765). In fact, at day 14 the p-value was less than 0.01, while at day 21 it was less than 0.05.

The total amount of drug released by CaP_7DC at day 28 was 15.78 ± 0.13 µg (67.0 ± 0.5 %), while that of CaP_7D was 16.59 ± 0.20 µg (63.2 ± 0.7 %). Therefore, both types did not release the entirety of the encapsulated drug despite 28 days of soaking in PBS. These trends and the absence of statistically significant differences at day 28 could be due to a rearrangement of the deposited PEs over time as a function of the stimuli present in solution. Importantly, the DOXO release curves never reached the plateau for the CaP_7D and CaP_7DD configurations, testifying to a continuous diffusion process of the drug even weeks apart.

Furthermore, it would have been interesting to study the release profile of DOXO by NPs under more acidic pH conditions (e.g. pH 5) that simulate the pH of tumours. Indeed, under such acidic conditions, NPs should have a less controlled and more rapid drug release than those obtained at pH 7.4.

Moreover, in vitro analyses are quite limiting as they do not present physical stimuli, cells, enzymes that can effectively simulate the degradation and stimulation mechanisms of NPs as they circulate in the body.

3.2.3.3. Cytotoxicity Evaluation of CaP

Incubation of Saos-2 and U2OS with CaP_7DC, CaP_7L blank and free Doxo was done to test the cytotoxicity of the NPs after 24 h of seeding. For both cell types treated with CaP_7L, no alteration in metabolic activity was induced compared to the untreated control (Fig. 90). As the CaP_7L concentration increased, a very slight decrease in cell viability is observed for both cell types, especially for U2OS when seeded with a NPs concentration of 500 µg/mL (94.7 ± 3.9%).

However, these decreases in metabolic activity were not statistically different from concentrations of 250 µg/mL. Furthermore, the 500 µg/mL concentration is quite extreme.

The slight decrease in viability rate may be due to the toxic effect of CH on osteosarcoma cells. Parisa Maleki Dana et al. 2020 reported that pure CH and combinations of CH with other compounds are effective against certain cancer cell lines, including osteosarcoma cells, exerting anti-tumour roles such as inhibition of proliferation, induction of apoptosis exerting anti-oxidative activities and suppressing metastasis through the involvement of mitochondrial pathways, inhibition of Exh2 expression (as evidenced by the reduction of membrane potential), cytochrome c release and G0/G1 cell cycle arrest.

Thus, the high presence of positively charged particles may have destabilised the membrane potential of the cells, leading some of them to death. However, CH alone is not able to inhibit osteosarcoma cell activity, as the assay also showed.

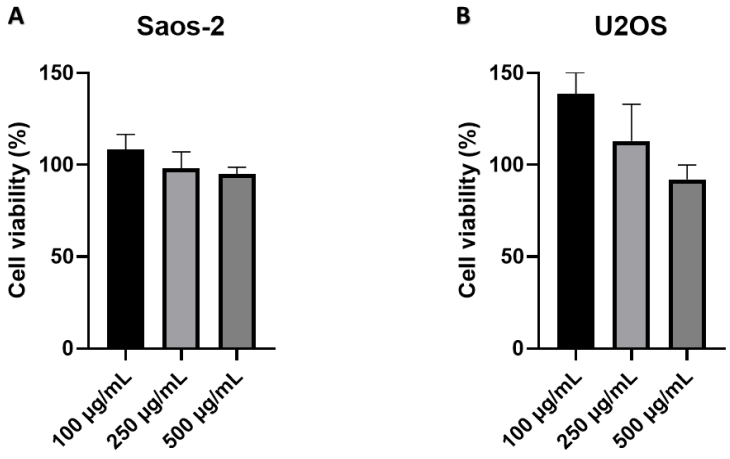

Fig. 90: PrestoBlue assay of Saos-2 (A) and U2OS (B) seeded with CaP_7L.

Cells incubated with CaP_7DC showed different results for the two cell types tested (Fig. 91). Both cell types had a decreasing trend in metabolic activity as the concentration of the tested NPs increased. This evidenced that the NPs had a positive effect on cancer cells, confirming the therapeutic efficacy of these NPs by exploiting the EPR effect of cancer cells.

Starting with Saos-2 cells, a net decay in cell viability was observed from the lowest tested concentration of CaP_7DC, which was 5 µg/mL, exhibiting a rate of 54.9 ± 1.5 %. For CaP_7DC concentrations above 10 µg/mL, Saos-2 showed a survival rate that was half that of the control (48.5 ± 4.6 %). This result is crucial because at low concentrations there was significant treatment efficacy. Furthermore, an almost complete absence of metabolic activity was noted for Saos-2 cells treated with a concentration of 250 and 500 µg/mL CaP_7DC, resulting in a cell viability of 7.4 ± 3.6 % and 1.7 ± 2.9 %, respectively. Between the latter two concentrations, there was no statistically significant difference in terms of treatment efficacy. However, these two concentrations are very extreme and, therefore, not suitable for clinical applications.

U2O2 cells exhibited a higher survival rate than Saos-2 cells tested with the same CaP_7DC concentrations. The metabolic activity of the U2OS cells was less than 50 % only at the extreme concentration of 500 µg/mL CaP_7DC, showing a survival rate of 35.3 ± 4.1 % and a statistically significant difference to the 250 µg/mL concentration of CaP_7DC (p-value < 0.05). At lower concentrations, metabolic activity was between 60 and 100 % compared to the untreated control, especially at concentrations of 5 and 10 µg/mL CaP_7DC. The 100 µg/mL concentration of CaP_7DC showed a metabolic activity rate of 67.9 ± 3.3 % compared to the control.

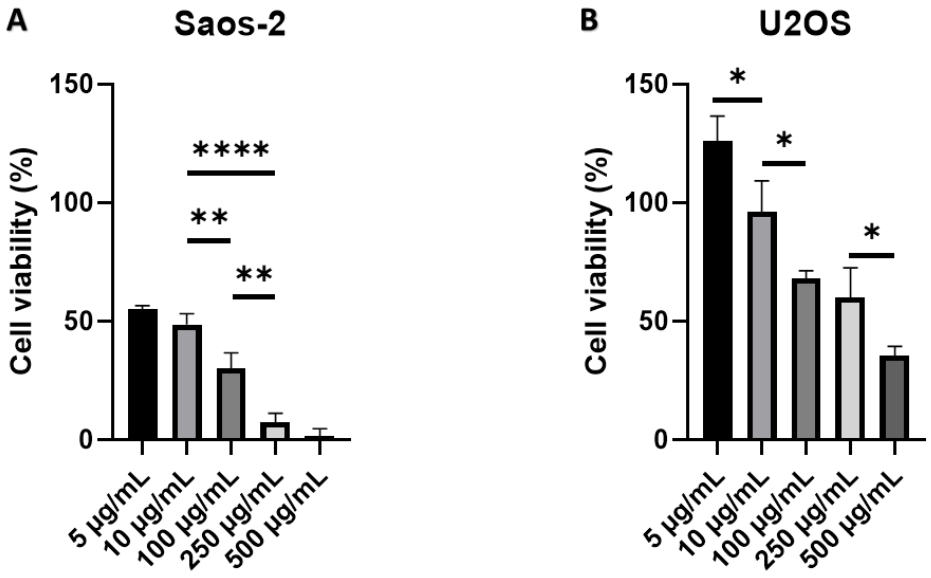

Fig. 91: PrestoBlue assay of Saos-2 (A) and U2OS (B) seeded with CaP_7DC.

Finally, both cell types tested with the same concentrations of free DOXO show a zero-cell survival rate.

The possible causes for these differences in results between U2OS and Saos-2 are many and are widely discussed and controversial. The higher cell viability rate of U2OS may be caused by the greater proliferative capacity of this cell type compared to Saos-2 (Christoph Pautke et al., 2004). Therefore, it was possible that the ratio of the number of NPs to the number of cells seeded in the wells was disproportionate, thus not allowing a net effect to be visualised in the cells analysed.

Moreover, the two types of cells tested are quite different from each other. In fact, the Saos-2 cells show the more mature osteoblastic phenotype, whereas the U2OS cell line is classified as fibroblastic (Christoph Pautke et al., 2004). Furthermore, Saos-2 cells are characterised by a p53-null-type mutation, whereas U2OS show a p53-wild type. Thus, these two cell types have different mechanisms of resistance to DOXO.

It is known that DOXO is a chemotherapeutic agent that activates p53 to induce apoptosis. In fact, according to Yifu Sun et al. (2016), the type of tumour suppressor p53 plays a critical role in the cytotoxicity of anticancer agents.

Regarding U2OS, DOXO was able to induce TGF-β/Smad3 signal transduction, leading to apoptosis. Furthermore, upregulation of Bax and downregulation of Bcl-2 in U2OS cells are believed to be mediated by transcriptional regulation by wild-type p53 (W.P Tsang et al., 2003). On the other hand, in cells that possessed p53-null, the pro-apoptotic effect of doxorubicin was profoundly reduced, showing less Smad3 activity in response to TGF-β1 stimulation, suggesting that apoptosis is dependent only on possible p53 mutations (as in Saos-2).

However, there are two mechanisms by which DOXO acts in the cancer cell: intercalation into the cellular DNA resulting in the disruption of DNA repair mediated by topoisomerase-II (which has just been discussed), and alternatively, the oxidation of DOXO to semiquinone (an unstable metabolite), which is converted back to DOXO in a process that releases reactive oxygen species (ROS) that can lead to mitochondria damage, lipid peroxidation and membrane damage, DNA damage and oxidative stress in a manner that triggers apoptotic pathways of cell death (Thorn et al. , 2011). The actual role of DOXO in inhibiting cancer cell proliferation is openly debated in the literature. Lately, researchers have moved towards demonstrating that apoptosis can be induced by DOXO mainly through p53-independent pathways.

W. P. Tsang et al. (2003) treated p53-null Saos-2 cells with DOXO at a concentration of 100 nM and found that DOXO increased intracellular levels of hydrogen peroxide and superoxide, inducing mitochondrial membrane depolarisation, cytochrome c release, caspase-3 activation, and finally cell apoptosis. In addition, DOXO treatment also increased Bax levels and reduced Bcl-2 levels in cells. Therefore, the results of the present study suggest that ROS can act as signal molecules for DOXO-induced cell death and that the process is totally independent of p53. Furthermore, the longer the incubation time of DOXO, the greater the accumulation of ROS in the cells.

A similar study was also done on wild-type U2OS by Seung Han Shin et al. (2016), that reports that ROS are known to mediate DOXO-induced apoptosis and are the main cause of DOXO toxicity to cancer cells. The

results showed that the oxidative stress on U2OS induced by the amount of ROS produced by DOXO is dose dependent. Furthermore, for low doses of DOXO (< 500 nM) and for timescales of less than 48 h, the ROS produced by DOXO promoted the survival of tumour cells and their invasiveness, through the induction of MMP-9. In contrast, for high concentrations of DOXO (> 500 nM) and after 48 h, high levels of ROS inhibited U2OS tumour cell growth. These data indicated that dose and timing were important factors for the antitumour effect of DOXO. Thus that, DOXO-induced apoptosis via p53-independent pathways would justify the results obtained with the PrestoBlue assay, in view of the greater sensitivity of Saos-2 to ROS than U2OS. However, in cell cultures seeded with CaP_7DC, the ROS values produced were not tested.

Therefore, it would be necessary to verify the levels of ROS production to validate what has just been discussed. Furthermore, to restore low levels of ROS induced by DOXO, osteosarcoma cells may have protective detoxification mechanisms consisting of detoxification enzymes (e.g. glutathione-S-transferase P1-1) that are responsible for drug inactivation (Louise Marchandet et al., 2021). However, this type of drug resistance has not been studied for Saos-2 and U2OS types.

In literature, there is a study by Jennifer Adamski et al. (2013) where the correlation between the tumour hypoxic environment and the drug resistance of osteosarcoma cells was assessed. Indeed, significant hypoxia-induced drug resistance was found in the U2OS cell line that significantly reduced cell apoptosis. This was because hypoxia had attenuated drug-induced p53 activation in U2OS cells. However, the mechanisms inducing the hypoxia-induced resistance are unknown and do not depend on stabilisation of HIF-1α, overexpression of phosphoinositide 3-kinase (PI3K) or activation of Akt pathways in osteosarcoma cells. Therefore, further work is needed to identify a target pathway on which hypoxia-induced drug resistance in osteosarcoma depends.

Contrary to what has just been stated, A. Galembikova and S.V. Boichuk (2021) claimed that osteosarcoma cells showed activation of the AKT signalling pathway following treatment of the cells with DOXO. In particular, the expression of the phosphorylated form of Akt in Saos-2 cells was found to be less pronounced than in U2OS cells, allowing U2OS cells to survive longer than Saos-2 cells. Thus, this would corroborate the results obtained with PrestoBlue.

Finally, cancer cells can sometimes resist chemotherapeutic treatment by enhancing the DNA repair pathway through the potential of the BER mechanism and upregulation of the apurin endonuclease enzyme APE-1 (Louise Marchandet et al., 2021). It is possible that U2OS have an enhanced BER mechanism associated with the upregulation of APE-1, which would allow for increased drug resistance against DOXO. This would also explain the results obtained by the Prestoblue assay; however, this type of drug resistance has not been documented for Saos-2 and U2OS.

Moreover, Live/Dead assay (Fig.) showed the viability (coloured in green) and damage/mortality (coloured in red) of the two cell types following the incubation of CaP_7DC and their blanks after 24 h. For both phenotypes tested, the Live/Dead images showed a climax of red staining as a function of increased CaP_7DC

particle concertation, thus showing consistent, if qualitative, results. This testified the increasing presence of cells showing a rupture of their cell membrane, indicating that the NPs treatment had taken effect and that the NPs were penetrating the cytoplasm. This allowed the ethidium-1 homodimer to penetrate the damaged cells and bind to the nucleic acids, showing red fluorescence. Furthermore, cells with very low metabolic activity were visually less adherent than the controls (CaP_7L and CTRL). This was possible because the apoptotic cells no longer showed plate adhesion receptors and thus floated in the seeding solution. Therefore, these cells were removed during the washing steps with PBS before staining.

The controls showed diffuse and homogeneously distributed cells throughout the substrate. Furthermore, they showed a high rate of proliferation and confluence by both cell types, demonstrating the absence of any contamination and that the experiment was therefore conducted successfully.

The CaP_7L particles showed an exclusively green colouration, due to the presence of intracellular esterases that convert the non-fluorescent and cell-permeable acetoxymethyl calcein into the intensely fluorescent calcein (Fig. 92). Thus, the images confirmed the high biocompatibility of the tested NPs, also showing wells with high degrees of aggregation and spreading by the cells. Consistent with the PrestoBlue analysis, it was possible to see the presence of a few dead cells in the CaP_7L-treated samples.

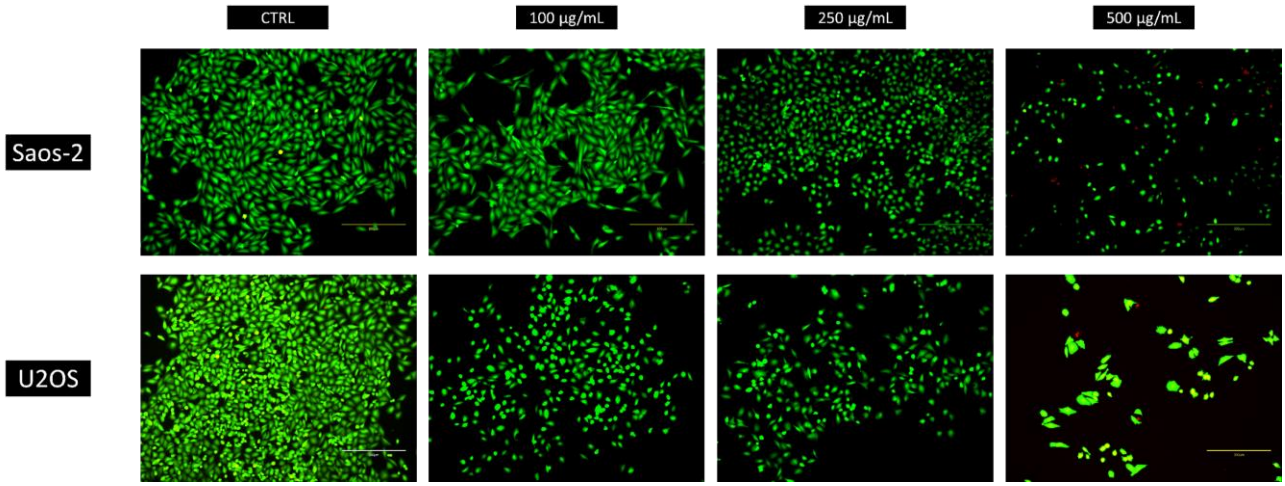

Fig. 92: Live/Dead images of Saos-2 (up) and U2OS (bottom) with or without CaP_7L at different concentrations.

Despite repeated washing of the wells in PBS, some wells still had NPs after the application of the staining. This was visible in some images captured under the microscope, as the NPs interfered in the staining of the red channel, probably due to the sulphates and CQDs present in the CS. This was particularly evident in the images captured for the different concentrations of CaP_7DC (Fig. 93). Concentrations of 250 and 500 µg/mL CaP_7DC showed images rich in dead cells, consistent with the PrestoBlue results. The lower concentrations actually showed green colourations, demonstrating that a proportion of cells had evaded treatment. U2OS showed more live cells than Saos-2 for the same concentrations, with a greater presence of cell aggregates. This further confirmed the results obtained by the PrestoBlue assay.

Furthermore, it must be emphasised that the Saos-2 and U2OS cells that survived the seeding of CaP_7DC were almost exclusively located in the edges of the well. Thus, it was possible that the seeding of the cells had not been performed correctly, thus allowing the cells in the borders to escape CaP_7DC treatment to a greater extent. On the other hand, it was possible that the cancer cells had severed their local adhesion domains expressed by integrins (Xinxin Zhao et al. 2015). Thus, it was possible that the cells had detached from the substrate in which they were adhered and floated to other regions of the substrate. However, Live/Dead staining did not detect the suffering state of these cells.

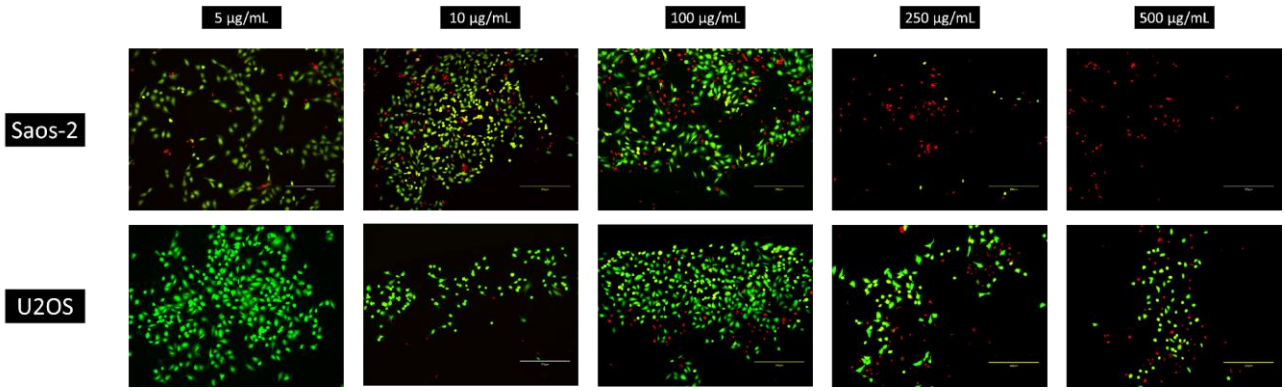

Fig. 93: Live/Dead images of Saos-2 (up) and U2OS (bottom) with CaP_7DC at different concentrations.

Subsequently, immunostaining analysis of the two osteosarcoma cell types was performed following the seeding of the CaP_7DCs and their blanks after 24 h, as shown in Fig. 94 and Fig. 95. This assay allowed staining of the nuclei (blue) and visualisation of the distribution, morphology, and organisation of the cytoskeleton (red) of the osteosarcoma cells. This test confirmed what was visualised with the previous assays.

Briefly, the cytoskeletons of the CaP_7L-treated cells were well elongated, randomly spreading in all directions on the surface of the well, while the nuclei were round and well-defined. These two factors underlined the low cytotoxicity of CaP_7L for the two cell types tested (Xinxin Zhao et al. 2015). Furthermore, no visible changes in terms of morphology were present between the control cells and the CaP_7L-treated samples.

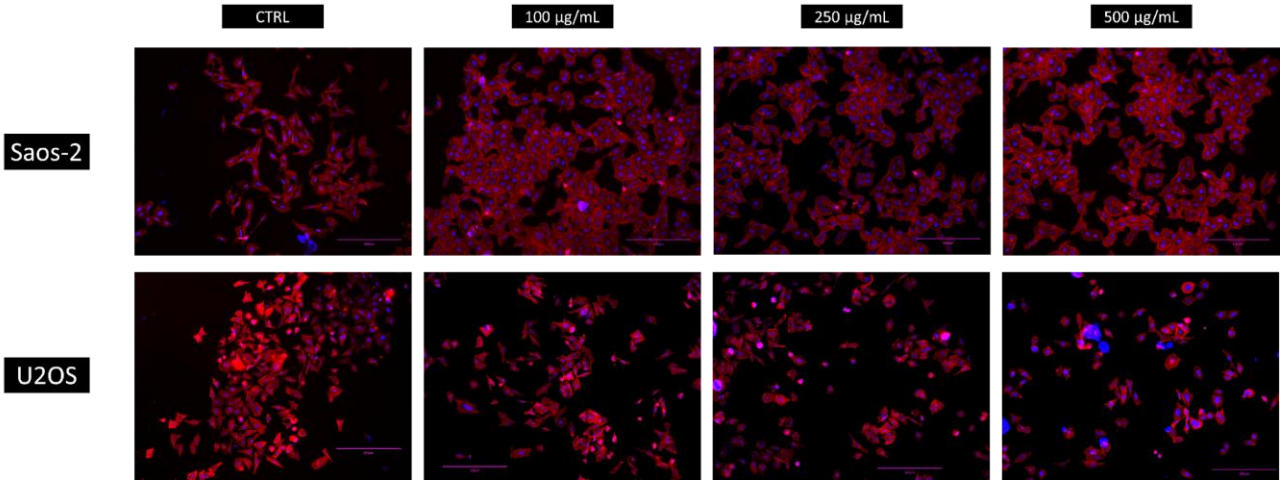

Fig. 94: Immunostaining images of Saos-2 (up) and U2OS (bottom) with and without CaP_7L at different concentrations.

Cells treated with CaP_7L showed a very high percentage of nuclei compared to samples treated with CaP_7DC. This demonstrated the high biocompatibility of CaP_7L and treatment efficiency of CaP_7DC (Xinxin Zhao et al. 2015; E. B. Dolan et al., 2012).

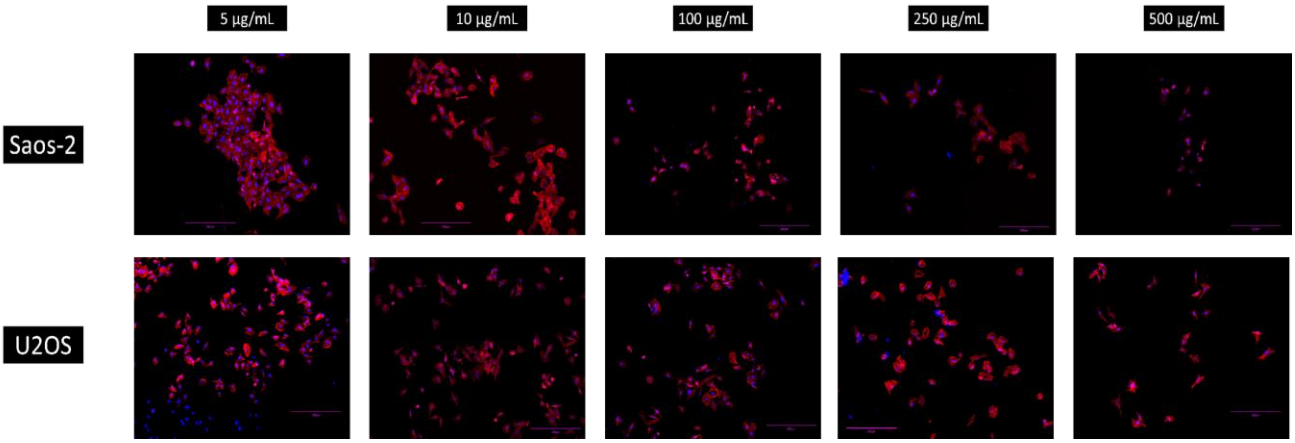

Fig. 95: Immunostaining images of Saos-2 (up) and U2OS (bottom) with CaP_7DC at different concentrations.

Also in this assay, it was possible to visualise that the Saos-2 and U2OS cells that survived the seeding of CaP_7DC at higher concentrations (250 and 500 µg/mL) were almost exclusively located in the edges of the well. Some of these cells showed an elongated and diffuse morphology, especially for the U2OS samples; these were typical features of healthy cells. Other cells, on the other hand, had a small, rounded cytoskeleton that wrapped around the nucleus, and were much smaller in size than their healthy, well-spread counterparts. This suggested the presence of membrane blebbing, characteristic of cell necrosis and apoptosis (E. B. Dolan et al., 2012). Thus, these cells presented a morphology indicative of suffering and imminent death. Furthermore, this morphology was more present in the samples seeded with the highest

CaP_7DC concentrations. This confirmed the previous hypothesis that the cells severed the local adhesion domains expressed by integrins; thus, they floated mainly in the edges of the wells (Xinxin Zhao et al. 2015). Quantitatively, the number of live cells was significantly lower than in the CaP_7L-treated and untreated samples. Furthermore, the number of surviving cells was strongly concentration-dependent, in agreement with what was obtained from the Live/Dead and PrestoBlue assays.

To assess the morphology of the cell and the organisation of its organelles, Saos-2 cells treated with a concentration of 500 µg/mL CaP_7DC were analysed by TEM (Fig. 96). Through these images, it was possible to qualitatively assess the encapsulation of CaP_7DC by Saos-2 cells.

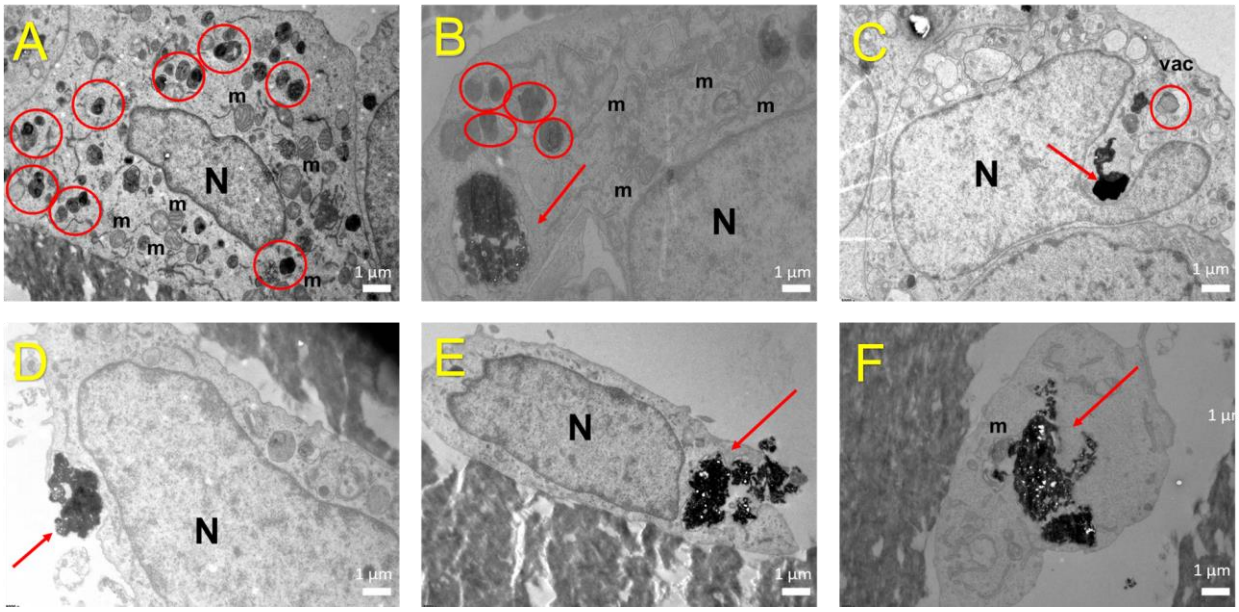

Fig. 96: TEM images of Saos-2 cells treated with a concentration of 500 µg/mL CaP_7DC; Abbreviation list: "N" nucleous; "m" mitochondrion; "vac" vacuole; circle endosomes and lysosomes; Red arrows endosome escape mechanism.

TEM of dissected Saos-2 cells exposed to CaP_7DC for 24 h showed that the particles were internalised. A common feature of particle systems is that they are initially taken up by cells through one or more endocytic mechanisms following their interaction with the cell surface through specific ligand-receptor interactions or through non-specific interactions such as electrostatic and hydrophobic interactions (Siddharth Patel et al., 2019). In the specific case of CaP_7DC, the internalisation of NPs is enabled by electrostatic interactions between the cell membrane and the outer cationic layer of the particles. The mechanisms of internalisation prevent the formation of early endosomes (which have a slightly acidic pH of ~6.3) and gradually mature into late endosomes, during which the luminal pH is progressively lowered to ~5.5 by the proton pumps of the vacuolar ATPase that actively transport protons into the endosome. Finally, the late endosome fuses with the lysosome (pH 4-5) and the intraluminal content is degraded by lysosomal enzymes, allowing the cancer cells to survive treatment (Siddharth Patel et al., 2019). In the case of CaP_7DC, the mechanism of endocytosis could be clearly observed as the particles are clustered in the cytoplasm by localising in the

lysosomes, not reaching the nucleus (Fig. A). This mechanism was visible due to the numerous changes in cell topography as a result of the interaction of CaP_7DC across cell membranes. In fact, visible changes were noted in the conformation of the cell membrane, in the conformation of the nucleus following endocytosis and, in the organisation and number of organelles present in the cytoplasm (Fig. A), indicators of the activation of the endomembrane system (Ekaterina Naumenko et al., 2021). In addition, the lysosomes showed an opaque black colouration caused by the internalisation of CaP_7DC, thus the presence of CQDs.

However, cargo must reach the cytosol, so it is essential that NPs escape the endosomal/lysosomal pathway before being degraded within the lysosome.

Unfortunately, the endosomal escape process is very inefficient (generally believed to be a few percent or less) and is still not fully understood, in fact several hypotheses have been put forward in literature (Dehua Pei and Marina Buyanova, 2019). In the specific case of CaP_7DC, there were three possible mechanisms of escape from endocytosis.

The 'proton sponge' hypothesis is often invoked to explain cytosolic drug delivery via polycations, which have a large buffering capacity close to the physiological pH. When polycation/drug complexes are internalised into early endosomes, it is hypothesised that polyamines prevent endosomal acidification by acting as 'proton sponges' and that, as a result, proton pump ATPases continue to transport protons into endosomes (Dehua Pei and Marina Buyanova, 2019). To balance the charge within the vesicles, chloride ions are also transported into the endosomes, causing osmotic swelling of the endosomes leading to the rupture of their membrane (osmotic lysis) and the release of the endosomal contents into the cytosol (Siddharth Patel et al., 2019). However, this 'proton sponge' hypothesis has been challenged by several experimental observations as not all polymers that buffer in the pH range 5-7 are able to induce endosomal escape and as some of them do not undergo protonation in the pH range 5-7, but can still escape from the endosome (Dehua Pei and Marina Buyanova, 2019).

Due to the inadequacy of the previous hypothesis, membrane destabilisation and/or disruption is increasingly used to describe the endosomal escape of polymeric NPs. Briefly, NPs interact directly with the endosomal luminal membrane through charge-charge and/or hydrophobic interactions, leading to local membrane destabilisation and permeability (Dehua Pei and Marina Buyanova, 2019). However, this mechanism requires NPs to physically move through a lipid bilayer, which is not easy given the size.

Finally, the possible role of NPs in dissolving and collapsing endosomal vesicles through a budding mechanism has recently been discussed in the literature. In this mechanism, NPs selectively bind to the luminal leaflet of the endosomal membrane, inducing membrane curvature and budding of amorphous lipid/peptide aggregate domains containing NPs (Dehua Pei and Marina Buyanova, 2019). These budding vesicles are very unstable and easily disintegrate, resulting in the release of vesicular contents into the cytosol (Sorina Suarasan et al., 2016).

In the case of CaP_7DC, the predominant mechanism of cargo release from endosomes is not known. However, through these slices it was possible to observe the triggering of the mechanism of NPs escape from the more labile pinocytic vesicles (Fig. 96 B-C), allowing drug release to continue within the cytosol and into contact with the cell nucleus (Fig. 96 B-F). This mechanism leads to the distortion and damage of the cell membrane morphology (Fig. 96 B and D-E) and the subsequent disintegration of the cell nucleus, leading to apoptosis or cell necrosis of cancer cells (Fig. 96 C and F) (Virginia Cebrián et al., 2011).

Indeed, TEM images showed some cells undergoing a necrosis-induced death mechanism. This was because the release of the drug into the cytosol which caused swelling of cell organelles (such as the endoplasmic reticulum and mitochondria (Fig. 96 A-B) and resulted in the presence of large vacuoles and subsequent rupture of the plasma membrane (Fig. 96 D-E), with eventual lysis of the cell (Fig. 96 C and F) (Khalid N and Azimpouran M., Necrosis In: StatPearls [Internet], Treasure Island (FL): StatPearls Publishing; 2022).

Regarding the interaction underlying endocytosis, there are several papers in the literature that consider the theory of a cellular interaction driven solely by electrostatic interactions between NPs and the cell membrane to be too simplistic. In fact, Valérie Forest et al. (2015) explains that, once introduced into a biological environment, NPs are surrounded by a wide variety of biomolecules that rapidly adsorb onto the surface and entirely cover the nanomaterial, modifying the original physicochemical characteristics of the nanoparticle, including the surface charge.

Similarly, the composition of the protein corona varies depending on the environment in which the nanoparticles are found. Therefore, some studies show that protein adsorption on nanoparticles decreases their cellular internalisation, while others tend to show the opposite.

In particular, the latter argue that NPs with a greater number of proteins on the surface may have a greater chance of exposing ligands that can recognise membrane receptors and facilitate transmembrane internalisation. Therefore, the conflicting results could be related to different endocytosis pathways.

3.2.4. CQDs multicapsules synthesis

3.2.4.1. Physico-chemical and morphological analysis

In this work, hydrophilic and negatively charged CHBOCQDs carbon dot complexes were used as cores for the formation of fluorescent nanocapsules prepared using the LbL technique and involving the release of two chemotherapeutic drugs (DOXO and DTX). First, a concentration of 0.2 mg/mL negatively charged CHBOCQDs was dissolved in 1 mL of sodium acetate buffer. After centrifugation of the CQDs solution, the supernatant was replaced by 1 mL of CH solution to stabilise the CQDs core by deposition of a polymer coating (CQDs_1L) as described in par. 2.2.2.5. The functional groups present on the surface of CQDs_1L were identified through FTIR-ATR analysis, as shown in Fig. 97.

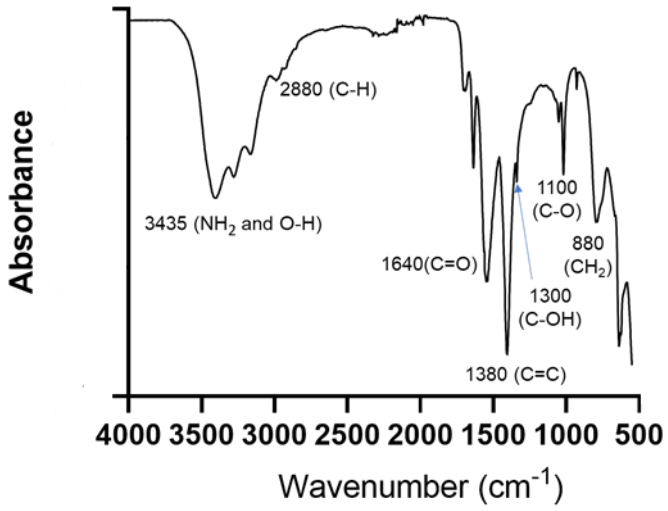

Fig. 97: FTIR-ATR of CQDs_1L.

FTIR-ATR analysis revealed a spectrum characterised by numerous peaks belonging to the CHBOCQDs, including the C-H ~2900 cm^{-1}, C=O ~1600 cm^{-1}, C=C ~ 1300 cm^{-1} and C-O ~ 1100 cm^{-1}. In addition, some of these peaks in CQDs_1L had the negative motifs of CHBOCQDs, which were the C=O and C-H. All this testified to the presence of the CQDs within the NPs. In addition, an NH_2 peak (~3435 cm^{-1}) of moderate intensity was present in this sample. This positive group belonged to CH and testified the deposition of polycation on the CQDs.

To verify the correct polycation deposition, ζ-Potential analysis of the CQDs_1L was carried out. This analysis revealed the overcompensation of the charge of the CQDs, which testified to the actual presence of the NH_2 surface groups in the NPs. In fact, following the deposition of the first CH layer, the ζ-Potential of the NPs changes from -23.2 ± 1.7 mV to +31.1 ± 0.3 mV.

Subsequently, the deposition procedure of the remaining six layers of CH and CS was started in the CQDs_1L template, resulting in the CQDs_7L configuration. For all polyelectrolyte depositions, the same concentration of 1 mg/mL was used. The characterisation of the surface charge of the CQDs_7L following the deposition of each layer is shown in Fig. 98.

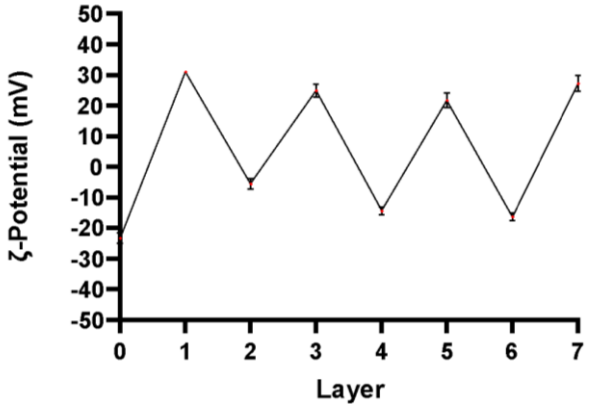

Fig. 98: ζ-potential graph of the LbL of CQDs_7L.

The LbL deposition was characterized by a charge inversion between 24.9 ± 2.1 mV and - 16.2 ± 1.2 mV, however, the saturation of anionic layers had not been reached. Moreover, the deposition phase of the negative layers could exhibit the formation of particle aggregates due to the weak repulsive forces of the NPs. In general, there are many parameters that control the growth characteristics of the deposited layers, including the physico-chemical properties of the template. Among these, the charge density of the surface and the stability of the template created may have had a greater influence on the interactions between the substrate and the deposited layers (Eduardo Guzmán et al., 2020). In the case just discussed, it is possible that the core had an inhomogeneous charge density due to the presence of CQDs and clusters of these of different sizes. Furthermore, it is possible that the CQDs_1L were unstable. These two reasons were essentially due to the composition of the NPs' core as they were formed by clusters of CQDs that may be non-uniform in size and shape. Thus, the lack of surface saturation during the deposition of the successive layers could be due to these events. Moreover, an increase in the negative charge was observed as the number of negative layers deposited increases. This trend showed that the first three layers of the CQDs_7L were necessary to give the NPs greater stability and to achieve the final multilayer structure. Therefore, the first three PEs depositions will be considered as pre-layers (Regine v. Klitzing, 2006; Eduardo Guzmán et al., 2020).

Next, the deposition of polyelectrolytes in combination with DOXO (previously dissolved in CH) and then the combination of CQDs with DOXO and DTX (added in the CS solution) was tested. The two types obtained will be referred to CQDs_7D and CQDs_7DD, respectively. For all polyelectrolyte depositions, the same concentration of 1 mg/mL was used. The ζ-potential results following the deposition of each layer are shown in Fig. 99.

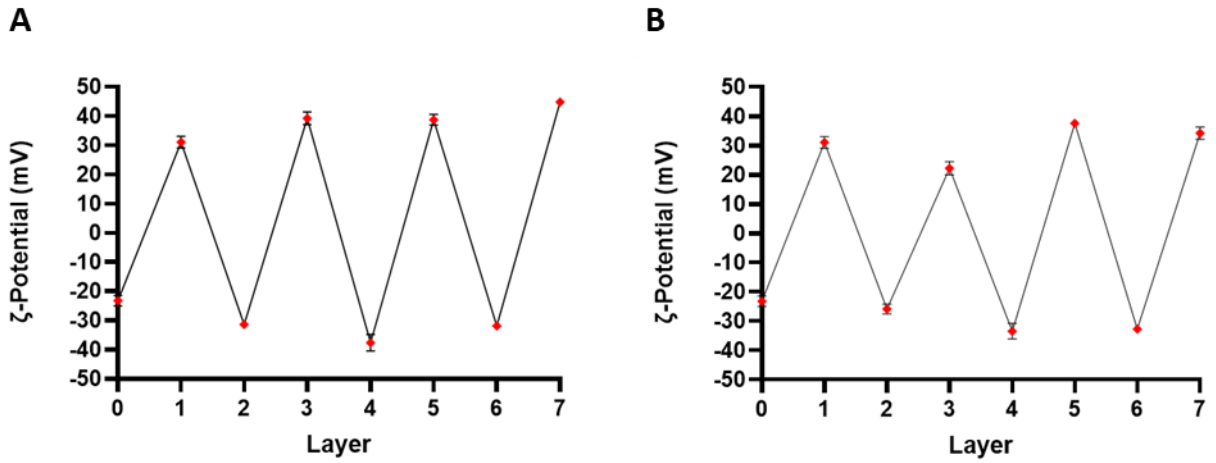

Fig. 99: ζ-potential graph of the LbL of CQDs_7D (A) and CQDs_7DD (B) configurations.

The phenomenon of overcompensation of layer charge occurred for both configurations, showing intensity peaks between +39.1 ± 2.2 mV and -31.4 ± 1.4 mV for CQDs_7D and from +34.2 ± 2.9 mV to -25.9 ± 1.7 mV for CQDs_7DD. In addition, each deposited layer showed a surface charge higher than the charge of the deposition solution; therefore, the layers deposited in the NPs were saturated. Finally, all the layers exhibited values > +25 mV (for CH/DOXO layers) or < 25 mV (for CS and CS/DTX layers), so these NPs were particularly stable and obviated the aggregation mechanisms due to the intensity of the charges on the surfaces of the NPs for each deposited layer.

Compared with the CQDs_7L configuration, the encapsulation of DOXO in the core stabilized the polyelectrolyte deposition more, inducing an increase in surface charge and complete saturation of the layers. It is conceivable that DOXO molecules had localised in the porosities created by the CQD cluster, thus ensuring a greater structural stability of the deposited CH layer and the subsequent layers created. This makes the deposition of pre-layers no longer necessary. A similar argument can be applied to layers number 3 and 5 in the CQDs_7D and CQDs_7DD configuration. Furthermore, due to the presence of DTX, the CH layers showed a lower positive charge than CQDs_7D. This could have been caused by the larger topological polar surface area of DTX (224 Å²) compared to DOXO molecules (206 Å²). Thus, the size of the DTX could have affected the deposition of the positive layers. This is corroborated by the decay of the positive charge from the third layer (thus just after the first DTX deposition), which was not the case in the CQDS_7D configuration. However, it is not possible for DOXO or DTX to interfere with PE charges, as both have zero formal charge. Therefore, any kind of charge-charge interaction between molecules and PEs that could have led to these results must be ruled out.

After freeze-drying the samples, the process yield (Y) for CQDs_7L was 11.0 ± 0.4 %, while for CQDs_D was 18.3 ± 0.3 %. The CQDs_DD samples showed a Y (%) of 30.3 ± 0.1 %. The increase in Y(%) in the NPs

encapsulating DTX and DOXO was precisely due to the encapsulation of the two drugs that make the NPs heavier, preventing their dispersion (thus their loss) during the washing and centrifugation steps.

The quantity of particles obtained is significantly low for all types obtained, in particular for CQDs_7L. This is mainly caused by the method used for manufacture. In fact, the LbL of NPs is a handmade manufacturing method, so there is a massive loss of template cause of the NPs' collection and washing processes.

Furthermore, a small amount of material may have been lost during freeze-drying due to the very light weight of the NPs and also due to the size of the holes created manually on the parafilm. However, the latter mechanism discussed may have limited Y(%) values to small percentages.

Using DLS methods, the hydrodynamic diameter of NPs produced by LbL could be analysed (Fig. 100). The NPs consisting of the core of CQDs and coated with the single layer of CH/DOXO (CQDs(DOXO)_1L) exhibited a hydrodynamic diameter of 84.19 ± 7.71 nm with the lowest PDI of 0.21 ± 0.01. The CQDs_7L exhibited a diameter size of 103.94 ± 3.37 nm associated with a PDI of 0.56 ± 0.08. Finally, CQDs_7D had a hydrodynamic diameter and PDI of 96.60 ± 5.49 nm and 0.59 ± 0.06, while the size of 104.64 ± 1.33 nm and 0.89 ± 0.16 PDI belonged to the CQDs_7DD type.

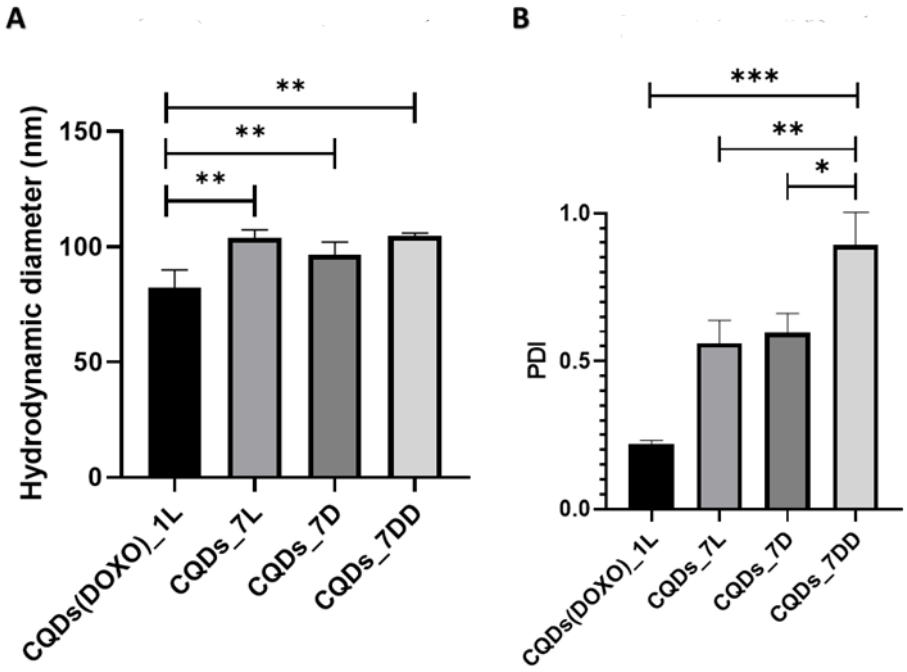

Fig. 100: DLS measurements: hydrodynamic diameter (A) and PDI (B) of CQDs(DOXO)_1L, CQDs_7L, CQDs_7D and CQDs_7DD.

The PDI value obtained from the CQDs(DOXO)_1L indicated the homogeneity between the particles. This indicated that the DOXO molecules were arranged in the porosities created by the clusters of CQDs, thus creating more uniform templates. However, the CQDs_7L, CQDs_7D and especially CQDs_7DD had a PDI between 0.5 and unity, so they were very polydisperse and inhomogeneous. Between the drug-encapsulating

and drug-free particles, there was no statistically significant difference in size, demonstrating that the encapsulation of drug molecules did not affect the final size of the NPs. On the other hand, the PDI recited discrepancies between the CQDs_7DD particles and the CQDs_7L and CQDs_7D types. From the result obtained through DLS, the simultaneous encapsulation of the DTX with the DOXO in the layers led to a lower homogeneity of the particles in terms of morphology. Furthermore, no statistically significant difference was shown between the CQDs_7D and CQDs_7L types, exhibiting a very similar PDI between them. Therefore, the simultaneous encapsulation of DOXO and DTX induced a distribution of these molecules that resulted in a distinct morphological change in the conformation of the layers, leading to the creation of non-homogeneous capsules. This may be due to an excessive amount of DOXO and/or DTX molecules encapsulated in the layers or even by the larger size of the DTX molecules compared to those of DOXO (224 Å² versus 206 Å² polar topological surface area for DTX and DOXO, respectively).

To better understand the results obtained and verify their correctness, the structures mentioned above were observed by TEM analysis, as shown in Fig. 101.

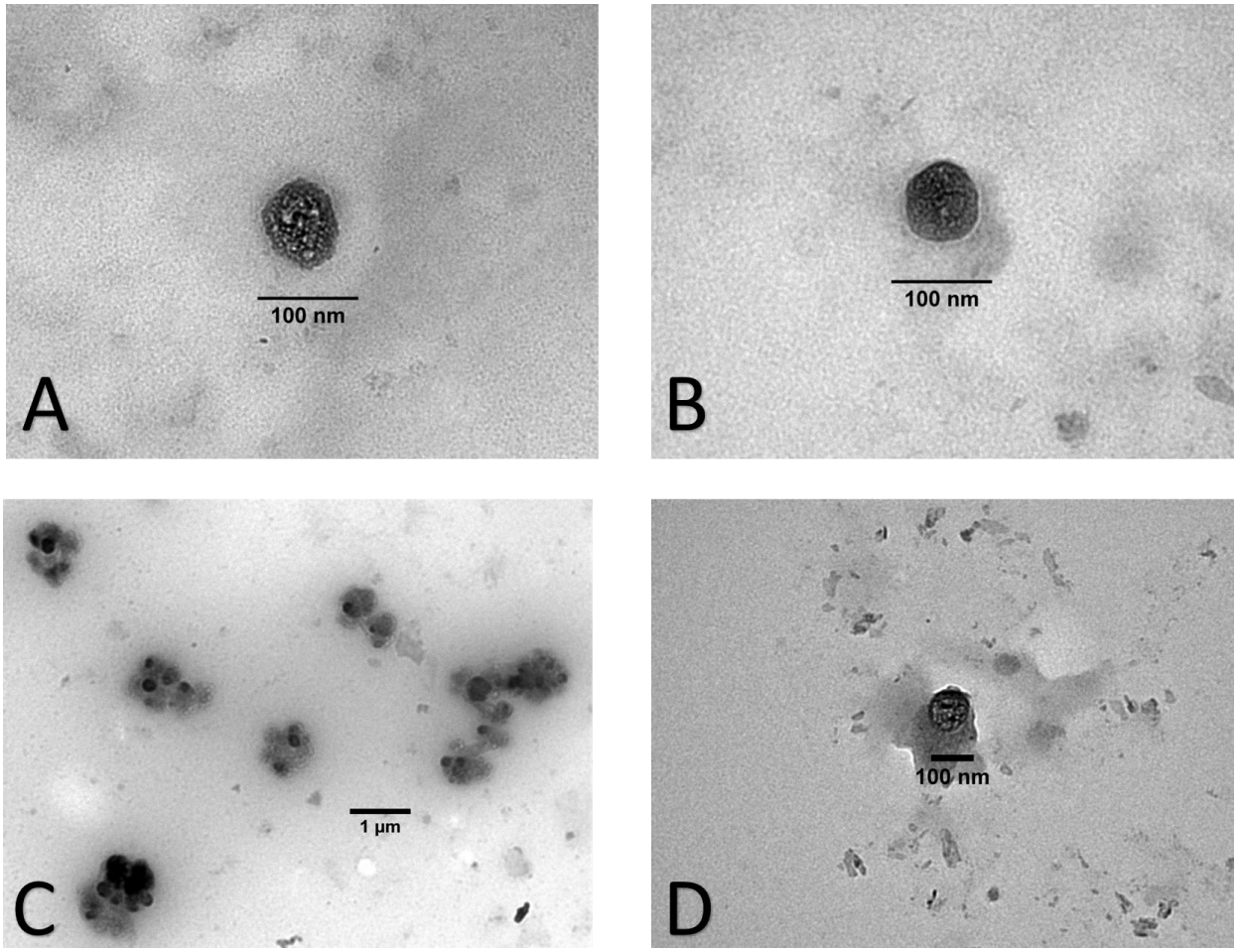

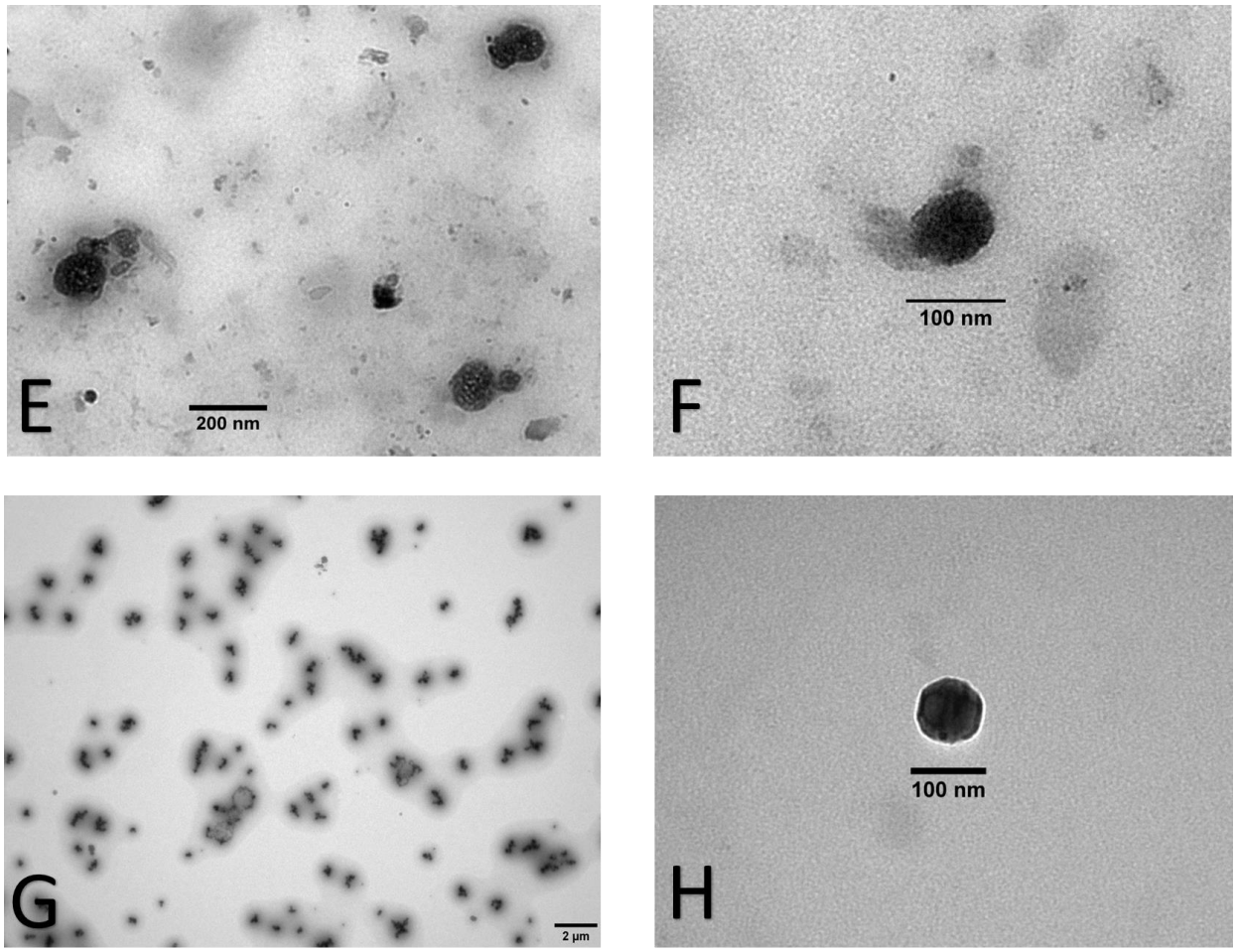

Fig. 101: TEM images of CQDs_1L (A-B), CQDs_7L (C-D), CQDs_7D (E-F) and CQDs_7DD (G-H).

Through this analysis, it is possible to ascertain many NPs whose morphologies were uniform and spherical, also showing a certain surface roughness that is a distinctive sign of the coatings' deposition.

Thus, although TEM analysis is a qualitative analysis, it is possible to state that the analysis provided by the PDIs obtained using DLS are not fully descriptive of the NPs tested.

On the other hand, the dimensions of the NPs analysed at TEM were consistent with those obtained by DLS analysis. In fact, CQDs(DOXO)_1L exhibited a diameter size of 75.27 ± 12.68 nm, while CQDs_7L showed a diameter size of 109.51 ± 19.41 nm. Finally, CQDs_7D exhibited a diameter size of 112.63 ± 4.95 nm, while CQDs_7DD exhibited a diameter size of 104.34 ± 15.63 nm.

Although seven layers were deposited on the CHBOCQDs, all NPs were slightly thicker than 100 nm, demonstrating that the coatings were nanometric. Assuming the growth mechanism during deposition to be linear, the thickness of each layer was 3.29 ± 0.10 nm for CQDs_7L, 2.07 ± 0.12 nm for CQDs_7D and 3.40 ± 0.04 nm for CQDs_7DD. However, further analysis would be required to better understand the interaction between the PEs, both in the presence and absence of drugs. Quartz Crystal Microbalance analysis could be useful for this purpose.

Next, the effectiveness of DOXO encapsulation in the core of the NPs and the effectiveness of DOXO and DTX encapsulation via the layers on the CQDs_7D and CQDs_7DD systems were evaluated (Fig. 102). Concerning the drug encapsulated in the core of the CQDs(DOXO)_1L, the results obtained by spectrophotometry analysis showed an encapsulation efficiency of the DOXO of 69.2 ± 2.0 % (13.38 ± 0.39 µg) compared to the amount of drug supplied for template synthesis (19.33 µg).

This result showed that CQDs(DOXO)_1L were made up of clusters of CQDs, thus presenting porosities on which a large amount of drug was deposited. Furthermore, the presence of the coating hindered the release of DOXO during subsequent washing steps, allowing the drug molecules in the core to be retained. This may be due to the high thickness of the coating, which allowed the drug molecules to diffuse without being released into the bulk solution, remaining trapped in the PE lattices.

To the best of my knowledge, there is no study in the literature involving the formation of templates consisting of CQDs and drugs. Consequently, the method of manufacturing CQDs(DOXO)_1L appears to be innovative, easy to process and non-toxic to humans and the environment.

Subsequently, the amount of DOXO released from the core of the NPs during the synthesis process was assessed. For this purpose, six drug-free PEs layers were deposited on the CQDs(DOXO)_1L and, for each step (of deposition and washing), the amount of DOXO released from the NPs core was quantified. This structure will be named CQDs_1L6L. After creation of the multilayers, a DOXO release of 17.1 ± 1.3 % (2.29 ± 0.17 µg) was found. This quantity came exclusively from the core of the NPs. Thus, the deposition of the next six layers reduced the core encapsulation efficiency from 69.2 ± 2.0 % (13.38 ± 0.39 µg) to 52.1 ± 3.9 % (10.06 ± 0.74 µg). The result obtained indicates the presence of significant drug diffusion from the core to the outermost layer during NPs synthesis. This was mainly caused by the continuous stress imposed on the NPs during the numerous stirring steps of the deposition and washing solutions, but also by the numerous centrifugations performed at high speed. In fact, the highest percentage of DOXO release from the core was found after the deposition of the fourth layer (6.7 ± 0.8 % of DOXO), whereas the release of DOXO following the deposition of layers number 2 and 3 was close to zero.

Next, the effectiveness of DOXO and DTX encapsulation by the CQDs_7D and CQDs_7DD systems were evaluated (Fig. 102). The effectiveness of DOXO encapsulation in the CQDs_7D configuration was 25.6 ± 1.7 % (14.85 ± 0.97 µg), while CQDs_7DD showed an encapsulation of 23.0 ± 0.7 % (13.37 ± 0.42 µg). The amount of DTX encapsulated by the layers in the CQDs_7DD configuration was 29.1 ± 0.9 % (1.41 ± 0.04 µg).

Interpolating the data obtained on the encapsulation efficiency of DOXO by the layers, the deposition step of the layer allowed an average DOXO entrapment of 20.3 ± 0.4 % for CQDs_7D, while for CQDs_7DD it was 16.6 ± 1.5 %. Thus, the deposition steps resulted in very low drug encapsulation.

On the other hand, the washing steps removed a fair percentage of drug, especially in the case of CQDs_7DD. In fact, two consecutive washes removed 29.6 ± 3.1 % of drug trapped in the layer previously deposited on the CQDs_7D. In contrast, the CQDs_7DD showed a removal of 33.1 ± 5.6 % of DOXO. For both types analysed,

the first washing step always removed most of the drug weakly adsorbed on the surface, in agreement with the technique used (J. J. Richardson, Bjornmalm and Caruso, 2015).

A similar argument applies to the encapsulation of DTX by layers. Indeed, only 28.9 ± 0.6 % of DTX was encapsulated during the deposition of a layer. However, the next two washing steps showed a removal of DTX close to zero, so the DTX encapsulated in the previous step remains in the deposited layers. This may be due to the higher molecular weight of DTX compared to DOXO, which allows it a lower intra-reticular diffusivity during the washing steps (Guzmán E. et al., 2017; Eduardo Guzmán et al., 2020). Another possible explanation is the size of DTX molecules, which are larger than those of DOXO; therefore, it is possible that they were more trapped within PEs lattices due to their size.

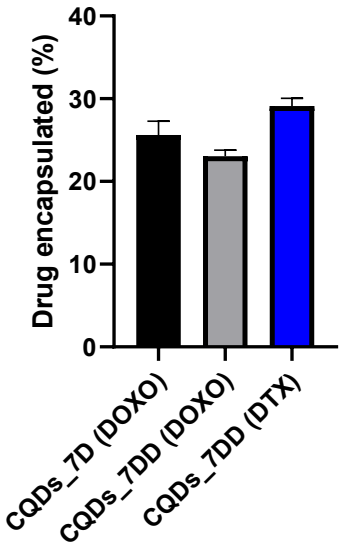

Fig. 102: Efficiency of DOXO and DTX encapsulation by layers of CQDs_7D and CQDs_7DD.

From the point of view of DOXO encapsulation, there was no significant statistical difference in the encapsulation of DOXO by the layers between the CQDs_7D and CQDs_7DD configurations (p-value = 0.477). Thus, it is possible to say that the presence of DTX molecules in the adjacent layers did not hinder the entrapment of DOXO molecules within the layers. However, it is possible that DOXO molecules may diffuse during the deposition of the subsequent layers (M. Adamczak et al., 2012), just like the drug in the CQDs_1L6L configuration. Thus, drug molecules can interpenetrate PE lattices and become trapped in the adjacent CH and CS layers. Generally, the percentages of drugs encapsulated by the layers were a few µg, showing relatively low encapsulation rates compared to the amounts encapsulated in the core and the amounts encapsulated in the CaP particle layers. The difference in the amount of drug encapsulated by the layers compared to the core was due to the different way in which DOXO is encapsulated. In fact, in the case of the core, the drug molecules will fill macroporosities caused by the clusters of CQDs, while in the layers they will occupy the different nanoporosities created by the PEs lattices.

On the other hand, the difference between CQDs_7D and CaP_7DD in the percentage of drug trapped by the layers was evident. This may be caused by a combination of reasons. The thickness of the layers was not different between the two types of NPs as both had thicknesses in the order of 2-3 nm. Therefore, although the PEs used are the same, they were dissolved in different media, so the interactions underlying the PEs' assembly will be different. In particular, it would appear that PEs in sodium acetate buffer create multilayer layers that are more interconnected, not creating nanoporosity on which drug molecules can be trapped (Guzmán E. et al., 2020). This may be caused by the different ionic strength of the solution, but also by the different degree of protonation of the PEs depending on the pH of the solutions (pH 6 for CaP_7DDs and pH 5 for CQDs_7DDs). Furthermore, the deposition template was completely different between the two types mentioned, so it is possible that the type and intensity of the interconnection forces of the polyelectrolytes were different due to this diversity (Guzmán E. et al., 2020). However, further analyses would be necessary to better understand the interaction between PEs depending on where they were dissolved and on the different template. Quartz crystal microbalance analysis could be useful for this purpose.

Finally, the DOXO and DTX release profiles from the CQDs_1L, CQDs_1L6L, CQDs_7D and CQDs_7DD systems in PBS solutions at 37 °C were studied. Furthermore, to better characterise the burst release, the release rate of DOXO from the layers was calculated by plotting the trend line for the first three time points. Subsequently, the trend line (straight line y=mx+q) was calculated, then the slope (i.e. the drug release rate) was derived (Fig. 103).

The cumulative DOXO release profile by the CQDs_1L configuration is shown in Fig. 103A. The curve was characterized for 28 consecutive days, showing a DOXO release of 43.8 ± 5.2 % at day 1 and 61.4 ± 1.3 % at day 28. Moreover, this type of NPs showed a halved release time at day 7 (50.0 ± 4.1 %). This suggests that particles that presented a single layer already have a controlled drug release over time.

The release profile was characterized by the burst release effect on day 1 probably due to the diffusion of the drug from the core to the outermost layer. In addition, another cause of accelerated drug release from the carrier may also be due to ionization of DOXO in the medium at pH 7.4 (Daria Kalenichenko et al., 2021). On days following day one, drug release appeared to be controlled over time until it stabilizes at day 28, suggesting that DOXO is released from the carrier core. From day 7 to day 28, the release profile was characterized by a similar plateau, indicating a relatively modest DOXO release (~18 % growth in release of DOXO). This phenomenon may be due to several aspects, including the possibility that DOXO molecules are trapped within the thick PE layer or that the drug has been unable to diffuse from within the nucleus because it is hindered by CQDs.

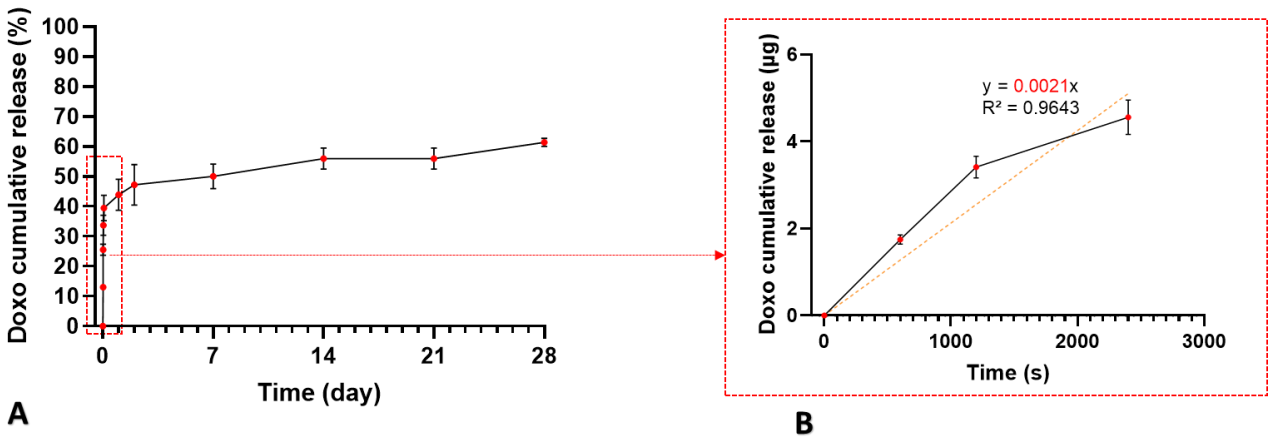

Fig. 103: Doxo cumulative release profiles (A) and the study of burst release rate (B) from CQDs_1L.

Subsequently, the amount of DOXO released from the core in the CQDs_1L6L configuration was characterised (Fig. 104A). From the data obtained, a maximum DOXO release of 46.1 ± 0.3 % at day 28 can be seen. Thus, this type of NPs never reached 50 % release, even over long timescales. This is mainly due to the presence of the 7 outer layers that hinder drug release, allowing a controlled release over time.

This configuration was also characterised by the burst release phenomenon; however, it is statistically different from that obtained from the CQDs_1L (p-value was 0.0013). In fact, the DOXO burst release was reduced from 43.8 ± 5.2 % to 26.5 ± 1.5 % compared to CQDs_1L using the LbL technique.

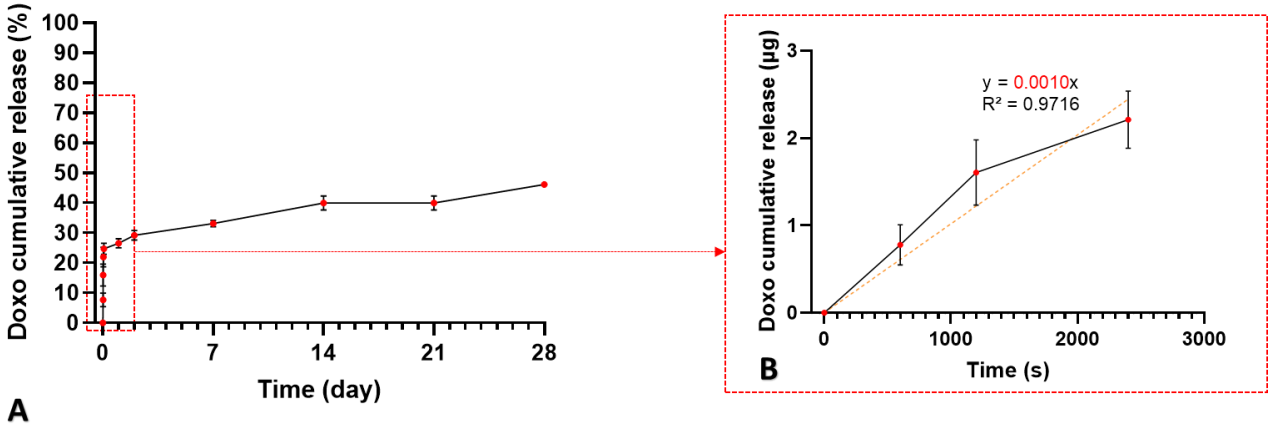

Fig. 104: Doxo cumulative release profiles (A) and the study of burst release rate (B) from CQDs_1L6L.

The release of DOXO by the CQDs_7D is shown in Fig. 105A. The burst release was increased from 43.8 ± 5.2 % to 61.7 ± 5.8 % compared to CQDs_1L, moving the halved release time after 2 h (54.1 ± 6.6 %). After 28 days, almost complete drug release was observed (90.0 ± 2.7 %), showing accelerated DOXO release between day 7 (68.9 ± 5.3 %) and day 21 (85.9 ± 5.9 %).

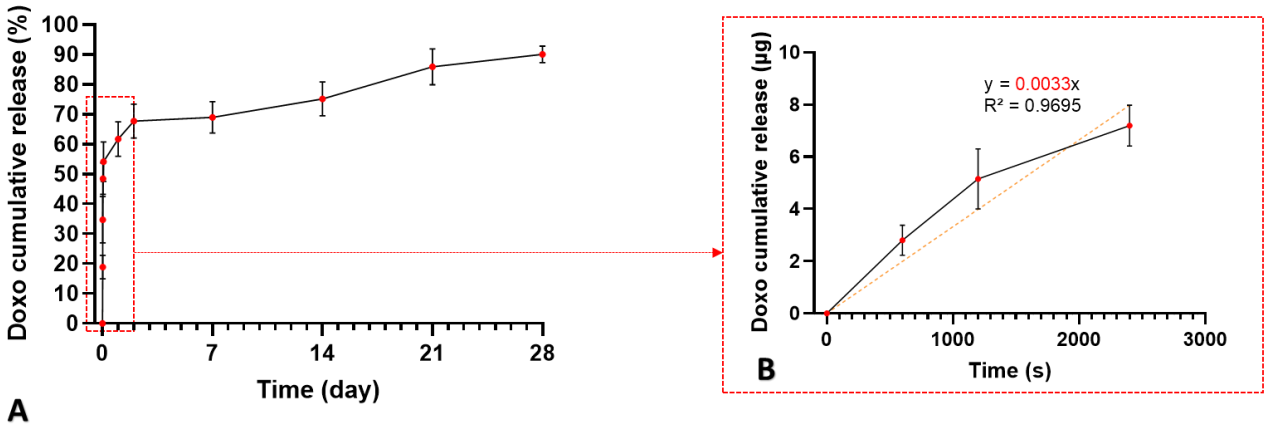

Fig. 105: Doxo cumulative release profiles (A) and the study of burst release rate (B) from CQDs_1L6L.

The proposed system showed a controlled drug release over time due to the presence of the layers, especially between day 1 and day 7. However, much of the drug was released after only a few hours and this should be avoided. This could be caused by the large amount of drug in the layers and by the diffusion of the drug molecules during the synthesis of the NPs layers, causing them to localise near the outermost layers. This would cause their immediate release in the first few hours of immersion in PBS. Possible causes for the acceleration of drug diffusion are physical stimuli, such as the temperature increase to 37 °C, which causes the reorganisation and partial dehydration of the layers, changing the permeability and release profile. In addition, the use of centrifuges may also have caused tensions that induced partial rupture of the capsule, triggering accelerated drug release. Therefore, a pH-shock may have occurred as the particles were produced at pH 5 while PBS had a pH of 7.4. This could have caused a rearrangement of the PEs chains that could have led to the accelerated release of DOXO. Also related to pH-shock, another possible cause could be poor core stability. It is possible that some NPs cores became destabilised once they were placed in the PBS solution, thus showing a release of the drug encapsulated in the core.

It should be noted that the DOXO releases of the CQDs_7D configurations were almost complete. One of the possible causes is the degradation of the layers. Polymer degradation (hydrolytic and erosion processes) is an uncontrollable phenomenon that damages the coatings of the NPs, thus increasing the drug release from the CQDs_7D.

A similar trend was also observed for the CQDs_7DD configuration (Fig. 106). The DOXO burst release phenomenon is also present here, showing a release of 57.5 ± 2.9 % at day 1. Furthermore, no statistically significant difference was present between the amount of DOXO released after 24 h by CQDs_7D and CQDs_7DD (p-value 0.0829). Moreover, the DOXO release rates in the first-time steps of the two configurations appear to be identical. Regarding burst release slopes, the CQDs_D and CQDs_DD configurations exhibit a higher release rate than the other configurations. This is due to the greater amount of drug encapsulated by CQDs_D and CQDs_DD compared to configurations that encapsulated DOXO

exclusively in the core. Therefore, the values obtained from the slopes were consistent with the configuration of the particles tested. In addition, accelerated drug release is present between day 7 (60.9 ± 1.5 %) and day 14 (70.4 ± 2.3 %) and between day 21 (71.2 ± 3.6 %) and day 28 (85.2 ± 3.1 %).

In terms of the final amount of DOXO released, the CQDs_D and CQDs_DD configurations showed statistically significant differences after 28 days (p-value was 0.0048). It can therefore be stated that the release of DOXO by CQDs_DD is influenced by the presence of DTX.

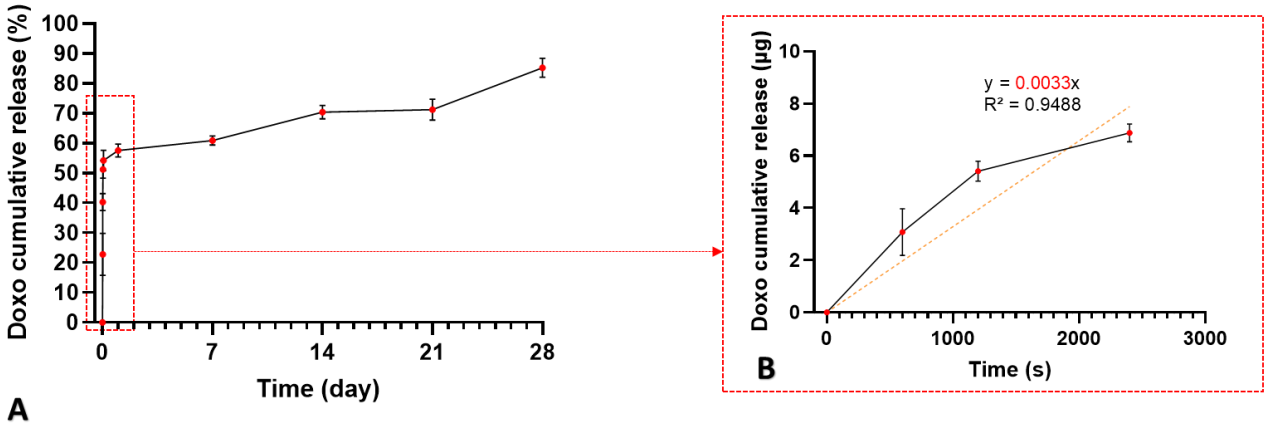

Fig. 106: Doxo cumulative release profiles (A) and the study of burst release rate (B) from CQDs_7DD.

As for DTX, it is only encapsulated in the negative layers of the multilayered capsules (Fig.107). After 24 h, a DTX release of 62.4 ± 7.1 % can be observed, thus showing a very pronounced burst release. This supports the previous hypothesis that the drug tended to localise mainly in the outermost layers in order to be released within a few hours. Indeed, after 2 h there is a DTX release of 48.4 ± 8.3 %.

However, in the following days the release is controlled over time, reaching a final value of 79.5 ± 3.4 % at day 28. The magnitude of the standard deviation is due to the low amount of encapsulated drug (1.41 ± 0.04 µg) and thus to the sensitivity of the equipment used for the analysis.

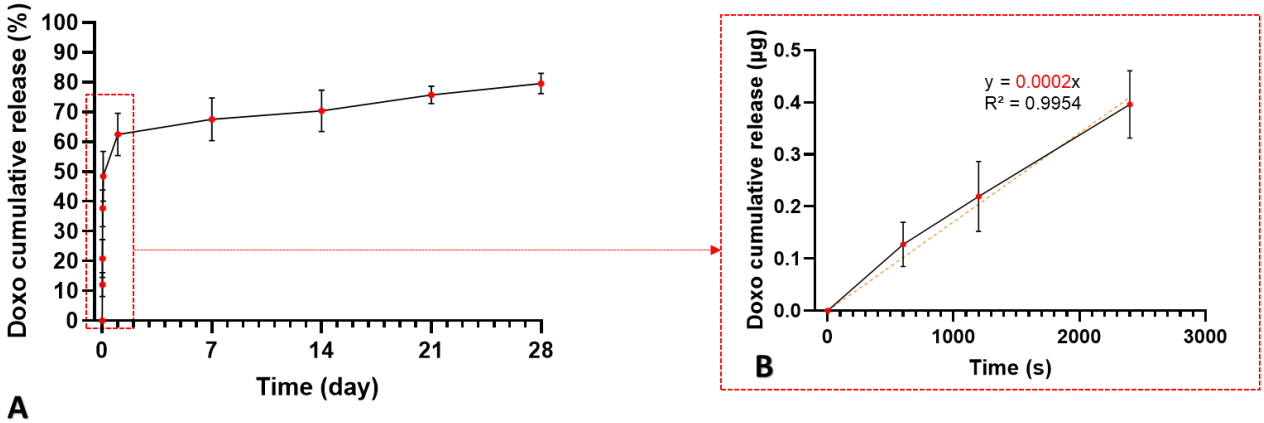

Fig. 107: DTX cumulative release profiles (A) and the study of burst release rate (B) from CQDs_7DD.

It is important to note that all the drug release curves obtained never reach plateau, testifying to a continuous process of drug release even weeks later. It would also be interesting to study the DOXO release profile of NPs under pH conditions simulating the tumour environment (pH 3-5). Indeed, under such acidic conditions, NPs should possess a less controlled and more rapid drug release than those obtained at pH 7.4.

Moreover, *in vitro* analyses are quite limiting as they do not present physical stimuli, cells, enzymes that can effectively simulate the degradation and stimulation mechanisms of NPs during their circulation in the body.

Finally, to assess the effective encapsulation of CHBOCQDs in the core of the capsules, the CQDs_7DD particles were excited with a wavelength of 365 nm (Fig. 108). The NPs solution exhibited blue coloration, indicating the actual presence of the dots within the structure.

Fig. 108: Excitation of CQDs_7DD by a wavelength of 365 nm.

3.2.4.2. Cytotoxicity Evaluation of CQDs_7L, CQDs_7D and CQDs_7DD

Incubation of SaoS-2 and U2O2 with CQDs_DD, CQDs_D, with the blanks of CQDs_7L and the free-Doxo, free-DTX and free-DTX/DOXO was done to test the cytotoxicity of the NPs and drugs after 24 h of seeding.

For both cell types, CaP_7L showed no alteration in metabolic activity compared to the untreated control for NPs concentrations below 10 µg/mL (Fig. 109). For higher concentrations, a very slight decrease in cell viability can be observed on both types of cells tested, depending on the concentrations used. Specifically, a concentration of 100 µg/mL provided a cell viability of 80.9 ± 13.1%, on Saos-2 while on U2OS it provided a viability of 85.9 ± 12.3%. However, the viability values obtained for concentrations above 10 µg/mL do not show a statistically significant difference to the 5 µg/mL concentration, which has a similar or higher metabolic activity rate than the control for both cell types tested. The slight decrease in viability rate may be due to the toxic effect of CH on osteosarcoma cells, which is present as the last layer in NPs (Parisa Maleki Dana et al., 2020).

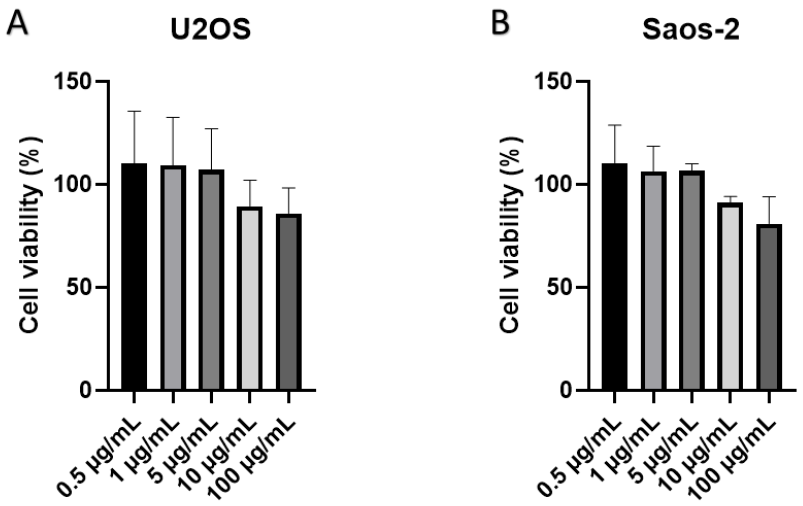

Fig. 109: PrestoBlue assay of U2OS (A) and Saos-2 (B) seeded with CQDs_7L.

The cells treated with the free drugs showed no survival rate for all concentrations used. Cells incubated with CQDs_7D or CQDs_7DD showed different results for the two cell types tested (Fig. 110). Both cell types recorded a variable metabolic activity depending on the concentration of NPs used. In fact, as the concentration of NPs tested increased, the metabolic activity of the cells decreased. This testifies that the NPs had a positive effect on cancer cells, confirming the therapeutic efficacy of these NPs by exploiting the EPR effect of cancer cells.

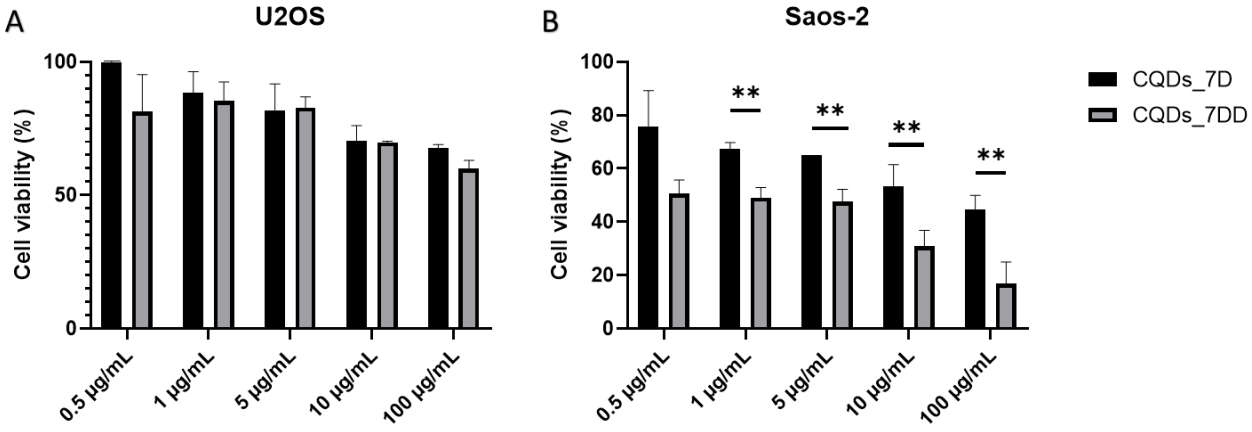

Fig. 110: PrestoBlue assay of U2OS (A) and Saos-2 (B) seeded with CQDs_7D and CQDs_7DD.

Starting from Saos-2 cells, a synergistic effect of the two drugs encapsulated in the CQDs_7DD was observed. In fact, the metabolic activity of the cells decreased more significantly in the presence of the two drugs than in the presence of DOXO alone in the CQDs_7Ds, as shown in Fig. 110.

For CQDs_7D concentrations higher than 10 µg/mL, Saos-2 showed a survival rate that was half that of the control (44.8 ± 5.1 %). For lower concentrations, a markedly higher cell survival rate was observed, ranging from 75.8 ± 5.1 % for a CQDs_7D concentration of 0.5 µg/mL to 53.2 ± 8.2 % for a CQDs_7D concentration of 10 µg/mL. Furthermore, there is no statistically significant difference between the 10 and 100 µg/mL concentration of CQDs_D (p-value = 0.3985).

On the other hand, for CQDs_7DD concentrations of 0.5 µg/mL, cell viability was 50.6 ± 5.0 %, so a 50 % decrease in cell metabolic activity can already be observed. Thus, with low concentrations of NPs, an effective and significant treatment of Saos-2 can be achieved. The 1 and 5 µg/mL concentrations of CQDs_DD did not show a statistically significant difference to the 0.5 µg/mL concentration (they have a p-value of 0.9946 and 09431 respectively). However, a 10 µg/mL concentration of CQDs_DD resulted in a decrease in cellular metabolic activity of 30.7 ± 6.0 %, whereas a 100 µg/mL concentration of CQDs_DD showed a decrease of 16.8 ± 8.1 %. The latter two concentrations did not show a statistically significant difference (p-value 0.1547). However, the concentration of 100 µg/mL is quite extreme for future clinical practice.

Interestingly, there was a significant difference between CQDs_7D and CQDs_7DD in terms of efficacy for all concentrations tested, indicating the extreme efficacy of the synergy of the two drugs used compared to the single use of DOXO as a chemotherapeutic drug. In particular, for the concentrations of 10 and 100 µg/mL there is a statistically significant difference between CQDs_DD and CQDs_D, assuming p-values of 0.0325 and 0.0016 respectively.

As far as U2O2 cells, they showed a higher survival rate than Saos-2 cells tested with the same concentrations of NPs. Particularly significant is the difference in efficacy of the synergistic treatment of DTX and DOXO against the two cell types. In fact, U2OS showed no significant decrease in metabolic activity in the presence of the two drugs compared to treatment with NPs encapsulating DOXO alone.

Furthermore, the viability rate of U2OS never fell below 50 %. In fact, the absolute minimum was reached at the 100 µg/mL concentration of CQDs_7DD with a rate of 59.8 ± 3.1 % compared to the untreated control. Interestingly, for lower concentrations of CQDs_7D and CQDs_7DD (such as 0.5, 1 and 5 µg/mL) the metabolic activity of U2OS was close to that of the untreated control. Between the 5 and 10 µg/mL concentration of CQDs_7D or CQDs_7DD there was not a statistically significant difference, (p-value of 0.315 for CQDs_7D and 0.5640 for CQDs_7DD), but also did not show statistically significant difference between the two types of NPs (p-value >0.9999). In fact, the survival rates for the 10 µg/mL concentration were 70.4 ± 5.7 % and 69.7 ± 0.5 %, respectively.

Finally, as found for the CaP_7DC particle type, Saos-2 and U2OS cells incubated with NPs that exclusively encapsulated DOXO showed completely different treatment efficacies. Explanations for this different drug-resistance on the part of osteosarcoma cells are given in section no. 3.2.3.3.

On the other hand, there are several reasons for the different efficacy of DTX on the two osteosarcoma cell types. The antitumour effects of Taxol (DTX belongs to this drug family) are linked to the role of p53, which

induces increased polymerisation of tubulin and its subsequent clustering to form highly stable, non-functional microtubules, leading to cell cycle arrest in the G2/M phase and inhibition of angiogenesis. Although the effects of DTX have been extensively studied, the biochemical mechanism that induces apoptosis remains largely unclear.

For this reason, Jung Hye Kim et al. (2003) further investigated the effect of DTX on osteosarcoma cells, also demonstrating the differential effect of the tumour suppressor gene p53 on DTX-induced apoptosis in p53-defected Saos-2 and p53-expressed wild type U2OS cell lines. In this work, an increase in DTX-induced cytotoxicity was demonstrated in p53-defected Saos-2. This agrees with the results obtained in this thesis. DTX treatment induced DNA fragment ladder structure, which is a biochemical sign of apoptosis, in a dose-dependent manner in Saos-2 cells, but insignificantly in U2OS cells (Jung Hye Kim et al. 2003).

In addition, p53-defected Saos-2 cells experienced relevant increases in caspase 3 activity (which are hydrolytic enzymes capable of inducing apoptosis), elevated expression of cyclin B1 and polo-like kinases, and upregulation of Bax (which is a pro-apoptotic factor). In contrast, Bcl-xL (which is anti-apoptotic factor) was clearly reduced in Saos-2 cells compared to U2OS cells. From these results, it was concluded that p53-defected Saos-2 cells were much more sensitive to DTX-induced apoptosis than p53-expressed U2OS cells. In addition, the differential expressions of U2OS and Saos-2 cells were correlated with the dose of DTX (Jung Hye Kim et al. 2003).

To qualitatively and to visually verify the results obtained from the PrestoBlue assay, a Live/Dead assay was conducted on Saos-2 and U2OS cells treated with the same NPs and concentrations as in the cytotoxicity assay. For both phenotypes tested, the Live/Dead images show increasing red staining as the particle concentration increases, thus showing results consistent with the PrestoBlue assay, albeit qualitative.

Furthermore, it was found that cells with very low metabolic activity had visually fewer adherent cells than controls (CQDs_7L and CTRL). This is possible because the apoptotic cells no longer had the adhesion receptors for the substrate, which consequently floated in the seeding solution. Therefore, these cells were removed during the PBS wash steps before staining.

The controls showed diffuse and homogeneously distributed cells throughout the substrate. In addition, they showed a high rate of proliferation and confluence by both cell types, demonstrating the absence of any contamination and that the experiment was therefore conducted successfully.

The CaP_7L particles showed more green staining, indicating some red domains of dead cells, consistent with the PrestoBlue assay (Fig. 111). However, the images confirmed the high biocompatibility of the tested NPs, also showing wells with high degrees of aggregation and spreading by the cells.

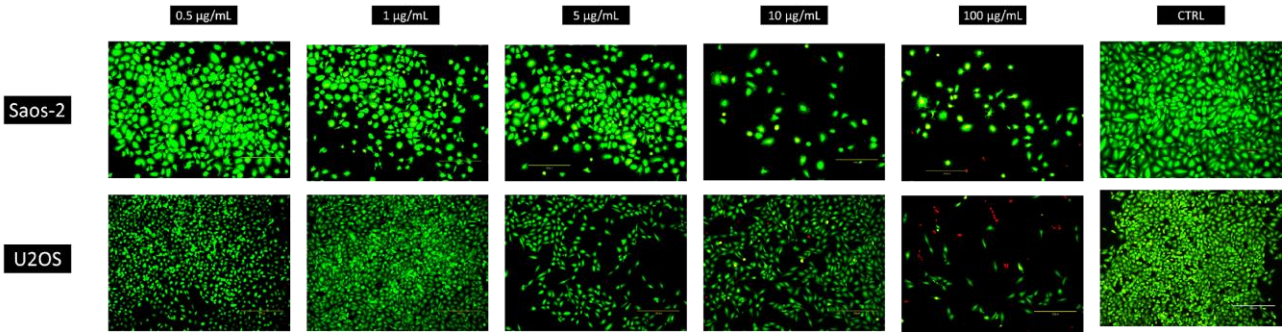

Fig. 111: Live/Dead images of Saos-2 (up) and U2OS (bottom) with or without CaP_7L at different concentrations.

For Saos-2, the 100 µg/mL concentration of CQDs_7D and CQDs_7DD showed rich images of dead cells (Fig. 112), consistent with the PrestoBlue results. The lower concentrations actually showed green colourations, showing that a proportion of cells had evaded treatment.

The U2OS showed more live cells than their Saos-2 counterparts for the same concentrations, with a greater presence of cell aggregates (Fig. 113). Furthermore, no significant differences could be observed between the CQDs_7D and CQDs_7DD images for the U2OS cells. This further confirms the results obtained by the PrestoBlue assay, i.e. the ineffectiveness of the treatment due to the combination of drugs.

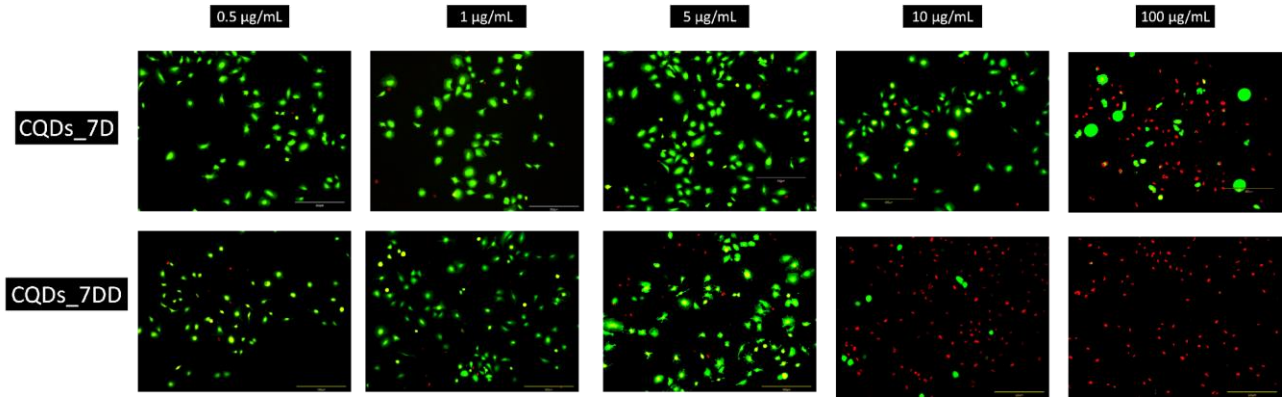

Fig. 112: Live/Dead images of Saos-2 with CQDs_7D (up) and CQDs_7D (bottom) at different concentrations.

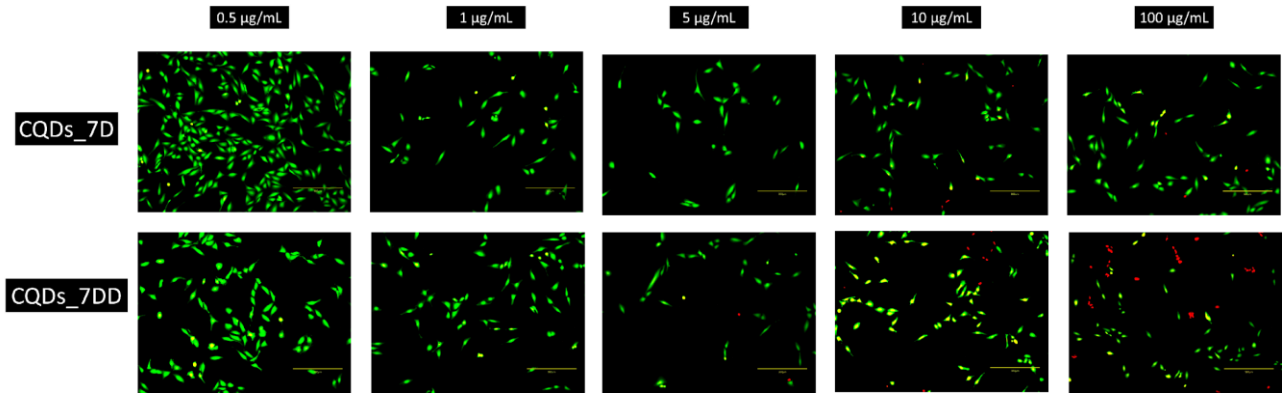

Fig. 113: Live/Dead images of U2OS with CQDs_7D (up) and CQDs_7D (bottom) at different concentrations.

Finally, osteosarcoma cells treated with DTX, DOXO and DTX/DOXO showed no green domain (Fig. 114 and 115), in agreement with the PrestoBlue assay. The cells treated with free-DOXO were numerically and visually inferior to those treated with free-DTX and DTX/DOXO, demonstrating greater cleavage of the adhesion domains of the treated cells. Furthermore, by increasing the concentration of free drugs, the number of cells adhered to the substrate decreased. Therefore, it can be stated that these cells were removed by washing in PBS before staining, especially for the DOXO-treated samples.

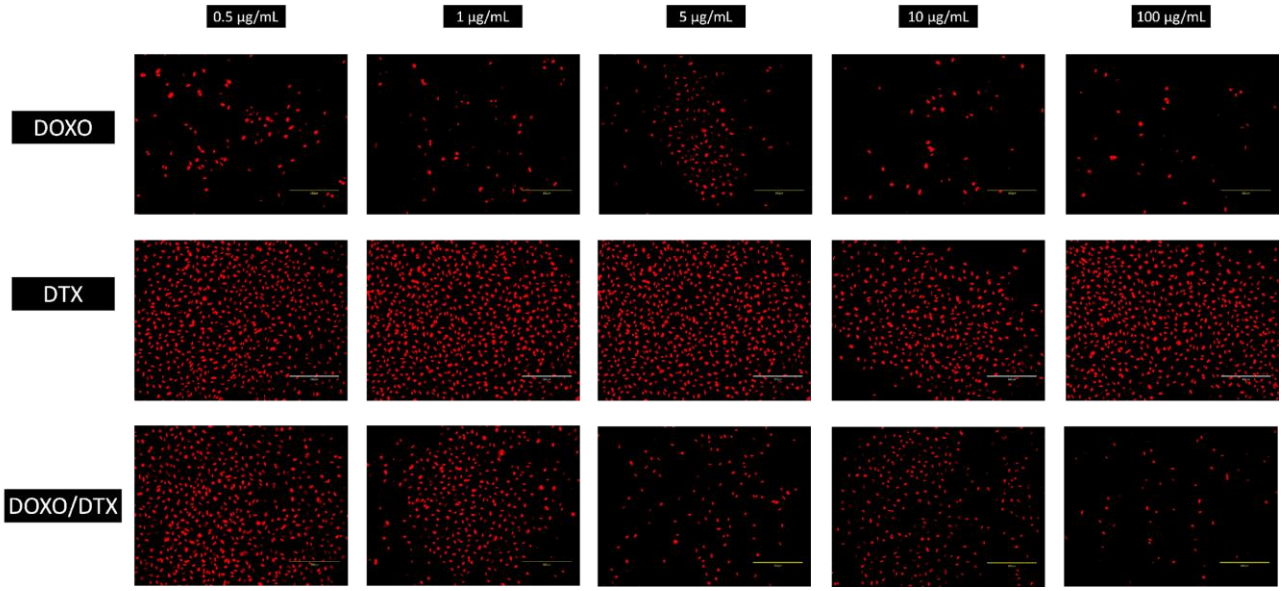

Fig. 114: Live/Dead images of Saos-2 with DOXO, DTX and DOXO/DTX solutions at different concentrations.

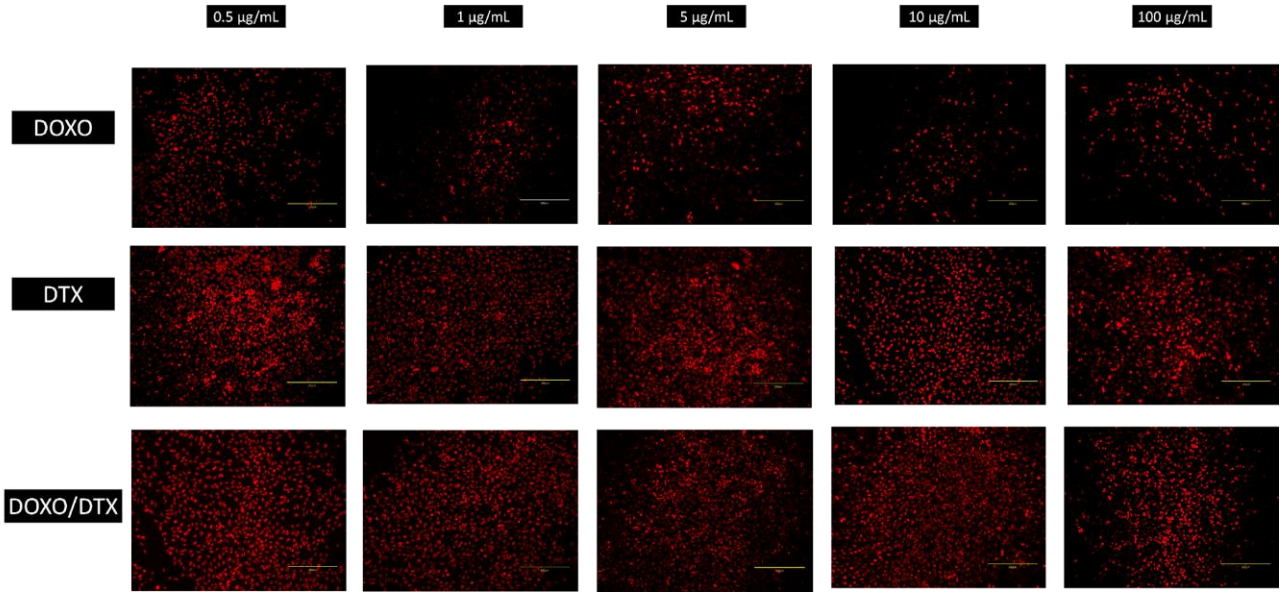

Fig. 115: Live/Dead images of U2OS with DOXO, DTX and DOXO/DTX solutions at different concentrations.

3.2.4.3. Computational approach on drug kinetics release from multilayer capsules

Regarding nanotheranostic drug delivery systems, it is very important to characterize and control drug release kinetics as much as possible to ensure adequate therapeutic efficacy. To obviate the long timelines and costs associated with in vitro drug release experiments, the implementation of in silico models that can predict the mechanism of drug release prior to in vitro testing may play a key role. For this purpose, the data obtained from in vitro drug release experiments (DOXO and DTX) related to CQDs_7DD were compared with results obtained from a mathematical model implemented for drug release from NPs, which are shown in Fig. 117.

To solve the mathematical problem of equations no. 7-10, the finite element method was used by COMSOL Multiphysics software (COMSOL Multiphysics, 2019). Therefore, the geometric and physical parameters (i.e. the diameter of the NPs, the volume of the NPs and the amounts of drugs encapsulated in the core and layers separately) were provided as input to obtain the triangular FEM mesh of the CQDs_7DD (Fig. 116).

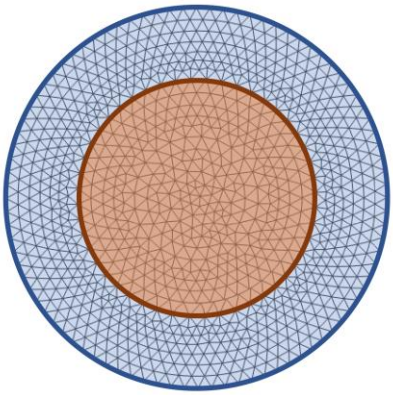

Fig. 116: FEM mesh in a core-shell spherical particle.

In addition, the specific dissolution rate of drugs (β), the solubility of drugs in PBS (S), the drug diffusion rates (k) and the exponent α (which considers the possible effects on the dissolution rate due to the variation of the surface area of the particles) were set manually to obtain the best fit on the experimental data and in agreement with the values found in literature.

Fig. 117 shows the computational releases of DOXO and DTX described by the developed two-layer dissolution-diffusion model. The experimental release curves appear well described by the developed mathematical model.

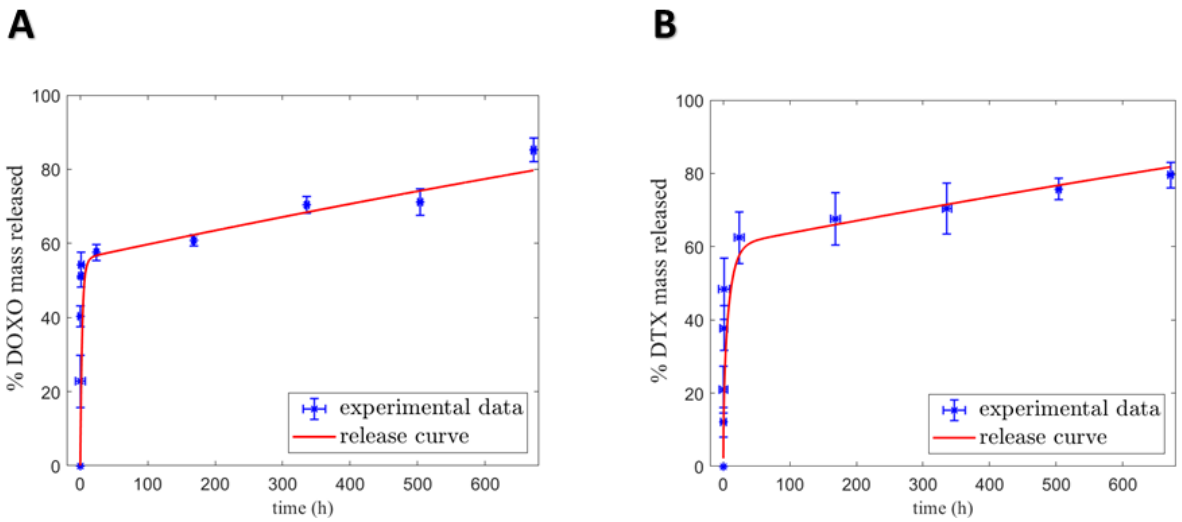

Fig. 117: Cumulative drug release of DOXO (A) and DTX (B) obtained from CQDs_7DD by in vitro (blue) and in silico (red) experiments.

The proposed model is very advantageous because, once calibrated, it can be used predictively for the release of drugs from multilayer and non-multilayer capsules. This would reduce the number of experiments and the relatively associated costs. However, one of the main difficulties is the estimation of the set of parameters that can guarantee a release similar to that of the intended application. On the other hand, numerical results offer a new understanding of drug mass transfer and the influence of different parameters, such as particle shape and multilayer strength, on the mechanism of drug release in any release medium (Barchiesi E. et al., 2022). Therefore, this model can be used to find and optimise processing parameters that ensure controlled drug release over time.

3.2.4.4. Deposition of PE solutions in sodium acetate buffer on CHCQDs.

As a proof of concept, the fabrication of NPs with a hydrophobic core of CQDs (CHCQDS) was conducted following the work reported in the literature by M. Adamczaka et al. (2013). The protocol involved two phases: the creation of emulsions consisting of a mixture of linseed oil and chloroform by using the spontaneous emulsion technique, and the subsequent deposition of polyelectrolytes to stabilize and create the multilayered nanocapsules.

In particular, lecithin-stabilised linseed oil emulsions were characterised by their small size, low polydispersity and stable surface charge, making them good candidates for further encapsulation within polyelectrolytes (M. Adamczaka et al., 2013). Furthermore, both components are natural products and biocompatible.

The LbL method used is based on the gradual formation of consecutive layers on the initial emulsion without the intermediate rinsing step. Their growth was evidenced by capsule sizes and ζ-potential measurements.

The zeta potential of the emulsion was found to be -38.59 ± 1.79 mV, which is sufficiently high to ensure the electrostatic stability of the system, in agreement with what was stated by M. Adamczak et al. (2013). The encapsulation of the nanoemulsion template within the first polyelectrolyte layer (CHCQDs_S1) resulted in a reversal of the zeta potential of the emulsion droplets to a positive value of 21.85 ± 1.14 mV. The average size of the nanoemulsion coated with a first layer obtained by DLS was 100.73 ± 11.94 nm with a PDI of a 0.28 ± 0.09. Therefore, the NPs were quite homogeneous with each other and had a nanometre size, in agreement with what was stated by M. Adamczak et al. (2013).

Subsequently, consecutive layers of polyelectrolytes were formed, always resulting in a charge reversal on the surface of the NPs (Fig. 118). This configuration will be named CHCQDs_S7.

However, the values obtained were always below to those of the starting solution of the PEs, so the saturation method was not observed. In addition, all deposited negative layers had values greater than -25 mV, so these NPs were not particularly stable and could not overcome the aggregation mechanisms of the templates due to their low charge intensity on the surfaces.

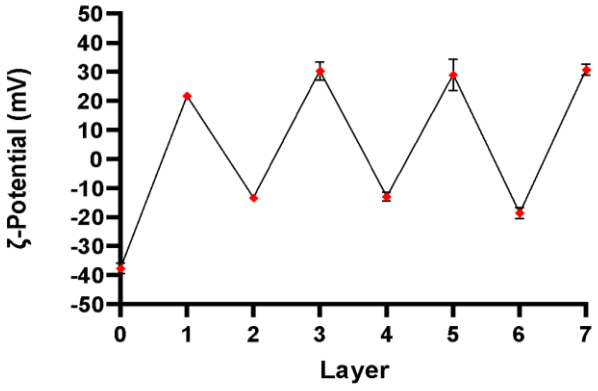

Fig. 118: ζ-potential graph of the LbL of CHCQDs_S7.

The average size of the CQDs_S7 was 377.79 ± 96.49 nm with a PDI of a 0.72 ± 0.15 (Fig. 119).

In contrast to the findings of M. Adamczak et al. (2013), the NPs obtained were relatively large and polydisperse, with different shapes and sizes. This could have been caused by the different preparation of PEs compared to M. Adamczak et al. (2013). In fact, the solutions of PLA/PGA are aqueous whereas those of CH/CS are in sodium acetate buffer. Thus, the dispersion and assembly medium of the PEs was also completely different, resulting in differences in the chemical-physical properties that governed the PEs' deposition interactions on the emulsion substrates.

Therefore, this may have allowed M. Adamczak et al. (2013) to achieve layer saturation and surface charges above 25 mV for deposited polycations and below -25 mV for deposited polyanions.

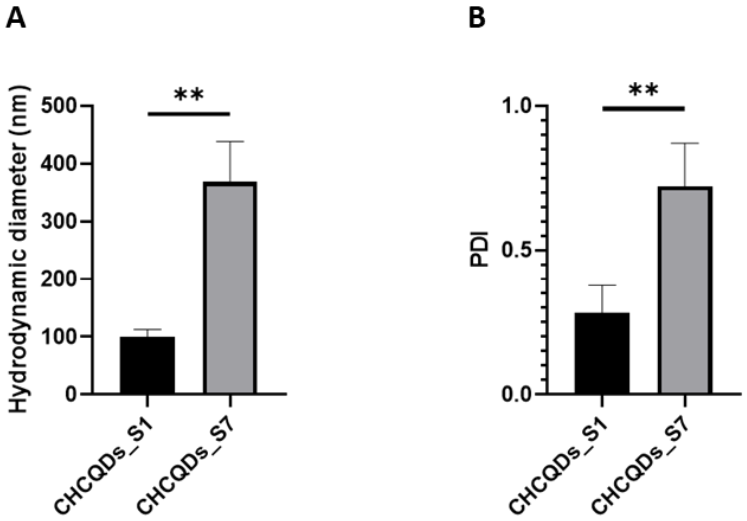

Fig. 119: DLS measurements: hydrodynamic diameter (A) and PDI (B) of CHCQDs_S1 and CHCQDs_S7.

To better understand the results obtained by DLS and verify their correctness, the structures mentioned above were observed by TEM analysis, as shown in Fig. 120.

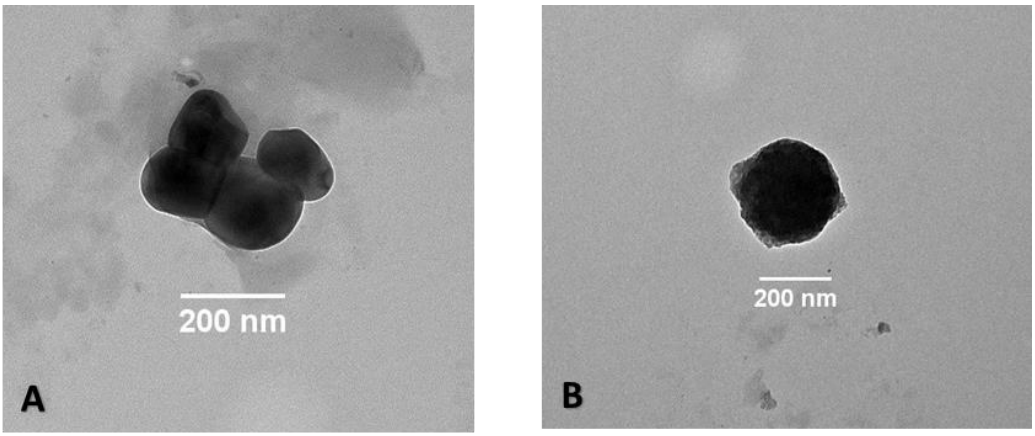

Fig. 120: TEM image of CHCQDs_S1 (A) and CHCQDs_S7 (B).

The dimensions of the NPs analysed by TEM were consistent with those obtained from DLS analysis. In fact, a diameter of 136.58 ± 27.69 nm was obtained for CHCQDs_S1 and a size of 247.81 ± 23.22 nm for CHCQDs_S7.

During the TEM analysis of the CHCQDs_S1, a high presence of particle aggregates emerged due to the low surface charge intensity of the CH-covered NPs, as shown in Fig. A.

Furthermore, a topographic difference of the tested NPs can be observed. The CHCQDs_S1 showed a different texture than the CHCQDs_S7, which appeared rough and more spherical, demonstrating both the deposition of the PEs and the stabilisation conferred by the deposited layers to the nanoemulsion droplets.

Finally, to assess the effective encapsulation of CHCQDs in the core of the capsules, the CQDs_7DD particles were excited with a wavelength of 365 nm (Fig. 121). The NPs solution exhibited blue coloration, indicating the actual presence of the dots within the structure.

Fig. 121: Excitation of CQDs_7DD by a wavelength of 365 nm.

CHAPTER 4: Conclusion and Future Perspectives

In this thesis, the already established synthesis for the generation of CQDs from various biomass wastes using the pyrolysis and hydrothermal carbonisation method was verified with chitin biomass waste. The use of biomass ensures unlimited access to raw materials for the manufacture of CQDs and the possibility of continuous material recycling, resulting in an environmentally friendly and totally green production route.
In addition, bio-oil, previously considered a waste material of the pyrolysis step, could be introduced into the HTC step, and proved to be able to successfully generate extremely soluble CQDs with excellent photoluminescent properties and a good quantum yield, without implementing surface modifications on the dots. Finally, CHBOCQDs showed excellent cytocompatibility towards Neo-dermal fibroblasts even for high concentrations of CQDs (up to 500 µg/mL). Compared to their counterparts made of semiconductor crystals, the developed CQDs had a lower quantum yield. To improve the quantum yield, surface passivation and interatomic doping methods can usually be applied; however, this was not studied in this thesis.

Due to the limitations of current anti-cancer treatments, the development of nanotheranostics platforms, which combine the therapeutic potential of drug compounds with the diagnostic potential of imaging probes in the same vehicle, allowed for improved drug delivery to specific sites and real-time tracking of the vehicle. By combining nanotheranostics NPs and LbL technology, two different types of NPs were produced that featured time- and space-controlled drug release, overcoming the drawbacks of conventional cancer therapies, such as poor selectivity, nonspecific biodistribution, low doses and side effects.
Specifically, the nanotheranostic systems have been developed by using CH and CS as PEs for the deposition of seven layers for both systems produced. In addition, the deposition of the layers allows the encapsulation of CQDs and drugs (DOXO and/or DTX). The first system involved the fabrication of a calcium phosphate (CaP) core containing Doxorubicin (DOXO) stabilized by the deposition PAH through a pumping system. Then, DOXO and GCCQDs were incorporated into the layers after dissolution in CH and CS, respectively. The second system was a drug codelivery (CQDs_7DD) consisting of a negative core of CHBOCQDs coated with CH and CS as polyelectrolytes containing DOXO and Docetaxel (DTX).
Using the saturation method, the final multi-layered NPs loaded with drugs and/or CQDs showed a size of about 100 nm with a spherical and mostly uniform morphology.
The process yields were objectively lower than those found in the literature. This could have been due to the poor optimisation of the centrifugation process (as in the case of CaP_7DC) or the handmade assembly method used. To improve this aspect, the LbL method could be modified towards automated systems using ultrasound, electromagnetic fields, and microfluidic chips, which would allow for a controlled deposition of PEs in less time, also avoiding the loss of NPs characteristic of the immersive LbL method. In fact, researchers are focusing more on this type of LbL.

Furthermore, it would be interesting to produce CaP particles completely made of natural materials. In this thesis, the substitution of PAH with CH was tested; however, the experiment was unsuccessful due to the poor optimisation of the PE deposition conditions on the CaP surface. On the other hand, there are other natural cationic materials that could be used and tested for the this propose which can better adapt to the pH conditions used and without having to be dissolved in acidic conditions, which are aggressive towards CaP.

The LbL assembly was perfectly suited to create a strong and stable shell, incorporating the CQDs and drugs into the nanolayers, in a meaningful way for CaP_7DC. On the other hand, the CQDs_7DD type showed a lower drug encapsulation capacity. This could have been due to the different layer deposition conditions between the two types of NPs; therefore, it would be necessary to study the interaction of the PEs used as a function of the layer assembly conditions and the encapsulated components. Quartz crystal microbalance analysis may be useful for this purpose.

Furthermore, it would be important to quantitatively verify the encapsulation capacity of CQDs across layers using Fluorescence activated cell sorting (FACS) analysis. The DOXO release profiles of the CaP_7DCs showed a controlled release over time, releasing half of its content three weeks later. However, CQDs_7DDs showed an accelerated release of DOXO and DTX after a few hours, allowing the release of almost 60 % of the NPs content. This could be from the diffusion of drug molecules from the innermost layers during the synthesis process of the layers.

Further characterisation studies of the release profiles would be necessary. For example, it would also be interesting to study the DOXO and DTX release profiles of NPs under pH conditions simulating the tumour environment (pH 3-5). Indeed, under such acidic conditions, NPs should possess a less controlled and more rapid drug release than those obtained at pH 7.4.

Moreover, *in vitro* analyses are quite limiting as they do not present physical stimuli, cells, enzymes that can effectively simulate the degradation and stimulation mechanisms of NPs during their circulation in the body. Subsequently, the NPs produced were tested on Osteosarcoma cells (Saos-2 and U2OS cells) to assess their cytotoxicity and their ability to be internalised by the cells via passive targeting (EPR effect) and via endocytosis mechanisms.

For both cell types tested, the results obtained showed a high biocompatibility of NPs consisting solely of 7 layers without drugs or CQDs. The slight decrease in viability rate may be due to the toxic effect of CH on osteosarcoma cells is confirmed in literature where bare CH and combinations of CH with other compounds are effective against some tumour cell lines, including osteosarcoma cells, exerting antitumour roles such as inhibition of proliferation, induction of apoptosis and exerting anti-oxidative activities. Therefore, the high presence of positively charged particles may have destabilised the membrane potential of the cells, leading some of them to death.

In the case of Saos-2, the synergistic effect of the two drugs in the CQDs_7DD could be appreciated even for low particle concentrations. However, this did not occur for U2O2 cells. CaP_7DC showed an absence of Saos-2 cell viability for a NPs concentration of 500 μg/mL. A totally different trend was observed for U2O2 cells.

The greater DOXO-resistance by U2OS than Saos-2 cells is widely documented in the literature, often with controversial arguments. In general, researchers have moved towards demonstrating that apoptosis can be induced by DOXO mainly through p53-independent pathways. This is indeed in agreement with the results obtained in this thesis.

On the other hand, DTX showed a differential effect on apoptosis as a function of the suppressor gene in p53-defected Saos-2 and U2OS wild type p53-expressed cell lines, showing an increase in DTX-induced cytotoxicity in p53-defected Saos-2. This was because DTX treatment (at same concentration) induced DNA fragment ladder structure significantly in Saos-2 cells, but insignificantly in U2OS cells (Jung Hye Kim et al. 2003). From these results, it was concluded that p53-defected Saos-2 cells were much more sensitive to DTX-induced apoptosis than p53-expressing U2OS cells. This agreed with the results obtained in this thesis.

Finally, TEM analysis of Saos-2 confirmed the therapeutic efficacy of these NPs by exploiting the EPR effect of tumour cells and their internalisation mechanisms via endocytosis.

In these images, it was also possible to note the mechanism of CaP_7DC escape from endosomes, leading towards drug release in the cytosol, thus towards apoptosis or necrosis of Saos-2 cells.

To visualise the internalisation of NPs containing CQDs, it could be useful to carry out a confocal microscope analysis, which would allow the localisation of the capsules within the cytoplasm of the cells.

This allowing the cytoarchitecture of samples to be preserved in an environment as closely as possible to their biological reality.

Furthermore, it might be interesting to conduct a FACS analysis on the different types of cells treated with the different types of NPs. This would make it possible to understand how many cells actually encapsulated NPs containing CQDs and/or drugs. In addition, LbL capsules can also be used for active targeting, through the deposition of biomolecules with ligand-receptor interaction capabilities.

Finally, it would be interesting to test the effect of NPs on three-dimensional Saos-2 and U2OS cultures and to assess the differences in terms of efficacy with two-dimensional cultures.

References

A. Galembikova and S.V. Boichuk, 64P Tyrosine kinase signaling profile in osteosarcomas: A potential therapeutic target for sensitization to doxorubicin, volume 32, supplement 6, s1365, october 01, 2021, https://doi.org/10.1016/j.annonc.2021.08.2060

Abdelhamid, A. S., Helmy, M. W., Ebrahim, S. M., Bahey-El-Din, M., Zayed, D. G., Zein El Dein, E. A., El-Gizawy, S. A., & Elzoghby, A. O. (2018). Layer-by-layer gelatin/chondroitin quantum dots-based nanotheranostics: Combined rapamycin/celecoxib delivery and cancer imaging. Nanomedicine, 13(14), 1707–1730. https://doi.org/10.2217/nnm-2018-0028

Adamczak, M., Hoel, H. J., Gaudernack, G., Barbasz, J., Szczepanowicz, K., & Warszyński, P. (2012). Polyelectrolyte multilayer capsules with quantum dots for biomedical applications. Colloids and Surfaces B: Biointerfaces, 90(1), 211–216. https://doi.org/10.1016/j.colsurfb.2011.10.028

Adamczak, M., Krok, M., Pamuła, E., Posadowska, U., Szczepanowicz, K., Barbasz, J., & Warszyński, P. (2013). Linseed oil based nanocapsules as delivery system for hydrophobic quantum dots. Colloids and Surfaces B: Biointerfaces, 110, 1–7. https://doi.org/10.1016/j.colsurfb.2013.04.014

Adamski J, Price A, Dive C, Makin G. Hypoxia-induced cytotoxic drug resistance in osteosarcoma is independent of HIF-1Alpha. PLoS One. 2013 Jun 13;8(6):e65304. doi: 10.1371/journal.pone.0065304. PMID: 23785417; PMCID: PMC3681794.

Akita, H., Kudo, A., Minoura, A., Yamaguti, M., Khalil, I. A., Moriguchi, R., Masuda, T., Danev, R., Nagayama, K., Kogure, K., & Harashima, H. (2009). Multi-layered nanoparticles for penetrating the endosome and nuclear membrane via a step-wise membrane fusion process. Biomaterials, 30(15), 2940–2949. https://doi.org/10.1016/j.biomaterials.2009.02.009

Alas, M. O.; Alkas, F. B.; Aktas Sukuroglu, A.; Genc Alturk, R.; Battal, D. Journal of Materials Science 2020, 55, (31), 15074-15105

Ali, A., Zafar, H., Zia, M., ul Haq, I., Phull, A. R., Ali, J. S., & Hussain, A. (2016). Synthesis, characterization, applications, and challenges of iron oxide nanoparticles. In Nanotechnology, Science and Applications (Vol. 9, pp. 49–67). Dove Medical Press Ltd. https://doi.org/10.2147/NSA.S99986

Amit Jaiswal, Siddhartha Sankar Ghosh and Arun Chattopadhyay, One step synthesis of C-dots by microwave mediated caramelization of poly(ethylene glycol), Chem. Commun., 2012, 48, 407-409, DOI: 10.1039/C1CC15988G

Amjad Z., Calcium Phosphates in Biological and Industrial Systems, 1998, Springer, Boston, MA

An, H. W., Li, L. L., Wang, Y., Wang, Z., Hou, D., Lin, Y. X., Qiao, S. L., Wang, M. di, Yang, C., Cong, Y., Ma, Y., Zhao, X. X., Cai, Q., Chen, W. T., Lu, C. Q., Xu, W., Wang, H., & Zhao, Y. (2019). A tumour-selective cascade activatable self-detained system for drug delivery and cancer imaging. Nature Communications, 10(1). https://doi.org/10.1038/s41467-019-12848-5

Anderson, N. M., & Simon, M. C. (2020). The tumor microenvironment. In Current Biology (Vol. 30).

Andrea Lončarević, Marica Ivanković, Anamarija Rogina (2017) Lysozyme-Induced Degradation of Chitosan: The Characterisation of Degraded Chitosan Scaffolds. Journal of Tissue Repair and Regeneration - 1(1):12-22.

Andresen, T. L., Thompson, D. H., & Kaasgaard, T. (2010). Enzyme-triggered nanomedicine: Drug release strategies in cancer therapy (Invited Review). In Molecular Membrane Biology (Vol. 27, Issue 7, pp. 353–363). https://doi.org/10.3109/09687688.2010.515950

Aryal, S., Park, H., Leary, J. F., & Key, J. (2019). Top-down fabrication-based nano/microparticles for molecular imaging and drug delivery. In International Journal of Nanomedicine (Vol. 14, pp. 6631–6644). Dove Medical Press Ltd. https://doi.org/10.2147/IJN.S212037

Atchudan, R., Edison, T. N. J. I., Perumal, S., Muthuchamy, N., & Lee, Y. R. (2020). Hydrophilic nitrogen-doped carbon dots from biowaste using dwarf banana peel for environmental and biological applications. Fuel, 275. https://doi.org/10.1016/j.fuel.2020.117821

Attia, M. F., Anton, N., Wallyn, J., Omran, Z., & Vandamme, T. F. (2019). An overview of active and passive targeting strategies to improve the nanocarriers efficiency to tumour sites. In Journal of Pharmacy and Pharmacology (Vol. 71, Issue 8, pp. 1185–1198). Blackwell Publishing Ltd. https://doi.org/10.1111/jphp.13098

Baghban, R., Roshangar, L., Jahanban-Esfahlan, R., Seidi, K., Ebrahimi-Kalan, A., Jaymand, M., Kolahian, S., Javaheri, T., & Zare, P. (2020). Tumor microenvironment complexity and therapeutic implications at a glance. In Cell Communication and Signaling (Vol. 18, Issue 1). BioMed Central Ltd. https://doi.org/10.1186/s12964-020-0530-4

Bai, X., Wang, Y., Song, Z., Feng, Y., Chen, Y., Zhang, D., & Feng, L. (2020). The basic properties of gold nanoparticles and their applications in tumor diagnosis and treatment. In International Journal of Molecular Sciences (Vol. 21, Issue 7). MDPI AG. https://doi.org/10.3390/ijms21072480

Barani, M., Mukhtar, M., Rahdar, A., Sargazi, S., Pandey, S., & Kang, M. (2021). Recent advances in nanotechnology-based diagnosis and treatments of human osteosarcoma. In Biosensors (Vol. 11, Issue 2). MDPI. https://doi.org/10.3390/bios11020055

Baskoutas, S., & Terzis, A. F. (2006). Size-dependent band gap of colloidal quantum dots. Journal of Applied Physics, 99(1). https://doi.org/10.1063/1.2158502

Bazban-Shotorbani, S., Hasani-Sadrabadi, M. M., Karkhaneh, A., Serpooshan, V., Jacob, K. I., Moshaverinia, A., & Mahmoudi, M. (2017). Revisiting structure-property relationship of pH-responsive polymers for drug delivery applications. In Journal of Controlled Release (Vol. 253, pp. 46–63). Elsevier B.V. https://doi.org/10.1016/j.jconrel.2017.02.021

Beik, J., Khateri, M., Khosravi, Z., Kamrava, S. K., Kooranifar, S., Ghaznavi, H., & Shakeri-Zadeh, A. (2019). Gold nanoparticles in combinatorial cancer therapy strategies. In Coordination Chemistry Reviews (Vol. 387, pp. 299–324). Elsevier B.V. https://doi.org/10.1016/j.ccr.2019.02.025

Bera, D., Qian, L., Tseng, T. K., & Holloway, P. H. (2010). Quantum dots and their multimodal applications: A review. In Materials (Vol. 3, Issue 4, pp. 2260–2345). MDPI AG. https://doi.org/10.3390/ma3042260

Bharti, C., Gulati, N., Nagaich, U., & Pal, A. (2015). Mesoporous silica nanoparticles in target drug delivery system: A review. International Journal of Pharmaceutical Investigation, 5(3), 124. https://doi.org/10.4103/2230-973x.160844

Bielack, S. S., Hecker-Nolting, S., Blattmann, C., & Kager, L. (2016). Advances in the management of osteosarcoma. In F1000Research (Vol. 5). Faculty of 1000 Ltd. https://doi.org/10.12688/f1000research.9465.1

Blanco, E., Shen, H., & Ferrari, M. (2015). Principles of nanoparticle design for overcoming biological barriers to drug delivery. In Nature Biotechnology (Vol. 33, Issue 9, pp. 941–951). Nature Publishing Group. https://doi.org/10.1038/nbt.3330

Bogart, L. K., Pourroy, G., Murphy, C. J., Puntes, V., Pellegrino, T., Rosenblum, D., Peer, D., & Lévy, R. (2014). Nanoparticles for imaging, sensing, and therapeutic intervention. ACS Nano, 8(4), 3107–3122. https://doi.org/10.1021/nn500962q

Bourguignon, L. Y. W., Zhu, H., Chu, A., Iida, N., Zhang, L., & Hung, M. C. (1997). Interaction between the adhesion receptor, CD44, and the oncogene product, p185(HER2), promotes human ovarian tumor cell activation. Journal of Biological Chemistry, 272(44), 27913–27918. https://doi.org/10.1074/jbc.272.44.27913

Brenner, W., Bohuslavizki, K. H., & Eary, J. F. (n.d.). PET Imaging of Osteosarcoma*. http://www.snm.org/education/ce_online.html

Burrows, N. D., Harvey, S., Idesis, F. A., & Murphy, C. J. (2017). Understanding the Seed-Mediated Growth of Gold Nanorods through a Fractional Factorial Design of Experiments. Langmuir, 33(8), 1891–1907. https://doi.org/10.1021/acs.langmuir.6b03606

Cai, S., Yang, Q., Bagby, T. R., & Forrest, M. L. (2011). Lymphatic drug delivery using engineered liposomes and solid lipid nanoparticles. In Advanced Drug Delivery Reviews (Vol. 63, Issues 10–11, pp. 901–908). https://doi.org/10.1016/j.addr.2011.05.017

Cebrián, V., Martín-Saavedra, F., Yagüe, C., Arruebo, M., Santamaría, J., & Vilaboa, N. (2011). Size-dependent transfection efficiency of PEI-coated gold nanoparticles. Acta Biomaterialia, 7(10), 3645–3655. https://doi.org/10.1016/j.actbio.2011.06.018

Chaffer, C. L., & Weinberg, R. A. (n.d.). A Perspective on Cancer Cell Metastasis. https://www.science.org

Chai, F., Sun, L., He, X., Li, J., Liu, Y., Xiong, F., Ge, L., Webster, T. J., & Zheng, C. (2017). Doxorubicin-loaded poly (Lactic-co-glycolic acid) nanoparticles coated with chitosan/alginate by layer by layer technology for antitumor applications. International Journal of Nanomedicine, 12, 1791–1802. https://doi.org/10.2147/IJN.S130404

Chaitanya Kantak, Sebastian Beyer, Levent Yobas, Tushar Bansal and Dieter Trau, A 'microfluidic pinball' for on-chip generation of Layer-by-Layer polyelectrolyte microcapsules, Lab Chip, 2011, 11, 1030-1035, DOI: 10.1039/C0LC00381F

Chang, L., Liu, J., Zhang, J., Deng, L., & Dong, A. (2013). PH-sensitive nanoparticles prepared from amphiphilic and biodegradable methoxy poly(ethylene glycol)-block-(polycaprolactone-graft-poly(methacrylic acid)) for oral drug delivery. Polymer Chemistry, 4(5), 1430–1438. https://doi.org/10.1039/c2py20686b

Chen, F., Hong, H., Shi, S., Goel, S., Valdovinos, H. F., Hernandez, R., Theuer, C. P., Barnhart, T. E., & Cai, W. (2014). Engineering of hollow mesoporous silica nanoparticles for remarkably enhanced tumor active targeting efficacy. Scientific Reports, 4. https://doi.org/10.1038/srep05080

Chen, J., Du, H., Xu, Y., Ma, B., Zheng, Z., Li, P., & Jiang, Y. (2021). A turn-on fluorescent sensor based on coffee-ground carbon dots for the detection of sodium cyclamate. Journal of Materials Science: Materials in Electronics, 32(10), 13581–13587. https://doi.org/10.1007/s10854-021-05933-3

Chen, Y., Zhao, Y., Zou, X., & Sun, L. (2021). Porous silica nanocarriers with gold/carbon quantum dots for photo-chemotherapy and cellular imaging. Journal of Drug Delivery Science and Technology, 61. https://doi.org/10.1016/j.jddst.2020.102141

Chitra Rajani, Pooja Borisa, Tukaram Karanwad, Yogeshwari Borade, Vruti Patel, Kuldeep Rajpoot, Rakesh K. Tekade, 7 - Cancer-targeted chemotherapy: Emerging role of the folate anchored dendrimer as drug delivery nanocarrier, Editor(s): Abhay Chauhan, Hitesh Kulhari, In Micro and Nano Technologies, Pharmaceutical Applications of Dendrimers, Elsevier, 2020, Pages 151-198, ISBN 9780128145272, https://doi.org/10.1016/B978-0-12-814527-2.00007-X

Christowitz, C., Davis, T., Isaacs, A., van Niekerk, G., Hattingh, S., & Engelbrecht, A. M. (2019). Mechanisms of doxorubicin-induced drug resistance and drug resistant tumour growth in a murine breast tumour model. BMC Cancer, 19(1). https://doi.org/10.1186/s12885-019-5939-z

Cong, S., Liu, K., Qiao, F., Song, Y., & Tan, M. (2019). Biocompatible fluorescent carbon dots derived from roast duck for in vitro cellular and in vivo C. elegans bio-imaging. Methods, 168, 76–83. https://doi.org/10.1016/j.ymeth.2019.07.007

Convertine, A. J., Benoit, D. S. W., Duvall, C. L., Hoffman, A. S., & Stayton, P. S. (2009). Development of a novel endosomolytic diblock copolymer for siRNA delivery. Journal of Controlled Release, 133(3), 221–229. https://doi.org/10.1016/j.jconrel.2008.10.004

D'Souza, S. L., Deshmukh, B., Bhamore, J. R., Rawat, K. A., Lenka, N., & Kailasa, S. K. (2016). Synthesis of fluorescent nitrogen-doped carbon dots from dried shrimps for cell imaging and boldine drug delivery system. RSC Advances, 6(15), 12169–12179. https://doi.org/10.1039/c5ra24621k

Dadfar, S. M., Roemhild, K., Drude, N. I., von Stillfried, S., Knüchel, R., Kiessling, F., & Lammers, T. (2019). Iron oxide nanoparticles: Diagnostic, therapeutic and theranostic applications. In Advanced Drug Delivery Reviews (Vol. 138, pp. 302–325). Elsevier B.V. https://doi.org/10.1016/j.addr.2019.01.005

Dager, A.; Uchida, T.; Maekawa, T.; Tachibana, M. Scientific Reports 2019, 9, (1), 14004.

Das, S., Idate, R., Regan, D. P., Fowles, J. S., Lana, S. E., Thamm, D. H., Gustafson, D. L., & Duval, D. L. (2021). Immune pathways and TP53 missense mutations are associated with longer survival in canine osteosarcoma. Communications Biology, 4(1). https://doi.org/10.1038/s42003-021-02683-0

Dasari, S., Njiki, S., Mbemi, A., Yedjou, C. G., & Tchounwou, P. B. (2022). Pharmacological Effects of Cisplatin Combination with Natural Products in Cancer Chemotherapy. International Journal of Molecular Sciences, 23(3). https://doi.org/10.3390/ijms23031532

de Azevedo, J. W. V., de Medeiros Fernandes, T. A. A., Fernandes, J. V., de Azevedo, J. C. V., Lanza, D. C. F., Bezerra, C. M., Andrade, V. S., de Araújo, J. M. G., & Fernandes, J. V. (2020). Biology and pathogenesis of human osteosarcoma (Review). In Oncology Letters (Vol. 19, Issue 2, pp. 1099–1116). Spandidos Publications. https://doi.org/10.3892/ol.2019.11229

de Rooij, J. F., Heughebaert, J. C., & Nancollas, G. H. (1984). A pH Study of Calcium Phosphate Seeded Precipitation.

Decher, G., Eckle, M., Schmitt, J., & Struth, B. (1998). Layer-by-layer assembled multicomposite films. Current Opinion in Colloid and Interface Science, 3(1), 32–39. https://doi.org/10.1016/S1359-0294(98)80039-3

Decuzzi, P., Pasqualini, R., Arap, W., & Ferrari, M. (2009). Intravascular delivery of particulate systems: Does geometry really matter? In Pharmaceutical Research (Vol. 26, Issue 1, pp. 235–243). https://doi.org/10.1007/s11095-008-9697-x

Denduluri, S. K., Wang, Z., Yan, Z., Wang, J., Wei, Q., Mohammed, M. K., Haydon, R. C., Luu, H. H., & He, T. C. (2016). Molecular pathogenesis and therapeutic strategies of human osteosarcoma. In Journal of Biomedical Research (Vol. 30, Issue 1, pp. 5–18). Nanjing Medical University. https://doi.org/10.7555/JBR.30.20150075

Deng, Z., Huang, Z., Ding, Y., Su, Y., Chan, C. M., & Niu, X. (2020). High-Grade Surface Osteosarcoma: Clinical Features and Oncologic Outcome. Journal of Bone Oncology, 23. https://doi.org/10.1016/j.jbo.2020.100288

Desai, S. A., Manjappa, A., & Khulbe, P. (2021). Drug delivery nanocarriers and recent advances ventured to improve therapeutic efficacy against osteosarcoma: an overview. In Journal of the Egyptian National Cancer Institute (Vol. 33, Issue 1). Springer Science and Business Media Deutschland GmbH. https://doi.org/10.1186/s43046-021-00059-3

Desmond, L. J., Phan, A. N., & Gentile, P. (2021). Critical overview on the green synthesis of carbon quantum dots and their application for cancer therapy. In Environmental Science: Nano (Vol. 8, Issue 4, pp. 848–862). Royal Society of Chemistry. https://doi.org/10.1039/d1en00017a

Dolan, E. B., Haugh, M. G., Tallon, D., Casey, C., & McNamara, L. M. (2012). Heat-shock-induced cellular responses to temperature elevations occurring during orthopaedic cutting. Journal of the Royal Society Interface, 9(77), 3503–3513. https://doi.org/10.1098/rsif.2012.0520

Dong, H., Ma, J., Wang, J., Wu, Z. S., Sinko, P. J., & Jia, L. (2016). A Biofunctional Molecular Beacon for Detecting Single Base Mutations in Cancer Cells. Molecular Therapy - Nucleic Acids, 5, e302. https://doi.org/10.1038/mtna.2016.18

Dong, L., Xia, S., Wu, K., Huang, Z., Chen, H., Chen, J., & Zhang, J. (2010). A pH/Enzyme-responsive tumor-specific delivery system for doxorubicin. Biomaterials, 31(24), 6309–6316. https://doi.org/10.1016/j.biomaterials.2010.04.049

Dong, Y., Pang, H., Yang, H. bin, Guo, C., Shao, J., Chi, Y., Li, C. M., & Yu, T. (2013). Carbon-based dots co-doped with nitrogen and sulfur for high quantum yield and excitation-independent emission. Angewandte Chemie - International Edition, 52(30), 7800–7804. https://doi.org/10.1002/anie.201301114

Du, F., Zhang, M., Li, X., Li, J., Jiang, X., Li, Z., Hua, Y., Shao, G., Jin, J., Shao, Q., Zhou, M., & Gong, A. (2014). Economical and green synthesis of bagasse-derived fluorescent carbon dots for biomedical applications. Nanotechnology, 25(31). https://doi.org/10.1088/0957-4484/25/31/315702

Dubas, S. T., & Schlenoff, J. B. (2001). Swelling and smoothing of polyelectrolyte multilayers by salt. Langmuir, 17(25), 7725–7727. https://doi.org/10.1021/la0112099

Duong, V. A., Nguyen, T. T. L., & Maeng, H. J. (2020). Preparation of solid lipid nanoparticles and nanostructured lipid carriers for drug delivery and the effects of preparation parameters of solvent injection method. In Molecules (Vol. 25, Issue 20). MDPI AG. https://doi.org/10.3390/molecules25204781

Efros, A. L., & Brus, L. E. (2021). Nanocrystal Quantum Dots: From Discovery to Modern Development. In ACS Nano (Vol. 15, Issue 4, pp. 6192–6210). American Chemical Society. https://doi.org/10.1021/acsnano.1c01399

Ekladious, I., Colson, Y. L., & Grinstaff, M. W. (2019). Polymer–drug conjugate therapeutics: advances, insights and prospects. In Nature Reviews Drug Discovery (Vol. 18, Issue 4, pp. 273–294). Nature Publishing Group. https://doi.org/10.1038/s41573-018-0005-0

Elizarova, I. S., & Luckham, P. F. (2016). Fabrication of polyelectrolyte multilayered nano-capsules using a continuous layer-by-layer approach. Journal of Colloid and Interface Science, 470, 92–99. https://doi.org/10.1016/j.jcis.2016.02.052

Elsabahy, M., & Wooley, K. L. (2012). Design of polymeric nanoparticles for biomedical delivery applications. Chemical Society Reviews, 41(7), 2545–2561. https://doi.org/10.1039/c2cs15327k

Endo, M., Yoshida, T., Yamamoto, H., Ishii, T., Setsu, N., Kohashi, K., Matsunobu, T., Iwamoto, Y., & Oda, Y. (2013). Low-grade central osteosarcoma arising from bone infarct. Human Pathology, 44(6), 1184–1189. https://doi.org/10.1016/j.humpath.2012.11.011

Esfandiari N, Bagheri Z, Ehtesabi H, Fatahi Z, Tavana H, Latifi H. Effect of carbonization degree of carbon dots on cytotoxicity and photo-induced toxicity to cells. Heliyon. 2019 Dec 5;5(12):e02940. doi: 10.1016/j.heliyon.2019.e02940. PMID: 31872119; PMCID: PMC6909074.

Estelrich, J., & Antònia Busquets, M. (2018). Iron oxide nanoparticles in photothermal therapy. In Molecules (Vol. 23, Issue 7). MDPI AG. https://doi.org/10.3390/molecules23071567

Fanelli, M., Tavanti, E., Patrizio, M. P., Vella, S., Fernandez-Ramos, A., Magagnoli, F., Luppi, S., Hattinger, C. M., & Serra, M. (2020). Cisplatin Resistance in Osteosarcoma: In vitro Validation of Candidate DNA Repair-Related Therapeutic Targets and Drugs for Tailored Treatments. Frontiers in Oncology, 10. https://doi.org/10.3389/fonc.2020.00331

Fang, L., Zhang, L., Chen, Z., Zhu, C., Liu, J., & Zheng, J. (2017). Ammonium citrate derived carbon quantum dot as on-off-on fluorescent sensor for detection of chromium(VI) and sulfites. Materials Letters, 191, 1–4. https://doi.org/10.1016/j.matlet.2016.12.098

Farghaly, R., Zaki, I., Gouda, I., Abdelfatah, M., Ghoneimy, A. el, Sherbiny, M. el, Soliman, R., & Zamzam, M. (2017). Value of dynamic magnetic resonance imaging in preoperative evaluation of pediatric osteosarcoma. Egyptian Journal of Radiology and Nuclear Medicine, 48(2), 461–465. https://doi.org/10.1016/j.ejrnm.2016.06.022

Feng, M., Wang, Y., He, B., Chen, X., & Sun, J. (2022). Chitin-Based Carbon Dots with Tunable Photoluminescence for Fe3+Detection. ACS Applied Nano Materials, 5(5), 7502–7511. https://doi.org/10.1021/acsanm.2c01512

Fernandes, I., Melo-Alvim, C., Lopes-Brás, R., Esperança-Martins, M., & Costa, L. (2021). Osteosarcoma pathogenesis leads the way to new target treatments. International Journal of Molecular Sciences, 22(2), 1–19. https://doi.org/10.3390/ijms22020813

Ferreira, Q., Gomes, P. J., Ribeiro, P. A., Jones, N. C., Hoffmann, S. v., Mason, N. J., Oliveira, O. N., & Raposo, M. (2013). Determination of degree of ionization of poly(allylamine hydrochloride) (PAH) and poly[1-[4-(3-carboxy-4 hydroxyphenylazo)benzene sulfonamido]-1,2- ethanediyl, sodium salt] (PAZO) in layer-by-layer films using vacuum photoabsorption spectroscopy. Langmuir, 29(1), 448–455. https://doi.org/10.1021/la304036h

Forest, V., Cottier, M., & Pourchez, J. (2015). Electrostatic interactions favor the binding of positive nanoparticles on cells: A reductive theory. Nano Today, 10(6), 677–680. https://doi.org/10.1016/j.nantod.2015.07.002

Fu, C., & Ravindra, N. M. (2012). Magnetic iron oxide nanoparticles: Synthesis and applications. Bioinspired, Biomimetic and Nanobiomaterials, 1(4), 229–244. https://doi.org/10.1680/bbn.12.00014

Fukuhara, K., Ikawa, K., Morikawa, N., & Kumagai, K. (2008). Population pharmacokinetics of high-dose methotrexate in Japanese adult patients with malignancies: A concurrent analysis of the serum and urine concentration data. Journal of Clinical Pharmacy and Therapeutics, 33(6), 677–684. https://doi.org/10.1111/j.1365-2710.2008.00966.x

Funhoff, A. M., van Nostrum, C. F., Koning, G. A., E Schuurmans-Nieuwenbroek, N. M., A Crommelin, D. J., & Hennink, W. E. (2004). Endosomal Escape of Polymeric Gene Delivery Complexes Is Not Always Enhanced by Polymers Buffering at Low pH. https://doi.org/10.1021/bm034041

Gamberi G, Benassi M, S, Bohling T, Ragazzini P, Molendini L, Sollazzo M, R, Pompetti F, Merli M, Magagnoli G, Balladelli A, Picci P: C-myc and c-fos in Human Osteosarcoma: Prognostic Value of mRNA and Protein Expression. Oncology 1998;55:556-563. doi: 10.1159/000011912

Gamcsik, M. P., Kasibhatla, M. S., Teeter, S. D., & Colvin, O. M. (2012). Glutathione levels in human tumors. In Biomarkers (Vol. 17, Issue 8, pp. 671–691). https://doi.org/10.3109/1354750X.2012.715672

Gao, N., Yang, W., Nie, H., Gong, Y., Jing, J., Gao, L., & Zhang, X. (2017). Turn-on theranostic fluorescent nanoprobe by electrostatic self-assembly of carbon dots with doxorubicin for targeted cancer cell imaging, in vivo hyaluronidase analysis, and targeted drug delivery. Biosensors and Bioelectronics, 96, 300–307. https://doi.org/10.1016/j.bios.2017.05.019

Gao, Z., Zhao, G. S., Lv, Y., Peng, D., Tang, X., Song, H., & Guo, Q. N. (2019). Anoikis-resistant human osteosarcoma cells display significant angiogenesis by activating the Src kinase-mediated MAPK pathway. Oncology Reports, 41(1), 235–245. https://doi.org/10.3892/or.2018.6827

García, M. C., Aloisio, C., Onnainty, R., & Ullio-Gamboa, G. (2018). Self-assembled nanomaterials. In Nanobiomaterials: Nanostructured Materials for Biomedical Applications (pp. 41–94). Elsevier Inc. https://doi.org/10.1016/B978-0-08-100716-7.00003-9

Gaspar, N., Marques da Costa, M. E., Fromigue, O., Droit, R., Berlanga, P., & Marchais, A. (2020). Recent advances in understanding osteosarcoma and emerging therapies. Faculty Reviews, 9. https://doi.org/10.12703/r/9-18

Gaynanova, G. A., Bekmukhametova, A. M., Kashapov, R. R., Pavlov, R. v., Vasilieva, E. A., Lenina, O. A., Nizameev, I. R., Kadirov, M. K., Ziganshiń, A. Y., Petrov, K. A., & Zakharova, L. Y. (2020). The synthesis of CdSe quantum dots stabilized by polymers and polyelectrolyte capsules. Surface Innovations, 8(1–2), 38–45. https://doi.org/10.1680/jsuin.19.00045

Gennady N. Machak, Sergey I. Tkachev, Yuriy N. Solovyev, Pavel A. Sinyukov, Stanislav M. Ivanov, Natalya V. Kochergina, Alexey D. Ryjkov, Valery V. Tepliakov, Benjamin Y. Bokhian, Valeria V. Glebovskaya, Neoadjuvant Chemotherapy and Local Radiotherapy for High-Grade Osteosarcoma of the Extremities, Mayo Clinic Proceedings, Volume 78, Issue 2, 2003, Pages 147-155, ISSN 0025-6196, https://doi.org/10.4065/78.2.147.

Gill, J., & Gorlick, R. (2021). Advancing therapy for osteosarcoma. In Nature Reviews Clinical Oncology (Vol. 18, Issue 10, pp. 609–624). Nature Research. https://doi.org/10.1038/s41571-021-00519-8

Gratton SE, Ropp PA, Pohlhaus PD, Luft JC, Madden VJ, Napier ME, DeSimone JM. The effect of particle design on cellular internalization pathways. Proc Natl Acad Sci U S A. 2008 Aug 19;105(33):11613-8. doi: 10.1073/pnas.0801763105

Goel, G., Kumar, A., Puniya, A. K., Chen, W., & Singh, K. (2005). Molecular beacon: A multitask probe. In Journal of Applied Microbiology (Vol. 99, Issue 3, pp. 435–442). https://doi.org/10.1111/j.1365-2672.2005.02663.x

Gomes, M. F., Gomes, Y. F., Lopes-Moriyama, & A., de Barros Neto, E. L., & Pereira De Souza, C. (n.d.). Design of carbon quantum dots via hydrothermal carbonization synthesis from renewable precursors. https://doi.org/10.1007/s13399-019-00387-4/Published

Gorlick, R., & Khanna, C. (2010). Osteosarcoma. In Journal of Bone and Mineral Research (Vol. 25, Issue 4, pp. 683–691). https://doi.org/10.1002/jbmr.77

Gudimella, K. K., Appidi, T., Wu, H. F., Battula, V., Jogdand, A., Rengan, A. K., & Gedda, G. (2021). Sand bath assisted green synthesis of carbon dots from citrus fruit peels for free radical scavenging and cell imaging. Colloids and Surfaces B: Biointerfaces, 197. https://doi.org/10.1016/j.colsurfb.2020.111362
Guimarães, D., Cavaco-Paulo, A., & Nogueira, E. (2021). Design of liposomes as drug delivery system for therapeutic applications. In International Journal of Pharmaceutics (Vol. 601). Elsevier B.V. https://doi.org/10.1016/j.ijpharm.2021.120571

Guzmán E., Raquel Chuliá-Jordán , Francisco Ortega and Ramón G. Rubio, Influence of the percentage of acetylation on the assembly of LbL multilayers of poly(acrylic acid) and chitosan, Phys. Chem. Chem. Phys., 2011, 13, 18200-18207, DOI: 10.1039/C1CP21609K

Guzmán, E., Ritacco, H., Rubio, J. E. F., Rubio, R. G., & Ortega, F. (2009). Salt-induced changes in the growth of polyelectrolyte layers of poly(diallyl-dimethylammonium chloride) and poly(4-styrene sulfonate of sodium). Soft Matter, 5(10), 2130–2142. https://doi.org/10.1039/b901193e

Guzmán, E., Ritacco, H. A., Ortega, F., & Rubio, R. G. (2012). Growth of polyelectrolyte layers formed by poly(4-styrenesulfonate sodium salt) and two different polycations: New insights from study of adsorption kinetics. Journal of Physical Chemistry C, 116(29), 15474–15483. https://doi.org/10.1021/jp304522t

Guzmán, E., Mateos-Maroto, A., Ruano, M., Ortega, F., & Rubio, R. G. (2017). Layer-by-Layer polyelectrolyte assemblies for encapsulation and release of active compounds. In Advances in Colloid and Interface Science (Vol. 249, pp. 290–307). Elsevier B.V. https://doi.org/10.1016/j.cis.2017.04.009

Hameddbarabadii, M. (n.d.). Nanotechnology in the Life Sciences Cancer Nanotheranostics Volume 2. http://www.springer.com/series/15921

Hammond, P. T. (2011). Engineering materials layer-by-layer: Challenges and opportunities in multilayer assembly. In AIChE Journal (Vol. 57, Issue 11, pp. 2928–2940). https://doi.org/10.1002/aic.12769

Hanahan, D., & Weinberg, R. A. (2000). The Hallmarks of Cancer Review evolve progressively from normalcy via a series of pre. In Cell (Vol. 100).

Hanahan, D., & Weinberg, R. A. (2011). Hallmarks of cancer: The next generation. In Cell (Vol. 144, Issue 5, pp. 646–674). https://doi.org/10.1016/j.cell.2011.02.013

Hattinger, C. M., Patrizio, M. P., Fantoni, L., Casotti, C., Riganti, C., & Serra, M. (2021). Drug resistance in osteosarcoma: Emerging biomarkers, therapeutic targets and treatment strategies. In Cancers (Vol. 13, Issue 12). MDPI. https://doi.org/10.3390/cancers13122878

Hong, X., Li, J., Wang, M., Xu, J., Guo, W., Li, J., Bai, Y., & Li, T. (2004). Fabrication of magnetic luminescent nanocomposites by a layer-by-layer self-assembly approach. Chemistry of Materials, 16(21), 4022–4027. https://doi.org/10.1021/cm049422o

Howell, J. D. (1995). Technology in the hospital : transforming patient care in the early twentieth century. Johns Hopkins University Press.

Hu, Q., Sun, W., Qian, C., Wang, C., Bomba, H. N., & Gu, Z. (2015). Anticancer Platelet-Mimicking Nanovehicles. Advanced Materials, 27(44), 7043–7050. https://doi.org/10.1002/adma.201503323

Huang, H. S., & Hainfeld, J. F. (2013). Intravenous magnetic nanoparticle cancer hyperthermia. International Journal of Nanomedicine, 8, 2521–2532. https://doi.org/10.2147/IJN.S43770

Huang, X., Wu, W., Yang, W., Qing, X., & Shao, Z. (2020). Surface engineering of nanoparticles with ligands for targeted delivery to osteosarcoma. In Colloids and Surfaces B: Biointerfaces (Vol. 190). Elsevier B.V. https://doi.org/10.1016/j.colsurfb.2020.110891

Idrees H, Zaidi SZJ, Sabir A, Khan RU, Zhang X, Hassan SU. A Review of Biodegradable Natural Polymer-Based Nanoparticles for Drug Delivery Applications. Nanomaterials (Basel). 2020 Oct 5;10(10):1970. doi: 10.3390/nano10101970. PMID: 33027891; PMCID: PMC7600772.

Iravani, S., & Varma, R. S. (2020). Green synthesis, biomedical and biotechnological applications of carbon and graphene quantum dots. A review. In Environmental Chemistry Letters (Vol. 18, Issue 3, pp. 703–727). Springer. https://doi.org/10.1007/s10311-020-00984-0

Itoh, K., Tokumi, S., Kimura, T., & Nagase, A. (2008). Reinvestigation on the buildup mechanism of alternate multilayers consisting of poly(L-glutamic acid) and poly(L-, D-, and DL-lysines). Langmuir, 24(23), 13426–13433. https://doi.org/10.1021/la8015832

Iturrioz-Rodríguez, N., Correa-Duarte, M. A., & Fanarraga, M. L. (2019). Controlled drug delivery systems for cancer based on mesoporous silica nanoparticles. In International Journal of Nanomedicine (Vol. 14, pp. 3389–3401). Dove Medical Press Ltd. https://doi.org/10.2147/IJN.S198848

J.H. Goldie, L.A. Price, K.R. Harrap, Methotrexate toxicity: Correlation with duration of administration, plasma levels, dose and excretion pattern, European Journal of Cancer (1965), Volume 8, Issue 4, 1972, Pages 409-414, ISSN 0014-2964, https://doi.org/10.1016/0014-2964(72)90125-9.

J. Lyklema, Fundamentals of Interface and Colloid Science, Elsevier, 2005, Volume IV

Jack A. Roth, Richard J. Cristiano, Gene Therapy for Cancer: What Have We Done and Where Are We Going?, JNCI: Journal of the National Cancer Institute, Volume 89, Issue 1, 1 January 1997, Pages 21–39, https://doi.org/10.1093/jnci/89.1.21

Jamieson, T., Bakhshi, R., Petrova, D., Pocock, R., Imani, M., & Seifalian, A. M. (2007). Biological applications of quantum dots. In Biomaterials (Vol. 28, Issue 31, pp. 4717–4732). https://doi.org/10.1016/j.biomaterials.2007.07.014

Jana, P., & Dev, A. (2022). Carbon quantum dots: A promising nanocarrier for bioimaging and drug delivery in cancer. In Materials Today Communications (Vol. 32). Elsevier Ltd. https://doi.org/10.1016/j.mtcomm.2022.104068

Jasieniak, J., Califano, M., & Watkins, S. E. (2011). Size-dependent valence and conduction band-edge energies of semiconductor nanocrystals. ACS Nano, 5(7), 5888–5902. https://doi.org/10.1021/nn201681s

Jeelani S, Reddy RC, Maheswaran T, Asokan GS, Dany A, Anand B. Theranostics: A treasured tailor for tomorrow. J Pharm Bioallied Sci. 2014 Jul;6(Suppl 1):S6-8. doi: 10.4103/0975-7406.137249.

Jeon, H., Kim, J., Lee, Y. M., Kim, J., Choi, H. W., Lee, J., Park, H., Kang, Y., Kim, I. S., Lee, B. H., Hoffman, A. S., & Kim, W. J. (2016). Poly-paclitaxel/cyclodextrin-SPION nano-assembly for magnetically guided drug delivery system. Journal of Controlled Release, 231, 68–76. https://doi.org/10.1016/j.jconrel.2016.01.006

Jiang, C., Wu, H., Song, X., Ma, X., Wang, J., & Tan, M. (2014). Presence of photoluminescent carbon dots in Nescafe® original instant coffee: Applications to bioimaging. Talanta, 127, 68–74. https://doi.org/10.1016/j.talanta.2014.01.046

Jiang, Q., jing, Y., Ni, Y., Gao, R., & Zhou, P. (2020). Potentiality of carbon quantum dots derived from chitin as a fluorescent sensor for detection of ClO−. Microchemical Journal, 157. https://doi.org/10.1016/j.microc.2020.105111

Jourdainne, L., Lecuyer, S., Arntz, Y., Picart, C., Schaaf, P., Senger, B., Voegel, J. C., Lavalle, P., & Charitat, T. (2008). Dynamics of poly(L-lysine) in hyaluronic acid/poly(L-lysine) multilayer films studied by fluorescence recovery after pattern photobleaching. Langmuir, 24(15), 7842–7847. https://doi.org/10.1021/la7040168

Junttila, M. R., & de Sauvage, F. J. (2013). Influence of tumour micro-environment heterogeneity on therapeutic response. In Nature (Vol. 501, Issue 7467, pp. 346–354). https://doi.org/10.1038/nature12626

Kalenichenko, D., Nifontova, G., Karaulov, A., Sukhanova, A., & Nabiev, I. (2021). Designing functionalized polyelectrolyte microcapsules for cancer treatment. Nanomaterials, 11(11). https://doi.org/10.3390/nano11113055

Kango, S., Kalia, S., Thakur, P., Kumari, B., & Pathania, D. (2014). Semiconductor–polymer hybrid materials. Advances in Polymer Science, 267, 283–312. https://doi.org/10.1007/12_2014_295

Kartalou, M., & Essigmann, J. M. (2001). Mechanisms of resistance to cisplatin. In Mutation Research (Vol. 478).

Khalid N, Azimpouran M. Necrosis. In: StatPearls. StatPearls Publishing, Treasure Island (FL); 2022. PMID: 32491559.

Kim, J. H., Chin, B. R., Kim, Y., Kim, J. R., & Baek, S. H. (n.d.). Differential Sensitivity of Taxol-induced Apoptosis in U2OS and SaOS2 Osteogenic Sarcoma Cells.

Kubo, T., Furuta, T., Johan, M. P., Adachi, N., & Ochi, M. (2016). Percent slope analysis of dynamic magnetic resonance imaging for assessment of chemotherapy response of osteosarcoma or Ewing sarcoma: systematic review and meta-analysis. Skeletal Radiology, 45(9), 1235–1242. https://doi.org/10.1007/s00256-016-2410-y

Kue, C. S., Kamkaew, A., Burgess, K., Kiew, L. v., Chung, L. Y., & Lee, H. B. (2016). Small Molecules for Active Targeting in Cancer. Medicinal Research Reviews, 36(3), 494–575. https://doi.org/10.1002/med.21387

Kumar, S., Sub- and Supercritical Water Technology for Biofuels. In *Advanced Biofuels and Bioproducts*, Lee, J. W., Ed. Springer New York: New York, NY, 2013; pp 147-183.

Kumari, A., Yadav, S. K., & Yadav, S. C. (2010). Biodegradable polymeric nanoparticles based drug delivery systems. In Colloids and Surfaces B: Biointerfaces (Vol. 75, Issue 1, pp. 1–18). https://doi.org/10.1016/j.colsurfb.2009.09.001

Kunde, S. S., & Wairkar, S. (2021). Platelet membrane camouflaged nanoparticles: Biomimetic architecture for targeted therapy. In International Journal of Pharmaceutics (Vol. 598). Elsevier B.V. https://doi.org/10.1016/j.ijpharm.2021.120395

Kuo, T. R., Lee, C. F., Lin, S. J., Dong, C. Y., Chen, C. C., & Tan, H. Y. (2011). Studies of intracorneal distribution and cytotoxicity of quantum dots: Risk assessment of eye exposure. Chemical Research in Toxicology, 24(2), 253–261. https://doi.org/10.1021/tx100376n

Kurian, M., & Paul, A. (2021). Recent trends in the use of green sources for carbon dot synthesis-A short review. Carbon Trends, 3, 32. https://doi.org/10.1016/j.cartre.2021.10

Labelle, M., Begum, S., & Hynes, R. O. (2011). Direct Signaling between Platelets and Cancer Cells Induces an Epithelial-Mesenchymal-Like Transition and Promotes Metastasis. Cancer Cell, 20(5), 576–590. https://doi.org/10.1016/j.ccr.2011.09.009

Ladam, G., Schaad, P., Voegel, J. C., Schaaf, P., Decher, G., & Cuisinier, F. (2000). In situ determination of the structural properties of initially deposited polyelectrolyte multilayers. Langmuir, 16(3), 1249–1255. https://doi.org/10.1021/la990650k

LeBert, D. C., Squirrell, J. M., Rindy, J., Broadbridge, E., Lui, Y., Zakrzewska, A., Eliceiri, K. W., Meijer, A. H., & Huttenlocher, A. (2015). Matrix metalloproteinase 9 modulates collagen matrices and wound repair. Development (Cambridge), 142(12), 2136–2146. https://doi.org/10.1242/dev.121160

Lee, B. K., Yun, Y. H., & Park, K. (2015). Smart nanoparticles for drug delivery: Boundaries and opportunities. Chemical Engineering Science, 125, 158–164. https://doi.org/10.1016/j.ces.2014.06.042

Li, F., Liang, Z., Liu, J., Sun, J., Hu, X., Zhao, M., Liu, J., Bai, R., Kim, D., Sun, X., Hyeon, T., & Ling, D. (2019). Dynamically Reversible Iron Oxide Nanoparticle Assemblies for Targeted Amplification of T1-Weighted Magnetic Resonance Imaging of Tumors. Nano Letters, 19(7), 4213–4220. https://doi.org/10.1021/acs.nanolett.8b04411

Li, S. D., & Huang, L. (2009). Nanoparticles evading the reticuloendothelial system: Role of the supported bilayer. Biochimica et Biophysica Acta - Biomembranes, 1788(10), 2259–2266. https://doi.org/10.1016/j.bbamem.2009.06.022

Li, Y.; Liu, Y.; Tan, H.; Zhang, Y.; Yue, M. *Int J Environ Res Public Health* 2016, 13, (5), 461.

Li, X., Rui, M., Song, J., Shen, Z. and Zeng, H. (2015), Carbon and Graphene Quantum Dots for Optoelectronic and Energy Devices: A Review. Adv. Funct. Mater., 25: 4929-4947. https://doi.org/10.1002/adfm.201501250

Li, X., Zhou, L., Wei, Y., El-Toni, A. M., Zhang, F., & Zhao, D. (2014). Anisotropic growth-induced synthesis of dual-compartment janus mesoporous silica nanoparticles for bimodal triggered drugs delivery. Journal of the American Chemical Society, 136(42), 15086–15092. https://doi.org/10.1021/ja508733r

Liideritz, O., Galanos, C., Lehmann, V., Nurminen, M., Rietschel, E. T., Rosenfelder, G., Simon, M., Westphal, O., & Liide-Ritz, O. (1973). Lipid A: Chemical Structure and Biological Activity. In THE JOURNAL OF INFECTIOUS DISEASES • (Vol. 128). https://academic.oup.com/jid/article/128/Supplement_1/S17/926628

Lim, C., Sim, T., Hoang, N. H., & Oh, K. T. (2017). A stable nanoplatform for antitumor activity using PEG-PLL-PLA triblock co-polyelectrolyte. Colloids and Surfaces B: Biointerfaces, 153, 10–18. https://doi.org/10.1016/j.colsurfb.2017.01.027

Lin, J., & Alexander-Katz, A. (2013). Cell membranes open “doors” for cationic nanoparticles/ biomolecules: Insights into uptake kinetics. ACS Nano, 7(12), 10799–10808. https://doi.org/10.1021/nn4040553

Lin, Y. S., Tsai, C. P., Huang, H. Y., Kuo, C. T., Hung, Y., Huang, D. M., Chen, Y. C., & Mou, C. Y. (2005). Well-ordered mesoporous silica nanoparticles as cell markers. Chemistry of Materials, 17(18), 4570–4573. https://doi.org/10.1021/cm051014c

Lipton, J., Weng, G. M., Röhr, J. A., Wang, H., & Taylor, A. D. (2020). Layer-by-Layer Assembly of Two-Dimensional Materials: Meticulous Control on the Nanoscale. In Matter (Vol. 2, Issue 5, pp. 1148–1165). Cell Press. https://doi.org/10.1016/j.matt.2020.03.012

Lomis, N., Westfall, S., Farahdel, L., Malhotra, M., Shum-Tim, D., & Prakash, S. (2016). Human serum albumin nanoparticles for use in cancer drug delivery: Process optimization and in vitro characterization. Nanomaterials, 6(6). https://doi.org/10.3390/nano6060116

Luetke, A., Meyers, P. A., Lewis, I., & Juergens, H. (2014). Osteosarcoma treatment - Where do we stand? A state of the art review. In Cancer Treatment Reviews (Vol. 40, Issue 4, pp. 523–532). https://doi.org/10.1016/j.ctrv.2013.11.006

Maeda, * H, Wu, J., Sawa, T., Matsumura, Y., & Hori, K. (2000). Tumor vascular permeability and the EPR effect in macromolecular therapeutics: a review a , a a b c. In Journal of Controlled Release (Vol. 65). www.elsevier.com/locate/jconrel

Maeda, H., Nakamura, H., & Fang, J. (2013). The EPR effect for macromolecular drug delivery to solid tumors: Improvement of tumor uptake, lowering of systemic toxicity, and distinct tumor imaging in vivo. In Advanced Drug Delivery Reviews (Vol. 65, Issue 1, pp. 71–79). https://doi.org/10.1016/j.addr.2012.10.002

Maleki Dana, P., Hallajzadeh, J., Asemi, Z., Mansournia, M. A., & Yousefi, B. (2021). Chitosan applications in studying and managing osteosarcoma. In International Journal of Biological Macromolecules (Vol. 169, pp. 321–329). Elsevier B.V. https://doi.org/10.1016/j.ijbiomac.2020.12.058

Marchandet, L., Lallier, M., Charrier, C., Baud'huin, M., Ory, B., & Lamoureux, F. (2021). Mechanisms of resistance to conventional therapies for osteosarcoma. In Cancers (Vol. 13, Issue 4, pp. 1–24). MDPI AG. https://doi.org/10.3390/cancers13040683

Marie-France Penet, Balaji Krishnamachary, Zhihang Chen, Jiefu Jin, Zaver M. Bhujwalla, Chapter Seven - Molecular Imaging of the Tumor Microenvironment for Precision Medicine and Theranostics, Editor(s): Martin G. Pomper, Paul B. Fisher, Advances in Cancer Research, Academic Press, Volume 124, 2014, Pages 235-256, ISSN 0065-230X, ISBN 9780124116382, https://doi.org/10.1016/B978-0-12-411638-2.00007-0.

Markman, J. L., Rekechenetskiy, A., Holler, E., & Ljubimova, J. Y. (2013). Nanomedicine therapeutic approaches to overcome cancer drug resistance. In Advanced Drug Delivery Reviews (Vol. 65, Issues 13–14, pp. 1866–1879). Elsevier B.V. https://doi.org/10.1016/j.addr.2013.09.019

Martin-Liberal, J., Ochoa de Olza, M., Hierro, C., Gros, A., Rodon, J., & Tabernero, J. (2017). The expanding role of immunotherapy. In Cancer Treatment Reviews (Vol. 54, pp. 74–86). W.B. Saunders Ltd. https://doi.org/10.1016/j.ctrv.2017.01.008

Mateos-Maroto, A., Fernández-Peña, L., Abelenda-Núñez, I., Ortega, F., Rubio, R. G., & Guzmán, E. (2022). Polyelectrolyte Multilayered Capsules as Biomedical Tools. In Polymers (Vol. 14, Issue 3). MDPI. https://doi.org/10.3390/polym14030479

Mateos-maroto, A., Abelenda-núñez, I., Ortega, F., Rubio, R. G., & Guzmán, E. (2021). Polyelectrolyte multilayers on soft colloidal nanosurfaces: A new life for the layer-by-layer method. In Polymers (Vol. 13, Issue 8). MDPI AG. https://doi.org/10.3390/polym13081221
Meazza, C., Cefalo, G., Massimino, M., Daolio, P., Pastorino, U., Scanagatta, P., Morosi, C., Podda, M., Ferrari, A., Terenziani, M., Spreafico, F., Casanova, M., Parafioriti, A., Collini, P., Gandola, L., Bastoni, S., Biassoni, V., Schiavello, E., Chiaravalli, S., … Luksch, R. (2017). Primary metastatic osteosarcoma: results of a prospective study in children given chemotherapy and interleukin-2. Medical Oncology, 34(12). https://doi.org/10.1007/s12032-017-1052-9

Meng, W., Bai, X., Wang, B., Liu, Z., Lu, S., & Yang, B. (2019). Biomass-Derived Carbon Dots and Their Applications. In Energy and Environmental Materials (Vol. 2, Issue 3, pp. 172–192). John Wiley and Sons Inc. https://doi.org/10.1002/eem2.12038

Miele, E., Spinelli, G. P., Miele, E., Tomao, F., & Tomao, S. (2009). Albumin-bound formulation of paclitaxel (Abraxane ® ABI-007) in the treatment of breast cancer. In International Journal of Nanomedicine.

Miller, C., Rousseau, J., Ramogida, C.F., Celler, A., Rahmim, A., Uribe, C.F. (2022). Implications of physics, chemistry and biology for dosimetry calculations using theranostic pairs. Theranostics, 12(1), 232-259. https://doi.org/10.7150/thno.62851.

Misaghi, A., Goldin, A., Awad, M., & Kulidjian, A. A. (2018). Osteosarcoma: A comprehensive review. In SICOT-J (Vol. 4). EDP Sciences. https://doi.org/10.1051/sicotj/2017028

Mohseny, A. B., MacHado, I., Cai, Y., Schaefer, K. L., Serra, M., Hogendoorn, P. C. W., Llombart-Bosch, A., & Cleton-Jansen, A. M. (2011). Functional characterization of osteosarcoma cell lines provides representative models to study the human disease. Laboratory Investigation, 91(8), 1195–1205. https://doi.org/10.1038/labinvest.2011.72

Molaei, M. J. (2019). Carbon quantum dots and their biomedical and therapeutic applications: A review. RSC Advances, 9(12), 6460–6481. https://doi.org/10.1039/c8ra08088g

Moon, G. D., Choi, S. W., Cai, X., Li, W., Cho, E. C., Jeong, U., Wang, L. v., & Xia, Y. (2011). A new theranostic system based on gold nanocages and phase-change materials with unique features for photoacoustic imaging and controlled release. Journal of the American Chemical Society, 133(13), 4762–4765. https://doi.org/10.1021/ja200894u

Morton, S. W., Herlihy, K. P., Shopsowitz, K. E., Deng, Z. J., Chu, K. S., Bowerman, C. J., Desimone, J. M., & Hammond, P. T. (2013). Scalable manufacture of built-to-order nanomedicine: Spray-assisted layer-by-layer functionalization of PRINT nanoparticles. Advanced Materials, 25(34), 4707–4713. https://doi.org/10.1002/adma.201302025

Mousavi, S. M., Zarei, M., Hashemi, S. A., Ramakrishna, S., Chiang, W. H., Lai, C. W., & Gholami, A. (2020). Gold nanostars-diagnosis, bioimaging and biomedical applications. In Drug Metabolism Reviews (Vol. 52, Issue 2, pp. 299–318). Taylor and Francis Ltd. https://doi.org/10.1080/03602532.2020.1734021

Müller, M., Vörös, J., Csúcs, G., Walter, E., Danuser, G., Merkle, H. P., Spencer, N. D., & Textor, M. (2003). Surface modification of PLGA microspheres. Journal of Biomedical Materials Research - Part A, 66(1), 55–61. https://doi.org/10.1002/jbm.a.10502

Mura, S., & Couvreur, P. (2012). Nanotheranostics for personalized medicine. In Advanced Drug Delivery Reviews (Vol. 64, Issue 13, pp. 1394–1416). https://doi.org/10.1016/j.addr.2012.06.006

Nair, R. v., Thomas, R. T., Sankar, V., Muhammad, H., Dong, M., & Pillai, S. (2017). Rapid, Acid-Free Synthesis of High-Quality Graphene Quantum Dots for Aggregation Induced Sensing of Metal Ions and Bioimaging. ACS Omega, 2(11), 8051–8061. https://doi.org/10.1021/acsomega.7b01262
Nakamura, Y., Mochida, A., Choyke, P. L., & Kobayashi, H. (2016). Nanodrug Delivery: Is the Enhanced Permeability and Retention Effect Sufficient for Curing Cancer? In Bioconjugate Chemistry (Vol. 27, Issue 10, pp. 2225–2238). American Chemical Society. https://doi.org/10.1021/acs.bioconjchem.6b00437

Nakhaei, P., Margiana, R., Bokov, D. O., Abdelbasset, W. K., Jadidi Kouhbanani, M. A., Varma, R. S., Marofi, F., Jarahian, M., & Beheshtkhoo, N. (2021). Liposomes: Structure, Biomedical Applications, and Stability Parameters With Emphasis on Cholesterol. In Frontiers in Bioengineering and Biotechnology (Vol. 9). Frontiers Media S.A. https://doi.org/10.3389/fbioe.2021.705886

Narges Hadjesfandiari, Anilkumar Parambath, 13 - Stealth coatings for nanoparticles: Polyethylene glycol alternatives, Editor(s): Anilkumar Parambath, In Woodhead Publishing Series in Biomaterials, Engineering of

Biomaterials for Drug Delivery Systems, Woodhead Publishing, 2018, Pages 345-361, ISBN 9780081017500,https://doi.org/10.1016/B978-0-08-101750-0.00013-1.

Naumenko, E., Akhatova, F., Rozhina, E., & Fakhrullin, R. (2021). Revisiting the cytotoxicity of cationic polyelectrolytes as a principal component in layer-by-layer assembly fabrication. Pharmaceutics, 13(8). https://doi.org/10.3390/pharmaceutics13081230

Nguyen, H. A.; Srivastava, I.; Pan, D.; Gruebele, M. ACS Nano 2020, 14, (5), 6127-6137.

Neda Alasvand, Aleksandra M. Urbanska, Maryam Rahmati, Maryam Saeidifar, P. Selcan Gungor-Ozkerim, Farshid Sefat, Jayakumar Rajadas, Masoud Mozafari, Chapter 13 - Therapeutic Nanoparticles for Targeted Delivery of Anticancer Drugs, Editor(s): Alexandru Mihai Grumezescu, Multifunctional Systems for Combined Delivery, Biosensing and Diagnostics, Elsevier, 2017, Pages 245-259, ISBN 9780323527255, https://doi.org/10.1016/B978-0-323-52725-5.00013-7.

Nigam, S., & Bahadur, D. (2018). Doxorubicin-loaded dendritic-Fe3O4 supramolecular nanoparticles for magnetic drug targeting and tumor regression in spheroid murine melanoma model. Nanomedicine: Nanotechnology, Biology, and Medicine, 14(3), 759–768. https://doi.org/10.1016/j.nano.2018.01.005

Novoselova, M. v., Loh, H. M., Trushina, D. B., Ketkar, A., Abakumova, T. O., Zatsepin, T. S., Kakran, M., Brzozowska, A. M., Lau, H. H., Gorin, D. A., Antipina, M. N., & Brichkina, A. I. (2020). Biodegradable Polymeric Multilayer Capsules for Therapy of Lung Cancer. ACS Applied Materials and Interfaces, 12(5), 5610–5623. https://doi.org/10.1021/acsami.9b21381

Onzi, G., Guterres, S. S., Pohlmann, A. R., & Frank, L. A. (2021). Passive Targeting and the Enhanced Permeability and Retention (EPR) Effect. In The ADME Encyclopedia (pp. 1–13). Springer International Publishing. https://doi.org/10.1007/978-3-030-51519-5_108-1

Padeste, C., and S. Neuhaus. "Functional polymer structures." de Polymer Micro-and Nanografting, Reino Unido, William Andrew Publishing (2015): 1-10.

Pastorino, L., Dellacasa, E., Dabiri, M. H., Fabiano, B., & Erokhina, S. (2016). Towards the Fabrication of Polyelectrolyte-Based Nanocapsules for Bio-Medical Applications. BioNanoScience, 6(4), 496–501. https://doi.org/10.1007/s12668-016-0267-0

Patel, S., Kim, J., Herrera, M., Mukherjee, A., Kabanov, A. v., & Sahay, G. (2019). Brief update on endocytosis of nanomedicines. In Advanced Drug Delivery Reviews (Vol. 144, pp. 90–111). Elsevier B.V. https://doi.org/10.1016/j.addr.2019.08.004

Patel, A. (2020). Benign vs Malignant Tumors. In JAMA Oncology (Vol. 6, Issue 9, p. 1488). American Medical Association. https://doi.org/10.1001/jamaoncol.2020.2592

Patra, J. K., Das, G., Fraceto, L. F., Campos, E. V. R., Rodriguez-Torres, M. D. P., Acosta-Torres, L. S., Diaz-Torres, L. A., Grillo, R., Swamy, M. K., Sharma, S., Habtemariam, S., & Shin, H. S. (2018). Nano based drug delivery systems: Recent developments and future prospects 10 Technology 1007 Nanotechnology 03 Chemical Sciences 0306 Physical Chemistry (incl. Structural) 03 Chemical Sciences 0303 Macromolecular and Materials Chemistry 11 Medical and Health Sciences 1115 Pharmacology and Pharmaceutical Sciences

09 Engineering 0903 Biomedical Engineering Prof Ueli Aebi, Prof Peter Gehr. In Journal of Nanobiotechnology (Vol. 16, Issue 1). BioMed Central Ltd. https://doi.org/10.1186/s12951-018-0392-8

Pautke C, Schieker M, Tischer T, Kolk A, Neth P, Mutschler W, Milz S. Characterization of osteosarcoma cell lines MG-63, Saos-2 and U-2 OS in comparison to human osteoblasts. Anticancer Res. 2004 Nov-Dec;24(6):3743-8. PMID: 15736406.

Pei, D., & Buyanova, M. (2019). Overcoming Endosomal Entrapment in Drug Delivery. In Bioconjugate Chemistry (Vol. 30, Issue 2, pp. 273–283). American Chemical Society. https://doi.org/10.1021/acs.bioconjchem.8b00778

Piao, J. G., Wang, L., Gao, F., You, Y. Z., Xiong, Y., & Yang, L. (2014). Erythrocyte membrane is an alternative coating to polyethylene glycol for prolonging the circulation lifetime of gold nanocages for photothermal therapy. ACS Nano, 8(10), 10414–10425. https://doi.org/10.1021/nn503779d

Prabaharan, M., Grailer, J. J., Pilla, S., Steeber, D. A., & Gong, S. (2009). Gold nanoparticles with a monolayer of doxorubicin-conjugated amphiphilic block copolymer for tumor-targeted drug delivery. Biomaterials, 30(30), 6065–6075. https://doi.org/10.1016/j.biomaterials.2009.07.048

Prabhakar, U., Maeda, H., K. Jain, R., Sevick-Muraca, E. M., Zamboni, W., Farokhzad, O. C., Barry, S. T., Gabizon, A., Grodzinski, P., & Blakey, D. C. (2013). Challenges and key considerations of the enhanced permeability and retention effect for nanomedicine drug delivery in oncology. Cancer Research, 73(8), 2412–2417. https://doi.org/10.1158/0008-5472.CAN-12-4561

Prasannan, A.; Imae, T. Industrial & Engineering Chemistry Research 2013, 52, (44), 15673-15678.

Printezi, M. I., Kilgallen, A. B., Štibler, U., Teske, A. J., Cramer, M. J., G Sluijter, J. P., van Laake, L. W., G Bond, M. J., A Punt, C. J., May, A. M., van Laake, L. W., Printezi, M. I., Kilgallen, A. B., G Bond, M. J., Štibler, U., Putker, M., Teske, A. J., Cramer, M. J., A Punt, C. J., … May, A. M. (2022). Toxicity and efficacy of chronomodulated chemotherapy: a systematic review. In Review Lancet Oncol (Vol. 23). www.thelancet.com/oncology

Quadir, M. A., Morton, S. W., Deng, Z. J., Shopsowitz, K. E., Murphy, R. P., Epps, T. H., & Hammond, P. T. (2014). PEG-polypeptide block copolymers as pH-responsive endosome-solubilizing drug nanocarriers. Molecular Pharmaceutics, 11(7), 2420–2430. https://doi.org/10.1021/mp500162w

Rai, M., & Jamil, B. (2019). Nanotheranostics: Applications and limitations. In Nanotheranostics: Applications and Limitations. Springer International Publishing. https://doi.org/10.1007/978-3-030-29768-8

Rathore, R., & van Tine, B. A. (2021). Pathogenesis and current treatment of osteosarcoma: Perspectives for future therapies. In Journal of Clinical Medicine (Vol. 10, Issue 6, pp. 1–18). MDPI. https://doi.org/10.3390/jcm10061182

Reddick, W. E., Wang, S., Xiong, X., Glass, J. O., Wu, S., Kaste, S. C., Pratt, C. B., Meyer, W. H., & Fletcher, B. D. (2001). Dynamic magnetic resonance imaging of regional contrast access as an additional prognostic factor in pediatric osteosarcoma. Cancer, 91(12), 2230–2237. https://doi.org/10.1002/1097-0142(20010615)91:12<2230::AID-CNCR1253>3.0.CO;2-T

Reshma, V. G., & Mohanan, P. v. (2019). Quantum dots: Applications and safety consequences. In Journal of Luminescence (Vol. 205, pp. 287–298). Elsevier B.V. https://doi.org/10.1016/j.jlumin.2018.09.015

Richardson, J. J., Björnmalm, M., & Caruso, F. (2015). Technology-driven layer-by-layer assembly of nanofilms. In Science (Vol. 348, Issue 6233). American Association for the Advancement of Science. https://doi.org/10.1126/science.aaa2491

Rodan, S. B., Imai, Y., Thiede, M. A., Wesolowski, G., Thompson, D., Bar-Shavit, Z., Shull, S., Mann, K., & Rodan1, G. A. (1987). Characterization of a Human Osteosarcoma Cell Line (Saos-2) with Osteoblastic Properties. In CANCER RESEARCH (Vol. 47). http://aacrjournals.org/cancerres/article-pdf/47/18/4961/2428287/cr0470184961.pdf

Rosen, S. T., Lurie, R. H., Jaffe, N., Bruland, Ø. S., & Bielack, S. (n.d.). Cancer Treatment and Research Series Editor Pediatric and Adolescent Osteosarcoma edited by. www.springer.com/series/5808

Rozanova, N., & Zhang, J. (2009). Photothermal ablation therapy for cancer based on metal nanostructures. Science in China, Series B: Chemistry, 52(10), 1559–1575. https://doi.org/10.1007/s11426-009-0247-0

S. Busco, C. Buzzoni, S. Mallone, and A. Trama (2016). The burden of rare cancers in Italy, Epidemiol. Prev., vol. 40, no. Suppl 2:1, pp. 1-120.

Sadauskas, E., Wallin, H., Stoltenberg, M., Vogel, U., Doering, P., Larsen, A., & Danscher, G. (2007). Kupffer cells are central in the removal of nanoparticles from the organism. Particle and Fibre Toxicology, 4. https://doi.org/10.1186/1743-8977-4-10

Sager, R. (1991). Senescence As a Mode of Tumor Suppression. In Environmental Health Perspectives (Vol. 93).

Sahoo, B., Devi, K. S. P., Banerjee, R., Maiti, T. K., Pramanik, P., & Dhara, D. (2013). Thermal and pH responsive polymer-tethered multifunctional magnetic nanoparticles for targeted delivery of anticancer drug. ACS Applied Materials and Interfaces, 5(9), 3884–3893. https://doi.org/10.1021/am400572b

Saifuddin, A., Sharif, B., Gerrand, C., & Whelan, J. (2019). The current status of MRI in the pre-operative assessment of intramedullary conventional appendicular osteosarcoma. In Skeletal Radiology (Vol. 48, Issue 4, pp. 503–516). Springer Verlag. https://doi.org/10.1007/s00256-018-3079-1

Sakamoto, A., & Iwamoto, Y. (2008). Current Status and Perspectives Regarding the Treatment of Osteo-sarcoma: Chemotherapy. In Reviews on Recent Clinical Trials (Vol. 3).

Salomaki, M., & Kankare, J. (2009). Influence of synthetic polyelectrolytes on the growth and properties of hyaluronan-chitosan multilayers. Biomacromolecules, 10(2), 294–301. https://doi.org/10.1021/bm8010177

Santos, A. C., Pattekari, P., Jesus, S., Veiga, F., Lvov, Y., & Ribeiro, A. J. (2015). Sonication-Assisted Layer-by-Layer Assembly for Low Solubility Drug Nanoformulation. ACS Applied Materials and Interfaces, 7(22), 11972–11983. https://doi.org/10.1021/acsami.5b02002

Saurabh Bhatia, Natural Polymer Drug Delivery Systems: Nanoparticles, Plants, and Algae 1st ed. 2016, Springer Nature

Schneider, J., Reckmeier, C. J., Xiong, Y., von Seckendorff, M., Susha, A. S., Kasak, P., & Rogach, A. L. (2017). Molecular fluorescence in citric acid-based carbon dots. Journal of Physical Chemistry C, 121(3), 2014–2022. https://doi.org/10.1021/acs.jpcc.6b12519

Schwiertz, J., Meyer-Zaika, W., Ruiz-Gonzalez, L., González-Calbet, J. M., Vallet-Regí, M., & Epple, M. (2008). Calcium phosphate nanoparticles as templates for nanocapsules prepared by the layer-by-layer technique. Journal of Materials Chemistry, 18(32), 3831–3834. https://doi.org/10.1039/b803609h

Sears, S. M., Orwick, A., & Siskind, L. J. (2022). Modeling Cisplatin-Induced Kidney Injury to Increase Translational Potential. Nephron, 1–4. https://doi.org/10.1159/000525491

Shchipunov, Y. A., Khlebnikov, O. N., & Silant'ev, V. E. (2015). Carbon quantum dots hydrothermally synthesized from chitin. Polymer Science - Series B, 57(1), 16–22. https://doi.org/10.1134/S1560090415010121

Shen, L., Chaudouet, P., Ji, J., & Picart, C. (2011). PH-amplified multilayer films based on hyaluronan: Influence of HA molecular weight and concentration on film growth and stability. Biomacromolecules, 12(4), 1322–1331. https://doi.org/10.1021/bm200070k

Shi, Y., Li, C., Yang, M., Pan, X., & Hu, J. (2022). Docetaxel-loaded redox-sensitive nanoparticles self-assembling from poly(caprolactone) conjugates with disulfide-linked poly(ethylene glycol). Journal of Biomaterials Science, Polymer Edition. https://doi.org/10.1080/09205063.2022.2099664

Shin, S.H., Choi, Y.J., Lee, H. et al. Oxidative stress induced by low-dose doxorubicin promotes the invasiveness of osteosarcoma cell line U2OS in vitro. Tumor Biol. 37, 1591–1598 (2016). https://doi.org/10.1007/s13277-015-3702-x

Siafaka, P. I., Okur, N. Ü., Karantas, I. D., Okur, M. E., & Gündoğdu, E. A. (2021). Current update on nanoplatforms as therapeutic and diagnostic tools: A review for the materials used as nanotheranostics and imaging modalities. In Asian Journal of Pharmaceutical Sciences (Vol. 16, Issue 1, pp. 24–46). Shenyang Pharmaceutical University. https://doi.org/10.1016/j.ajps.2020.03.003

Siegel, R. L., Miller, K. D., Fuchs, H. E., & Jemal, A. (2022). Cancer statistics, 2022. CA: A Cancer Journal for Clinicians, 72(1), 7–33. https://doi.org/10.3322/caac.21708

Siepmann, J., & Siepmann, F. (2012). Modeling of diffusion controlled drug delivery. In Journal of Controlled Release (Vol. 161, Issue 2, pp. 351–362). https://doi.org/10.1016/j.jconrel.2011.10.006

Simionescu, Bogdan C., and Daniela Ivanov. "Natural and synthetic polymers for designing composite materials." Handbook of bioceramics and biocomposites. Springer, Cham, 2016. 233-286.

Singh, I., Arora, R., Dhiman, H., & Pahwa, R. (2018). Carbon quantum dots: Synthesis, characterization and biomedical applications. In Turkish Journal of Pharmaceutical Sciences (Vol. 15, Issue 2, pp. 219–230). Turkish Pharmacists Association. https://doi.org/10.4274/tjps.63497

Singh, S. K., Banala, V. T., Gupta, G. K., Verma, A., Shukla, R., Pawar, V. K., Tripathi, P., & Mishra, P. R. (2015). Development of docetaxel nanocapsules for improving in vitro cytotoxicity and cellular uptake in MCF-7 cells. Drug Development and Industrial Pharmacy, 41(11), 1759–1768. https://doi.org/10.3109/03639045.2014.1003220

Sk, M. A., Ananthanarayanan, A., Huang, L., Lim, K. H., & Chen, P. (2014). Revealing the tunable photoluminescence properties of graphene quantum dots. Journal of Materials Chemistry C, 2(34), 6954–6960. https://doi.org/10.1039/c4tc01191k

Smith, S. A., Selby, L. I., Johnston, A. P. R., & Such, G. K. (2019). The Endosomal Escape of Nanoparticles: Toward More Efficient Cellular Delivery. In Bioconjugate Chemistry (Vol. 30, Issue 2, pp. 263–272). American Chemical Society. https://doi.org/10.1021/acs.bioconjchem.8b00732

Sonali, Viswanadh, M. K., Singh, R. P., Agrawal, P., Mehata, A. K., Pawde, D. M., Narendra, Sonkar, R., & Muthu, M. S. (2018). Nanotheranostics: Emerging strategies for early diagnosis and therapy of brain cancer. In Nanotheranostics (Vol. 2, Issue 1, pp. 70–86). Ivyspring International Publisher. https://doi.org/10.7150/ntno.21638

Sriram, V., & Lee, J. Y. (2021). Calcium phosphate-polymeric nanoparticle system for co-delivery of microRNA-21 inhibitor and doxorubicin. Colloids and Surfaces B: Biointerfaces, 208. https://doi.org/10.1016/j.colsurfb.2021.112061

Steven M Frisch, Robert A Screaton, Anoikis mechanisms, Current Opinion in Cell Biology, Volume 13, Issue 5, 2001, Pages 555-562, ISSN 0955-0674, https://doi.org/10.1016/S0955-0674(00)00251-9.

Stewart, D. J. (2007). Mechanisms of resistance to cisplatin and carboplatin. In Critical Reviews in Oncology/Hematology (Vol. 63, Issue 1, pp. 12–31). https://doi.org/10.1016/j.critrevonc.2007.02.001

Suarasan, S., Focsan, M., Potara, M., Soritau, O., Florea, A., Maniu, D., & Astilean, S. (2016). Doxorubicin-incorporated nanotherapeutic delivery system based on gelatin-coated gold nanoparticles: Formulation, drug release, and multimodal imaging of cellular internalization. ACS Applied Materials and Interfaces, 8(35), 22900–22913. https://doi.org/10.1021/acsami.6b07583

Sultana, N., & Wang, M. (2008). Fabrication of HA/PHBV composite scaffolds through the emulsion freezing/freeze-drying process and characterisation of the scaffolds. Journal of Materials Science: Materials in Medicine, 19(7), 2555–2561. https://doi.org/10.1007/s10856-007-3214-3

Sun Y, Xia P, Zhang H, Liu B, Shi Y. P53 is required for Doxorubicin-induced apoptosis via the TGF-beta signaling pathway in osteosarcoma-derived cells. Am J Cancer Res. 2015 Dec 15;6(1):114-25. PMID: 27073729; PMCID: PMC4759403.

Surendran, P., Lakshmanan, A., Vinitha, G., Ramalingam, G., & Rameshkumar, P. (2020). Facile preparation of high fluorescent carbon quantum dots from orange waste peels for nonlinear optical applications. Luminescence, 35(2), 196–202. https://doi.org/10.1002/bio.3713

Swords, K. E., Bartline, P. B., Roguski, K. M., Bashaw, S. A., & Frederick, K. A. (2011). Assessment of polyelectrolyte coating stability under dynamic buffer conditions in CE. Journal of Separation Science, 34(18), 2427–2432. https://doi.org/10.1002/jssc.201100044

Tan, W., Wang, K., & Drake, T. J. (2004). Molecular beacons. In Current Opinion in Chemical Biology (Vol. 8, Issue 5, pp. 547–553). https://doi.org/10.1016/j.cbpa.2004.08.010

Tautzenberger, A., Kovtun, A., & Ignatius, A. (2012). Nanoparticles and their potential for application in bone. In International Journal of Nanomedicine (Vol. 7, pp. 4545–4557). https://doi.org/10.2147/IJN.S34127

Teja, A. S., & Koh, P. Y. (2009). Synthesis, properties, and applications of magnetic iron oxide nanoparticles. In Progress in Crystal Growth and Characterization of Materials (Vol. 55, Issues 1–2, pp. 22–45). https://doi.org/10.1016/j.pcrysgrow.2008.08.003

Torresmartinderosales, R., Tavaré, R., Paul, R. L., Jauregui-Osoro, M., Protti, A., Glaria, A., Varma, G., Szanda, I., & Blower, P. J. (2011). Synthesis of 64CuII- bis(dithiocarbamatebisphosphonate) and its conjugation with superparamagnetic iron oxide nanoparticles: In vivo evaluation as dual-modality PET-MRI agent. Angewandte Chemie - International Edition, 50(24), 5509–5513. https://doi.org/10.1002/anie.201007894

Urch, H., Vallet-Regi, M., Ruiz, L., Gonzalez-Calbet, J. M., & Epple, M. (2009). Calcium phosphate nanoparticles with adjustable dispersability and crystallinity. Journal of Materials Chemistry, 19(15), 2166–2171. https://doi.org/10.1039/b810026h

v N, N. B., & Ksyadav, H. (n.d.). DIFFERENT TECHNIQUES FOR PREPARATION OF POLYMERIC NANOPARTICLES-A REVIEW.

Vandarkuzhali, S. A. A., Jeyalakshmi, V., Sivaraman, G., Singaravadivel, S., Krishnamurthy, K. R., & Viswanathan, B. (2017). Highly fluorescent carbon dots from Pseudo-stem of banana plant: Applications as nanosensor and bio-imaging agents. Sensors and Actuators, B: Chemical, 252, 894–900. https://doi.org/10.1016/j.snb.2017.06.088

Vasudevan, D., Gaddam, R. R., Trinchi, A., & Cole, I. (2015). Core-shell quantum dots: Properties and applications. In Journal of Alloys and Compounds (Vol. 636, pp. 395–404). Elsevier Ltd. https://doi.org/10.1016/j.jallcom.2015.02.102

Vivero-Escoto, J.L., Slowing, I.I., Trewyn, B.G. and Lin, V.S.-Y. (2010), Mesoporous Silica Nanoparticles for Intracellular Controlled Drug Delivery. Small, 6: 1952-1967. https://doi.org/10.1002/smll.200901789

Volodkin, D. v., Larionova, N. I., & Sukhorukov, G. B. (2004). Protein encapsulation via porous CaCO3 microparticles templating. Biomacromolecules, 5(5), 1962–1972. https://doi.org/10.1021/bm049669e

Vozar, S., Poh, Y. C., Serbowicz, T., Bachner, M., Podsiadlo, P., Qin, M., Verploegen, E., Kotov, N., & Hart, A. J. (2009). Automated spin-assisted layer-by-layer assembly of nanocomposites. Review of Scientific Instruments, 80(2). https://doi.org/10.1063/1.3078009

W.P Tsang, Sophia P.Y Chau, S.K Kong, K.P Fung, T.T Kwok, Reactive oxygen species mediate doxorubicin induced p53-independent apoptosis, Life Sciences, Volume 73, Issue 16, 2003, Pages 2047-2058, ISSN 0024-3205, https://doi.org/10.1016/S0024-3205(03)00566-6.

Wang, K., Tang, Z., Yang, C. J., Kim, Y., Fang, X., Li, W., Wu, Y., Medley, C. D., Cao, Z., Li, J., Colon, P., Lin, H., & Tan, W. (2009). Molecular engineering of DNA: Molecular beacons. In Angewandte Chemie - International Edition (Vol. 48, Issue 5, pp. 856–870). https://doi.org/10.1002/anie.200800370

Wang, X., Zhang, Y., Kong, H., Cheng, J., Zhang, M., Sun, Z., Wang, S., Liu, J., Qu, H., & Zhao, Y. (2020). Novel mulberry silkworm cocoon-derived carbon dots and their anti-inflammatory properties. Artificial Cells, Nanomedicine and Biotechnology, 48(1), 68–76. https://doi.org/10.1080/21691401.2019.1699810

Wang, Z., Yu, J., Zhang, X., Li, N., Liu, B., Li, Y., Wang, Y., Wang, W., Li, Y., Zhang, L., Dissanayake, S., Suib, S. L., & Sun, L. (2016). Large-Scale and Controllable Synthesis of Graphene Quantum Dots from Rice Husk Biomass: A Comprehensive Utilization Strategy. ACS Applied Materials and Interfaces, 8(2), 1434–1439. https://doi.org/10.1021/acsami.5b10660

Wareing, T. C., Gentile, P., & Phan, A. N. (2021). Biomass-Based Carbon Dots: Current Development and Future Perspectives. In ACS Nano (Vol. 15, Issue 10, pp. 15471–15501). American Chemical Society. https://doi.org/10.1021/acsnano.1c03886

Wei Wang, Yongmao Li, Lu Cheng, Zhiqiang Cao and Wenguang Liu, Water-soluble and phosphorus-containing carbon dots with strong green fluorescence for cell labeling, J. Mater. Chem. B, 2014, 2, 46-48, DOI: 10.1039/C3TB21370F

Werner, R. A., Higuchi, T., Pomper, M. G., & Rowe, S. P. (2021). Theranostics in oncology—thriving, now more than ever. Diagnostics, 11(5). https://doi.org/10.3390/diagnostics11050805
Wicki, A., Witzigmann, D., Balasubramanian, V., & Huwyler, J. (2015). Nanomedicine in cancer therapy: Challenges, opportunities, and clinical applications. In Journal of Controlled Release (Vol. 200, pp. 138–157). Elsevier B.V. https://doi.org/10.1016/j.jconrel.2014.12.030

Wilhelm, S., Tavares, A. J., Dai, Q., Ohta, S., Audet, J., Dvorak, H. F., & Chan, W. C. W. (2016). Analysis of nanoparticle delivery to tumours. In Nature Reviews Materials (Vol. 1). Nature Publishing Group. https://doi.org/10.1038/natrevmats.2016.14

Winkler, J., Abisoye-Ogunniyan, A., Metcalf, K. J., & Werb, Z. (2020). Concepts of extracellular matrix remodelling in tumour progression and metastasis. In Nature Communications (Vol. 11, Issue 1). Nature Research. https://doi.org/10.1038/s41467-020-18794-x

Woo Kim, K., Choi, T.-Y., Min Kwon, Y., & Young Hwan Kim, J. (2020). Simple synthesis of photoluminescent carbon dots from a marine polysaccharide found in shark cartilage. https://doi.org/10.1016/j.ejbt.2020.07

Woodard, L. N., & Grunlan, M. A. (2018). Hydrolytic Degradation and Erosion of Polyester Biomaterials. In ACS Macro Letters (Vol. 7, Issue 8, pp. 976–982). American Chemical Society. https://doi.org/10.1021/acsmacrolett.8b00424

Wu, P., & Yan, X. P. (2013). Doped quantum dots for chemo/biosensing and bioimaging. Chemical Society Reviews, 42(12), 5489–5521. https://doi.org/10.1039/c3cs60017c

Wu, C. C., Beird, H. C., Andrew Livingston, J., Advani, S., Mitra, A., Cao, S., Reuben, A., Ingram, D., Wang, W. L., Ju, Z., Hong Leung, C., Lin, H., Zheng, Y., Roszik, J., Wang, W., Patel, S., Benjamin, R. S., Somaiah, N., Conley, A. P., … Futreal, P. A. (2020). Immuno-genomic landscape of osteosarcoma. Nature Communications, 11(1). https://doi.org/10.1038/s41467-020-14646-w

Wucherpfennig, K. W., Gagnon, E., Call, M. J., Huseby, E. S., & Call, M. E. (2010). Structural biology of the T-cell receptor: insights into receptor assembly, ligand recognition, and initiation of signaling. In Cold Spring Harbor perspectives in biology (Vol. 2, Issue 4). https://doi.org/10.1101/cshperspect.a005140

Wytrwal, M., Koczurkiewicz, P., Wõjcik, K., Michalik, M., Kozik, B., Zylewski, M., Nowakowska, M., & Kepczynski, M. (2014). Synthesis of strong polycations with improved biological properties. Journal of Biomedical Materials Research - Part A, 102(3), 721–731. https://doi.org/10.1002/jbm.a.34744

Xiaojuan Zhang, Zhe Guan, PET/CT in the diagnosis and prognosis of osteosarcoma, Frontiers In Bioscience, Landmark, 23, 2157-2165, June 1, 2018

Xu, H., Xie, L., & Hakkarainen, M. (2017). Coffee-Ground-Derived Quantum Dots for Aqueous Processable Nanoporous Graphene Membranes. ACS Sustainable Chemistry and Engineering, 5(6), 5360–5367. https://doi.org/10.1021/acssuschemeng.7b00663

Xu, R., Zhang, G., Mai, J., Deng, X., Segura-Ibarra, V., Wu, S., Shen, J., Liu, H., Hu, Z., Chen, L., Huang, Y., Koay, E., Huang, Y., Liu, J., Ensor, J. E., Blanco, E., Liu, X., Ferrari, M., & Shen, H. (2016). An injectable nanoparticle generator enhances delivery of cancer therapeutics. Nature Biotechnology, 34(4), 414–418. https://doi.org/10.1038/nbt.3506

Xu, X., Ray, R., Gu, Y., Ploehn, H. J., Gearheart, L., Raker, K., & Scrivens, W. A. (2004). Electrophoretic analysis and purification of fluorescent single-walled carbon nanotube fragments. Journal of the American Chemical Society, 126(40), 12736–12737. https://doi.org/10.1021/ja040082h

Yang, S. T., Wang, X., Wang, H., Lu, F., Luo, P. G., Cao, L., Meziani, M. J., Liu, J. H., Liu, Y., Chen, M., Huang, Y., & Sun, Y. P. (2009). Carbon dots as nontoxic and high-performance fluorescence imaging agents. Journal of Physical Chemistry C, 113(42), 18110–18114. https://doi.org/10.1021/jp9085969

Yang, Y., Cui, J., Zheng, M., Hu, C., Tan, S., Xiao, Y., Yang, Q., & Liu, Y. (2012). One-step synthesis of amino-functionalized fluorescent carbon nanoparticles by hydrothermal carbonization of chitosan. Chemical Communications, 48(3), 380–382. https://doi.org/10.1039/c1cc15678k

Yang, Y. H., Haile, M., Park, Y. T., Malek, F. A., & Grunlan, J. C. (2011). Super gas barrier of all-polymer multilayer thin films. Macromolecules, 44(6), 1450–1459. https://doi.org/10.1021/ma1026127

Yasuhiro Matsumura, Hiroshi Maeda; A New Concept for Macromolecular Therapeutics in Cancer Chemotherapy: Mechanism of Tumoritropic Accumulation of Proteins and the Antitumor Agent Smancs1. Cancer Res 1 December 1986; 46 (12_Part_1): 6387–6392.

Yokoi, K., Chan, D., Kojic, M., Milosevic, M., Engler, D., Matsunami, R., Tanei, T., Saito, Y., Ferrari, M., & Ziemys, A. (2015). Liposomal doxorubicin extravasation controlled by phenotype-specific transport properties of tumor microenvironment and vascular barrier. Journal of Controlled Release, 217, 293–299. https://doi.org/10.1016/j.jconrel.2015.09.044

Yola, A. M., Campbell, J., & Volodkin, D. (2021). Microfluidics meets layer-by-layer assembly for the build-up of polymeric scaffolds. Applied Surface Science Advances, 5. https://doi.org/10.1016/j.apsadv.2021.100091

Yu, X., & Pishko, M. v. (2011). Nanoparticle-based biocompatible and targeted drug delivery: Characterization and in vitro studies. Biomacromolecules, 12(9), 3205–3212. https://doi.org/10.1021/bm200681m

Yuan, X., Gajan, A., Chu, Q., Xiong, H., Wu, K., & Wu, G. S. (2018). Developing TRAIL/TRAIL death receptor-based cancer therapies. In Cancer and Metastasis Reviews (Vol. 37, Issue 4, pp. 733–748). Springer New York LLC. https://doi.org/10.1007/s10555-018-9728-y

Yuan, Xiaochan, Zhiming Liu, Zhouyi Guo, Yanhong Ji, Mei Jin, and Xinpeng Wang. 2014. 'Cellular Distribution and Cytotoxicity of Graphene Quantum Dots with Different Functional Groups'. Nanoscale Research Letters 9 (1): 108. https://doi.org/10.1186/1556-276X-9-108.

Yuan, W., Dong, H., Li, C. M., Cui, X., Yu, L., Lu, Z., & Zhou, Q. (2007). pH-controlled construction of chitosan/alginate multilayer film: Characterization and application for antibody immobilization. Langmuir, 23(26), 13046–13052. https://doi.org/10.1021/la702774a

Yuan, Y., Guo, B., Hao, L., Liu, N., Lin, Y., Guo, W., Li, X., & Gu, B. (2017). Doxorubicin-loaded environmentally friendly carbon dots as a novel drug delivery system for nucleus targeted cancer therapy. Colloids and Surfaces B: Biointerfaces, 159, 349–359. https://doi.org/10.1016/j.colsurfb.2017.07.030

Zhang, Y., Yang, J., Zhao, N., Wang, C., Kamar, S., Zhou, Y., He, Z., Yang, J., Sun, B., Shi, X., Han, L., & Yang, Z. (2018). Progress in the chemotherapeutic treatment of osteosarcoma. In Oncology Letters (Vol. 16, Issue 5, pp. 6228–6237). Spandidos Publications. https://doi.org/10.3892/ol.2018.9434

Zhang, Y., Cai, K., Li, C., Guo, Q., Chen, Q., He, X., Liu, L., Zhang, Y., Lu, Y., Chen, X., Sun, T., Huang, Y., Cheng, J., & Jiang, C. (2018). Macrophage-Membrane-Coated Nanoparticles for Tumor-Targeted Chemotherapy. Nano Letters, 18(3), 1908–1915. https://doi.org/10.1021/acs.nanolett.7b05263

Zhao, N., Shi, F., Wang, Z., & Zhang, X. (2005). Combining layer-by-layer assembly with electrodeposition of silver aggregates for fabricating superhydrophobic surfaces. Langmuir, 21(10), 4713–4716. https://doi.org/10.1021/la0469194

Zhao, X., Wu, Q., Gong, X., Liu, J., & Ma, Y. (2021). Osteosarcoma: a review of current and future therapeutic approaches. In BioMedical Engineering Online (Vol. 20, Issue 1). BioMed Central Ltd. https://doi.org/10.1186/s12938-021-00860-0

Zhao, S., Lan, M., Zhu, X., Xue, H., Ng, T. W., Meng, X., Lee, C. S., Wang, P., & Zhang, W. (2015). Green Synthesis of Bifunctional Fluorescent Carbon Dots from Garlic for Cellular Imaging and Free Radical Scavenging. ACS Applied Materials and Interfaces, 7(31), 17054–17060. https://doi.org/10.1021/acsami.5b03228

Zhou, H., Fan, Z., Deng, J., Lemons, P. K., Arhontoulis, D. C., Bowne, W. B., & Cheng, H. (2016). Hyaluronidase Embedded in Nanocarrier PEG Shell for Enhanced Tumor Penetration and Highly Efficient Antitumor Efficacy. Nano Letters, 16(5), 3268–3277. https://doi.org/10.1021/acs.nanolett.6b00820

Zhou, J.; Sheng, Z.; Han, H.; Zou, M.; Li, C. Materials Letters 2012, 66, (1), 222-224.

Zhou, Y., & Dai, Z. (2018). New Strategies in the Design of Nanomedicines to Oppose Uptake by the Mononuclear Phagocyte System and Enhance Cancer Therapeutic Efficacy. In Chemistry - An Asian Journal (Vol. 13, Issue 22, pp. 3333–3340). John Wiley and Sons Ltd. https://doi.org/10.1002/asia.201800149

Zhu, H., Luo, H., Zhang, W., Shen, Z., Hu, X., & Zhu, X. (2016). Molecular mechanisms of cisplatin resistance in cervical cancer. In Drug Design, Development and Therapy (Vol. 10, pp. 1885–1895). Dove Medical Press Ltd. https://doi.org/10.2147/DDDT.S106412

Zhu, J., Zhu, F., Yue, X., Chen, P., Sun, Y., Zhang, L., Mu, D., & Ke, F. (2019). Waste Utilization of Synthetic Carbon Quantum Dots Based on Tea and Peanut Shell. Journal of Nanomaterials, 2019. https://doi.org/10.1155/2019/7965756

Zitka, O., Skalickova, S., Gumulec, J., Masarik, M., Adam, V., Hubalek, J., Trnkova, L., Kruseova, J., Eckschlager, T., & Kizek, R. (2012). Redox status expressed as GSH:GSSG ratio as a marker for oxidative stress in paediatric tumour patients. Oncology Letters, 4(6), 1247–1253. https://doi.org/10.3892/ol.2012.931

Zrazhevskiy, P., Sena, M., & Gao, X. (2010). Designing multifunctional quantum dots for bioimaging, detection, and drug delivery. Chemical Society Reviews, 39(11), 4326–4354. https://doi.org/10.1039/b915139g

Website

https://medical-dictionary.thefreedictionary.com/bone

https://www.who.int/health-topics/cancer#tab=tab_1

https://my.clevelandclinic.org/health/diseases/22213-metastasis-metastatic-cancer

https://www.airc.it

https://www.cancer.net/cancer-types/osteosarcoma-childhood-and-adolescence/introduction

https://www.cancer.net/cancer-types/osteosarcoma-childhood-and-adolescence/statistics

http://www.sarcomahelp.org/reviews/who-classification-sarcomas.html

http://www.sarcomahelp.org/reviews/who-classification-sarcomas.html

https://tumoursurgery.org/tumour-education/bone-tumours/types-of-bone-tumours/telangiectatic-osteosarcoma.aspx

https://tumoursurgery.org/tumour-education/bone-tumours/types-of-bone-tumours/telangiectatic-osteosarcoma.aspx

https://musculoskeletalkey.com/small-cell-osteosarcoma/

https://www.pathologyoutlines.com/topic/bonelgcentralosteo.html

https://radiopaedia.org/articles/parosteal-osteosarcoma-1?lang=us

https://www.cancer.net/cancer-types/osteosarcoma-childhood-and-adolescence/introduction

https://labeling.pfizer.com/ShowLabeling.aspx?id=530#section-1

https://en.wikipedia.org/wiki/Cisplatin

https://go.drugbank.com/drugs/DB01181

https://www.aimac.it/farmaci-tumoure/chemioterapici/cisplatino

https://en.wikipedia.org/wiki/Ifosfamide

https://www.humanitas.it/enciclopedia/principi-attivi/antineoplastici-antitumourali/leucovorin/

https://www.aimac.it/farmaci-tumoure/chemioterapici/ifosfamide#potenziali).

https://en.wikipedia.org/wiki/Methotrexate

https://en.wikipedia.org/wiki/Docetaxel

https://www.pfizermedicalinformation.com/en-us/docetaxel-0/contradictions

https://www.ema.europa.eu/en/documents/product-information/taxotere-epar-product-information_it.pdf

https://www.atcc.org/products/htb-85

https://www.accessdata.fda.gov/drugsatfda_docs/label/1999/50718s06lbl.pdf#:~:text=DESCRIPTION%20Doxil%C2%AE%28doxorubicin%20%20HCl%20liposome%20injection%29%20is%20,relative%20to%20those%20of%20the%20%20unencapsulated%20drug